On the dynamics of tidal plume fronts in the Rhine Region of Freshwater Influence

Rijnsburger, S.

DOI
10.4233/uuid:279260a6-b79e-4334-9040-e130e54b9360

Publication date
2021

Document Version
Final published version

Citation (APA)
Rijnsburger, S. (2021). *On the dynamics of tidal plume fronts in the Rhine Region of Freshwater Influence*. [Dissertation (TU Delft), Delft University of Technology]. https://doi.org/10.4233/uuid:279260a6-b79e-4334-9040-e130e54b9360

On the dynamics of tidal plume fronts in the Rhine Region of Freshwater Influence

ON THE DYNAMICS OF TIDAL PLUME FRONTS IN THE RHINE REGION OF FRESHWATER INFLUENCE

Dissertation

for the purpose of obtaining the degree of doctor
at Delft University of Technology,
by the authority of the Rector Magnificus Prof. dr. ir. T.H.J.J. van der Hagen,
Chair of the Board for Doctorates,
to be defended publicly on
Thursday 14 January 2021 at 15:00 o'clock

by

Sabine RIJNSBURGER

Master of Science in Civil Engineering,
Delft University of Technology, the Netherlands
born in The Hague, the Netherlands.

This dissertation has been approved by

promotor: Prof. dr. J. D. Pietrzak
promotor: Prof. dr. A. R. Horner-Devine
promotor: Prof. dr. A. J. Souza

Composition of the doctoral committee:

Rector Magnificus,	chairperson
Prof. dr. J. D. Pietrzak	Delft University of Technology, promotor
Prof. dr. A. R. Horner-Devine	University of Washington, promotor
Prof. dr. A. J. Souza	CINVESTAV, promotor
Independent members:	
Dr. W. R. Geyer	Woods Hole Oceanographic Institution
Prof. dr. H Burchard	Leibniz-Institute for Baltic Sea Research Warnemünde
Prof. dr. ir. M. Snellen	Delft University of Technology
Prof. dr. ir. M. Verlaan	Delft University of Technology
Prof. dr. ir. S. G. J. Aarninkhof	Delft University of Technology, reserve member

This research was funded by the Applied and Engineering Sciences programme of the Dutch Research Council (NWO).

Printed by Gildeprint - www.gildeprint.nl

Cover design by Sabine Rijnsburger; the cover is based on a Copernicus Sentinel-1 C-band synthetic-aperture radar image at 10-02-2015 06:00.

ISBN 978-94-6366-355-7

An electronic copy of this dissertation is available at http://repository.tudelft.nl/.

CONTENTS

Summary vii

Samenvatting ix

1 Introduction 1
- 1.1 Global importance . . . 1
- 1.2 Conceptual model and key characteristics of river plumes . . . 3
- 1.3 An introduction to the Rhine River plume. . . . 6
- 1.4 Objectives and thesis outline . . . 10

2 Simultaneous measurements of tidal straining and advection 15
- 2.1 Introduction . . . 16
- 2.2 Measurements . . . 19
- 2.3 Results . . . 23
- 2.4 Discussion . . . 30
- 2.5 Conclusion . . . 35

3 The Influence of Tide and Wind on the Propagation of Fronts 39
- 3.1 Introduction . . . 40
- 3.2 Gravity current theory . . . 42
- 3.3 Measurements . . . 43
- 3.4 Results . . . 46
- 3.5 Discussion . . . 57
- 3.6 Conclusion . . . 60
- 3.A Front tracking procedure . . . 61

4 Evolution of multiple plume fronts 63
- 4.1 Introduction . . . 64
- 4.2 Methods . . . 68
- 4.3 Comparison of the model with the field-data . . . 73
- 4.4 Results . . . 77
- 4.5 Discussion . . . 88
- 4.6 Conclusions. . . . 93

5 Multiple internal wave packets 95
- 5.1 Introduction . . . 96
- 5.2 Methods . . . 98
- 5.3 Results . . . 101
- 5.4 Discussion . . . 110
- 5.5 Conclusions. . . . 113

6 Discussion and outlook **115**
6.1 The dynamics in the far-field plume . . . 115
6.2 Tidal plume fronts . . . 116
6.3 Evolution and trapping of tidal plume fronts . . . 117
6.4 The role of internal solitary waves. . . . 117
6.5 Synoptic picture of the Rhine ROFI . . . 118
6.6 Global importance . . . 120
6.7 Future research . . . 121

Bibliography **123**

Acknowledgements **137**

List of Publications **141**

SUMMARY

River plumes are the link between the river and the ocean, and therefore play an important role for the health of coastal and marine ecosystems. As a result of human activity in coastal areas, the freshwater discharge transports anthropogenic inputs into the ocean. It is therefore important to understand the processes controlling transport, dilution and dispersion in river plumes from the river mouth up to tens of kilometers and beyond. River plumes are buoyant bodies of brackish water overlaying saltier water created by freshwater outflow. This thesis focuses on an improved understanding of the dynamics in the Rhine River Plume, which is influenced by strong tidal currents and bottom friction due to a shallow shelf. In particular, we study the plume in two different regimes: 70 - 80 km north of the river mouth and close to the river mouth (within a radius of 20 km).

First, we use field-data to unravel the processes controlling the river plume dynamics 80 km north from the river mouth. The concept of potential energy anomaly is applied to isolate and assess the relative importance of each subprocess. This analysis shows that straining (differential advection) and depth mean advection in cross- and alongshore direction are mainly responsible for the behaviour of the river plume far from the river mouth. From these processes, cross-shore tidal straining has the largest contribution similar to 30 km north of the river outflow. These two processes, in both along- and cross-shore direction, suffice to describe the pathway of freshwater and other substances by extension.

Second, we focus on the dynamics of the tidal plume fronts close to the river mouth. Here, the ebb flow modulates the river discharge periodically. This results in a pulse of freshwater that is bounded by a tidal plume front, which corresponds to an abrupt change in density. Salinity and velocity measurements and radar images indicate that the tidal current, wind speed and direction influence the propagation speed and thickness of the tidal plume fronts, where advection of the fronts plays an important role. As a result of the more energetic spring period, the fronts are thinner, faster and mixed compared to a calm neap tide. Winds can generate thick and fast fronts that correspond to large seabed stresses around the frontal passage. These high stresses near the seabed indicate that the passage of tidal plume fronts in shallow coastal regions can contribute to sediment resuspension and transport.

Third, a three-dimensional hydrostatic numerical model is used to complement the field-data and obtain insight into the evolution of these fronts in time and space. Passive tracers are used to identify and follow the tidal plume fronts during multiple tidal cycles. The model is in good agreement with the field-data. We demonstrate that the tidal plume fronts move onshore and are sustained for multiple tidal cycles. In addition, we show that tidal advection results in elliptical paths, ultimately leading to the “trapping”

of tidal plume fronts close to the river mouth. The Rhine river plume therefore constitutes a multi-frontal system.

Fourth, a combination of the field-data, satellite images, the aforementioned numerical model and a two-dimensional non-hydrostatic numerical model, allows us to show that a tidal plume front is able to release a packet of internal solitary waves propagating horizontally at the boundary of fresh and salt water layers. We hypothesize that the "trapped" tidal plume fronts are able to release internal solitary waves as well, resulting in multiple internal solitary wave packets propagating within the river plume.

Overall, this study leads to an improved synoptic picture of the dynamical processes controlling the transport, dispersion and mixing in the Rhine River Plume.

SAMENVATTING

Rivierpluimen zijn de schakel tussen de rivier en de oceaan en spelen daarom een belangrijke rol voor de gezondheid van kust en zee-ecosystemen. De rivierafvoer transporteert nutriënten en vervuiling in de oceaan als gevolg van menselijke activiteiten in kustgebieden. Daarom is het belangrijk om te begrijpen hoe de processen die het rivierwater vervoeren, verspreiden en vermengen werken over een afstand van de riviermonding tot tientallen kilometers ervandaan. Een rivierpluim ontstaat doordat het zoetere rivierwater bovenop het zoute zeewater drijft. Het doel van dit proefschrift is om de dynamica van de Rijnpluim beter te begrijpen. Die wordt vooral bepaald door sterke getij-gedreven stromingen en bodemwrijving als gevolg van een ondiepe zee. In het bijzonder bestuderen we twee verschillende delen van de rivierpluim: 70-80 km ten noorden van de riviermonding en dichtbij de riviermonding (met een maximale straal van 20 km).

Ten eerste gebruiken we veldmetingen om te onderzoeken welke processen de rivierpluim 80 km ten noorden van de riviermonding beheersen. Het concept van de potentiële energie anomalie is gebruikt om de bijdrage van elk individueel proces te onderzoeken. Deze analyse laat zien dat kustlangse en kustdwarse schering van horizontale dichtheid gradiënten (differentiële advectie ofwel “straining”) en diepte gemiddelde advectie de belangrijkste processen zijn voor het gedrag van de rivierpluim ver weg van de riviermonding. De grootste bijdrage wordt geleverd door kustdwarse getijde-schering net als 30 km ten noorden van de riviermonding. Deze twee processen, in kustlangse- en kustdwarse richting, voldoen om het pad van rivierwater en andere substanties te beschrijven.

Ten tweede richten we ons op de dynamica van de zoetwater fronten dichtbij de riviermonding. In dit gebied wordt de rivierafvoer periodiek gereguleerd door de eb stroming. Dit resulteert in een puls van zoetwater dat omgeven is door een zoetwater front dat een abrupte verandering in dichtheid is. Saliniteitsmetingen, snelheidsmetingen en radarbeelden laten zien dat de getijstroming, windsnelheid en windrichting de snelheid en dikte van de fronten beïnvloed. Advectie van de fronten speelt hierbij een grote rol. De fronten zijn dunner, sneller en zouter tijdens een energieke hoogtijperiode in vergelijking met een rustige laagtijperiode. De wind kan dikke en snelle fronten creëren die overeenkomen met een hoge bodemschuifspanning wanneer het front voorbijkomt. Deze hoge bodemschuifspanningen duiden aan dat de zoetwater fronten bij kunnen dragen aan transport en het in suspensie brengen van sediment in ondiepe kustgebieden.

Ten derde een driedimensionaal hydrostatisch numeriek model is gebruikt om de veldmetingen ruimtelijk aan te vullen en is daarom gebruikt om inzicht te krijgen in de dynamica van de fronten in tijd en ruimte. Passieve numerieke merkstoffen (“tracers”) zijn gebruikt om de zoetwaterfronten te identificeren en te volgen gedurende meerdere

getijcycli. Het model stemt goed overeen met de veldmetingen en de resultaten kunnen daarom gebruikt worden voor interpretatie. De modelresultaten laten zien dat de zoetwaterfronten richting de kust bewegen en voor meerdere getijcycli zichtbaar zijn aan het wateroppervlak. Daarbij laten we zien dat getij-gedreven advectie ertoe leidt dat de zoetwaterfronten de getijstroming volgen en daarom een pad afleggen in de vorm van een ellips. Dit leidt uiteindelijk tot het “vangen” of “recirculeren” van deze fronten in een straal van ongeveer 20 km van de riviermonding. De Rijnpluim is daarom een systeem dat bestaat uit meerdere zoetwaterfronten.

Ten vierde een combinatie van veldmetingen, satellietbeelden, het bovengenoemde numerieke hydrostatische model en een tweedimensionaal niet-hydrostatisch numeriek model zijn gebruikt. Deze hebben laten zien dat een zoetwater front interne golven kan genereren die zich voortbewegen op de grens tussen zoet en zout waterlagen. We veronderstellen dat de “gevangen” zoetwaterfronten ook interne golven kunnen genereren wat resulteert in meerdere interne golfgroepen die zich voortbewegen in een rivierpluim.

Tenslotte heeft deze studie geleid tot vernieuwde inzichten in de dynamische processen die het transport, de verspreiding en de menging in de Rijnpluim beheersen.

1

INTRODUCTION

1.1. GLOBAL IMPORTANCE

River plumes are coastal highways transporting freshwater, fine sediments, phytoplankton and human waste (*Halpern et al.*, 2008). The transport of these substances from rivers into the ocean underpins the global significance of river plumes. River plumes are formed by the river discharge creating buoyant bodies of brackish water overlaying saltier water. These structures can extend up to tens of kilometers away from the river mouth, alter the along- and cross-shelf transport, and determine the final fate of these substances (e.g. *Fong and Geyer*, 2001; *Horner-Devine et al.*, 2015; *Sharples et al.*, 2017). Worldwide, hundreds of river plumes serve as the link between rivers and the ocean. However, the geographic location, the geometry of the coast, the magnitude of the discharge, tidal amplitude, wind stress and many more processes determine the structure of the river plume, the transport of freshwater, the cross-shelf exchange and the rate of mixing with ocean water (*Horner-Devine et al.*, 2015). This results in a variety of river plumes worldwide, each with a different structure, pathway, and impact on the local and global environment.

The pathway of a river plume is dependent among other things on its geographic location due to the influence of the Earth's rotation. For example close to the equator at low latitudes, Earth's rotation hardly influences the freshwater released from the mouth of the river, resulting in an offshore propagating river plume, which reaches far into the ocean. Examples are rivers such as the Amazon and the Congo, which are the largest and second largest rivers in the world (e.g *Lentz and Limeburner*, 1995; *Chao et al.*, 2015). At mid- to high-latitudes, you find river plumes that turn clockwise (anti-clockwise) forming density driven coastal currents that follow the coastline in the Northern Hemisphere (Southern Hemisphere), with examples such as the Delaware (*Whitney and Garvine*, 2006), and the Connecticut River (*Garvine and Monk*, 1974). However, at high-latitudes an extra complexity is added in the form of sea ice, and the river plumes are a source of heat influencing the ocean circulation. Example of high latitude rivers are the MacKenzie River (e.g *Macdonald et al.*, 1995, 1999; *Mulligan and Perrie*, 2019), and Yenisei River (e.g. *Osadchiev et al.*, 2017).

Additionally, the volume of the discharge determines the scale and the duration of the river plume. The Amazon (180,000 m^3/s), Congo (40,000 m^3/s) and Mississippi (30,000 m^3/s) discharges are very large resulting in persistent plumes influencing entire shelf seas and oceans up to 1000 km from the river mouth (e.g. *Lentz and Limeburner*, 1995; *Chao et al.*, 2015; *Cochrane and Kelly*, 1986; *Zavala-Hidalgo et al.*, 2003). In contrast, a very small discharge (5 m^3/s) results in a small buoyant plume that dissipates after reaching a distance of 2.5 - 3 km, such as the Teign River (*Pritchard and Huntley*, 2006). External forces, e.g. wind stress, influence the direction of the plume, as observed in the Columbia River plume (*Hickey et al.*, 2005). The interplay of these processes create region-specific river plumes which constitute unique and complex systems. The key attributes of a river plume, which are transport, rate of mixing (dilution) and spreading (dispersion), therefore have to be measured on a case-by-case basis to truly understand the impact on the marine environment. Additionally, human activities are changing the river plume systems, and therefore their pathways and long term impact.

Around one billion people are living near the coast putting pressure on coastal environments (*Nicholls and Cazenave*, 2010). Large quantities of wastewater, fertilizers, plastics, heavy metals and more human related materials are released into rivers and eventually into the ocean as a result of human activities. Several studies have shown that these large amounts of materials have a local impact on water quality and marine life (e.g. *van der Voet et al.*, 1996), this is further enhanced by coastal erosion which adds more fine sediment to river plumes. Coastal erosion is a global problem, where large populations and industries are at risk (*Nicholls et al.*, 2007). The Netherlands is a classic example of a low-lying country facing structural coastal erosion. They protect their coast nowadays with innovative mega nourishments, such as exemplified by the Sand Engine (*Stive et al.*, 2013; *de Schipper et al.*, 2016).

Furthermore, coastal areas are vulnerable to climate change. Climate change leads to sea level rise, an increase in river discharge and a change in wind fields, which will alter the behaviour of the river plume and therefore its long term impact. The wind will change the shape and direction of a river plume (*Hickey et al.*, 2005), while an increased discharge is expected to influence the transport, dispersion, dilution and overall structure of the plume. Further, climate change will exacerbate coastal erosion giving rise to a higher flood risk and more suspended sediment affecting water quality.

In addition, coastal areas are the engine of civilisation with substantial economic value. Large ports are often located near large rivers resulting in maintenance dredging of navigation channels. In addition, these areas are attractive for the construction of large-scale infrastructural works, such as land reclamations, coastal nourishment, and wind farms. All these human related activities may lead to an increase in fine sediment concentrations in the water column. This increase of sediment may impact the ecosystem by inhibiting light penetration, affecting photosynthesis by phytoplankton, and therefore affecting the food chain. Additionally, these infrastructural works will interact with the local flow field leading to different flow patterns such as recirculations and headland eddies (*Signell and Geyer*, 1991; *Radermacher and Reniers*, 2016).

In summary, there are many mechanisms leading to fine sediment suspension (e.g. fine sand, clay and silt) in river plume waters. Over the past years, many studies have been focusing on understanding suspended sediment transport (*Geyer et al.*, 2004; *Souza*

et al., 2008; *Spahn et al.*, 2009; *Souza and Lane*, 2013), and the transport of other substances such as phytoplankton and plastics (*Joordens et al.*, 2001; *Hickey et al.*, 2010; *van der Hout et al.*, 2017). These studies show that river plumes play an important role in the deposition, resuspension and transport of fine sediments. River-plume-induced stratification leads to a decrease in vertical mixing (*Geyer*, 1993a; *de Nijs et al.*, 2010), and therefore to the trapping of fine sediments near the sea bed (*Joordens et al.*, 2001; *Burchard and Baumert*, 1998; *McCandliss et al.*, 2002; *Pietrzak et al.*, 2011). As a consequence, sediment dynamics and primary production is influenced by the river plume.

Freshwater discharge is an important pathway by transporting anthropogenic inputs into the coastal ocean and beyond. If we want to manage our coasts sustainably, we need to be able to predict the impact of human activities on the local and global climate. This knowledge will allow us to make specific management decisions regarding the amount of anthropogenic nutrients discharged by rivers, dredging and construction in coastal seas. It is therefore important to understand the processes controlling transport, dilution and dispersion in river plumes from the river up to tens of kilometers and beyond.

1.2. CONCEPTUAL MODEL AND KEY CHARACTERISTICS OF RIVER PLUMES

As mentioned in the previous section, the impact of a river plume on the coastal and marine environment depends on many different factors and physical processes determining the structure and dynamics of a river plume. In addition, a river plume consists of regions that are dynamically very different as a result of the balance between physical processes. This thesis is focussed on river plume systems that are influenced by strong tidal currents and bottom friction. Therefore, this section will provide a short summary of the different regions of a river plume studied in this thesis, the influence of tidal currents and bottom friction based on previous studies.

1.2.1. RIVER PLUME ANATOMY

Throughout this thesis we use a classification of river plumes consisting of three dynamical regions: near-field, mid-field and far-field plume (*Garvine*, 1984; *Horner-Devine et al.*, 2015) (Figure 1.1). First, the near-field is the region close to the river mouth where the river water enters the ocean as a jet. The momentum of this freshwater layer exceeds its buoyancy, resulting in intense mixing with saltier sea water. In regions with large tides, the dynamics are dominated by the tidal frequency, and the near-field plume is often referred to as a tidal plume (*Horner-Devine et al.*, 2009; *Nash et al.*, 2009; *Kilcher and Nash*, 2010; *Horner-Devine et al.*, 2015).

Second, the river water flows from the near-field into the mid-field, which is the transition area from the near-field jet towards the buoyancy driven coastal current in the far-field. In this area, Earth's rotation starts to dominate, deflecting the offshore located near-field plume towards the coast. Then, the river water flows into the far-field, where the plume does not have a memory anymore of the initial momentum of the river discharge. The plume becomes a buoyancy driven coastal current balanced by Earth's rotation, wind stress, and sometimes bottom friction. The far-field plume can be forced offshore by wind and currents, otherwise it follows the coastline transferring diluted river

water up to tens of kilometers from the river mouth. We will refer to this direction as downstream, which is away from the river mouth to the right (in the Northern Hemisphere).

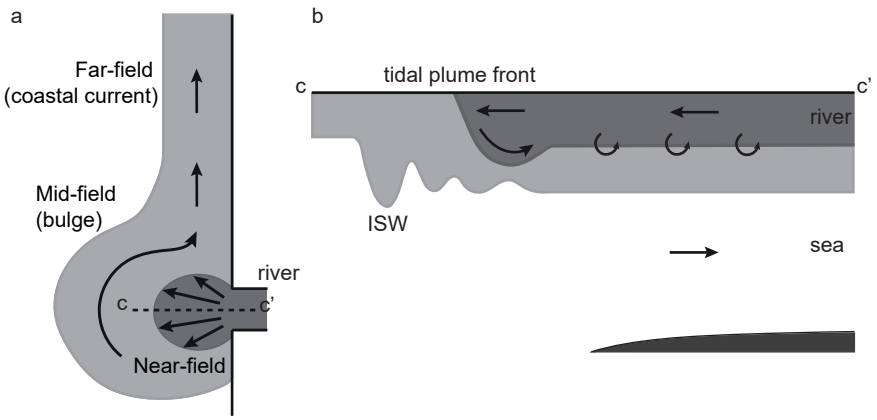

Figure 1.1: Schematic defining river plume with definitions. a) plan view of river plume based on (*Horner-Devine et al.*, 2015). b) cross-section of river outflow with tidal plume front and associated internal solitary waves (ISWs).

1.2.2. TIDAL PLUME FRONTS

In tidally dominated systems, the river discharge is strongly modulated by the tidal wave propagating into the estuary. Consequently, freshwater enters the coastal ocean as a pulse on every ebb forming a tidal plume at the river mouth (*Garvine and Monk*, 1974; *Luketina and Imberger*, 1987; *Horner-Devine et al.*, 2009). The edge of this newly formed plume is a narrow region at the sea surface where the density changes rapidly. This boundary is called the tidal plume front (*Garvine*, 1974a; *Horner-Devine et al.*, 2009). The tidal plume front spreads as a result of the horizontal density difference with the ocean water (Figure 1.1b). The propagation perpendicular to this front results in convergence forcing the receiving ocean and freshwater downward (*Garvine and Monk*, 1974; *O'Donnell*, 1988; *Marmorino and Trump*, 2000). From aerial photos this front is often visible at the sea surface as a line of foam and debris accompanied by fish, birds and phytoplankton, forming a convergence zone separating the riverine water from the ambient receiving water (*Cromwell and Reid Jr.*, 1956; *Garvine*, 1974a). In these frontal regions high amounts of nutrients and phytoplankton are collected due to the convergent flow explaining the large amounts of fish and birds (e.g. *Hickey et al.*, 2010).

The spreading of the riverine water leads to advection, vertical and horizontal mixing, thereby controlling the dispersal of substances (e.g *Garvine and Monk*, 1974; *O'Donnell et al.*, 2008; *Hickey et al.*, 2010; *Horner-Devine et al.*, 2015). Vertical exchange of nutrients between shelf and tidal plume water has been observed in the Columbia River plume (*Orton and Jay*, 2005), changing water mass properties. Therefore, the tidal plume front plays an important role in changing water properties of shelf and plume water. Addition-

ally, observations have shown that the Columbia River plume front can intensify near bed currents and therefore influence the bottom boundary layer leading to resuspension of fine sediments (*Orton and Jay*, 2005; *Spahn et al.*, 2009).

Furthermore, *Nash and Moum* (2005) demonstrated that tidal plume fronts are able to release large internal solitary waves (ISWs), which are waves that propagate within stratified waters (e.g *Ostrovsky and Stepanyants*, 1989) (Figure 1.1b). They suggested that these waves are important for the mixing and transport of plume water and associated biota away from the plume. In addition, these front-generated ISWs impact the dynamics of the tidal plume front by dissipating a large part of their energy into the coastal ocean (*Pan and Jay*, 2009a). In summary, these tidal plume fronts, and associated internal waves, are a large source of energy in the near-field plume that play a large role in setting the properties of plume water that is fed into the far-field.

1.2.3. BOTTOM FRICTION

Bottom friction is another dynamical parameter that impacts the structure, stratification and cross-shore scale of a river plume, which occurs in shallow coastal seas (waterdepth $\approx <$ 30 meters). These systems are also referred to as Regions of Freshwater Influence (ROFIs), with the following definition given by *Simpson* (1997): "the region between the shelf sea regime and the estuary where the local input of freshwater buoyancy from the coastal source is comparable with, or exceeds, the seasonal input of buoyancy as heat which occurs all over the shelf". Liverpool Bay and the Rhine ROFI are two examples of ROFI systems where a shallow shelf, tidal currents, Earth rotation and freshwater discharge control river plume dynamics. In this section, we discuss the role of bottom friction.

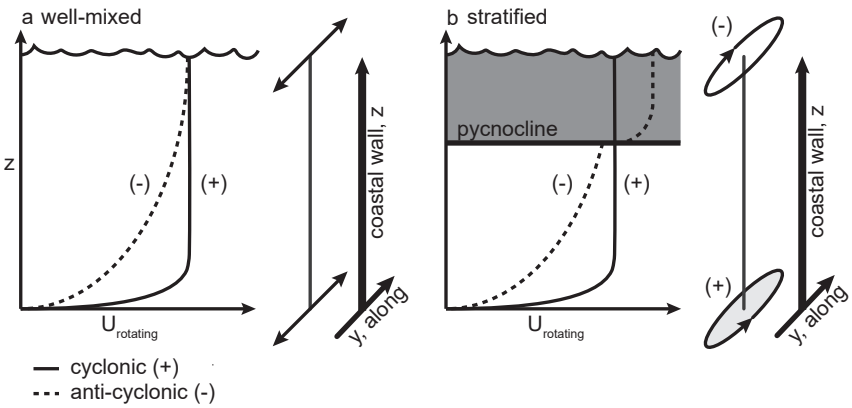

Figure 1.2: Conceptual sketch of the change in vertical structure of the tide, decomposed in a cyclonic (+) and anti-cyclonic (-) rotating velocity component (U), in the presence of a coastal wall. a) well-mixed water column, b) stratified water column. The figure is based on *Visser et al.* (1994) and *Souza and Simpson* (1996).

In shallow waters, bottom friction alters the vertical structure of tidal currents. To investigate this structure, the tidal current can be decomposed into two rotating velocity components following *Prandle* (1982a,b): one rotating cyclonically (+) and the other

one rotating anti-cyclonically (-). A cyclonic rotation is in the same direction as the Earth's rotation, which is anti-clockwise in the Northern Hemisphere. In homogenous waters, *Prandle* (1982a) found that the cyclonic velocity component is not as strongly affected by bottom friction as the anti-cyclonic velocity component. This means that the stresses induced by the bottom friction penetrate higher into the water column for the anti-cyclonic component than for the cyclonic component (Figure 1.2). The two rotating components together result in an almost rectilinear ellipse with a small anti-cyclonic rotation at the surface, and a small cyclonic rotation at the bottom (*Visser et al.*, 1994; *Souza and Simpson*, 1996).

In addition, the proximity of the coast requires that the depth averaged cross-shore velocity is zero. Here, we apply this theory to a tidal current that is parallel to the coastline, such as a progressive Kelvin wave, as in the southern North Sea (Figure 1.2). Therefore, the total horizontal pathway of the velocity vector is a rectilinear ellipse through the entire water column (*de Boer et al.*, 2006) (Figure 1.2).

As mentioned earlier, stratification dynamically decouples the water column as a consequence of reduced vertical mixing. This decoupling changes the tidal current structure, where the cyclonic velocity component is not affected as it is already free stream, but the anti-cyclonic component is decoupled (Figure 1.2). As seen in Figure 1.2, the upper layer is not influenced by bottom friction anymore due to the presence of the pycnocline and can reach a constant surface velocity. The lower layer increases in cyclonic rotation as a shorter water column allows bottom friction to induce a stronger velocity component in the direction of Earth rotation (*de Boer*, 2008). As a result, the upper layer velocity follows the path of an anticyclonic ellipse as it responds less to the Earth's rotation, while the lower layer velocity rotates cyclonically (Figure 1.2). These tidal current ellipses have been observed in both the Rhine and Liverpool Bay ROFI (*Visser et al.*, 1994; *Souza and Simpson*, 1996; *Palmer*, 2009; *Verspecht et al.*, 2009), and play an important role for water column structure and stability in time and space. As a result, bottom stresses increase as tidal turbulence is concentrated in the bottom layer.

The next question is how these tidal ellipses influence water column structure and stability in ROFI's. In shallow waters, large stresses from the tide (via bottom) and the wind (via surface) can penetrate into the water column inducing mixing. That can lead to a well-mixed ROFI for example during storms and large wave periods. However, during low energetic conditions, the freshwater input from rivers induces stratification. In addition, *Simpson et al.* (1990) observed that the vertical tidal shear, as a consequence of bottom friction, interacts with the horizontal density gradient generated by the freshwater discharge. This process is called tidal straining, which can be explained as differential advection of the horizontal density gradients. Tidal straining induces and destroys stratification within one tidal cycle (one elliptical rotation). As a result, a ROFI switches between a stratified and mixed state (*Simpson et al.*, 1990; *Simpson and Souza*, 1995; *Simpson*, 1997; *Rippeth et al.*, 2001), which has consequences on for example the sediment dynamics (*Pietrzak et al.*, 2011).

1.3. AN INTRODUCTION TO THE RHINE RIVER PLUME

This thesis focuses on the Rhine River plume or ROFI in the southern North Sea, which has a substantial impact on the water column structure and sediment dynamics along

the Dutch coast (*Simpson and Souza*, 1995) (Figure 1.3). The Dutch coast is a densely populated area, subject to coastal erosion, vulnerable to sea level rise and economically important because it is home to Europe's largest Port. In light of coastal protection and economic growth, the Dutch coastline has changed over the years, and especially during recent times due to the construction of the Sand Motor (*Stive et al.*, 2013) and the extension of the Port of Rotterdam (Maasvlakte 2). As a consequence of these large scale infrastructural works, the water column needed to be monitored to assess whether a significant increase in fine sediment has occurred. A deeper understanding of river plume processes on sediment dynamics is needed to assess the consequences of such structures in coastal environments for future projects. The rest of this section addresses the current knowledge of the processes controlling the Rhine River plume, where the semi-diurnal tide plays a dominant role.

The Rhine-Meuse River system discharges a yearly average of 2300 m^3/s into the southern North Sea forming the Rhine River plume or ROFI. This plume has a cross-shore width of 20-40 km and extends roughly 100 km downstream (northeastward) from the river mouth (*van der Giesen et al.*, 1990; *Simpson et al.*, 1993). Additionally, the southern North Sea is a shallow shelf with maximum water depths of 30 meters dominated by bottom friction (Figure 1.3). The semidiurnal tide is the most energetic force in the southern North Sea and can be described by a progressive Kelvin wave that propagates parallel to the coast in northeastward (flood) or southwestward (ebb) direction. As a consequence, the tide controls the river plume dynamics in multiple ways.

First, the river discharge is modulated by the tide forming a tidal plume front every ebb, which is a feature shared with other river plume systems (*de Ruijter et al.*, 1997). In the Rhine River plume, the pulse of freshwater formed each ebb is sometimes referred to as a lens. *Hessner et al.* (2001) found that the shape and position of the tidal plume front is primarily determined by the semi-diurnal tidal cycle and only secondarily by the discharge. For instance, the southward directed ebb flow inhibits the tidal plume front from spreading northwards, and therefore it only propagates during the flood phase of the tide (*van Alphen et al.*, 1988; *Hessner et al.*, 2001). When a new tidal plume front is formed, the tidal plume front released on the previous ebb is still visible roughly 8 km downstream of the river mouth (*van Alphen et al.*, 1988; *Hessner et al.*, 2001).

Second, the river plume shows a variation in stratification at a fortnightly frequency, where the freshwater input and tidal energy balance. Typically, the river plume is well-mixed during high energetic periods, such as storms and spring tide (Figure 1.4a), and is stratified during low energetic periods, such as neap tide (Figure 1.4b) (*Simpson et al.*, 1993). Third, *Simpson and Souza* (1995) found that the interaction between the tidal velocity shear and the density field results in the alternation of stratification at a semi-diurnal frequency. These semi-diurnal variations in stratification are only observed during low energetic conditions. During these conditions, the Kelvin wave travels through a two-layer system instead of a well-mixed system (*Visser et al.*, 1994; *Souza and James*, 1996; *Fischer et al.*, 2009).

As mentioned in section 1.2.3, tidal currents on shallow shelves exhibit a different vertical structure under well-mixed and stratified conditions. During well mixed conditions, the tidal current is rectilinear and directed parallel to the coastline (Kelvin wave)

https://www.portofrotterdam.com/en/our-port/port-development/maasvlakte-2

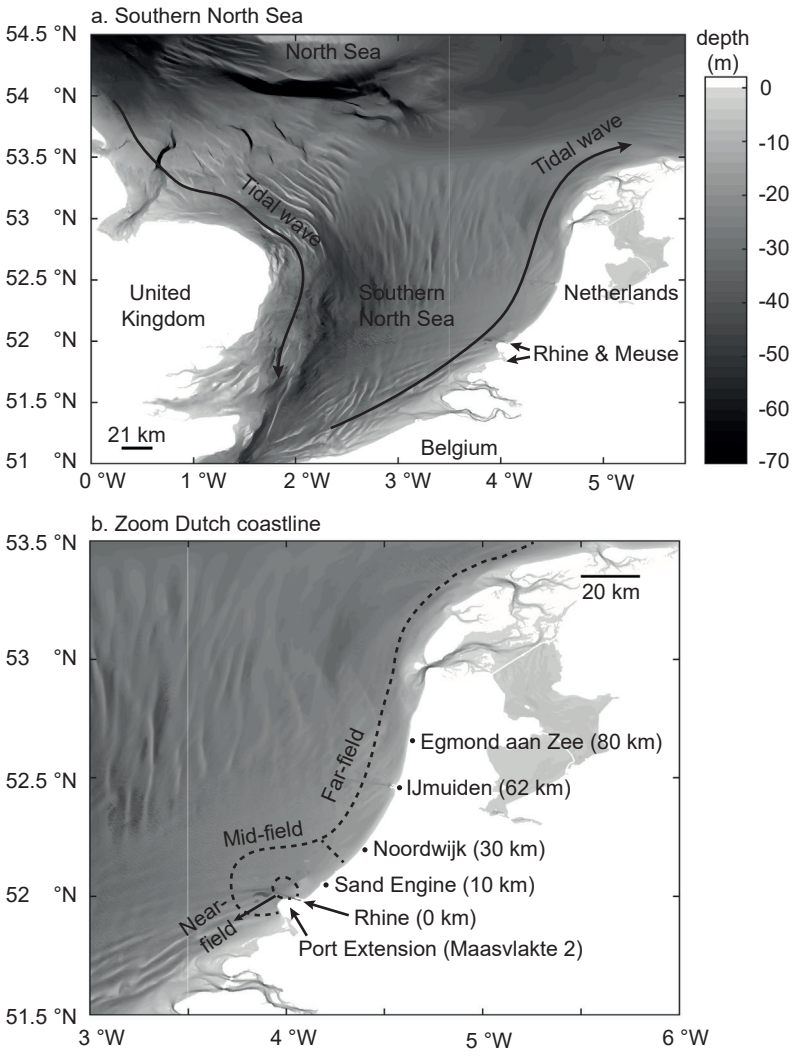

Figure 1.3: Overview of the Southern North Sea (a), and a zoom on the Ducth coast (b). The color represents bathymetry in meters. The dashed lines highlight a schematized Rhine ROFI with the different regions.

with a larger magnitude near the surface (Figures 1.2a and 1.4a). During stratified conditions, a two-layer Kelvin wave propagates along the coast resulting in tidal currents that follow an elliptical path each tidal cycle where the surface and bottom velocities are out of phase (*Visser et al.*, 1994; *Souza and James*, 1996; *Fischer et al.*, 2009). This vertical structure results in strong cross-shore vertically sheared tidal currents, which is the result of reduced vertical mixing generating two decoupled layers (Figures 1.2b and 1.4b). The surface currents rotate anticyclonically (clockwise) and the bottom currents rotate cyclonically (anti-clockwise). So, significant cross-shore currents are present dur-

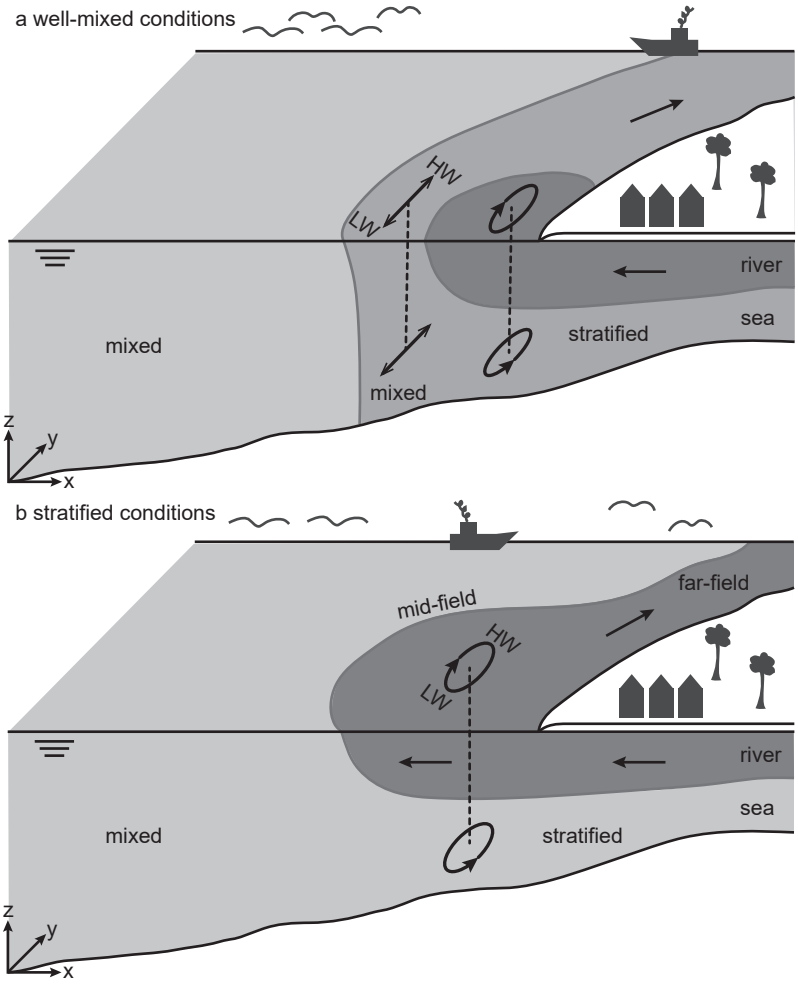

Figure 1.4: A schematic of the the Rhine River plume during a) well-mixed conditions (high energetic) and b) stratified conditions (low energetic). The ellipses show whether the tidal current is almost rectilinear (a) or a well developed ellipse (b) (Figure is after *Simpson* (1997) and *de Boer* (2008)).

ing stratified conditions, while these are almost negligible during well-mixed conditions and only happen close to the river mouth (Figure 1.4).

Simpson and Souza (1995) demonstrated that the aforementioned cross-shore currents interact with the cross-shore density gradient which is defined as tidal straining or cross-shore straining (Figure 1.5). Tidal straining can also be explained as differential advection which induces and destroys stratification during one tidal cycle. In the Rhine River plume, minimum vertical stratification is observed at low water (LW) and maximum vertical stratification at high water (HW). The surface currents rotate anticyclonic

resulting in onshore flow from HW to LW and offshore flow from LW to HW (opposite for the bottom currents) (Figure 1.5). Therefore, from LW to HW offshore surface currents transport freshwater over denser water establishing vertical stratification, while from HW to LW the onshore surface currents transport the freshwater back leading to an almost well-mixed water column again (Figure 1.5).

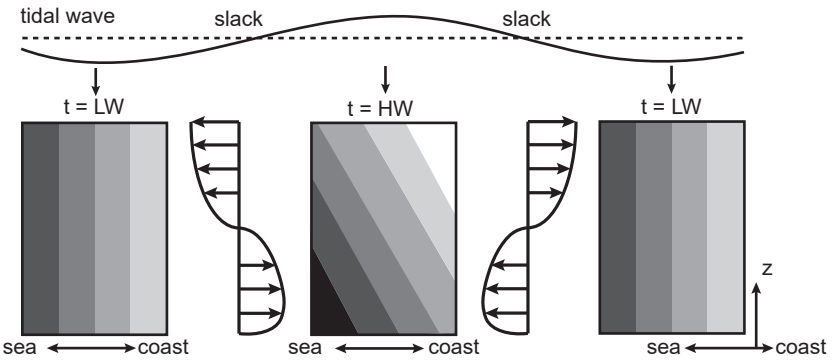

Figure 1.5: Cross-shore tidal straining along the Dutch coast, where the cross-shore current interacts with the horizontal density gradient.

Besides tidal straining, depth mean alongshore advection has been linked to periodic stratification as well (*van Alphen et al.*, 1988). Therefore, *de Boer et al.* (2008) used numerical modelling to investigate the contribution of advection to a vertically stratified river plume. Advection is the movement of the water column over a certain distance by the depth mean velocity without deformation of the water column, while straining deforms the water column due to the vertical shear. They showed that both straining and depth mean advection in both along- and cross-shore directions account for water column stability. Thus, the sum of these four processes determine stratification and is referred to as "advection and strain induced stratification" (ASIPS). However, cross-shore tidal straining has the largest contribution in the far-field, while alongshore depth mean advection dominates in the near- to mid-field plume (*de Boer et al.*, 2008).

The current knowledge of the Rhine River plume shows two main mechanisms controlling the dynamics: ASIPS and the tidal plume fronts. *de Boer et al.* (2008) showed that ASIPS is present at least up to 30 - 40 km from the river mouth. On top of that, the freshwater outflow dominates, resulting in persistent stratification in the near-field. We expect that the tidal plume fronts propagate on top of ASIPS. However, it is uncertain how these two processes influence one another. As river plumes consist of different dynamical regions each with their own processes, each region in this system will have a different dilution rate, impact on cross-shelf exchange, alongshore transport into the next region and finally a different impact on the coastal ecosystem.

1.4. OBJECTIVES AND THESIS OUTLINE

The Rhine River plume has gained relevance over the last years in light of the pressure from climate change, coastal erosion and large-scale engineering projects such as the

Sand Engine and the Port of Rotterdam extension. Turbidity levels were monitored due to the lack of a deeper understanding of the impact of river plume processes on sediment dynamics, and in a broader context the impact of anthropogenic changes on the marine environment. Therefore, the Port of Rotterdam Authority carried out a number of monitoring campaigns throughout the plume in the course of a few years. In addition, longer term measurements near the river mouth were missing. This led to the STRAINS (STRAtification Impacts on Nearshore Sediment transport) field-campaigns in 2013 and 2014, that took advantage of the unique opportunity to make measurements in a system that has been recently changed. The measurements from 2014 are part of this thesis. The overall goal of this thesis is to pursue a further understanding of the Rhine River plume dynamics ranging from the near- to the far-field plume.

This thesis focuses on two specific topics, which both add significant knowledge to other ROFI's and deeper river plume systems. First, this thesis builds on the study of *de Boer et al.* (2008) by exploring the role of straining and advection far downstream (far-field) with the use of a dataset with information in four dimensions: time, depth, along- and cross-shore direction. Second, we focus our attention on the tidal plume fronts present in the near- to mid-field plume, where we want to isolate and understand the role of these fronts. Our objectives are motivated from the need to obtain an improved picture of the river plume dynamics from the near- to the far-field plume and their long term impacts. Therefore, we make use of two novel field campaigns, 80 to 10 km downstream, a three-dimensional hydrostatic numerical model, a two-dimensional non-hydrostatic numerical model, radar and satellite images. These different methods complement each other and give temporal and spatial insights.

Previous studies were mainly performed in the area up to 30 to 40 km from the river mouth, where they highlighted the crucial role of straining and advection (*Simpson et al.*, 1993; *Simpson and Souza*, 1995; *de Boer et al.*, 2008). The existing knowledge on these processes is mainly based on limited in-situ data, such as sparse time series, cross-sections and synoptic remote sensing images, and numerical models that did not focus on the river plume further downstream than 50 to 60 km. Therefore, this thesis will start with an in-depth analysis of a data-set where two vessels sailed simultaneously along two cross-shore parallel transects during one-semi diurnal tidal cycle (chapter 2). This resulted in a four-dimensional dataset of temperature, salinity and velocity collected 70 and 80 km downstream in 2011. The main question addressed in chapter 2 is:

1. What is the contribution of advection and strain-induced stratification in both the cross- and alongshore direction in the far-field plume?

To identify the contribution of these different processes the concept of potential energy anomaly is applied. The potential energy anomaly is defined as the required energy needed to mix the entire water column (*Simpson et al.*, 1990), and is a common tool used in shelf seas for isolating different processes. Chapter 2 applies a 3D potential energy anomaly equation to the field-data to unravel the contribution of straining and advection in the water column stability.

In chapters 3 to 5 the focus switches from the far-field to the near- and mid-field plume, where tidal plume fronts add another dimension to river plume dynamics. Tidal plume fronts in deeper river plume systems have proven to play an important role in

the dispersion and transport of freshwater, phytoplankton and sediments. However, no detailed analysis and significance of these tidal plume fronts have been published so far for the Rhine ROFI. Therefore, in this thesis we elaborate on the current knowledge of these fronts by doing a more quantitative analysis. These chapters use the data obtained during the STRAINS field-campaign in September - October 2014, 10 km downstream of the river mouth at 2 and 6 km offshore.

Chapter 3 focuses on obtaining frontal properties, such as propagation speed, direction, thickness and structure, during different conditions. The semi-diurnal tide influences the propagation of the tidal plume fronts (*van Alphen et al.*, 1988; *de Ruijter et al.*, 1997; *Hessner et al.*, 2001). However, the influence of wind and the spring-neap tidal cycle is unknown, while these processes have been shown to control the structure, shape and position of river plumes (e.g. *Fong and Geyer*, 2001; *Lentz and Largier*, 2006). Therefore, the main research question that is dealt with in chapter 3 is:

2. How do wind and tide influence the propagation and properties of the tidal plume fronts?

This question is answered using the field-data and radar images. Both are used to calculate, observe and compare the different frontal properties.

The field-data gives insight into valuable dynamical properties of the tidal plume fronts. However, the data is limited to two locations and cannot be used to investigate the spatial and temporal movement of these fronts. Therefore, in chapter 4 a realistic 3D hydrostatic numerical model is used to complement the field-data and obtain a synoptic picture of the frontal structure in the near- to mid-field region of the Rhine River plume. This model is set-up as realistically as possible by using realistic bathymetry, coastal geometry, meteorological forcing and river discharges. First, the model is validated against the field-data to examine model performance. After that the model is used to answer the following question:

3. How do the tidal plume fronts evolve in time and space?

Passive tracers (coloured dye) are released by the model to identify and follow the tidal plume front throughout multiple tidal cycles. In total eight different tidal plume fronts are traced, where four relate to a calm neap tide and the other four to a calm spring tide. The evolution and longevity of these tidal plume fronts is assessed by tracing the thickness, propagation speed and horizontal density gradient in time and space. Finally, the processes maintaining or weakening the fronts are examined.

In the Columbia River plume, the tidal plume fronts release internal solitary waves under favourable conditions (e.g. *Nash and Moum*, 2005; *Jay et al.*, 2009). This fission mechanism changes the river and coastal dynamics on different scales. First, it changes the energetics of the tidal plume front itself (*Pan and Jay*, 2009a). Second, it has an impact on the dilution and dispersion of the entire plume (*Nash and Moum*, 2005). Additionally, internal solitary waves are known for their ability to generate large bottom currents impacting the seabed. The Rhine River plume occurs on a shallow shelf, and therefore an impact on the seabed would be a reasonable assumption if these waves would be present in this frictional dominated system. To obtain a more complete picture of the

dynamics of these tidal plume fronts, we would like to investigate the following question in chapter 5:

4. Are tidal plume fronts in a shallow shelf sea able to release ISWs and therefore impact the local mixing and transport processes?

To answer this question, again a combination of different methods is used; the STRAINS field-data is employed in combination with satellite images to find these waves, and estimate basic properties such as amplitude, period and direction. In addition, the numerical model developed in chapter 4 together with a two-dimensional non-hydrostatic numerical model are used to give insight into the possibility of ISW fission from the tidal plume front.

Finally, chapter 6 attempts to provide an answer to the proposed research questions, and discusses the findings obtained in chapters 2 to 5. In addition, suggestions for future research are proposed based on the findings in this thesis.

2

SIMULTANEOUS MEASUREMENTS OF TIDAL STRAINING AND ADVECTION AT TWO PARALLEL TRANSECTS FAR DOWNSTREAM IN THE RHINE ROFI

This study identifies and unravels the processes that lead to stratification and destratification in the far field of a ROFI. We present measurements that are novel for two reasons: (1) measurements were carried out with two vessels that sailed simultaneously over two cross shore transects; (2) the measurements were carried out in the far field of the Rhine ROFI, 80km downstream from the river mouth. This unique four dimensional dataset allows the application of the 3D Potential Energy Anomaly equation for one of the first times on field data. With this equation the relative importance of the depth mean advection, straining and non-linear processes over one tidal cycle is assessed. The data shows that the Rhine ROFI extends 80 km downstream and periodic stratification is observed. The analysis not only shows the important role of cross-shore tidal straining, but also the significance of alongshore straining and depth mean advection. In addition, the non-linear terms seem to be small. The presence of all the terms influences the timing of maximum stratification. The analysis also shows that the importance of each term varies in the cross-shore direction. One of the most interesting findings is that the data are not inline with several hypotheses on the functioning of straining and advection in ROFIs. This highlights the dynamic behaviour of the Rhine ROFI, which is valuable for understanding the distribution of fine sediments, contaminants and the protection of coasts.

This chapter is based on S. Rijnsburger, C.M. van der Hout, O. van Tongeren, G.J. de Boer, B.C. van Prooijen, W.G. Borst, and J.D. Pietrzak (2016). Simultaneous measurements of tidal straining and advection at two parallel transects far downstream in the Rhine ROFI. *Ocean Dynamics*, 66, 719-–736.

2.1. INTRODUCTION

Worldwide, river plumes are formed due to a large freshwater outflow of rivers into coastal seas and oceans. As a result of the Earth's rotation the fresh water discharge deflects towards the coast, forming a downstream plume along the coast (*Chao and Boicourt* (1986), *Fong* (1998), *Garvine* (1999)). River plumes are also referred to as Regions of Fresh water Influence (ROFI), a term introduced by *Simpson et al.* (1993) to demarcate this distinctive region in coastal seas and oceans. The fresh water outflow leads to stratification, while other forces (tide, wind and waves) result in mixing the water column over the vertical. River plumes affect the structure of currents in coastal seas, and thus affect the transport and fate of suspended particulate matter (SPM) in coastal seas. The influence of ROFI's on the distribution of SPM has been investigated for many years. *Geyer* (1993a) showed with numerical modelling that stratification shuts down turbulence at the pycnocline. *de Nijs et al.* (2010, 2011) were some of the first to use in-situ data to show this mechanism. More studies showed that the development of a halocline causes a drop in surface SPM concentrations and an increase in bottom concentrations (*Pietrzak et al.*, 2011; *Souza et al.*, 2007; *Burchard and Baumert*, 1998; *McCandliss et al.*, 2002; *Joordens et al.*, 2001). In addition, understanding the behaviour of SPM is important with respect to the effects of dredging activities, especially for maintenance and protection of the coast, on coastal ecosystems. Understanding the current structure and mixing is important for the biotic environment as SPM influences the light penetration which has an effect on the primary growth of algae (phytoplankton) (*Los et al.*, 2008). It is therefore of great importance to gain a better understanding of the processes influencing the currents along the Dutch coast.

Off the Dutch coast a complex hydrodynamic system is generated by the freshwater discharge of the Rhine River and Meuse River (Figure 2.1). These rivers discharge a yearly average of 2300 m^3/s fresh water into the Southern North Sea creating the Rhine ROFI. This ROFI can be split into a near-field bulge region, around the river mouth, and a downstream plume. The downstream plume can extend 100 km northwards of the river mouth and has a width of 20 to 40 km (*de Ruijter et al.*, 1997). The Rhine ROFI is dominated by friction and tides in contrast to classic river plumes (*Horner-Devine et al.*, 2015). In the Rhine ROFI the tides also determine the release of the freshwater lenses at the river mouth (*de Ruijter et al.*, 1997), which influence the evolution of the entire system. There is a strong interaction between the tides, wind, waves and buoyancy input. As a result, the Rhine ROFI switches between a well-mixed and a stratified state at multiple timescales.

The competition between stratifying and destratifying processes determines the state of the ROFI in time and space (*Simpson et al.*, 1990; *Simpson*, 1997; *Souza and Simpson*, 1997; *de Boer et al.*, 2008). The processes causing stratification and mixing can be classified into reversible and irreversible processes (see table 2.1). Advection and straining (differential advection) are reversible (sometimes called "elastic") and can act both to increase and to decrease stratification. Decrease of stratification can also be caused by irreversible mixing due to wind, wave and tidal energy. Stratification can also be increased by irreversible processes due to the supply of lower density water, such as heating of the surface and freshwater discharges.

The interaction between the tide and stratification in the Rhine ROFI acts on two

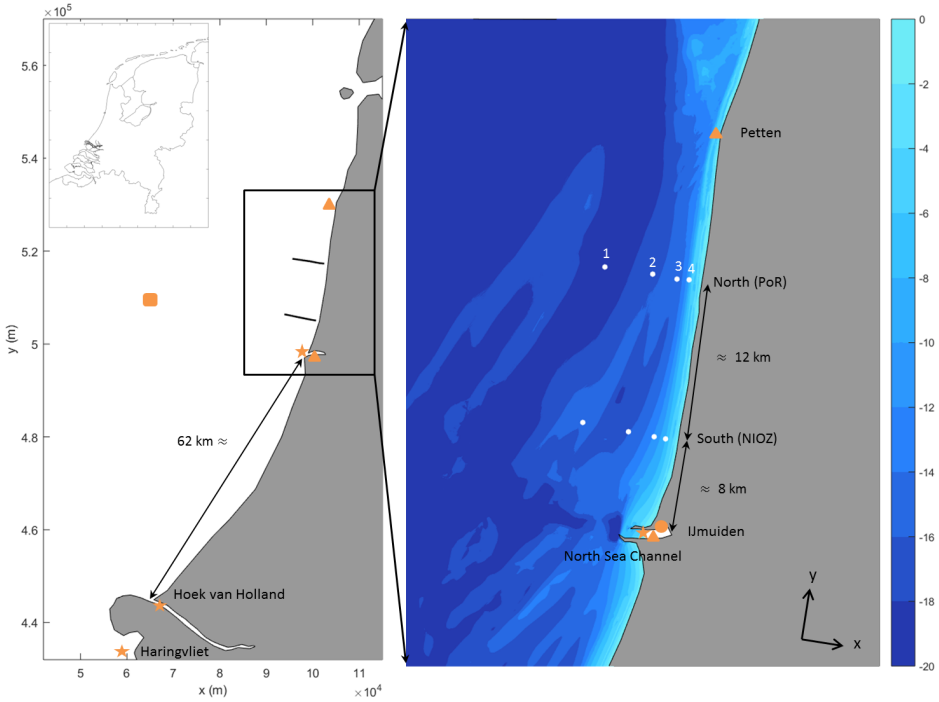

Figure 2.1: The measured transects at the 13th of October 2011. The northern transect is measured by PoR, NIOZ measured the southern transect. The four measuring stations per transect are located at 1,2,4 and 8 km from the coast and are each measured eight times. The triangles represent the measurement stations for the tidal elevations. The square represents the measurement station for the wave data. A circle represents a meteorological measurement station and stars represent stations for discharge data. The bottomtopography is shown in the right panel.

Table 2.1: Overview of the reversible and irreversible stratifying and stirring processes.

	Stratifying	**Destratifying**
Reversible	Strain (S_x, S_y), Advection (A_x,A_y)	Destrain (S_x, S_y), Advection (A_x,A_y)
Irreversible	Surface heating, River discharge	Radiation, Mixing (M_z)

time scales, the fortnightly and the semi-diurnal tidal cycle. First, the fortnightly spring-neap tidal cycle causes the Rhine ROFI to switch between a well-mixed and a stratified system. During spring tide the high kinetic energy enhances mixing and was found to result in a well-mixed ROFI at a location about 30 km downstream of the river mouth (*Simpson et al.*, 1993). In contrast, *Simpson et al.* (1993) showed that the ROFI is stratified during neap tide because of low kinetic energy. During these stratified conditions *Visser et al.* (1994) found tidal currents in the Rhine ROFI, which rotate anti-cyclonically at the surface and cyclonically near the bed.

Second, during low kinetic energy events such as neap tide, *Simpson and Souza* (1995) showed that a semi-diurnal signal of stratification and destratification is present in the Rhine ROFI as well. The aforementioned cross-shore currents interact with the cross-shore horizontal density gradient. This interaction between the tidal velocity shear and the horizontal density gradient is defined as tidal straining (*Simpson et al.*, 1990), which simply can be explained as differential advection and is also referred to as strain induced periodic stratification (SIPS). Tidal straining enhances stratification from low to high water and enhances destratification from high to low water. Besides SIPS and the release of fresh water lenses, also the depth mean alongshore advection has been shown to induce periodic stratification (*van Alphen et al.*, 1988).

From a numerical model study, where both processes SIPS and (alongshore) depth mean advection were investigated, it follows that both cross-shore straining and depth mean alongshore advection play a significant role in the bulge region and in the downstream plume (*de Boer et al.*, 2008). According to this study, one should refer to the sum of the processes as ASIPS (advection and strain induced periodic stratification).

In this study we use field data to investigate the contribution of advection and strain induced periodic stratification (ASIPS) in the along- and cross-shore direction. The novel field data presented here contributes to ROFI knowledge in two ways. First, the study area is located at 80 km downstream of the Rotterdam Waterway, which is in the far-field plume of the Rhine ROFI. Previous studies were performed in the area up to 40 km from the river mouth. Second, the novelty of the data lies in the fourth dimension. The existing knowledge on straining and advection in the Rhine ROFI is based on limited in-situ data only, such as sparse time-series, cross-shore transects and synoptic remote sensing images. Here, we present observations where 2 vessels sailed simultaneously along two cross-shore parallel transects during one semi-diurnal tidal cycle, while measuring over the water column. This resulted in a four-dimensional dataset which contains information in cross-shore, alongshore, depth and time.

This dataset allows us to apply the 3D Potential Energy Anomaly (φ,J/m^3) equation to analyse two parallel transects.*Becherer et al.* (2015) used a similar approach in a curved tidal inlet in the German Wadden Sea. Their study demonstrated the importance of lateral circulation, in addition to classic estuarine circulation. Here the potential energy anomaly equation is used to study the contribution of the stratifying and de-stratifying processes on the evolution of periodic stratification in the Rhine ROFI (*Simpson et al.*, 1990). Both, *de Boer et al.* (2008) and *Burchard and Hofmeister* (2008), derived a (φ) equation for three-dimensional flows in numerical models. We apply the 3D φ equation from *de Boer et al.* (2008) to the field data. The equation needs to be simplified to apply it to the space and time domain of the field data. In addition, not all processes can

be calculated. Section 2.2 describes the method and gives an overview of the dataset used. The most important processes such as straining and depth mean advection will be calculated and presented in the results section, Section 2.3. The relative importance of these processes will be analysed in the discussion, Section 2.4.

2.2. MEASUREMENTS

2.2.1. LOCATION AND INSTRUMENTATION

Two parallel transects were simultaneously measured with the BRA-7 hired by the Port of Rotterdam Authority (PoR) and the Navicula from NIOZ (the Royal Netherlands Institute for Sea Research). On the 13th of October 2011 they sailed simultaneously on two parallel cross-shore transects off the Dutch coast for thirteen hours (Figure 2.1). PoR collected the data of the northern transect located near Egmond aan Zee, 82 km from the New Waterway. The southern transect near Wijk aan Zee, 70 km from the river source, was sailed by NIOZ. Each transect consists of four measurement stations located respectively 1,2,4 and 8 km offshore.

The bathymetry in Figure 2.1 shows that at the Northern transect the depth is typically 20 m offshore decreasing to about 9.5 m onshore. At the Southern transect there is a depression between station 1 and 2 (respectively 8 and 4 km offshore). The depth at station 1, most offshore, is about 15-16 m, this is shallower than the depth at station 2. The depression has a depth of about 17 m. The bathymetry data is measured at 20 m intervals.

Both PoR and NIOZ used a CTD (Conductivity, Temperature and Depth sensors), an OBS (Optical Backscatter Sensor) and an ADCP (Acoustic Doppler Current Profiler) to measure vertical profiles of conductivity, temperature, turbidity and velocities at each station. The OBS and CTD were mounted on the same frame. The ADCP is mounted alongside both ships at a depth between 1-2 m below the water surface. The data is processed following a standard procedure where spikes are removed and the data is averaged over vertical bins. The ADCP data has vertical bins of 0.5 m and the CTD data bins of 0.05 m. Therefore, a general grid is made with steps of 0.5 m. The CTD data is averaged over 0.5 m. Then the CTD and ADCP data are displayed on the same grid.

The sensors of PoR and NIOZ needed intercalibration to be able to interpret the difference between the two transects. Therefore, calibration measurements were carried out at the 14th of October 2011. The two vessels sailed, next to each other, on both transects. The data were used to compare the sensors used by PoR and NIOZ, here we are only interested in the salinity and temperature data. The salinity data are in agreement. The temperature sensors showed a small consistent difference that was corrected. More detailed information on the used instrumentation and procedures can be found in *Rijnsburger* (2014).

2.2.2. ENVIRONMENTAL CONDITIONS

The meteorological data consists of wind, wave, discharge and sea surface data. Wind velocities and direction are measured by the Royal Dutch Meteorological Office (KNMI) at a station near IJmuiden. The sea surface, wave and discharge data are retrieved from the database of *Rijkswaterstaat* (2015). Figure 2.1 shows the location of the measure-

ment stations.

2.2.3. POTENTIAL ENERGY ANOMALY ANALYSIS

The potential energy anomaly, φ, is used to identify the different processes which are involved in the change of the vertical density profile at a given location (*Simpson et al.*, 1990). The potential energy anomaly is defined as the required depth averaged energy which would be needed to mix the entire watercolumn and can be written as

$$\varphi = \frac{1}{H}\int_{-h}^{\eta}(\overline{\rho}-\rho)gz\mathrm{d}z \tag{2.1}$$

The change of φ over time [W/m^3], also called the potential energy anomaly equation, is used to get information of the influence of the stratifying, destratifying and stirring processes.

$$\frac{\partial\varphi}{\partial t} = \frac{g}{H}\int_{-h}^{\eta}\frac{\partial(\overline{\rho}-\rho)}{\partial t}z\mathrm{d}z \tag{2.2}$$

where $H = h+\eta$ is the total water depth [m], η is the free surface relative to Mean Sea level (MSL) [m], h the distance between the bed and the mean water level [m], g is the gravitational acceleration (9,81 m^2/s), z is the vertical coordinate relative to MSL defined positively upwards [m], ρ is the water density [kg/m^3] and $\overline{\rho}$ the depth averaged density. φ defines the actual state of the water column. $\partial\varphi/\partial t$ defines whether the water column is stratifying or destratifying. When $\partial\varphi/\partial t$ is positive the water column is stratifying and when it is negative the water column destratifies or is being mixed.

This study uses the three dimensional potential energy anomaly equation derived for numerical modelling (*de Boer et al.*, 2008) and applies it to field data. The equation is given by

$$\begin{aligned}\frac{\partial\varphi}{\partial t} = \frac{g}{H}\int_{-h}^{\eta}&\left(\begin{array}{cccccc}\overbrace{\tilde{u}\frac{\partial\tilde{\rho}}{\partial x}}^{S_x} & \overbrace{\bar{u}\frac{\partial\tilde{\rho}}{\partial x}}^{A_x} & \overbrace{\tilde{u}\frac{\partial\tilde{\rho}}{\partial x}}^{N_x} & \overbrace{-\frac{1}{H}\frac{\partial\overline{\tilde{u}\tilde{\rho}}H}{\partial x}}^{C_x} & \overbrace{w\frac{\partial\rho}{\partial z}}^{W_z} & +\ldots\\ \underbrace{\tilde{v}\frac{\partial\tilde{\rho}}{\partial y}}_{S_y} & \underbrace{\bar{v}\frac{\partial\tilde{\rho}}{\partial y}}_{A_y} & \underbrace{\tilde{v}\frac{\partial\tilde{\rho}}{\partial y}}_{N_y} & \underbrace{-\frac{1}{H}\frac{\partial\overline{\tilde{v}\tilde{\rho}}H}{\partial y}}_{C_y} & \underbrace{+\frac{\partial\langle\rho' w'\rangle}{\partial z}}_{M_z} & \end{array}\right)zdz+\ldots\\ \int_{-h}^{\eta}&\left(\underbrace{\frac{\partial\langle\rho' u'\rangle}{\partial x}}_{D_x}+\underbrace{\frac{\partial\langle\rho' v'\rangle}{\partial y}}_{D_y}-\frac{1}{H}\left(\underbrace{\langle\rho' w'\rangle|_s}_{D_s}\underbrace{-\langle\rho' w'\rangle|_b}_{D_b}\right)\right)zdz\end{aligned} \tag{2.3}$$

where $\tilde{\rho} = \rho-\bar{\rho}$,$\tilde{u} = u-\bar{u}$ and $\tilde{v} = v-\bar{v}$ are the deviations from the depth mean values, u is the cross-shore component of the velocity and v the alongshore component. Straining in along- and cross-shore direction are presented by the terms S_x and S_y. The terms A_x and A_y are advection in cross- and alongshore direction. The nonlinear interaction between the deviation from both vertical density and velocity are described by N_x and N_y, in other words they represent non-linear straining. Dispersion is described by C_x and C_y. M_z represents the vertical mixing due to turbulence on the vertical density profile. W_z is the vertical advection term(up- and downwelling). The horizontal depth averaged

dispersion terms are described by D_x and D_y. The surface and bed density fluxes are presented by the terms D_s and D_b. The changes in surface elevation and water depth are small and have been neglected.

However, any observational study is limited in spatial extent and time. Therefore, assumptions have to be made and the full three-dimensional equation needs to be simplified in order to apply it to the data. As a result of the availability of the data the following terms from Eq. 2.3 could be calculated: reversible cross-shore straining S_x, alongshore straining S_y, cross-shore depth mean advection A_x, alongshore depth mean advection A_y, cross-shore non-linear straining N_x, alongshore non-linear straining N_y, dispersion in cross- and alongshore direction Cx, y and irreversible mixing M_z (see Eq.2.4). *de Boer et al.* (2008) demonstrated that these are the main terms that give an acceptable representation of the total change of φ in time at a location near the river mouth. The simplified equation becomes:

$$\frac{\partial \varphi_t}{\partial t} \approx \frac{g}{H}\int_{-h}^{\eta}\left(\begin{array}{l}\overbrace{\tilde{u}\frac{\partial\bar{\rho}}{\partial x}}^{S_x}+\overbrace{\bar{u}\frac{\partial\tilde{\rho}}{\partial x}}^{A_x}+\overbrace{\tilde{u}\frac{\partial\tilde{\rho}}{\partial x}}^{N_x}-\overbrace{\frac{1}{H}\frac{\partial\overline{\bar{u}\tilde{\rho}}H}{\partial x}}^{C_x}+\ldots \\ \underbrace{\tilde{v}\frac{\partial\bar{\rho}}{\partial y}}_{S_y}+\underbrace{\bar{v}\frac{\partial\tilde{\rho}}{\partial y}}_{A_y}+\underbrace{\tilde{v}\frac{\partial\tilde{\rho}}{\partial y}}_{N_y}-\underbrace{\frac{1}{H}\frac{\partial\overline{\bar{v}\tilde{\rho}}H}{\partial y}}_{C_y}\end{array}\right)z\mathrm{d}z$$
$$-\underbrace{\epsilon k\rho\left(\frac{|\overline{u}^3|}{h}\right)}_{M_{tide}}-\underbrace{\delta k_s\rho_a\left(\frac{W^3}{h}\right)}_{M_{wind}}-\underbrace{\eta\rho\frac{\pi^2}{h}\left(\frac{SWH}{T}\right)^3}_{M_{wave}} \quad (2.4)$$

Vertical mixing, M_z, is difficult to determine. Turbulent quantities are necessary, which are difficult to measure in the field. One way of determining this term is using the eddy viscosity principle (*Becherer et al.*, 2015). However, the collected dataset does not contain enough information to use this method. Therefore, M_z is calculated analytically following *Simpson et al.* (1990). They determine vertical mixing by dividing it into the components tidal stirring, M_{tide}, and wind stirring M_{wind}. Their study was in the Liverpool Bay area. The area of our transects is much shallower, therefore waves could play a role in mixing the water column as well. Therefore, wave energy is added here according *Wiles et al.* (2006). Within these mixing terms $\overline{u}$ is the depth mean tidal current, W is the wind velocity and ρ_a is the air density (kg/m^3).SWH is the significant waveheight, T the wave period and η is the wave mixing efficiency. A wave mixing efficiency of $4\cdot10^{-6}$ is used based on *Wiles et al.* (2006). The mixing coefficients for tide and wind energy are based on *Simpson et al.* (1991). The effective drag coefficient for bottom stresses, k, is 0.0025, the effective drag coefficient for surface stresses, k_s, is 6.4×10^{-5}, the efficiency for mixing, δ, is 0.039 and the efficiency for mixing, ϵ, is 0.0038. Equation 2.4 will show some difference from the original equation (eq. 2.2) as a result of the omission of the neglected terms of eq. 2.3, due to the limitation of the dataset. In addition the parameterization of the mixing term, M_z, will cause a deviation as well.

Before applying the simplified equation on the data, the missing surface values needed to be extrapolated. Otherwise the PEA terms will be underestimated. Subsequently, the

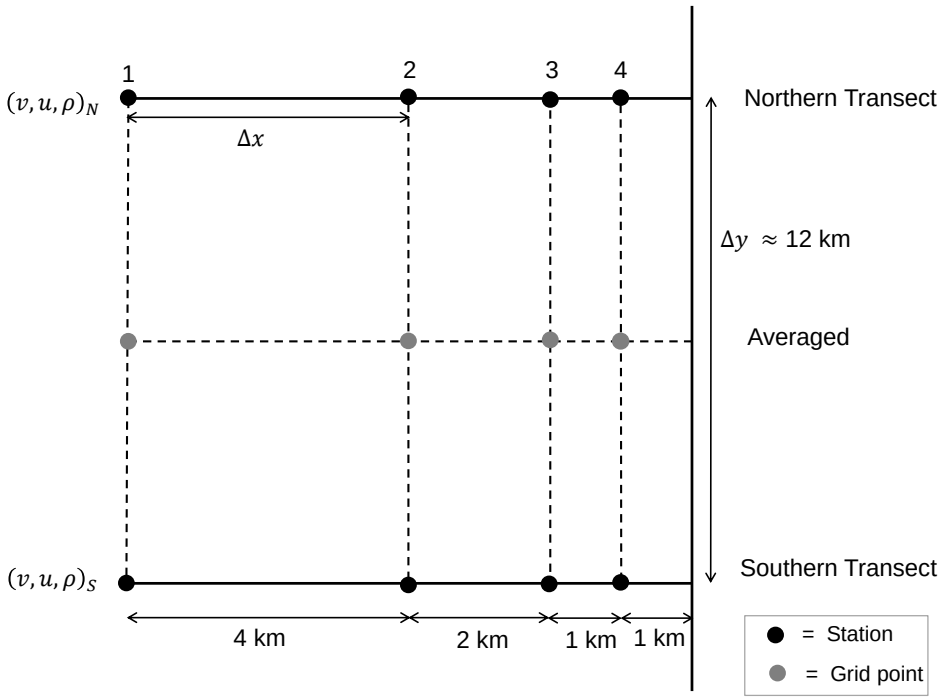

Figure 2.2: A grid of the two transects used for calculating the spatial gradients. Density (ρ) and velocity data (v and u) is available at four points at each transect. These black points represents the measurement stations. The change in density in along- and cross-shore direction is determined at the grey points, in between the two transects. Therefore, the terms of Eq. 2.4 are determined at the grey points as well.

simplified equation (Eq. 2.4) is applied to the study area. To discretize Equation 2.4, a grid is introduced. As gradients have to be defined, a staggered grid is proposed in the alongshore direction. Figure 2.2 shows the spatial grid used based on the two parallel transects. The grid has n by m grid points, where m are the points in alongshore direction and n in cross-shore direction. The outer grid points (m=0 and m=2) represent all the stations where the vessels collected data.

The alongshore terms were calculated in the y-direction with the use of the two transects. The partial derivatives of ρ were estimated at (n,1) between the two transects (at m=1). Due to the limited resolution the estimation of the cross-shore terms was more complicated. The partial derivatives of ρ in the x-direction for the most outer stations (n = 1,4) were calculated using a first order up- and downwind scheme. For the two inner points (n = 2,3) a central scheme was used to calculate the cross-shore derivative.

For calculating the cross-shore derivatives the time was assumed to be instantaneous. This was based on two criteria. First, the maximum time difference between two points iswas 45 minutes. This is much smaller than the duration of one tidal cycle. Secondly, the change of the density in time is small compared to the change in cross-shore direction. Therefore, the assumption of quasi-instantaneous transect measurements is

considered a reasonable approximation.

The accuracy of the equation was checked by comparing it to Equation 2.2, which was calculated based on the measured salinity, temperature and pressure data. If one examines the difference between Eq. 2.2 and Eq. 2.4 this will act as a measure for the missing terms needed for the closure of Eq. 2.3 and the errors introduced due to the different assumptions made for the calculation of the terms. Although we cannot calculate all the terms of Eq. 2.3, the difference allows us to assess what percentage of $\partial\varphi/\partial t$ is accounted for by Eq. 2.4.

2.3. RESULTS

Figure 2.3 highlights the background conditions. Figure 2.4 shows the alongshore velocity, temperature and salinity data in three dimensions, while Figures 2.5 and 2.6 show cross-sections of velocity, salinity, temperature, density difference and the potential energy anomaly per transect. In the following we first consider the background conditions in Section 2.3.1. Secondly, the velocity distribution is considered in Section 2.3.2, then the salinity distribution in Section 2.3.3 and in the end we show the potential energy anomaly analysis in Section 2.3.4.

2.3.1. BACKGROUND CONDITIONS

During the 13th of October the weather was quite calm, wind velocity varied between 3.75 and 4.5 m/s and the wind came from north easterly to easterly direction. The days before were windy, with wind velocity peaking around 12 m/s and blowing from south-west to north-west (Figure 2.3, second panel).

Significant wave heights of 2.5 meter occurred the days before due to the stormy weather. During the measurement campaign, the waves were coming from the North, and had a significant wave height of ~1 meter and a wave period varying between 5.5 and 6.5 seconds (Figure 2.3, third panel).

Figure 2.3 (upper panel) shows the tidal levels during the campaign and the week before. The measuring stations at IJmuiden and Petten Zuid are used to get an impression of the tidal level at both transects. The campaign was carried out one day before spring tide. The campaign lasted for thirteen hours starting just after high water and ending after the next high water. Therefore, an entire semi-diurnal tidal cycle was captured.

At two locations along the Dutch coast fresh river water is discharged into the North Sea. The Meuse and Rhine river discharge via the Maasmond and the Haringvliet into the southern North Sea. Figure 2.3 (lower panel) shows the discharges of both rivers, before and during the measurement period. South of the transect locations the North Sea Channel at IJmuiden releases freshwater at irregular time intervals into the North Sea. The days before the campaign the channel discharged an amount of about 120 m^3/s.

2.3.2. VELOCITY DISTRIBUTION

Distinct southward ebb and northward flood velocities are observed in the Figures 2.4, 2.5 and 2.6. The first panel of Figures 2.5 and 2.6 show that the tidal elevation is assymetrical and out of phase with the depth mean alongshore velocity. The alongshore velocity

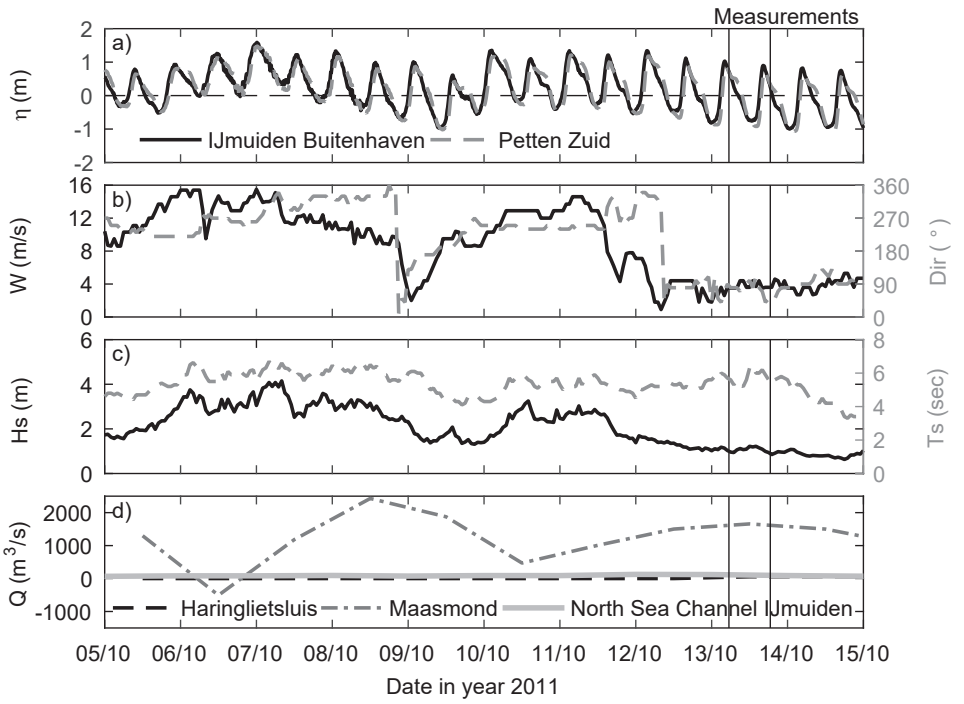

Figure 2.3: The conditions from the 5th of October till the 14th of October 2011. The upper panel shows the tidal elevations at IJmuiden and Petten Zuid. The second panel shows the wind speed and direction collected at a measuring station near IJmuiden. The significant wave height and direction is presented in the third panel. The data is collected from a measuring station near IJmuiden. The last panel gives the discharges from the Haringvliet, the Maasmond and the North Sea Channel IJmuiden. The tidal, wave and discharge information is obtained from the database of Rijkswaterstaat (*Rijkswaterstaat*, 2015). The wind data is retrieved from the KNMI database (www.knmi.nl).

is almost symmetrical though: six and a half hours between the two slack waters is observed. The figures show that the velocity leads the tidal elevation. During high water the velocity leads by one hour and during low water by three hours. The data also shows that the reversal from flood to ebb at the southern transect is about twenty minutes before the switch at the northern transect. No delay is observed when the velocity switches from ebb to flood.

The third panel in Figures 2.5 and 2.6 shows the presence of cross-shore components in the velocities. These velocities have a magnitude between 0 and ± 0.3 m/s. They are 50 % smaller than the alongshore velocity. The data shows periods where the bottom and surface currents are in opposite directions. In particular during the reversal from ebb to flood (track 5 and 6) offshore surface currents and onshore bottom currents are observed. During the reversal from flood to ebb mainly onshore currents are observed over depth. Conceptually, a picture of the plume emerges based on these velocities. During ebb the water flows southwards, the depth mean alongshore advection dominates. During the reversal from ebb to flood cross-shore differential advection is evident. The surface offshore directed and the near bed onshore directed advection of the flow will likely increase stratification during this phase of the tide. During flood the water flows northwards mainly due to depth mean advection and during the reversal from flood to ebb the cross-shore currents advect the fresher water shoreward throughout the water-column.

2.3.3. SALINITY DISTRIBUTION

Figure 2.4 shows the three-dimensional salinity and temperature distribution of both transects. Figures 2.5 and 2.6 also present the salinity and temperature profiles for both transects. They show a minimum salinity of 29.5 psu at the southern transect and 30 psu at the northern transect, which indicates the presence of fresh riverine water (based on e.g. *de Ruijter et al.* (1997) and *van der Giesen et al.* (1990)). Maximum salinity is 32.7 psu for the northern transect and 31.8 psu for the southern transect. Therefore, the southern transect contains fresher water than the northern transect. The northern salinity values are higher than those close to the river mouth. This can be explained by the mixing of the river plume with the surrounding seawater when the plume moves farther northwards. This results in higher salinity values further away from the river mouth. This is shown in the data as well. An alongshore salinity gradient is observed. The northern transect is more saline than the southern transect, with a maximum difference of about 1 psu. The alongshore differences are larger offshore (at 8 km) than closer to the shore. Offshore, a minimum and maximum depth mean alongshore salinity gradient of respectively $3.855 \cdot 10^{-5}$ psu/m and $8.353 \cdot 10^{-5}$ psu/m is observed, where positive is defined northwards. Near shore (at 1 km from the shore) the minimum depth mean salinity gradient is in the order of $1.383 \cdot 10^{-5}$ psu/m and the maximum depth mean salinity gradient is about $4.116 \cdot 10^{-5}$ psu/m. These depth mean salinity gradients indicate that the north is more saline.

In addition to the alongshore salinity gradient, a cross-shore salinity gradient is observed. Figure 2.4 shows more saline water offshore and fresher water onshore. These horizontal differences are an order of magnitude larger than the alongshore gradients. They are in the order of 1.5 psu and 2 psu, resulting in cross-shore salinity gradients of

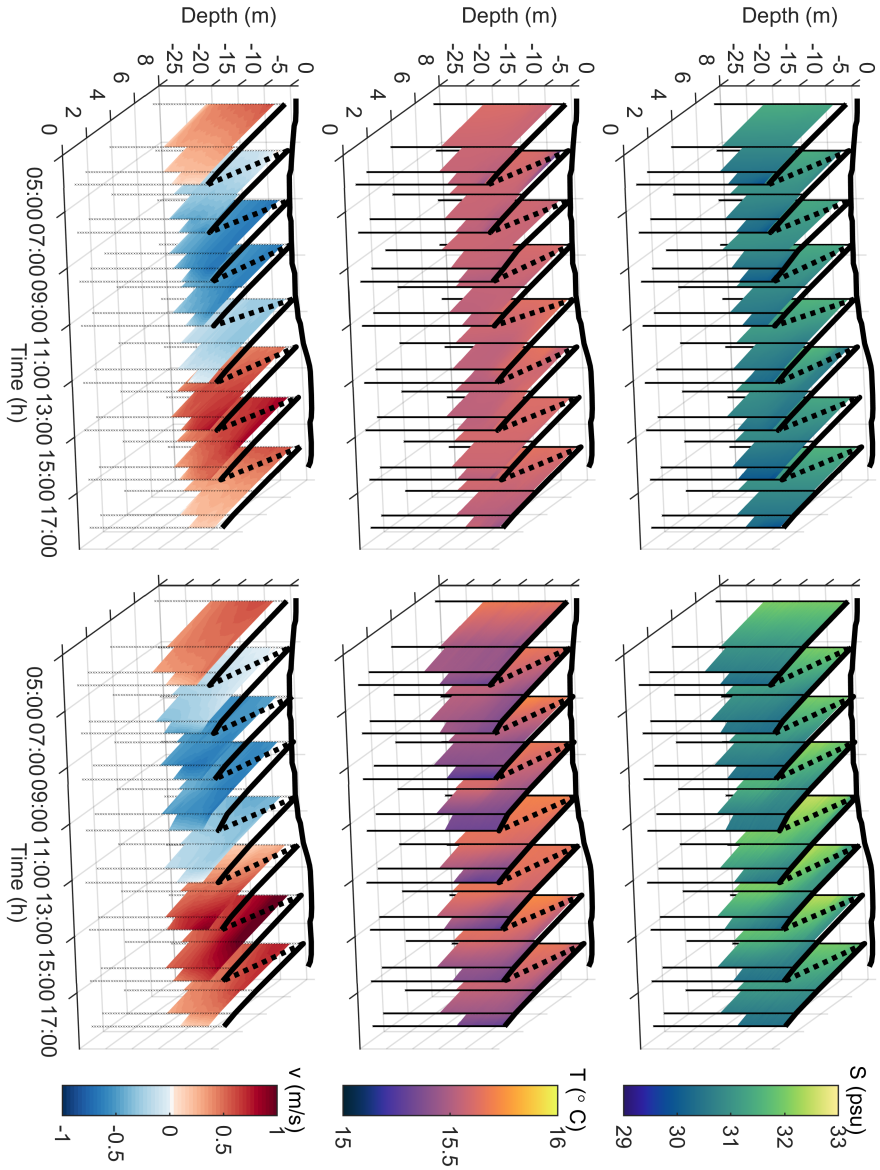

Figure 2.4: The salinity, temperature and alongshore velocity profiles in three-dimensions for both transects. On the left the profiles for the southern transect are shown and on the right for the northern transect. The vertical axis represents the depth and the horizontal axis the time and the distance to the shore. The alongshore tidal velocity is displayed at the back of the figure to indicate the time within the tidal cycle. The measurements started offshore and sailed onshore, this is called a track. From top to bottom the following information is presented: (1) salinity (psu), (2) temperature (°C) and (3) alongshore velocity (m/s), where positive is northwards.

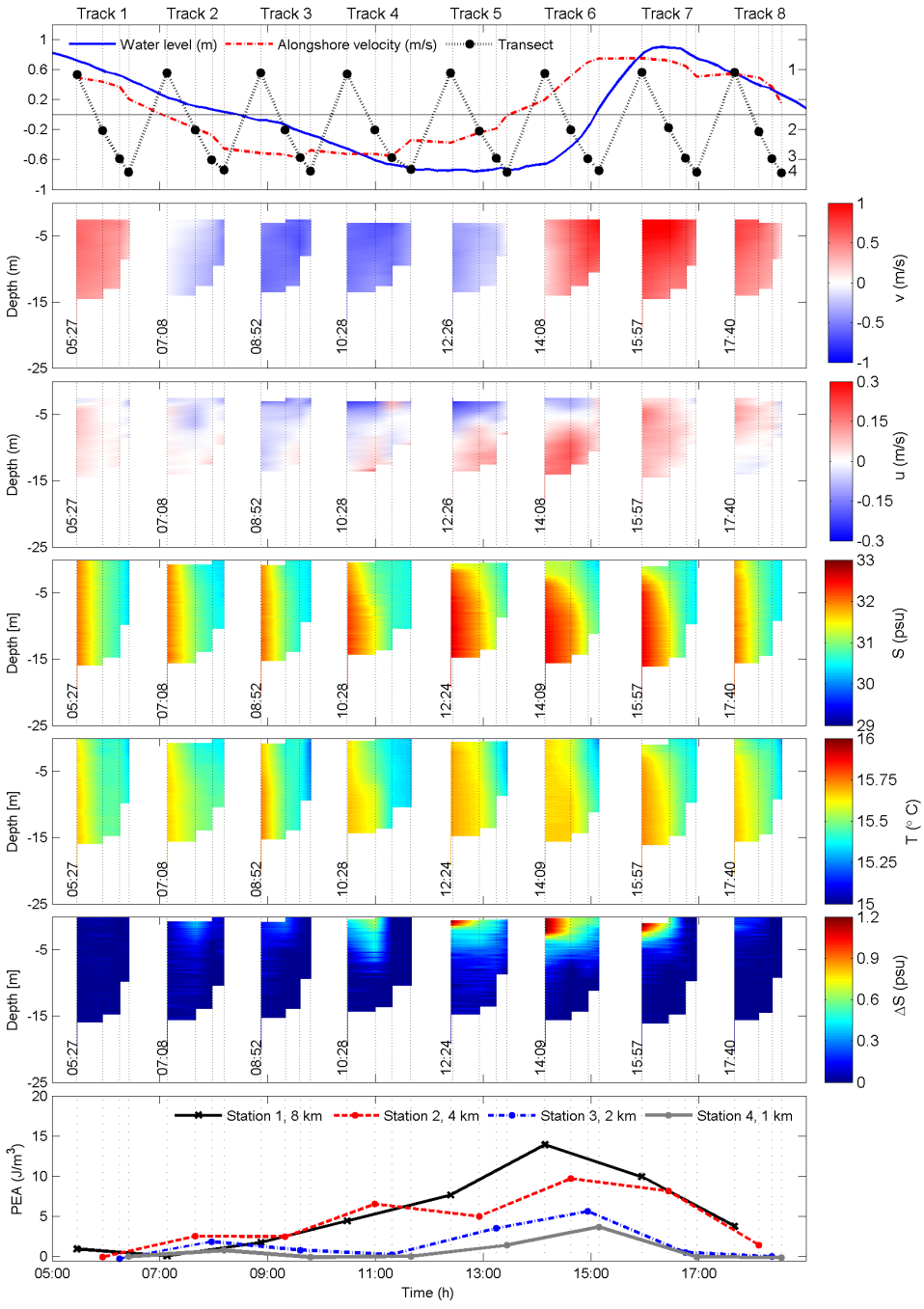

Figure 2.5: Data from the northern transect on the 13^{th} of October 2013. The vertical dotted lines represent the measurement stations with corresponding measurement time. For easy interpretation, the long sailing interval at the end of each track is not interpolated but left blank, unlike Figure 2.4. From top to bottom the following information is presented: (1) the blue line is the tidal elevation in m, in black the sailed traject (top is offshore, station 1). Each transect is sailed from offshore to nearshore. The red dotted line represents the depth mean alongshore velocity in m/s, where positive is northwards, (2) cross-sections of the alongshore velocity in m/s, where positive is northwards. (3) cross-sections of the cross-shore velocity in m/s, where positive is onshore. (4) cross-sections of salinity (psu),(5) cross-sections of temperature (°C) (6) cross-sections of the salinity difference between bottom and location in water column and (7) the potential energy anomaly (φ) in J/m^3.

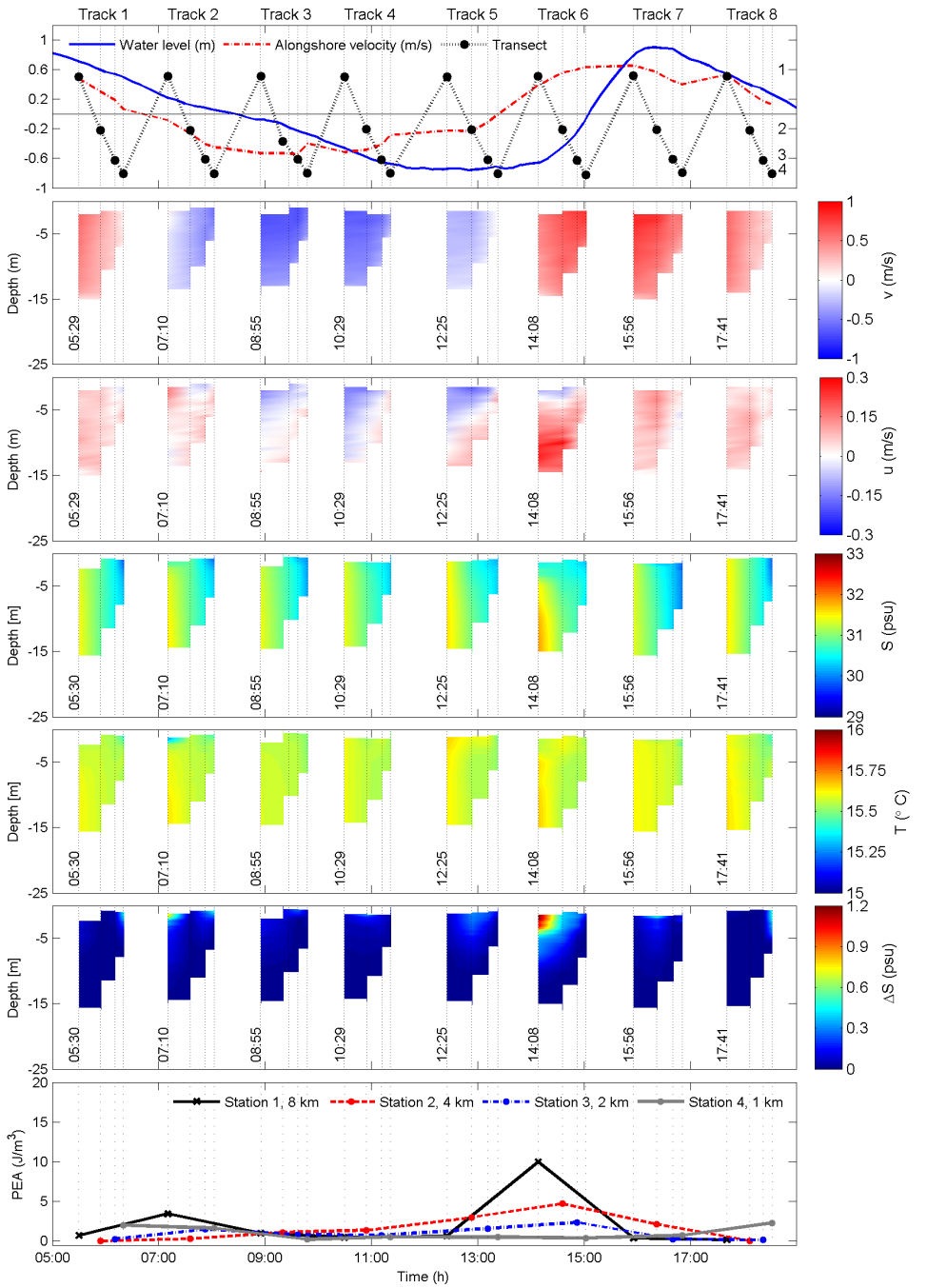

Figure 2.6: Data from the southern transect at the 13^{th} of October 2013. For further explanation see Figure 2.5.

$2.5 \cdot 10^{-4}$ psu/m for the northern transect and $2.0 \cdot 10^{-4}$ psu/m for the southern transect. A positive gradient is defined offshore. The cross-shore gradient is slightly higher for the northern transect.

At the start of the measurements the water column is well-mixed at both transects. During the day fresher water is flowing on top of more saline water, which results in maximum stratification at track 6 (ca. 1-1.5 hour before maximum flood velocities). This results in vertical salinity differences (see Figures 2.5 and 2.6, sixth panel). Both transects show this trend. The maximum vertical salinity difference for both transects is in the order of 1.3 psu. Figures 2.5 and 2.6 indicate a difference in stratification between the northern and southern transect. The northern transect is stratified for a much longer period than the southern transect. The southern transect shows (very) weak stratification at high water slack (between track 1 and 2). The water column returns immediately into a well-mixed state during ebb. Around 1-1.5 hour before maximum flood velocities, the water column is stratified again. The northern transect starts to stratify after maximum ebb velocities, also reaching maximum stratification 1-1.5 hour before maximum flood velocities. From these observations follow that the stratification at the northern transect is larger than at the southern transect (see figures 2.5 and 2.6). So the southern transect is less stratified over the vertical despite the fact that it is fresher, while it would be expected that the southern transect is fresher and more stratified (*de Ruijter et al.*, 1997). Therefore, this will affect ASIPS, because the alongshore depth mean advection A_y will advect a less stratified water column northwards during flood enhancing destratification instead of the other way around.

2.3.4. POTENTIAL ENERGY ANOMALY ANALYSIS

The change of φ in time ($\partial\varphi/\partial t$) is used to identify the competition between the stratifying and stirring processes. When $\partial\varphi/\partial t$ is larger than zero, the water column is stratifying while a negative $\partial\varphi/\partial t$ means that the water column is destratifying or mixing. Figure 2.7 shows the components of the simplified three-dimensional equation (Eq. 2.4) and $\partial\varphi/\partial t$ calculated from Eq. 2.2. It is evident from figure 2.7 that there is a difference between the simplified equation (Eq. 2.4) and $\partial\varphi/\partial t$ (Eq. 2.2). However, in general both equations do show the same trend.

The total response of the water column is interpreted as follows. The total value estimated from the simplified equation (Eq. 2.4) is slightly negative from one hour after maximum flood velocities till maximum ebb velocities, it works in a destratifying manner. At maximum ebb velocities the estimated value becomes increasingly positive, the water column is stratifying till it reaches maximum stratification 1-1.5 hour before maximum flood velocities. Then $\partial\varphi/\partial t$ computed from 2.4 decreases again and the water column goes slowly back to a well-mixed state.

In addition Figure 2.7 shows that each station behaves differently regarding the various terms of the simplified equation Eq. 2.4. Nearshore (at 1km) depth mean advection and straining are hardly present, almost zero and the mixing processes dominate and determine the state of the water column. In the offshore direction the depth mean advection and straining processes become increasingly larger. At 2 km offshore the mixing and $ASIPS + N_{x,y} + C_{x_y}$ terms are all of the same order. The water column is only stratifying just before maximum flood velocities (track 6). More offshore (4 and 8 km)

$ASIPS + N_{x,y} + C_{x_y}$ dominates. The water depth increases and therefore the contribution of mixing processes becomes less important.

Figure 2.7 shows that the total decrease or increase of $\partial\varphi/\partial t$ is mostly dependent on ASIPS, except close to the shore. This is inline with *de Boer et al.* (2008), who concluded that although $C_{x,y}$ and $N_{x,y}$ are large, their sum largely cancels out. Figure 2.8 gives insight into the influence of these individual terms, for each station. This figure shows that the sum of all non-linear terms ($C_{x,y} and N_{x,y}$) is small. Mainly ASIPS dominates at all the stations, except at track 5 and 6 (about one and an half hour till half an hour before maximum flood velocities). At that moment cross-shore dispersion (C_x) comes into play and slightly results in mixing. This is at the moment when the cross-shore surface velocity is directed offshore.

Onshore (1 km) all processes,except for cross-shore dispersion, are hardly preset. At the other stations cross-shore straining (S_x) is generally dominant. At 2 km offshore (station 3) cross-shore straining (S_x) is the main contributor, only at track 4,5 and 6 (about half an hour before till one hour after maximum flood velocities) cross-shore dispersion (C_x) comes into play. The cross-shore straining term, S_x, is in favour of stratification from high water slack till half an hour before maximum flood velocities (after track 2 till track 6). After track 6 (about half an hour before maximum flood velocities) cross-shore straining, S_x, becomes negative and works in favour of destraining the water column.

At the offshore stations (4 and 8 km) all the reversible ASIPS terms and C_x, except A_x, are contributing significantly. Especially from track 4 till 7 all the terms influence the state of the water column. Cross-shore depth mean advection (A_x) only occurs during flood (track 6 and 8). During ebb, from track 2 till track 5, the alongshore straining (S_y) is negative and works in favour of mixing. During ebb the alongshore velocity is headed southwards, as a result the freshwater is advected southwards by the higher surface velocity. During flood (after track 5) the freshwater at the surface is advected northward and act in a stratifying manner. Figure 2.8 shows that the alongshore depth mean advection (A_y) works in the opposite direction of S_y at all the stations. The alongshore depth mean advection (A_y) is positive during ebb and negative during flood, instead of negative during ebb and positive during flood. Based on *de Boer et al.* (2008) both were expected to work in the same direction.

2.4. DISCUSSION

This paper presents measurements off the Dutch coast that are novel in two ways. First, the dataset is collected in the far downstream plume (80 km) instead of close to the mouth of the Rotterdam Waterway as done for the historical cruises. Second, the data consists of two cross-shore parallel transects sailed simultaneously. The three-dimensional Potential Energy Anomaly equation is applied to this dataset to investigate the influence of straining and depth mean advection on stratification. In addition the equation is used to see whether non-linear straining and dispersion are very small. These two items are discussed below.

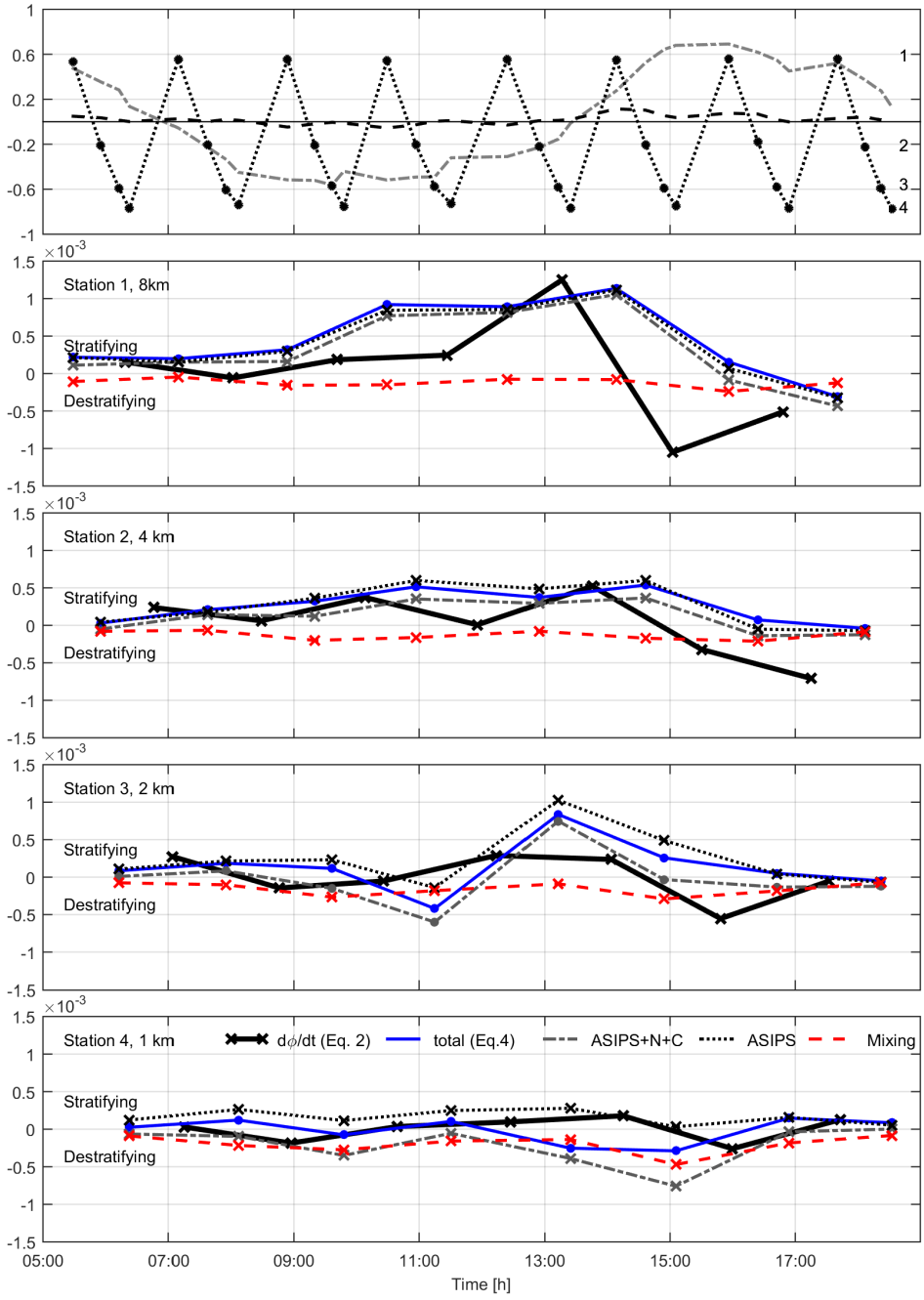

Figure 2.7: The upper panel represents the alongshore (grey dotted line), cross-shore velocity (black dotted line) and the transect sailed (top is offshore, station 1). Each transect is sailed from offshore to nearshore. The second till fifth panels show the contribution of the ASIPS and mixing terms separately, which are determined between the two transects. The local time rate of change of φ in time is also drawn in black (Eq. 2.2). The graph shows for each gridpoint, as in Fig. 2.2, in blue the total of all the terms in Eq.2.4, in grey with a dotted line ASIPS+N+C, with a small dotted black line ASIPS and in red with a dotted line the mixing part. The terms are expressed in W/m^3.

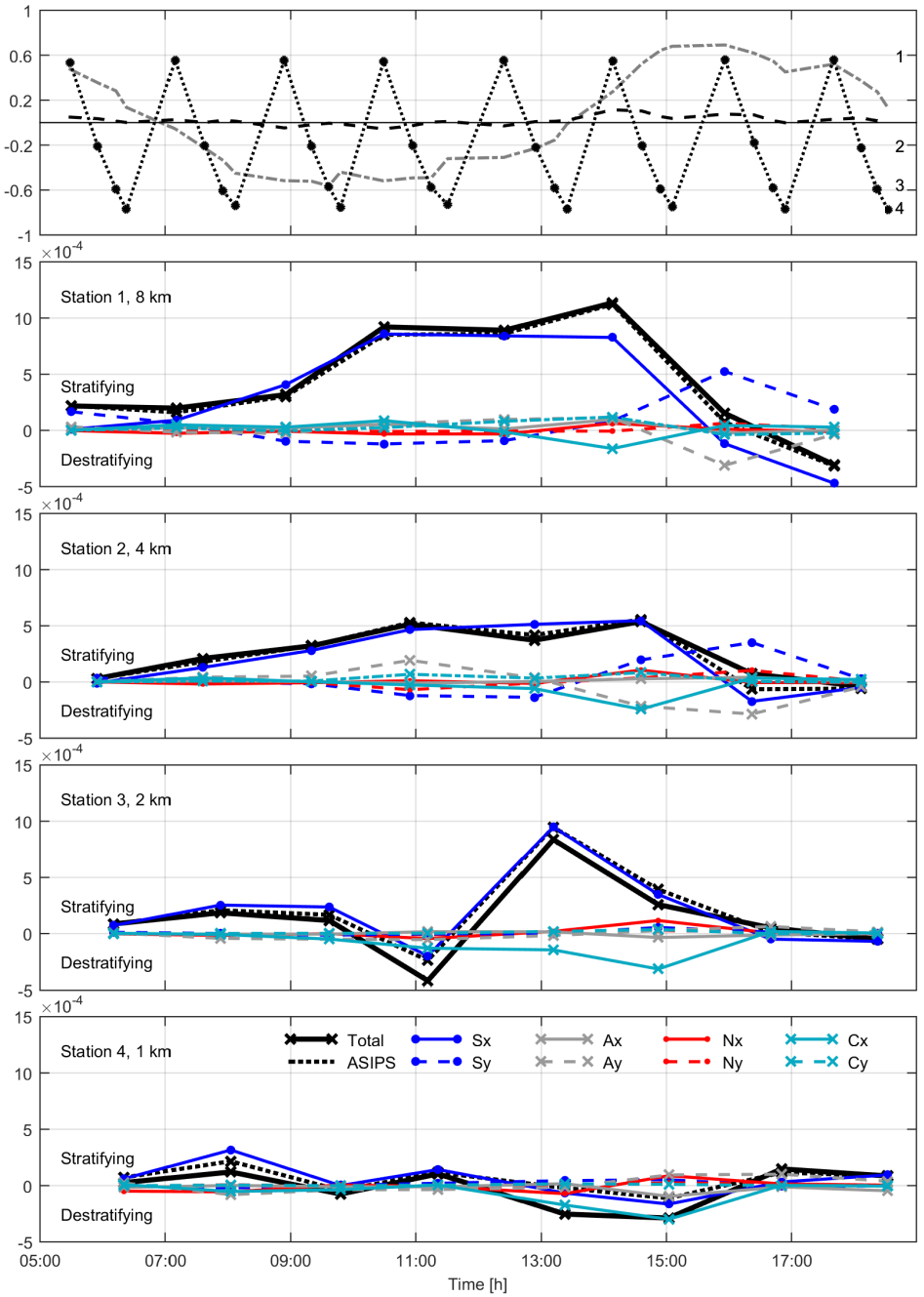

Figure 2.8: The upper panel represents the alongshore (grey dotted line), cross-shore velocity (black dotted line) and the transect sailed (top is offshore, station 1). Each transect is sailed from offshore to nearshore. The second till fifth panels represent the change of φ over time for each measuring station, based on the straining and advection terms (i.e. ASIPS). The terms are determined between the two transects. In black the behaviour of all the terms together (Eq. 2.4) is presented, the dotted black line is ASIPS, in blue the straining term is presented, in grey advection, in red non-linear straining and in light blue dispersion. Where a line represents the cross-shore direction and the dotted line the along-shore direction. The terms are expressed in W/m^3.

2.4.1. STRATIFIED 80 KM DOWNSTREAM

The field data presented here suggests that the Rhine ROFI extends over 80 km downstream, whereas previous studies focused on the area near the river mouth, and only treated the far downstream area as a secondary feature. The observations show periodic stratification at both transects over one tidal cycle. We also found that the southern transect - closer to the river mouth - has fresher waters than the northern transect, while the southern transect is vertically more homogeneous than the northern transect. This has consequences for the stratifying and destratifying processes, as we will discuss later on. Most studies analysing stratification in the ROFI have focused on the bulge region and the near field plume (*Simpson and Souza*, 1995; *Souza and Simpson*, 1997). However, stratification has been observed in the far plume region as well by *van der Giesen et al.* (1990). *de Ruijter et al.* (1992) found weak stratification at Callantsoog, 100 km downstream the river mouth. An analysis of satellite images (*de Boer et al.*, 2007; *Pietrzak et al.*, 2011) found that the plume is expected to extend even further downstream.

Previous studies indicated a stratified state only during neap tides (periods of low energy) and a mixed state during spring tide (*Simpson et al.*, 1990; *de Boer et al.*, 2006). Here we find that one day before spring tide stratification still occurs. The stratification is weak though with maximum vertical salinity difference between surface and bottom of 1.3 psu at both transects. The weak easterly wind could play a role, because it acts in the direction to enhance stratification (*Munchow and Garvine*, 1993; *Fong et al.*, 1997; *Wiechen*, 2011). The wind ageostrophically pushes the surface water in the direction of the wind. In addition wind driven Ekman dynamics advects the water towards the right, in this case northwards. Therefore, fresher surface water will flow over more saline water enhancing stratification.

2.4.2. TWO PARALLEL TRANSECTS

This study, in addition to *Becherer et al.* (2015), shows that a simplified φ equation such as Eq. 2.4 is a useful tool to capture the influence of processes such as straining, depth mean advection, non-linear processes and stirring. However, the change of φ as determined by the ASIPS, non-linear straining, dispersion and mixing terms does not fully describe the local time rate of change calculated with Eq. 2.2. These differences can be ascribed to the simplification of the formula, the parameterization of vertical mixing, interpolation artefacts between ADCP and CTD data, the chosen discretization method and the assumption that the transect measurements are instantaneously. Despite describing 50% of the signals variance, Figure 2.7 shows that the result of equation 2.4 follows the same trend. Therefore this approach can be used qualitatively on in-situ data to investigate the competing processes responsible for changing the stratification.

Korotenko et al. (2012) and *Korotenko et al.* (2014) show that vertical mixing due to tide, wind, waves and bottom topography is important for the vertical density structure. They show that bottom topography (a 5m deep plateau) can play an important role for producing turbulence. In this study the bathymetry is gently sloping with no shallow plateaus. We do not have bathymetry that will create turbulence throughout the water column (Figure 2.1). In addition their studies indicate that a bulk mixing parameterization, such as we applied here, is a rough approximation. However, *de Boer et al.* (2008) used a second order turbulence model (k-epsilon) in a similar fashion to *Korotenko et al.*

(2014) (Mellor-Yamada) to calculate vertical turbulent mixing. In this study *de Boer et al.* (2008) found that the influence of vertical mixing is much smaller than the influence of tidal straining on the evolution of stratification during a tidal cycle. This is in agreement with our findings for low wind speeds. The bulk parameterization was used here because of the limitations of the dataset and for a better closure of the equation.

The φ analysis shows that depth mean advection and straining are dominant at the offshore stations (4 and 8 km) and determine the periodic stratification. Therefore, this analysis shows that alongshore straining and depth mean advection not only contribute to (de)stratification in the bulge region but also in the river plume far downstream. *van Alphen et al.* (1988) suggested that the periodic stratification in the Rhine ROFI is caused by alongshore depth mean advection. In contrast, *Simpson and Souza* (1995) stated that cross-shore tidal straining dominates the ROFI in the downstream plume near Noordwijk (40 km downstream river mouth). Additionally, *de Boer et al.* (2008) showed the importance of both alongshore depth mean advection and cross-shore straining within the bulge and in the downstream plume close to the river mouth. Our data shows that all previous authors were partially right, in the sense that in the ROFI a complex interplay between all depth mean advection and straining modes occurs. Yet, here we find that cross-shore straining is still the largest contributor of ASIPS. It enhances stratification, from maximum ebb till maximum flood velocities, in line with the findings of *Simpson and Souza* (1995).

The non-linear straining terms and alongshore disperion are very small at all locations. However, some cross-shore dispersion is present between maximum ebb and maximum flood velocities. This is when cross-shore surface velocities are offshore directed. This process works in a mixing manner at the onshore and offshore stations. In general the non-linear straining and dispersion terms are small at locations downstream of the river mouth, as found for the case of no wind forcing by *de Boer et al.* (2008).

Onshore (1km from the shore) the mixing processes are dominant. Thus, at the onshore stations no stratification has been observed. This is in line with *de Ruijter et al.* (1997), who observed maximum mixing energy within 3 km from the shore. Closer to the coast it is shallower (the most offshore station is 16-20 m deep, the onshore station is 8 - 10 m deep) resulting in higher mixing energy due to tides, waves and wind. During the measurements the wind conditions were mild though (3.5 - 4 m/s), which resulted in a small contribution of wind and wave stirring.

In this study we find that the alongshore depth mean advection works in favour of stratification during ebb (from north to south) and in favour of de-stratification during flood. This means that exactly the opposite behaviour is observed than expected. According to *de Boer et al.* (2008) alongshore depth mean advection works in the same direction as alongshore straining. The unexpected working of the alongshore depth mean advection is a direct consequence of the more homogeneous waters observed at the southern transect compared to the northern transect. This effect is sketched at items 6 and 8 in Figure 2.9, where an increasing alongshore density gradient in northern direction is visible between the southern and northern transect. During flood the depth mean alongshore current advects a more homogeneous water column northwards, enhancing destratification. This is visible at the end of the flood period (Figure 2.9,item 8). During ebb a more stratified water column is advected southwards inducing stratification,

this is visible at the end of the ebb period(Figure 2.9,item 6). The fact that the northern transect is more stratified than the southern transect is not in line with plume theory. Generally plume theory assumes that on average further away from the river mouth the river plume gradually mixes up, leading to higher salinity and lower stratification (*de Ruijter et al.*, 1997). The field data captures an event that is not in line with this theory. This event might be due to a pulse of fresher water traversing the area during the campaign.

We found that the exact timing of maximum stratification differs from previous studies (*Simpson and Souza*, 1995; *van Alphen et al.*, 1988; *de Boer et al.*, 2008). Maximum stratification occurs between 1 - 1.5 hour before maximum flood velocities (Figure 2.9, between items 6 and 7). *Simpson and Souza* (1995) concluded that minimum stratification occurs at maximum ebb velocities under influence of only cross-shore tidal straining (Figure 2.9, item 1). And maximum stratification occurs at maximum flood velocities (Figure 2.9, item 3). In the situation of only alongshore depth mean advection and straining, minimum stratification was thought to occur at LW slack and maximum stratification at HW slack (*van Alphen et al.*, 1988)(Figure 2.9, items 2 and 4). *de Boer et al.* (2008) pointed out that when the sum of both cross- and alongshore straining and depth mean advection are equal (i.e. ASIPS) maximum stratification occurs at maximum flood velocities plus 1/8 of a tidal cycle.

The difference in timing observed in our campaign of 1-1.5 hour is close to this 1/8 of a tidal cycle. However, it is 1/8 before HW instead of after HW. This can be explained by the unexpected "reverse" behaviour of the alongshore depth mean advection. First, alongshore depth mean advection works in a stratifying manner during ebb velocities, enhancing stratification instead of destratification. Second, it cancels the mechanism of the alongshore straining, therefore the cross-shore processes have a larger contribution in determining the timing of maximum stratification. In normal conditions, where the northern transect is saltier and less stratified, maximum stratification is expected somewhere between t=3T/4 and t=T and minimum stratification between t=T/4 and t=T/2 (Figure 2.9, pattern //). When the northern transect is more stratified and more saline than the southern transect maximum stratification is expected between t=T/2 and t=3T/4 and minimum stratification between 0 and t=T/4(Figure 2.9, pattern \\). It can be concluded that the timing of maximum and minimum stratification depends on the proportion and the direction of ASIPS.

2.5. CONCLUSION

Within this study it is shown that the 3D Potential Energy Anomaly equation can be applied on field data. It showed that the different terms can be estimated giving a picture of the processes that lead to stratification and destratification. As *Simpson and Souza* (1995) showed classic cross-shore straining S_x, *de Boer et al.* (2008) found that depth mean alongshore advection A_y plays a role near the mouth as well. Here we show that both straining $S_{x,y}$ and depth mean alongshore advection A_y are important even in more well-mixed waters 80 km downstream the river mouth. In addition it is shown here that the sum of non-linear straining $N_{x,y}$ and dispersion $C_{x,y}$ are small compared to ASIPS. The importance of cross-shore dispersion increases towards the coast. The question remains about the terms we cannot calculate from Equation 2.3 and the assumptions made which are needed for the closure of this equation. The difference between Equa-

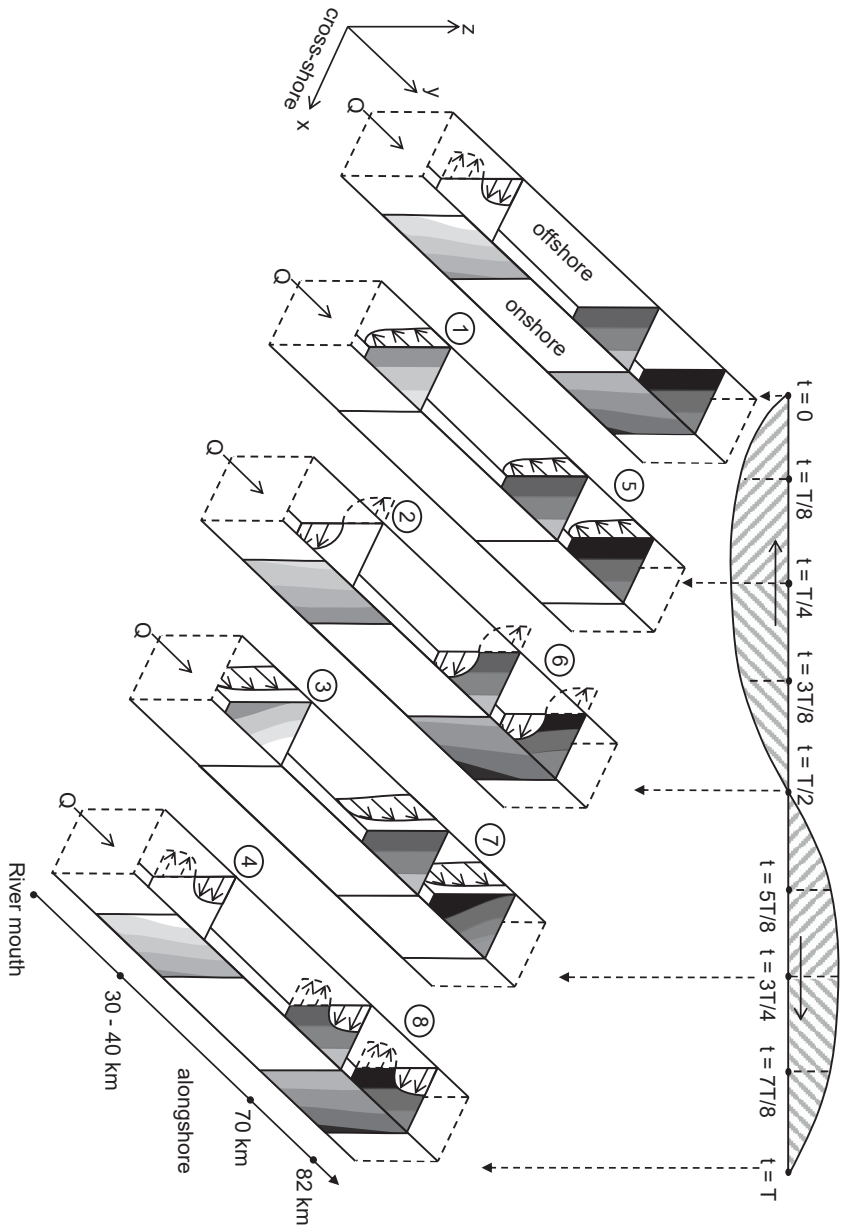

Figure 2.9: A sketch of the downstream plume of the Rhine ROFI in four dimensions, respectively time (with T the tidal period), depth, cross- and alongshore locations. The combined effect of alongshore depth mean advection A_y, alongshore straining S_y (in y direction) and cross-shore straining S_x (in x-direction) is sketched at two different locations in the plume, respectively 30-40 km and 70-82 km from the river mouth. For one tidal cycle, from t=0 till t=T, the influence of the different processes in cross- and alongshore direction is shown. The hashed grey area indicates the period in which minimum and maximum stratification could occur based on the direction and magnitude of all the processes in normal conditions (pattern //) where the north is more saline and less stratified and this campaign (pattern \\) where the northern transect is saltier and more stratified. The numbers 2 and 4 show the maximum influence of only the alongshore advection and straining at slack tide at 30-40 km downstream the river mouth (*van Alphen et al.*, 1988; *de Boer et al.*, 2008). The numbers 6 and 8 show the influence of the alongshore processes 70-82 km downstream that we found in this study. The numbers 1 and 3 show the maximum influence of cross-shore straining at maximum and minimum tidal velocities (*Simpson and Souza*, 1995). The influence of cross-shore straining at two parallel transects 70-82 km downstream is shown by the numbers 5, 6, 7 and 8.

tion 2.2 and Equation 2.4 suggests that these terms could play a role in this area, but this needs further investigation.

A ROFI is a complex interplay between the tidal velocity field and the history of the 3D density structure. This history includes phenomena of various origins at various time scales, such as meteo-driven advection and mixing, and river discharge variations ranging from seasonal to formation of tidal lenses in estuaries and sluices. It is of importance for ROFI knowledge to understand the influence of along and cross shore processes on stratification and the dispersion of the freshwater lenses. These processes are of a direct relevance for the transport of pollutants, SPM and nutrients. In addition, it helps to understand the influence of human interferences and the protection of coasts. The presence of stratification changes the tidal currents and therefore influences the distribution of SPM. As a result of the difference in stratification between the two transects, which are only 12 km apart, it is expected that the local response of SPM could be different. Numerical models such as those by *de Boer* (2008) are an important factor to understand the ROFI systems. They can help interpret the entire area. Field data can help improve these models to reproduce accurately the physics in these systems. This study shows that when companies and institutions strengthen together it can lead to new datasets and extending our knowledge of ROFIs.

3

THE INFLUENCE OF TIDE AND WIND ON THE PROPAGATION OF FRONTS IN A SHALLOW RIVER PLUME

In this study we used field data and radar images to investigate the influence of winds and tides on the propagation of tidal plume fronts. The measurements were collected in a shallow shelf region off the Dutch coast, 10 km north of the Rhine River mouth, and they clearly show the passage of distinct freshwater lenses and associated fronts at the surface that propagate all the way to the coastline. These fronts are observed as a sudden drop in near-surface salinity, accompanied by high cross-shore shear with onshore velocities at the surface. We determined the arrival time to our measurement site, frontal propagation speed, and structure of the fronts by combining the in situ data and radar images. Frontal Froude numbers show a wide range of values, with an average of 0.44. Our results show that fronts during spring tides are thinner, more mixed, and move faster relative to the ground during calm spring tides when compared to calm neap tides. Downwelling winds during spring tides result in thicker and faster fronts; however, the intrinsic frontal propagation speed indicates that the wind and tide control the frontal propagation mainly due to advection rather than by changing the frontal structure. Strong return currents in the near-bed layer resulting from fast and thick fronts increase near-bed turbulence and bed stresses. These high stresses suggest that the passage of fronts in shallow coastal areas can initiate sediment resuspension and contribute to transport processes.

This chapter is based on S. Rijnsburger, R.P. Flores, J.D. Pietrzak, A.R. Horner-Devine, and A.J. Souza (2018). The Influence of tide and wind on the propagation of fronts in a shallow river plume.*Journal of Geophysical Research: Oceans*, 123, 5426–5442.

3.1. INTRODUCTION

River plumes are key in transporting freshwater, nutrients, contaminants, biota and fine sediments into coastal areas (*Kourafalou et al.*, 1996; *Dagg et al.*, 2004; *Joordens et al.*, 2001). They impact the ambient stratification and current structure and could have an impact on sediment transport in shallow areas. Understanding the processes impacting cross-shelf circulation and transport is valuable for areas which are vulnerable to sea level rise and coastal erosion (*Kabat et al.*, 2009; *Nicholls and Cazenave*, 2010). The Dutch coast is a vulnerable coastal area dominated by the freshwater outflow of the Rhine and Meuse Rivers. The Rhine River flows into the shallow southern north sea, forming a 20−40 km wide plume that extends 100 km along the Dutch coast (*de Ruijter et al.*, 1992; *de Kok*, 1996; *de Kok et al.*, 2001). Shallow frictional river plumes are also often referred to as Regions of Freshwater Influence (ROFIs), which can be divided into three dynamical regions: the near-field, around the river mouth, the mid-field, where Earth's rotation starts dominating, and the far-field, where a buoyancy current flows parallel to the coast (*Horner-Devine et al.*, 2015).

River plume fronts are sharp discontinuities in density at the boundary of the river plume, which are often visible at the surface as a line of foam resulting from horizontal convergence and downwelling (*Garvine*, 1974b). Strong fronts are often observed in the Rhine River plume as a result of river water discharged from the estuary on ebb tide. Discharged pulses of freshwater form freshwater lenses which are advected by the tide, ultimately moving on top of the background plume before being mixed into it. At the edges of these lenses fronts are formed due to convergence with the ambient current. Using an idealized model both *de Boer et al.* (2008) and *Fischer et al.* (2009) observed the passage of a freshwater front 8-10 km north of the outflow area (around HW+2 hrs).

The fronts observed in the Rhine are similar to the tidal plume fronts observed in many river plume systems. Prior studies, such as *Garvine and Monk* (1974), found that tidal plume fronts in the near-field are dynamically similar to non-rotating gravity current fronts described using experimental and theoretical gravity current models (*Benjamin*, 1968; *Britter and Simpson*, 1978). In reality tidal plume fronts are seldom two-dimensional as shown in the Connecticut River plume, where an ambient tidal flow normal to the direction of frontal propagation has been observed to cause asymmetric spreading of the plume (*Garvine*, 1974a; *O'Donnell*, 1988, 1990). They found that part of the front is hindered by the opposite directed tidal flow causing the front to thicken. Additionally, field studies have observed convergence and downwelling at the tip of tidal plume fronts with convergence rates of -0.01 to -0.09 s^{-1} and corresponding downwelling velocities of -0.03 to -0.20 ms^{-1} (*Garvine and Monk*, 1974; *O'Donnell et al.*, 1998; *Marmorino and Trump*, 2000).

Prior studies have investigated the important influence of wind on plume dynamics and transport, showing that upwelling winds make the plume wider, thinner and eventually detach it from the coast (*Fong and Geyer*, 2001), whereas downwelling winds compress the plume against the coast, causing the plume to narrow and thicken (*Lentz and Largier*, 2006; *Moffat and Lentz*, 2012). These wind-induced plume dynamics are also expected to impact the behavior of the plume fronts. Upwelling winds are expected to mix and weaken the offshore plume front, while downwelling winds may intensify fronts as a result of deepening.

The Rhine ROFI is not a classical surface-advected plume attached to the coast as defined by *Yankovsky and Chapman* (1997). In the southern North Sea the combination of significant tidal amplitudes and a shallow shelf result in a strongly frictional system. The tide propagates as a Kelvin wave along the Dutch coast and the combination of the tidal dynamics, high friction, vertical stratification due to the plume and earth's rotation result in cross-shore tidal straining. *Visser et al.* (1994) found that during calm conditions (such as neap tide) tidal currents rotate anti-cyclonically near the surface and cyclonically near the bed, leading to counter rotating ellipses. This means that the direction of the tidal currents change at the surface and the bed during one semi-diurnal tidal cycle, leading to cross-shore vertically sheared tidal currents that interact with the horizontal density gradient inducing and destroying vertical stratification during one tidal cycle. This process is called cross-shore straining or tidal straining and is dominant in the far field, 30-80 km downstream from the river mouth (*Simpson and Souza*, 1995; *Souza and Simpson*, 1996; *de Boer et al.*, 2008; *Rijnsburger et al.*, 2016). From low water (LW) to high water (HW) the cross-shore currents are directed offshore at the surface and onshore near the sea bed. As a result the plume is displaced offshore and due to continuity this leads to upwelling at the coast (*de Boer et al.*, 2007) and an increase of vertical stratification. From LW to HW the cross-shore currents are directed onshore at the surface and offshore near the bed, advecting the plume back onshore. This leads to downwelling and mixing, resulting in a decrease of stratification. The entire Rhine ROFI, with freshwater lenses, is advected anti-cyclonically by the tidal currents during one tidal cycle.

Fine sediment transport is important for the Dutch coast, because of its vulnerability to coastal erosion and flooding. Therefore, limitations were set for the turbidity in the coastal region due to the construction of large scale engineering projects such as an extension of the Port of Rotterdam, and the Sand Engine (*Stive et al.*, 2013). Prior studies have shown that Rhine plume fronts can carry fine suspended sediment offshore, due to the cross-shore velocity associated with their passage (*Horner-Devine et al.*, 2017; *Flores et al.*, 2017). These studies showed that cross-shore sediment transport is dynamic and influenced by different processes, such as plume fronts, while alongshore transport based on resuspension or advection mainly is determined by the tide that moves back and forth along the coast. They did not explore the role of the fronts on the seabed, as was done for the Columbia River plume, wherestrong fronts were observed to impact the bottom boundary layer (*Orton and Jay*, 2005; *Spahn et al.*, 2009; *Nash et al.*, 2009).

The main objective of this study is to investigate the properties of the freshwater fronts, how wind and tide influence their propagation, and whether the tidal plume fronts impact the sea bed. To achieve this we use in-situ data taken 10 km North of the Rhine River mouth in the mid-field plume, were we have two moorings sites. First, we investigate the applicability of traditional gravity current theory (*Benjamin*, 1968; *Britter and Simpson*, 1978) on the propagation of freshwater fronts in the Rhine ROFI, where tidal advection and straining play an important role. We examine to what extent they are similar to the near-field tidal plume fronts found in other systems, such as the Connecticut or Columbia river plumes. Then, we explore how the edges of the freshwater lenses are influenced by winds and spring-neap tides. Finally, we ask whether these fronts can have an impact on the sea bed.

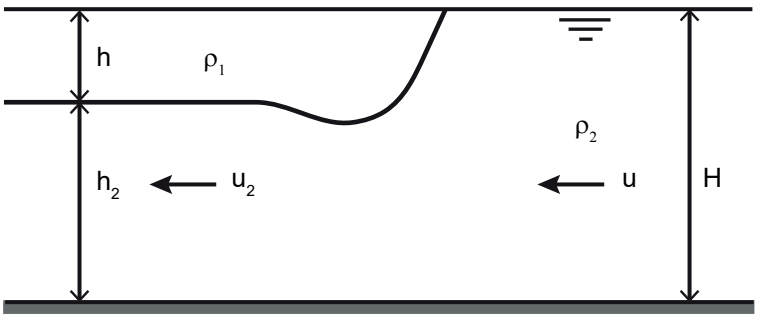

Figure 3.1: Schematic of an idealized gravity current in a front-following reference frame.

3.2. GRAVITY CURRENT THEORY

Many tidal plume fronts have been compared to gravity current theory (*Garvine and Monk*, 1974; *Luketina and Imberger*, 1987; *Kilcher and Nash*, 2010). A gravity current can be divided into two regions, the head region where mixing and large horizontal density gradients occur, and the tail where the current is stable (*Britter and Simpson*, 1978). Following *Benjamin* (1968), the theory describes the propagation of a gravity current moving with the front in a two-dimensional system. The front is stationary with respect to the ambient flow, the flow far up- and downstream are assumed hydrostatic and mixing and friction are neglected. Figure 3.1 shows a schematic of a 2D gravity current, where a surface current with a density of ρ_1 propagates into an ambient fluid with speed u. The ambient fluid has a density ρ_2 and a total depth H. The thickness of the surface current just after the head is defined as h, the thickness of the ambient flow there is h_2 with an assumed velocity of u_2. The ambient fluid should accelerate below the surface current based on continuity. Following the derivations, the return flow u_2 is a function of H/h_2 and u resulting in a larger u_2 for a larger h.

Benjamin (1968) defined the Froude number based on the reduced gravity and the relative thickness, h/H. Where h is the current depth and H the total depth. The Froude number is predicted as $F_h = u/\sqrt{g'h} = \sqrt{2}$ for a current in a deep ambient fluid. The Froude number is dependent on the total water depth, $F_H = u/\sqrt{g'H}$, when h/H = 0.5 and gives a value of $F_H = 0.5$. He found a maximum value of $F_H = 0.527$ for $h/H = 0.347$, for larger h/H the Froude number decreases again. When dissipation is included, the maximum current speed coincides with maximum dissipation corresponding to $h/H = 0.347$. In addition, *Britter and Simpson* (1978) showed with experiments that the mixing at the head of the current increases the estimated Froude numbers of *Benjamin* (1968). They found a maximum value of $F_h = 2.25$ for $h/H < 0.1$.

3.3. MEASUREMENTS

3.3.1. LOCATION AND INSTRUMENTATION

Field measurements were conducted from the 17th of September to the 17th of October 2014 (year days 259 to 290) off the Dutch coast, which captures two full spring-neap tidal cycles. Two moorings and three bottom frames were deployed 2 and 6 km offshore, corresponding to depths of about 12 and 18 m, located 10 km north-east of the mouth of the Rotterdam Waterway (see Figure 3.2). The moorings consisted of Seabird Microcat Conductivity Temperature Depth (CTD) instruments at different locations over the vertical. In total, nine CTD instruments were used with sampling frequencies ranging from 20 to 60 seconds. The CTD instruments at the 12 m site were mounted at -1,-3,-7,-8 and -10.5 m below the sea surface, and at the 18 m site at -1,-2.5,-10 and -15 m.

At both locations the vertical current structure was measured using a 4 beam RDI Workhorse Acoustic Doppler Current Profiler (ADCP), which was located at a bottom frame, with a frequency of 1200 kHz. The ADCP data has vertical bins of 0.25 m and the N-E velocity component is rotated into an along- and cross-shore component, with a rotation angle of 42.5 degrees from the North. Positive alongshore velocities are directed to the North-East and positive cross-shore velocities are directed offshore. The collected CTD and ADCP data are averaged over 10 minutes, based on the bursts of the ADCP. Unfortunately, the ADCP at the 18 m site only lasted until day 281.

The near bottom current structure at the 12m site was measured using three Sontek Acoustic Doppler Velocimetry (ADV) instruments which were located at a third bottom frame at 0.25, 0.50 and 0.75 m above the seabed. They sampled with a frequency of 16 Hz during bursts of 10 minutes every 15 minutes. The raw ADV data is despiked using the method of *Goring and Nikora* (2002). After despiking, the data is averaged over 10 minutes giving a mean velocity. Turbulent velocity components (u',v', and w') were obtained by removing the 10-minute averaged velocities. The N-E velocities are rotated into an along- and cross-shore component, in the same way as done for the ADCP instruments. The ADV instruments are located close to the seabed, where waves can influence the Reynolds stresses ($u'w'$,$v'w'$). The method of *Shaw and Trowbridge* (2001) is used to calculate the Reynolds stresses eliminating the influence of waves. This method requires two ADV instruments separated at a distance larger than the length scale of turbulent eddies, but smaller than the correlation scale of waves. For this calculation we used the lowest and highest ADV with a vertical distance of 0.5 m. This distance seems to be sufficient based on a comparison between the signal with and without wave removal. Additionally, the spectral density for the horizontal velocity component shows good agreement with the -5/3 slope characteristic of the inertial subrange (*Flores et al.*, 2017).

X-band radar images from SeaDarQ are available with a field of view spanning the 12m site and closer to shore. The raw data is averaged every 5 minutes resulting in time-averaged images. These images show tidal plume fronts propagating all the way to the coast, from which information such as frontal propagation speed (relative to the ground), the direction of propagation (respect to the coast), the exact location of the front in real world-coordinates, and the timing of frontal propagation through our mooring site can be extracted.

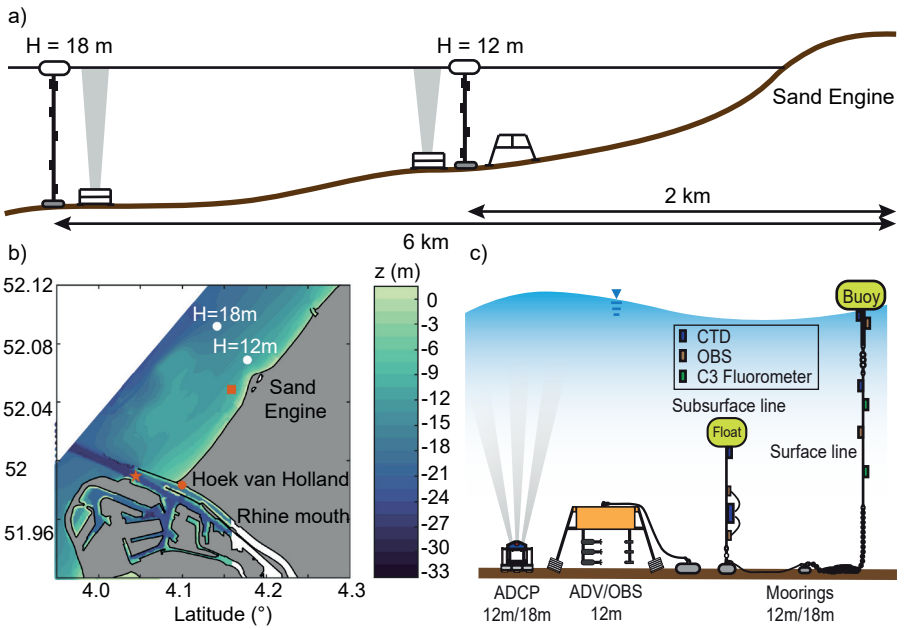

Figure 3.2: Study site and measurement set-up. (a) Cross-section of the measurement site, where at two locations a mooring and bottom frame are placed. The locations are at 12m and 18m depth (about 2 and 6 km from the original coastline). (b) The Dutch coast around the Rhine river mouth. The figure shows the bottom topography (colour), the Sand Engine and the 2 measurement sites (white dots), about 2 and 6 km offshore which are 10 km north-east of the river outflow. The orange square represents the measurement station for the wave data. The orange circle represents a meteorological measurement station and the star represents the location for discharge data. (c) Detailed schematic of the measurement set-up (Figure after *Flores et al.* (2017)). A third frame is placed at 12m depth.

3.3.2. ESTIMATION OF FRONTAL PROPERTIES

The thickness of a front (h) is estimated using the cross-shore velocity profile. At the mooring sites when the front arrives, the thickness of the onshore velocity layer is estimated by taking the distance between the sea surface elevation and the point where onshore velocities turn into offshore velocities. Figure 3.5c,d show this calculation procedure, where 1 minute averaged cross-shore velocity profiles are compared with the 10 minute averaged velocity profile. This method gives a good estimate of the bulk thickness of the stratified water mass for most of the fronts. It does not always give an accurate thickness of the head of the front. For some fronts the thickness might be underestimated with this method (figure 3.5a,c), which could have a small effect on our analyses.

We set-up a front tracking procedure to calculate the intrinsic frontal speed U_f using the radar images (see Appendix 3.6 for more details). The radar images are used to determine the orientation of the front and the frontal speed relative to the ground (u_f). The intrinsic frontal speed is defined relative to the motion of the ambient current in a front-normal system, $U_f = u_f - u_a$, where u_f is the total velocity at the timing of the front relative to the ground (*Benjamin*, 1968; *Garvine and Monk*, 1974). The adcp data and the orientation of the front are used to determine the front normal ambient velocity (u_a). The frontal speed is used to calculate the Froude number, $F_H = U_f \sqrt{\frac{\rho_2 - \rho_1}{\rho_2} gH}$, where ρ_1 is upper layer density, ρ_2 the lower layer density, H the water depth. The definition of the Froude number for large h/H has been chosen (*Benjamin*, 1968; *Shin et al.*, 2004). A quality check of the radar images resulted in a limited number of images that could be used, resulting in a total of 17 frontal speeds and Froude numbers.

Bottom stresses are determined as $\tau_b = (\rho(\overline{u'w'}^2 + \overline{v'w'}^2))^{1/2}$, where ρ is the density of the salter bottom water. The stresses are rotated into an along−front and across−front direction as explained above. In addition, the vertical fluctuation w' obtained from the ADV's is used to determine the TKE dissipation rate (ϵ) by fitting spectra to the inertial subrange (e.g. *Voulgaris and Trowbridge*, 1998).

3.3.3. ENVIRONMENTAL CONDITIONS

The environmental conditions were highly variable during the entire measurement period (Figure 3.3). Wind speed and direction were measured by the Royal Dutch Meteorological Office (KNMI) at a station near Hoek van Holland (Figure 3.2). These wind speeds have been used to estimate the alongshore wind stress using a quadratic drag law with a drag coefficient C_{10} of 0.001 and air density of 1 kgm^{-3} (*de Boer et al.*, 2006). Positive alongshore wind stress is directed to the northeast. The beginning of the field campaign coincided with neap tide and winds lower than 5 m/s (Figure 3.3a,b,c). During this period strong stratification was observed, reaching a maximum top-bottom salinity difference of 8 psu and a mean of 3.5 psu (Figure 3.3f). Northerly winds (360 degrees) with a maximum of about 15 m/s were present during the first storm from days 264 to 266. During this storm event no stratification was observed (Figure 3.3f), as upwelling winds mixed the plume and displaced it southward and offshore from the moorings. After the storm, wind speed ranged between 3 and 9 m/s with variable wind direction from days 266 to 280. The relaxation of the wind resulted in an onset of stratification after day 266. The maximum top-bottom salinity difference was 7.5 psu for spring tide and 8 psu

for neap tide (Figure 3.3f). The second storm reached wind speeds of about 12 m/s coming from the south (180-200 degrees) on days 280 to 284. Figure 3.3f shows the presence of low stratification during this storm event, which is the result of a downwelling wind.

Wave data were retrieved from a Waverider buoy 1 km southwest of the 12m measurement site. High significant wave heights were aligned with high wind intensities, with a maximum significant wave height of 2.5 m during the first storm and 1.5 m during the second storm (Figure 3.3d). During calm conditions significant wave heights below 1m were observed. The presence of waves during our field campaign led to the need of filtering the Reynolds stresses.

The discharge data of the Rhine and Meuse River are obtained from the database of *Rijkswaterstaat* (2015), where the discharges are extrapolated from data measured at Lobith, about 170 km upstream of the River mouth. Figure 3.3e shows the total discharge of both rivers, with a minimum of approximately 500 m^3s^{-1}, a maximum of about 2500 m^3s^{-1} and a mean value of 1600 m^3s^{-1}.

3.4. RESULTS

3.4.1. OBSERVATIONS

Figure 3.4 shows the time series of salinity, alongshore velocity, cross-shore velocity and bottom stresses at the 12m site, for two contrasting periods that were selected to analyse the variability in stratification and the impact of fronts. We chose a Neap tide with low winds as a low energy reference period and a spring tide with moderate winds as a high energy period (see Figure 3.3), where the moderate winds were not strong enough to mix out the front. Figure 3.4a-e shows results from the first two days of the measurement campaign during neap tide with winds below 5 m/s (between days 260 and 263). Figure 3.4f-j shows results from two days during spring tide with 7-10 m/s winds mainly coming from southwest (SW) (days 268 to 270). In both sub-figures a X-band radar image is shown for the corresponding neap and spring time series.

A sudden decrease in surface salinity was observed at day 260.4 during neap tide (Figure 3.4b), about two hours after high water (HW+2). At the same moment a strong cross-shore shear develops, where the surface current is directed onshore and the bottom current offshore (Figure 3.4d). Every tidal cycle the same pattern is visible. This sudden decrease in salinity is due to a front passing by the measurement site as confirmed by the X-band radar image from the same period (Figure 3.4a). The front travels onshore causing an offshore return flow near the bottom (*Horner-Devine et al.*, 2017). This passage of fronts is also observed during the spring tide period (Figure 3.4f,g), however the fronts arrive around HW at the 12m site.

Figure 3.4 shows a difference in the salinity and cross-shore velocity structure between the two periods. The cross-shore shear is higher during the windy spring period than during the calm neap period, with values of 0.8 m/s at day 269.1 and 0.3 m/s at day 260.4, respectively. The bottom and surface cross-shore currents reverse around the same time. The flow reversal for the calm neap period is different, close to the bottom the flow reverses first slowly followed by the layers above. This results in a three-layer density system for the calm neap period and a two-layer system for the windy spring period. This is reflected in the salinity data as well, where figure 3.4b shows a fresh upper

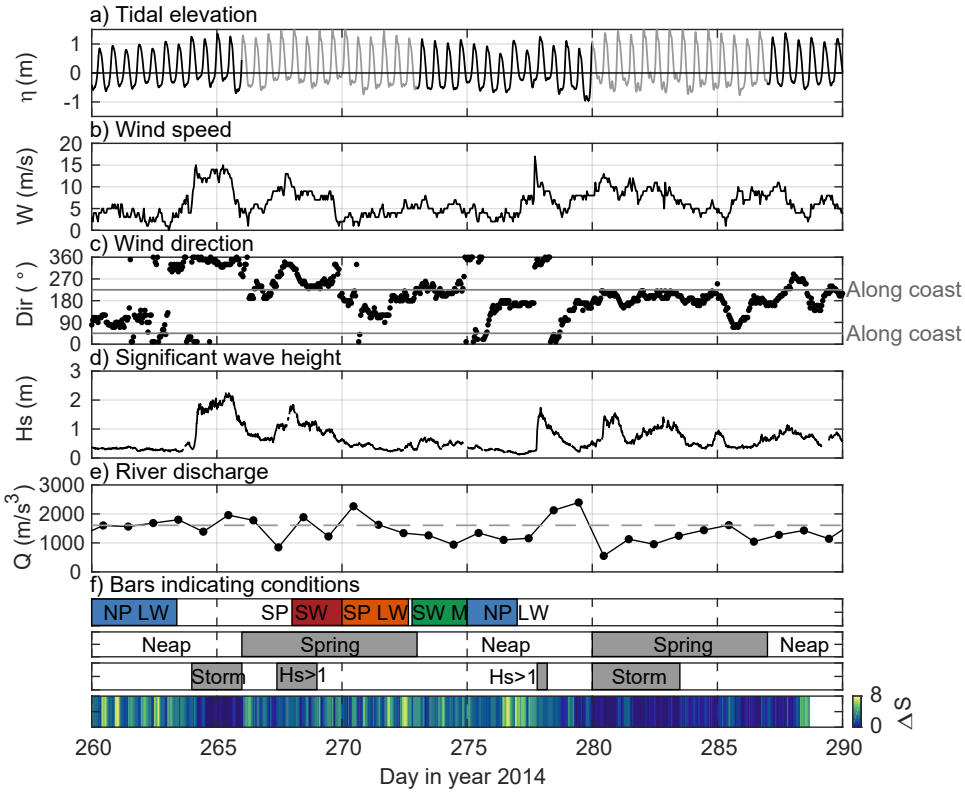

Figure 3.3: The conditions during the measurement campaign. a) the tidal elevation at Hoek van Holland ,10 km south-west of the measurement site (black is neap, grey is spring). b) the wind speed measured at Hoek van Holland, c) the wind direction measured at Hoek van Holland. The grey lines indicate the direction of the coast (42.5 degrees from the North) where the wind will be alongshore directed. d) significant wave height at wave rider buoy, e) total river discharge from New Waterway and Haringvliet sluices, where the dashed grey line indicates the mean discharge of 1600 m^3/s. f) Bars indicate different periods based on tide and wind, spring/neap, the presence of storms and when Hs>1, and vertical stratification in terms of salinity difference between bottom and surface (based on 12m site).

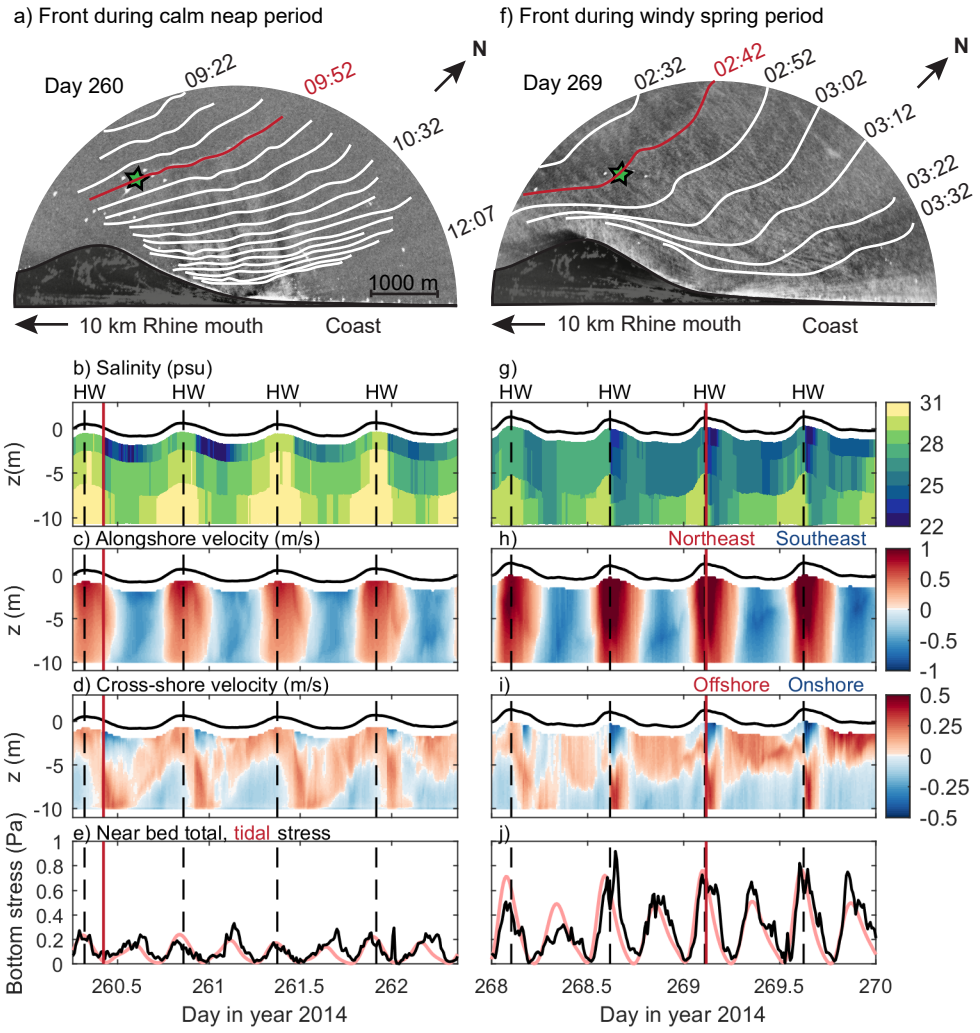

Figure 3.4: Radar images and time-series of salinity (psu), alongshore velocity (m/s), cross-shore velocity (m/s) and bed stresses at the 12m site. Panel a) and f) are X−band radar images with the trajectory of a front propagating towards the coast on day 260 and 269, where the green star represent the 12m measurement site. The white lines have a time step of 10 minutes. The red line corresponds to the red line in the lower panels, indicating frontal passage. The left panels (b−e) represent the first 2 days of the first Neap period with winds lower than 5 m/s. The panels show time-series of b) salinity (psu), c) alongshore velocity (m/s) where positive is northeastward, d) cross−shore velocity (m/s) where positive is offshore. The vertical axis represents the depth and the horizontal axis the time in days of year. e) Total stress 0.25 m above the bottom (Pa) averaged over 10 minutes (black line). The red line is the estimated tidal stress near the sea bed (Pa). The dashed black lines correspond to high water (HW). The right panels (g−j) represent two days during spring with moderate Southwest wind.

layer, a medium middle layer and a saline lower layer. Figure 3.4g shows a thick fresh upper layer and a saline lower layer, which looks like a two-layer system. The upper layer is more mixed in this case, due to more tidal and wind energy.

The radar images show that the front slows down and turns as it propagates towards the coast. At the 12m site the front propagates under an angle of about 30-40 degrees with the coast, turning to become more parallel to the coast as it propagates onshore (Figure 3.4a,f). During the calm neap period the front is at the 12 m site at 09:52. It takes 2 hours and 15 minutes to reach the onshore position at 12:07 (Figure 3.4a). During the windy spring period the front needs 50 minutes to propagate from the 12 m site starting at 02:42 to the onshore position at 3:32 (Figure 3.4f). Therefore, the front during the calm neap period propagates much slower towards the coast than the front during the windy spring period.

An increase in bed stress is observed around HW and LW for both periods (Figure 3.4e,j, black line). This response coincides with the estimated tidal shear stress (red line). The tidal shear stress is estimated using a quadratic drag law, where the tidal velocity is obtained through harmonic analysis using a near-bottom averaged velocity and the T-Tide package (*Pawlowicz et al.*, 2002). A drag coefficient C_D of about 0.0035 was found based on the measured wave-filtered Reynolds stresses and averaged bottom velocity. A second peak in the bed stress is observed just after HW during the spring tide period with moderate SW winds, which is just after the front passes through the mooring site (Figure 3.4j). This peak is not observed in the tidal stress. Therefore, the difference between the total bed stress and the estimated tidal stress indicates that besides the tide other processes increase the bed stress, such as the passage of the freshwater lens. For the calm neap period no second peak has been observed just after frontal arrival, the stress is mainly tidal driven.

The acoustic backscatter of the ADCP is used to get insight into the frontal structure (Figures 3.5a,b). Figure 3.5 shows 4.5 minutes of the structure of a calm neap front (a) and a windy spring front (b). The dashed line corresponds to the thickness inferred using the cross-velocities and seems to give a good approximation. The neap front shows first a raised head, followed by a minimum in thickness and then it increases to a constant thickness (Figure 3.5a). This structure is similar to the shape of gravity currents observed in the laboratory (*Britter and Simpson*, 1978; *Shin et al.*, 2004). The spring front shows a slightly different structure, it does not show a clear raised head. The edge of the front seems to be less thick than the body behind it. A high backscatter signal near the seabed is observed during energetic periods (Figure 3.5b), which makes the distinction between stratification and sediment more difficult.

3.4.2. TIDE AND WIND FORCING ON FRONTAL DYNAMICS

Figure 3.4 showed that the system behaves differently under different forcing conditions. In this section we investigate in more detail the influence of tide and wind forcing on the fronts. We look to the median properties of frontal thickness (h), reduced gravity (g') and frontal arrival time to our 12m mooring site relative to HW for different periods. Based on the entire time-series we selected a few periods to investigate the influence of wind and tide: Neap tide with low winds (NP LW,light blue), Spring tide with low winds (SP LW, orange), transition between Neap and Spring tide with SW winds between 4-7 m/s (SP-

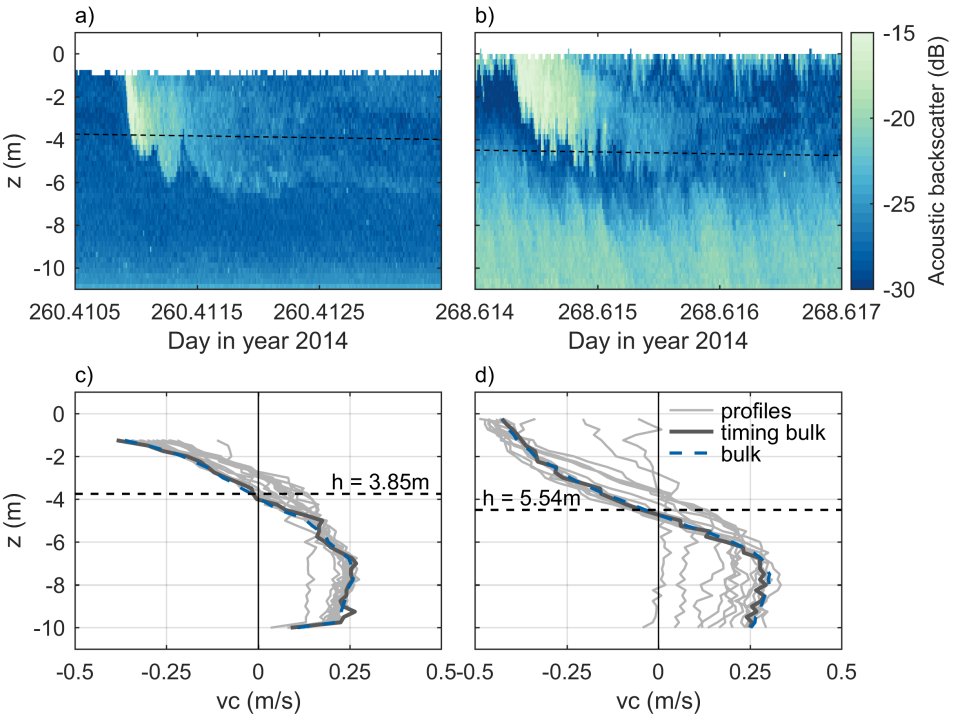

Figure 3.5: a,b) Acoustic backscatter (dB) around frontal head. The horizontal axes show a time series of about 4.5 minutes, the vertical axes represents the depth. Horizontal dashed line is the estimated thickness of the plume based on cross-shore velocity. a) Neap tide front, b) Spring tide front with moderate Southwest wind.c,d) Cross-shore velocity profile over the depth, where the dashed blue line is the 10-minute averaged data used (bulk), light grey lines are profiles of 1-minute averaged cross-shore velocity before the front arrives, dark grey line is the timing of the front for the 1-minute averaged velocity data (bulk timing). c) Neap tide front, d) spring tide front with moderate Southwest wind.

NP SW M, green), Spring tide with SW winds between 7 - 9 m/s (SP SW H, red) (see Figure 3.3f for the corresponding days). Low winds are defined here as wind speeds smaller than 5 m/s. These abbreviations are used throughout the manuscript. Unfortunately, no radar images are available from the SP LW period.

SPRING-NEAP VARIABILITY

The neap and spring periods with low winds are used to identify the spring-neap variability for the frontal properties. For NP LW we expect the fronts to arrive around HW+2 based on previous research (*Simpson and Souza*, 1995; *de Boer et al.*, 2006, 2008), which is inline with onshore advection and straining due to the tide. Figures 3.4b and 3.6c (blue) show indeed that the fronts on average arrive around HW+2. For SP LW the fronts arrive around 1 hour and 20 minutes after HW, which is earlier than on NP LW (Figure 3.6c, orange). The earlier arrival on a spring tide is in agreement with the higher along- and cross-shore advection and straining (*de Boer et al.*, 2006, 2008).

The larger advection and straining during spring tide is also visible in the upper layer velocity ($U_{1,adcp}$) as a function of tidal amplitude, where SP LW corresponds to larger velocities than NP LW (Figure 3.7b). These velocities and the arrival times include the effect of wind and tide, however, it does not reflect whether the intrinsic frontal speed is influenced by the tide. The frontal propagation speed shows a different result than the net velocity (Figure 3.7a), with a maximum speed of 0.55 m/s and a minimum speed of almost zero indicating an arrested front. A large tidal amplitude does not necessarily correspond to a front with high intrinsic frontal speed. Thus, Figure 3.7a suggests that tidal amplitude does not determine frontal propagation.

Figure 3.6 shows that neap fronts are thicker and more stratified than spring fronts under low wind conditions, suggesting that the spring fronts are more mixed. The lower g' on the spring tide reflects the stronger mixing expected during this period. So, neap fronts are thicker and more stratified than spring fronts. A stronger or weaker tidal flow impacts the advection velocity of the fronts, whereas it does not seem to determine the intrinsic frontal speed.

WIND VARIABILITY

Figure 3.8 shows the relationship between the wind direction, wind speed and the arrival time of the fronts relative to HW and the relative thickness of the fronts (h/H) for both mooring sites. The data is plotted in the form of a wind rose including the direction of the coast. The instruments for the 18m site only measured for 28 days, therefore fewer frontal points are shown in Figure 3.8a than in Figure 3.8b. A mean wind speed and direction averaged over 6 hours are used, to take the influence of the wind on the fronts beforehand into account as well.

Figure 3.8a,b indicates that winds from 195 - 270 degrees correlate with the early arrival of a front associated with a fast propagation speed relative to the ground (HW+<1 hour). This can be explained using the frictional and Ekman component of the winds compared to the direction of the frontal propagation. The frictional component displaces the plume northeastward along the coast in case of a southwesterly wind (225 degrees, alongshore). The Ekman component advects the plume and lenses within it towards the coast. The resulting wind velocity accelerates the front resulting in a higher speed. Figure 3.8c,d shows larger h/H for the fronts related to winds coming from 195 -

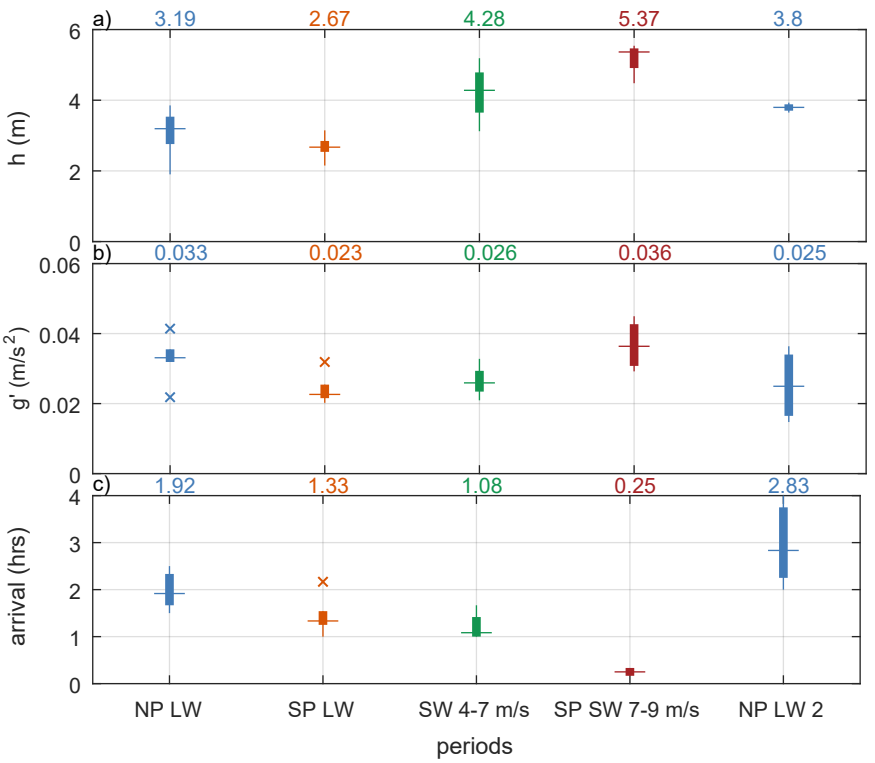

Figure 3.6: Boxplot of a) frontal thickness (h), b) reduced gravity (g'), and c) arrival time relative to HW. On the horizontal axis different periods are displayed: Neap tide and low winds (blue), Spring tide and low winds (orange), Spring-Neap 4-7 m/s SW winds (green), Spring 7-9 m/s SW winds (red), and another Neap tide with low winds (blue). The horizontal line is the median, the outliers are marked by a x, and the variability of the data is shown by the length of the box. The median is also written above each panel per period.

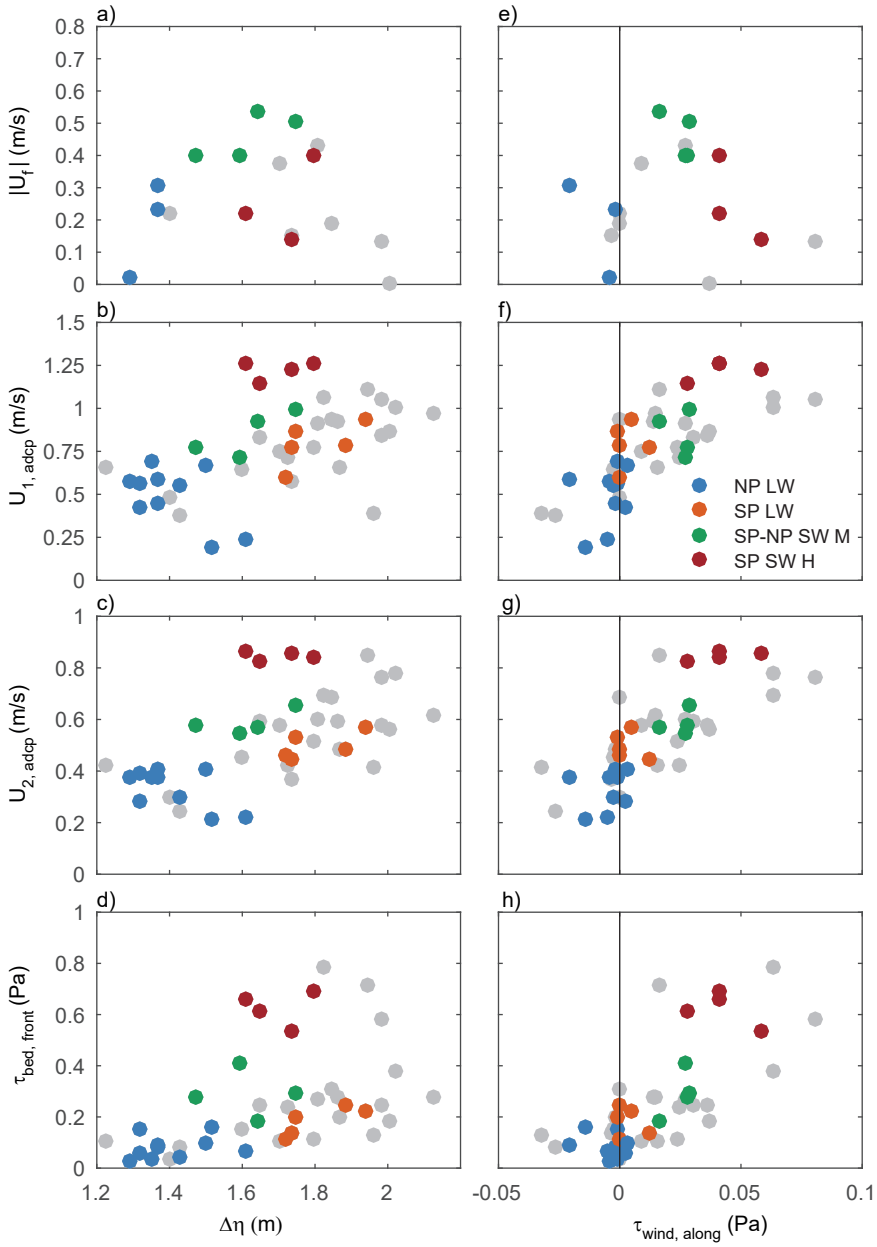

Figure 3.7: Tidal amplitude ($\Delta\eta$ in m) and alongshore wind stress ($\tau_{wind,along}$ in Pa). a,e) Absolute intrinsic frontal speed, U_f (m/s) b,f) Upper layer velocity at timing front relative to ground, $U_{1,adcp}$ (m/s) c,g) Lower layer velocity at timing front relative to ground, $U_{2,adcp}$ (m/s) d,h) Bed stress at timing front, $\tau_{bed,front}$ (Pa). Colours are related to different selected periods based on tide and wind, where blue is NP LW, orange is SP LW, green is SP-NP SW M, and red is SP SW H.

270 degrees. Winds from these directions are downwelling winds along the Dutch coast (from SW).

In contrast, wind directions between 0 and 195 degrees result mainly in a later arrival of the front (HW+>1-1.5 hour), which can be explained as follows. Northeasterly winds (45 degrees, alongshore) advect the front offshore (Ekman) and southwards (frictional), therefore the propagation of the front will be decelerated by the wind resulting in a lower propagation speed. An easterly wind (125 degrees, offshore) should advect the plume and lenses offshore (frictional) and northeastward (Ekman), which should decelerate the fronts relative to a situation without winds. Figure 3.8c-d shows that these winds on average correspond to thinner fronts (small h/H).

When we look to median properties for different periods, a distinct difference between low and high winds have been observed (Figure 3.6). The fronts during periods with SW winds are thicker and arrive earlier than the neap and spring periods with low winds. The fronts during spring tide with high SW winds are the thickest and fastest, and these fronts are highly stratified as well. Based on gravity current theory, we would expect that thick fronts with a large density difference have higher intrinsic frontal speeds. Figure 3.7e shows that these fronts (red) do not necessarily show a high intrinsic speed (U_f), but they show a large upper layer velocity relative to the ground ($U_{1,adcp}$). A larger positive alongshore wind stress corresponds to a higher upper layer velocity, but not necessarily to a higher frontal speed. The transition period between neap-spring with medium SW winds correspond to high U_f and with less scatter than for the NP LW and SP SW H periods.

3.4.3. BED STRESS

The observed differences in frontal dynamics under different tidal and wind forcing conditions suggest that we may also observe corresponding changes in bed stress resulting from frontal processes. Figure 3.4 showed a different behaviour in the bed stress around frontal arrival during two different periods. During neap tide with low winds the bed stress is mainly tidal, but during spring tide with high SW winds an extra peak seems to be present. Figure 3.7d,h investigates whether there is a relation between the signal of the bed stress and the tide and wind at the time of the fronts. Figure 3.7 shows clearly a tidal signal in the bed stresses, where higher tidal amplitudes have a slightly higher bed stress relative to low tidal amplitudes. A maximum bed stress of 0.3-0.4 Pa has been observed which is related to a tidal amplitude larger than 2 m, which seems to be mainly driven by the tide. However, there are some data points that behave differently. These data points correspond to higher bed stresses for different tidal amplitudes, suggesting that other processes also contribute.

Figure 3.7h shows good agreement between alongshore wind stress and bed stress at the time of the frontal passage. A positive wind stress is related to the downwelling component of the wind. So, large downwelling winds correspond to an increase in bed stress below the front. Large downwelling winds also relate to large upper and lower layer velocities (Figure 3.7), however, not necessarily to larger frontal speeds. Figures 3.6 and 3.8 showed that the fronts under forcing of SW winds are often thick. This should indicate that the increase in bed stress is observed under thicker fronts, which is confirmed by Figure 3.9b. So, high bed stresses are linked to thick fronts under forcing of SW winds.

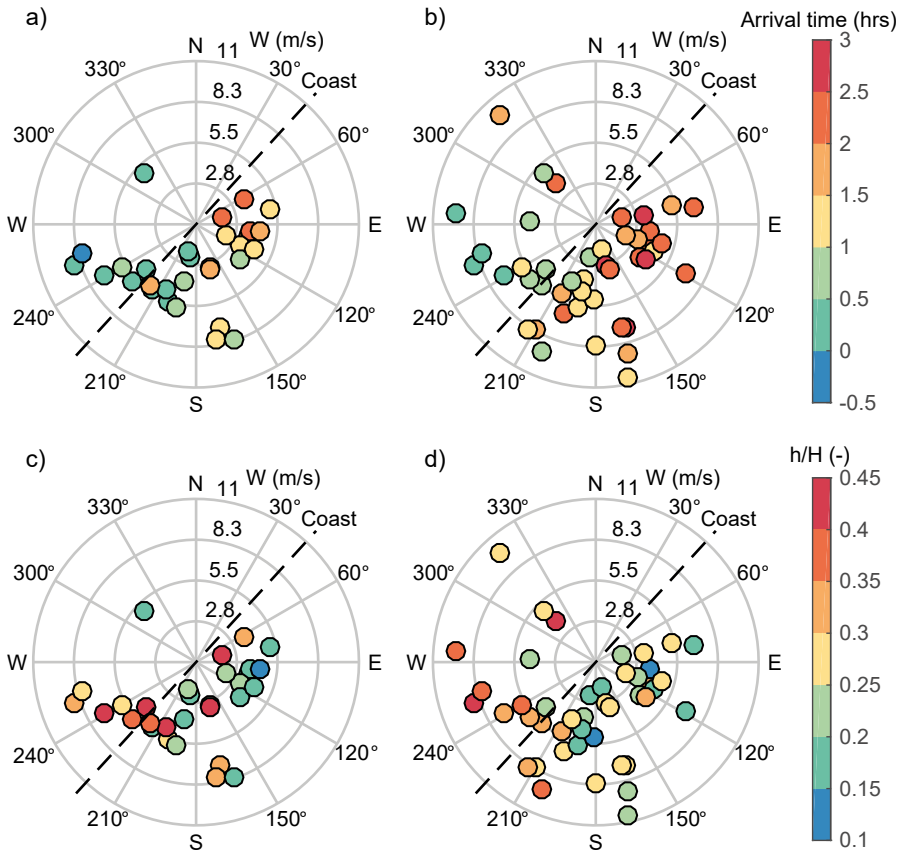

Figure 3.8: Wind rose diagram based on wind direction (following the circles) and wind speed. The dots represent the fronts, where the colors indicate arrival time (a-b) and relative thickness (c-d). a) The arrival time relative to HW (hrs) at the 18m site, b) The arrival time relative to HW (hrs) at the 12m site. c) Relative thickness h/H at the 12m site. d) Relative thickness h/H at the 18m site. The dashed line indicates the direction of the coastline (42.5 degrees from North).

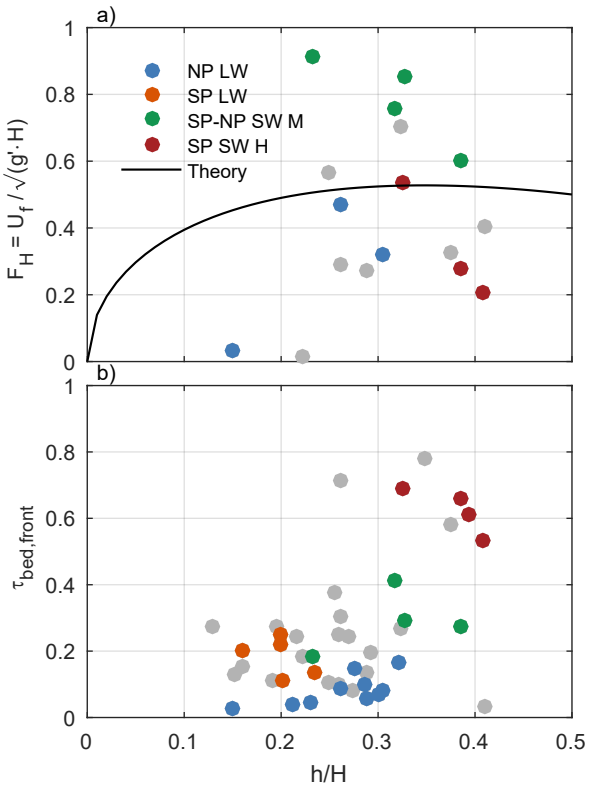

Figure 3.9: Relative thickness of fronts (h/H) versus a) Froude number based on water depth (F_H), b) bed stress (Pa) at timing front ($\tau_{bed,front}$). The colours relate to the selected periods based on wind and tide. The black curve in a) is the theoretical value based on *Benjamin* (1968).

3.5. DISCUSSION

3.5.1. COMPARISON TO THEORY AND PRIOR LABORATORY AND FIELD RESULTS

Benjamin (1968) found a Froude number of 0.5 for a gravity current which reaches about half depth. Figure 3.9a shows his theoretical curve for the Froude number as a function of relative thickness. For the Rhine plume fronts the average Froude number was 0.44; however the observed values ranged from 0.01 to 0.9 revealing a high degree of scatter around the theoretical value. One of the reasons could be the assumptions and estimates necessary for calculating the frontal speed (U_f), which could lead to some inaccuracy.

Estimates of frontal Froude number are challenging in the field due to the complexity of defining key quantities in three-dimensional irregular fronts. However, there are several physical processes that may also contribute to the scatter observed in the Froude number. One reason could be the location of our mooring site, for example, which is in the mid-field plume instead of near-field. This location means that the front already traveled 10 km along the coast, which we expect to be around 8-12 hrs after release. Therefore, we expect that the fronts already lost most of their energy and are influenced by earth rotation. This is different than most tidal plume front studies, where the fronts are studied in the near-field just after release (*Kilcher and Nash*, 2010, e.g.). Some simple non-hydrostatic numerical simulations, using the model of *Lamb* (1994), with and without earth rotation indicate that the addition of Coriolis will slow the transit time of the fronts by about an hour. Additionally, our mooring site is located in a system dominated by tidal advection and straining as result of friction and rotation. These tidal processes are key in determining the location and movement of the entire plume and lenses within it as shown by *de Ruijter et al.* (1997), *van Alphen et al.* (1988), *Simpson and Souza* (1995) and *de Boer et al.* (2008).

The relative thickness of the fronts in the Rhine plume is large compared to other tidal plume systems (*Garvine and Monk*, 1974; *Luketina and Imberger*, 1987; *Kilcher and Nash*, 2010; *Horner-Devine et al.*, 2013, e.g.). In these systems values for h/H are often in the range of 0.04 to 0.12, while we found values in the range of 0.13 to 0.41. For systems with thin fronts, Froude number in terms of the current depth is used, $F_h = U_f / \sqrt{g'h}$ where they found values in the range of 1 to 2.7. Mean frontal velocities of 0.7-0.8 m/s are found for the Columbia plume (*Orton and Jay*, 2005; *Nash and Moum*, 2005), while for the Merrimack a value of 0.39 m/s have been observed (*Horner-Devine et al.*, 2013). The frontal velocities we found are in the range of 0 to 0.54 m/s, which is in the same range as the values found in other plume systems. Our system is influenced by a strong tidal flow similar as observed by *Garvine and Monk* (1974) in the Connecticut. Near the mouth the spreading of the lenses should be asymmetrical as well due to the tidal background flow.

3.5.2. IMPACT OF WIND AND TIDE ON FRONTAL STRUCTURE

We observe that downwelling winds accelerate the fronts, presumably by advecting the front towards and along the coast, consistent with Ekman wind driven transport. However, at 10 km downstream we find Rossby numbers in the range of 0.2 to 0.5 based on a velocity of 1.2 m/s and a length scale in the range of 20 to 40 km (*de Kok*, 1997). *de Kok* (1997) stated that the plume is in semi-geostrophic balance 15 km downstream. In clas-

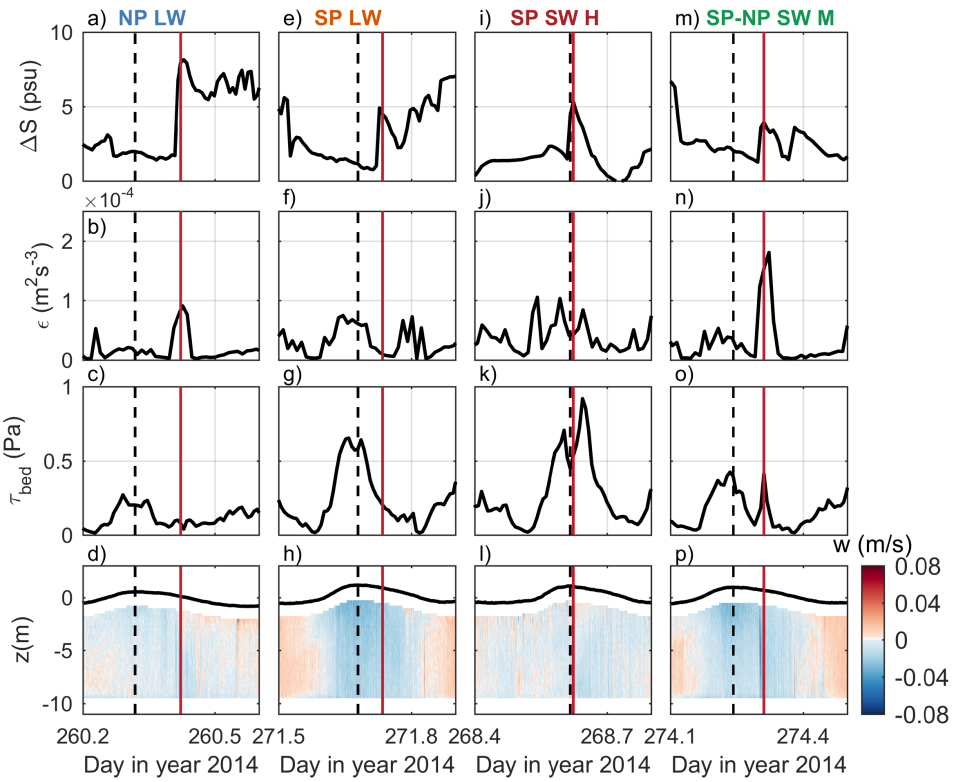

Figure 3.10: Near bed properties for different periods. The vertical axes represents salinity difference bottom-top (psu), dissipation (m^2s^{-3}), bed stress (Pa), depth (m). The horizontal axes represent different periods: NP LW, SP LW, SP SW H, SP-NP SW M. The colorbar in the fourth row represents vertical velocity (m/s) based on 1-minute averaged ADCP data, where positive is upwards and negative downwards. The dashed black lines indicate HW and the solid red lines indicate the front.

sic geostrophic downwelling theory a thicker upper layer and a faster current is expected (e.g. *Chao*, 1988; *Lentz and Largier*, 2006), where *Lentz and Largier* (2006) demonstrated that it is mainly moderate downwelling winds that increase the propagation speed and plume thickness. Our data suggest that this is also happening in our plume.

The arrival times of the fronts observed in Figure 3.6 seem to align with the work of *de Boer et al.* (2008). On a neap tide the fronts arrive around HW+2, which agrees with the timing of tidal straining and advection. During a spring tide the magnitude of advection increases, resulting in an earlier arrival (*de Boer et al.*, 2006). When downwelling winds are added the entire alongshore flow is accelerated resulting in an even earlier arrival of the fronts. If we compare the arrival of the fronts with the frontal speed (U_f) no clear relation has been found (Figure 3.7). Fast arrival does not align always with a fast frontal propagation; some with the fastest arrival have a quite low frontal speed compared to the other fronts. Therefore, it seems that the fronts in this system are mainly advected by the tide and winds. Additionally, no clear evidence of downwelling velocities has been observed for the thick and fast fronts on spring tide with high downwelling winds. Therefore, advection and suppression of the lenses seems to be the explanation of the thick fronts under SW winds.

The radar images in Figure 3.4a,g show that the front is moving towards the coast and alongshore, where the alongshore component appears to be larger during spring tide with SW winds than during neap tide. In Figure 3.11 the alongshore movement of the front is highlighted using two red crosses that follow an irregularity on the front. The higher alongshore movement during spring tide with SW winds coincides with the larger alongshore tidal currents and alongshore accelerated flow due to downwelling winds, respectively. The along-front velocity in the ambient flow and at the timing of the front confirms the presence of alongshore movement, which is larger for larger tidal amplitude and larger positive alongshore wind stress (not shown here). These results show that the intrinsic frontal speed could have an alongshore component, which is now neglected in our calculation, which could affect the magnitude and direction of U_f.

3.5.3. WHAT IS DRIVING BOTTOM IMPACT?

Peak bottom stresses are often observed at or near the time of frontal passage. However, the duration of elevated stress is often much longer than the time it takes for the front to pass and it is unclear whether the observed bed impacts are the result of processes localized at the front, or whether the front is associated with a change in the water column hydrodynamics that leads to increased bed stress. In other words, are the observed frontal impacts the result of strong tidal stresses modified by the rapidly changing stratification associated with frontal passage, or are their impacts associated with frontal processes themselves? Figures 3.4, 3.7 and 3.9 show that for periods with SW winds higher bed stresses are observed. Figure 3.4 shows clearly that the peak of the increasing bed stress happens after frontal arrival in the range of 0 to 30 minutes. For other periods, stresses close to the tidal stress seem to be observed. The extra observed peaks appear to be caused by other processes than the tide. Figure 3.10 will be used to investigate which mechanisms are causing the extra bed stress in the presence of strong stratification. Figure 3.10 shows the salinity difference, bed stress, dissipation and vertical velocity for the four selected periods in which a different response is observed. During the neap and

spring period with low winds there is no extra signal of bed stress observed besides the tide.

The alignment of the peaks of front, bed stress and dissipation during the period SP-NP SW M (Figure 3.10m-p) suggests elevated turbulence near the sea bed due to the arrival of the front. The dissipation values of 10^{-4} $m^2 s^{-3}$ are in agreement with values found in the Columbia river plume (*Orton and Jay*, 2005). In addition, a sudden increase in the magnitude of downwelling velocities are observed around frontal passage, resulting in velocities in the order of -8 cm/s. These vertical velocities are smaller than values found in the Connecticut plume of -15 to -20 cm/s (*O'Donnell et al.*, 1998) but larger than the values found in the Chesapeake Bay plume of -3 cm/s (*Marmorino and Trump*, 2000). *Orton and Jay* (2005) found downwelling velocities of -35 cm/s coinciding with strong near-bed velocities that were able to resuspend fine sediment in association with frontal passage during spring tide in the Columbia river plume.

The response near the seabed seems to be different during the spring period with high SW winds (Figure 3.10i-l). A large peak in bed stress has been observed 30 minutes after frontal arrival, which is a large time frame to be ascribed only to frontal passage. The lack of a peak in dissipation during frontal arrival suggests that other processes are key in exerting the bed stress. Figure 3.7f,g,h suggests that the alongshore wind stress accelerates the plume and lenses, resulting in a fast upper layer velocity and return flow below the front and lens. According to the classical theory the return current (u_2) below the upper layer accelerates relative to the (ambient) flow (u, see Figure 3.1), and it suggests that the return flow is larger for larger h. In our system, the return flow below the front acts at the same time and direction as cross-shore straining and advection. Therefore, the total acceleration of the return flow, due to frontal passage and straining, seems to be linked to the increase in bed stress. Because the system is so shallow the exchange flow at the coast due to fronts and straining can have a significant impact on sediment dynamics. Whether this mechanism operates in other systems is less clear for us.

3.6. CONCLUSION

This paper has presented that the leading edge of freshwater lenses in the Rhine river plume shows some basic frontal properties as observed in classical theory and other plume systems, such as a plunging head and the magnitude of frontal propagation speed. However, these Rhine plume fronts appear to behave quite differently as well, because of the mooring location and the 3D tidal currents in a frictional system. A Froude number analysis suggested that the wind and tide mainly influence the fronts by advection instead of changing their structure. We observed differences in structure, thickness and arrival time between a calm neap and spring tide. Fast advection and thick fronts are observed under downwelling winds. In addition, peak bed stresses are observed at or near the timing of frontal passage under forcing of downwelling winds, coinciding with high near bed velocities. The bed impact seems to be the result of strong tidal stresses modified by the rapidly changing stratification associated with frontal passage, however, sometimes the impact seems to be associated with frontal processes itself.

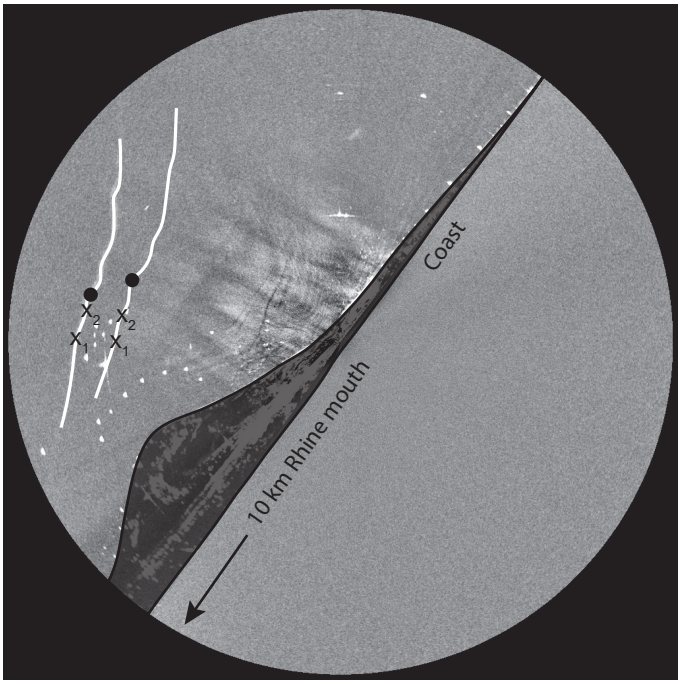

Figure 3.11: Front tracking system. Frontal speed is estimated by comparing radar images at two different times (white lines). Black crosses are used to estimate the frontal propagation speed and the black dots indicate the alongshore movement. Image is of September 17th 2014, 09:42 - 09:57 (day 260).

APPENDICES

3.A. FRONT TRACKING PROCEDURE

The X-band radar images in combination with the ADCP data are used to calculate frontal propagation speed U_f. This speed is defined as the speed relative to the ambient current normal to the front, $U_f = u_f - u_a$. The steps taken to derive U_f are explained below.

First, the radar images are used to estimate the frontal propagation speed relative to the ground (u_f) by following the front in time. More specific, a grid based on real world coordinates is made for every radar image. Then the distance between two frontal lines, which are 20 minutes apart, is estimated. The speed relative to the ground (u_f) is determined using the expression $\Delta u = \Delta x/\Delta t$. For each image two points on the first and second frontal line close to the 12m mooring site are selected (Figure 3.11, x_1 and x_2). The estimated front normal velocity for both points are averaged.

Second, the ambient velocity u_a has been computed using the ADCP data 20 minutes (2 bins) before frontal arrival averaged over the frontal/plume thickness. To be in a front-normal reference system, the ADCP data have been rotated into front-normal and along-front direction using the angle between the front and the coast. The information of the angle of the front has been extracted from the radar images.

Third, a quality check on the radar images has been performed, which resulted in

17 frontal occurrences that can be used. First, there are no images available of days 270.95 till 272.5 (September 27 till September 29). Then, sometimes the fronts are too light or not even visible to determine an accurate angle and velocity. In addition, a few images were discarded because the propagation of the front and angle was difficult to determine. These fronts seemed to be arrested and quite unstable for a certain amount of time.

Additionally, some radar images showed very clearly the alongshore propagation of the fronts. Therefore, a third point has been marked on Figure 3.11 (dot) which follows an irregularity on the front. The marker clearly shows the alongshore movement of the front. Not all images show a clear reference point to be able to calculate accurate along front velocities.

4

THE EVOLUTION OF MULTIPLE PLUME FRONTS IN THE TIDAL RHINE REGION OF FRESHWATER INFLUENCE

The Rhine Region of Freshwater Influence (ROFI) is strongly stratified, rotational, relatively shallow and has large tides, resulting in a dynamic field of fronts that are formed by multiple processes. We use a 3D numerical model to obtain a conceptual picture of the frontal structure and the responsible processes generating this multiple front structure in the Rhine ROFI. The horizontal salinity gradient and numerical tracers are used to identify the different fronts, consisting of the outer, inner, tidal plume and relic tidal plume fronts. Tidal plume front trajectories together with the tracers demonstrate that tidal plume fronts can sustain longer than one tidal cycle, which are then defined as relic tidal plume fronts. They seem to be enhanced on the flood tide and reduced on the ebb tide. The frontogenesis equation indicates that the presence of depth mean and differential alongshore advection, convergence (divergence), sinking (upwelling) and vertical mixing are primarily responsible for sustaining and weakening the tidal plume fronts, resulting in a multi frontal system. As a consequence of tidal advection, the tidal plume fronts are trapped within 20 km from the river mouth for at least four tidal cycles. The observation of a complex river plume system containing relic tidal plume fronts, is important for mixing, cross-shore exchange, transport and coastal ecology.

This chapter is based on S. Rijnsburger, R.P. Flores, J.D. Pietrzak, A.R. Horner-Devine, A.J. Souza, and F. Zijl (under revision). The evolution of multiple plume fronts in the tidal Rhine region of freshwater influence. *submitted to Journal of Geophysical research: Oceans*

4.1. INTRODUCTION

Oceanic fronts are strong lateral gradients of density forming a boundary between two different water masses (*Cromwell and Reid Jr.*, 1956). These fronts are associated with strong surface convergence resulting in downwelling, which leads to a clear surface signature in the form of foam with often floating debris and phytoplankton (*Cromwell and Reid Jr.*, 1956; *Garvine and Monk*, 1974). Fronts are observed on the boundaries and sometimes in the interior of river plumes, where they play an important role in the vertical and horizontal transport and mixing of river water with coastal waters (*Hickey et al.*, 2010; *Horner-Devine et al.*, 2015). The Rhine Region of Freshwater Influence (ROFI), also known as the Rhine River plume, includes multiple fronts that persist for more than one tidal cycle from the river mouth to 15–20 km downstream, and play an important role in mixing and transport processes (*Flores et al.*, 2017; *Horner-Devine et al.*, 2017; *Rijnsburger et al.*, 2018). The understanding of frontal dynamics and their impact on the environment is important for coastal regions vulnerable to sea level rise and coastal erosion, such as the Dutch coast (*Kabat et al.*, 2009; *Nicholls and Cazenave*, 2010). In this work we describe the dynamics of the fronts observed in the Rhine ROFI, classifying their different generation mechanisms and examining the processes by which they are maintained or weakened.

4.1.1. BACKGROUND

A river plume can be divided into different dynamical regions: the near-field, the mid-field and the far-field plume (*Garvine*, 1984; *Horner-Devine et al.*, 2015). A detailed description of the dynamics of the near-, mid- and far-field for a prototypical river plume can be found in *Horner-Devine et al.* (2015) (see their Figure 2). The near-field is the area closest to the river mouth, where the momentum of the discharged river water dominates over the buoyancy of the plume layer. The near-field evolves into the mid-field, where Earth's rotation becomes important turning the plume towards the coast. Ultimately, a density driven coastal current is formed, which is known as the far-field plume.

The entire plume is bounded by a front, also referred to as the outer front, separating from the denser seawater. This frontal boundary is mainly observed in large scale plumes, such as the Columbia River, Delaware Bay, Chesapeake Bay and Hudson River plume (*Garvine*, 1995; *Horner-Devine et al.*, 2015). This offshore front is in thermal wind balance and moves on- and offshore due to the wind (*Fong et al.*, 1997; *Fong and Geyer*, 2001). In addition, an inner front has been observed that separates the shallow coastal waters from the river plume, and that extends along the entire length of the river plume, from the river mouth to the far-field (Figure 4.1a). This inner front has been observed to move offshore under upwelling favourable winds by *Fong and Geyer* (2001) and by tidal straining by *de Boer et al.* (2007).

In systems where the estuarine outflow is modulated by the tide, the near-field plume strengthens and weakens with the tide and is referred to as a tidal plume (*Garvine and Monk*, 1974; *Luketina and Imberger*, 1987; *Marmorino and Trump*, 2000; *Horner-Devine et al.*, 2009; *Kilcher and Nash*, 2010). Tidal plume fronts are formed at the leading edge of the tidal plume as a result of convergence, which can lead to strong downwelling on the order of cm/s (*O'Donnell*, 1988). The persistence of the tidal plume fronts is related to the freshwater discharge. The Columbia River tidal plume front, with an annual mean dis-

charge of 10 000 m^3/s, lasts for approximately 6-9 hours after low water, but is sometimes still visible after 12-14 hours when a new tidal plume front is formed (*Horner-Devine et al.*, 2009; *Kilcher and Nash*, 2010). The stratification, due to previous tidal plumes, leads to complex fronts and the generation of internal waves (*Nash and Moum*, 2005; *Kilcher and Nash*, 2010). In contrast, the river Teign at Teignmouth UK, with a small discharge of 5 m^3/s, forms a tidal plume front that dissipates after roughly 4.5 hours (*Pritchard and Huntley*, 2006). Tidal plume fronts of a surface advected river plume are often associated with elevated turbulence (*Luketina and Imberger*, 1987; *Orton and Jay*, 2005; *O'Donnell et al.*, 2008; *Horner-Devine et al.*, 2013) and have been observed to impact the seabed at depths up to 60 m (*Orton and Jay*, 2005).

In the near-field, the dynamics of these tidal plume fronts are similar to non-rotating buoyant gravity currents observed in laboratory and theoretical studies (*Benjamin*, 1968; *Britter and Simpson*, 1978; *Luketina and Imberger*, 1987; *Marmorino and Trump*, 2000; *Kilcher and Nash*, 2010; *Yuan and Horner-Devine*, 2017). In reality, however, tidal plume fronts seldom spread symmetrically, as observed in the Columbia River plume (*Jay et al.*, 2009), or in the Connecticut River plume, where the lateral propagation of a part of the tidal plume front is hindered by a tidal cross-flow (*Garvine*, 1974b; *O'Donnell*, 1988, 1990). *O'Donnell* (1988) showed that this asymmetrical spreading led to an increased thickness of the hindered front.

4.1.2. DESCRIPTION OF THE FRONTAL STRUCTURE IN THE RHINE ROFI

The Rhine ROFI is formed by the discharge of the Rhine-Meuse rivers, with an annual mean discharge of 2300 m^3/s, into the shallow Southern North Sea. As a result of strong tides, stratification and frictional effects, elliptical tidal currents are generated and dominate the dynamics of the Rhine ROFI through tidal straining and alongshore advection (*Simpson and Souza*, 1995; *de Boer et al.*, 2008). Observations and modeling of the Rhine ROFI describe several different fronts that are differentiated based on their generation mechanism. These observations indicate that 10 km downstream tidal plume fronts are still important, but Froude numbers are below 1, suggesting that the observations are located within the mid-field plume (*Flores et al.*, 2017; *Rijnsburger et al.*, 2018). Throughout this study downstream is northeast from the river mouth, following the propagation direction of a Kelvin wave. Figure 4.1a indicates the different regions within the Rhine ROFI based on several observational and numerical studies (*de Boer et al.*, 2008; *Horner-Devine et al.*, 2015; *Flores et al.*, 2017; *Rijnsburger et al.*, 2018). Additionally, Figure 4.1a summarizes a conceptual picture of the different fronts in the Rhine ROFI, which will be further clarified using the modeling described in this work. In particular, we differentiate fronts of two types: tidal plume fronts and inner fronts.

TIDAL PLUME FRONTS

Modulation of the river outflow by the semi-diurnal tide results in the formation of a new tidal plume front on every ebb (*van Alphen et al.*, 1988; *de Ruijter et al.*, 1997; *Hessner et al.*, 2001) (Figure 4.1a). The progressive tidal wave along the Dutch coast inhibits the tidal plume front from spreading radially during the ebb, leading to an arrested front towards the northeast of the river mouth (*Hessner et al.*, 2001). At that moment the previously released (relic) tidal plume is carried southwards (*van Alphen et al.*, 1988). The

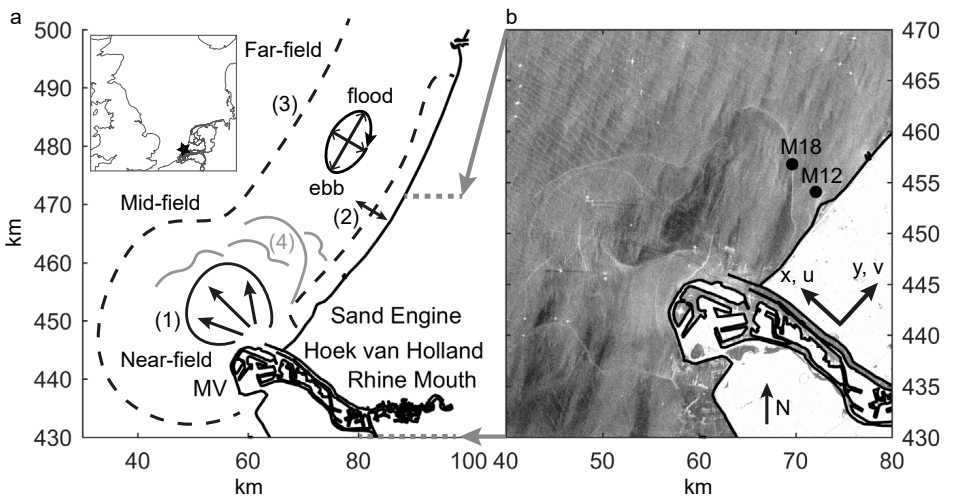

Figure 4.1: Schematic of different river plume fronts and regions a) Schematic of the Dutch coast with different types of river plume fronts: 1) tidal plume front, 2) inner front of entire plume, 3) outer front of entire plume, and 4) relic tidal plume fronts. b) Copernicus Sentinel-1 C-band synthetic-aperture radar image at day 10-02-2015 06:00 (HW + 0.5 hour). This data has a spatial resolution down to 5 m. There are no Sentinel-1 images during the field campaign. Black dots are measurement locations M18 and M12. MV refers to Maasvlakte, which is the Port Extension. The ellipse indicates the anti-cyclonic rotation of the surface tidal velocity, where flood is in northeast direction, and ebb is southwest direction. The horizontal and vertical axes are displayed in RD coordinates in km. The coordinate system is defined that x is the cross-shore direction, and y the along-shore direction. The grey dotted lines and arrows highlights the location of panel b within panel a.

northeastern front propagates away from the mouth due to its intrinsic speed and tidal advection at the start of the flood tide, moving quickly over a distance of 10 to 13 km in 4 to 6 hours (*van Alphen et al.*, 1988; *Hessner et al.*, 2001). Using radar images and idealized numerical modelling, *Hessner et al.* (2001) found that the shape and location of the tidal plume front in the near-field is strongly influenced by the phase of the semi-diurnal tidal cycle, and is only weakly influenced by the discharge volume, residual currents and spring-neap tidal cycle.

Field observations 10 km downstream of the river mouth, showed the onshore propagation of fronts which were associated with the tidal plume front, and had features in common with tidal plume fronts in other systems, such as a plunging head and similar propagation speed (*Flores et al.*, 2017; *Horner-Devine et al.*, 2017; *Rijnsburger et al.*, 2018). These field observations demonstrated the importance of the semi-diurnal tide on the dynamics of the tidal plume front, consistent with the results of *Hessner et al.* (2001). The tide and wind control the propagation of the fronts mainly by advection (*Rijnsburger et al.*, 2018), as a result of much larger ambient coastal currents than intrinsic frontal speeds. This is supported by scaling the typical maximum values for frontal speeds (u_f) and ambient tidal currents (u_0), leading to a ratio of $u_f/u_0 \approx 0.5/1 \approx 0.5$ (*Rijnsburger et al.*, 2018; *de Kok*, 1997). This ratio suggests the importance of advection in this system.

de Ruijter et al. (1997) suggested that the tidal plumes, which they refer to as "lenses", detach from the river mouth after one tidal cycle and are carried far enough from the river mouth each tidal cycle that they do not interact with each other. Therefore, these tidal plumes can propagate as distinct lenses that do not interact with each other along the coast or get mixed within the river plume (*van Alphen et al.*, 1988; *de Ruijter et al.*, 1997; *de Kok*, 1997). This spatial picture is different from other tidal plumes which stay connected to the river mouth (*Horner-Devine et al.*, 2009, 2015).

INNER FRONTS

A second type of front is observed in the Rhine ROFI, which forms a boundary between the river plume and the inner shore along the coastline over a distance of about 100 km. This is referred to here as the inner front (Figure 4.1a). As described in the idealized numerical model study of *de Boer et al.* (2007), the formation process of the inner front is a consequence of the fact that the Rhine ROFI is advected off- and onshore every tidal cycle due to tidal straining. Cross-shore tidal straining is the interaction of the horizontal density gradients with cross-shore shear, producing a semi-diurnal cycle of stratification (*Simpson et al.*, 1990). This requires the occurrence of strong cross-shore shear. *Visser et al.* (1994) found that the tidal currents rotate as counter rotating ellipses between the surface and the bed (see schematic of an ellipse in Figure 4.1a), as a result of the interaction between the progressive tide, stratification, friction and Earth rotation. The surface currents are offshore directed from LW to HW, and onshore directed from HW to LW. The bottom currents are directed in the opposite direction as the surface currents. Accordingly, the inner front moves approximately 5 - 10 km offshore between HW-3 and HW+3 leading to upwelling of colder water at the coast *de Boer et al.* (2007).

SPATIAL FRONTAL STRUCTURE

The Copernicus Sentinel-1 C-band synthetic-aperture radar (SAR) image shows a multi frontal structure in the Rhine ROFI (Figure 4.1b). Several recent studies (*Horner-Devine et al.*, 2017; *Flores et al.*, 2017; *Rijnsburger et al.*, 2018) confirm the presence of multiple fronts within the Rhine ROFI. These fronts were observed in field-data collected at two mooring sites roughly 10 km downstream from the river mouth (Figure 4.1b). However, these data did not allow them to investigate the spatial movement of these fronts or how they interact. Additionally, difficulties arose to identify and differentiate between the inner and tidal plume fronts in the field data because their predicted arrival time is similar (*Horner-Devine et al.*, 2017). Furthermore, these studies suspected the presence of more fronts in addition to the inner front and the most recently released tidal plume front (Figure 4.1). One of the motivations to investigate the dynamics of these fronts is that tidal plume fronts were shown to be able to increase bed stresses leading to resuspension (*Flores et al.*, 2017; *Rijnsburger et al.*, 2018). Additionally, radar images showed that these fronts propagate towards the coast generating a cross-shore exchange flow that causes offshore sediment transport (*Horner-Devine et al.*, 2017; *Flores et al.*, 2017).

We use a three-dimensional realistic numerical model that complements existing field studies in order to better understand the spatial structure and movement of fronts in the Rhine ROFI. Specifically, we investigate the evolution of the tidal plume front, the occurrence of multiple tidal plume fronts, and the processes responsible for the evolution of the front. The study area is restricted from the river mouth up to 20 km downstream, and from the coast to 30 km offshore. It should be noted that the tidal plume fronts are inherently non-hydrostatic. However, non-hydrostatic three-dimensional numerical models are computationally challenging to use. Therefore, we use a three-dimensional hydrostatic model to study frontal propagation and evolution. In a hydrostatic model the vertical velocity is obtained from the continuity equation, therefore vertical accelerations are not directly calculated. As a result, the model will not resolve the small-scale non-hydrostatic features of the fronts, but only estimates the larger scale properties such as propagation speed, direction, and corresponding horizontal salinity gradients.

The paper is organized as follows: In section 4.2, we describe the model set-up and the field-data used. In section 4.3, the model results are compared to in-situ data to evaluate the model performance. In section 4.4 we differentiate between the different fronts, investigate the dynamics of the tidal plume fronts, and the processes responsible for the multiple front system. We discuss the findings and ask ourselves how generic these fronts are in section 4.5. Finally, conclusions are presented in section 4.6.

4.2. METHODS

4.2.1. NUMERICAL MODEL CONFIGURATION

The FLOW module of Delft3D is used to simulate a hind cast of flow and transport in the Rhine ROFI for the period of 15 September to 07 October 2014 (yeardays 258 - 280). Delft3D-Flow solves the three dimensional non-linear shallow water equations using the Boussinesq and hydrostatic pressure approximation (*Deltares*, 2014; *Stelling and Van Kester*, 1994), and has been used for different applications in shallow seas, coastal areas and estuaries (*Lesser et al.*, 2004; *de Boer et al.*, 2006; *de Nijs and Pietrzak*, 2012). For this

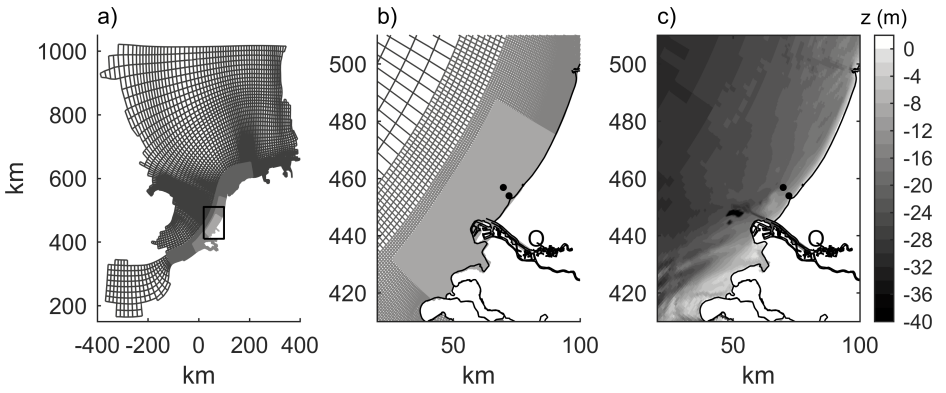

Figure 4.2: Model grid and bathymetry. a) The entire model domain consists of 4 grids with different resolution. b) Zoom on model grid along the Dutch coast. c) Model bathymetry along the Dutch coast. Black dots are measurement locations, and Q refers to the discharge location at the river in the model. The horizontal and vertical axes are displayed in RD coordinates (in km).

study we use a model setup describing the southern North Sea with increased horizontal resolution towards the Dutch coast using a domain decomposition technique (*Deltares*, 2014). This decomposition results in four curvi-linear computational grids with increasing grid size: a coarse, intermediate, fine and extra fine grid (Figure 4.2a,b). The refinement is in both horizontal directions by a factor 3, 2 and 3 between coarse-intermediate, intermediate-fine and fine-extra fine, where the finest grid has grid cells between 80–400 m in alongshore direction and 80–500 m in cross-shore direction. All four grids contain 20 non-equidistant sigma-layers in the vertical, with smaller cells at the surface and bottom. These vertical cells have a size in the range of 3 % to 6 % of the entire water column. This implies that the vertical resolution varies depending on the local water depth.

The model was forced on the northern and western boundaries by the astronomical tide, where the tidal constituents were obtained from the Dutch Continental Shelf Model (DCSM) (e.g. *Verboom et al.* (1992), *Verlaan et al.* (2005)). A space- and time-varying wind speed (at 10m height) and atmospheric pressure has been applied at the free-surface obtained from the Numerical Weather Prediction high-resolution limited area model (HiRLAM). In addition, a heat-flux model accounts for the exchange of heat through the air-sea interface using wind speed, air temperature (at 2m), cloud coverage and relative humidity from the same meteorological model (HiRLAM). The incoming solar radiation is computed based on the latitude and time. Additionally, 85 rivers discharging into the southern North Sea are implemented, under which the Meuse and Rhine Rivers are the most important. Time-varying values of the Dutch rivers are used based on the available data (Rijkswaterstaat). The temperature and salinity for the rivers in the coarser grids are set to 11 degrees and 0 PSU, while for the Dutch rivers the temperature and salinity are based on observations. Figure 4.3 shows the sea surface elevation, wind vectors at station M18 and the discharge at the river mouth corresponding to the period when field data was collected.

Space-varying bathymetry has been used in the model which is obtained from the

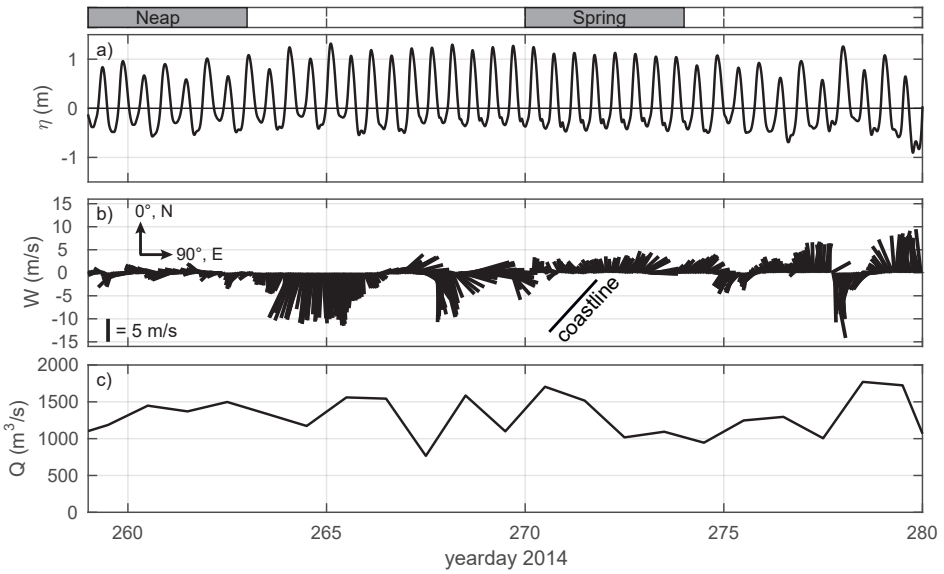

Figure 4.3: Time series of model forcing during two months in 2014 (15 September till 07 October 2014). a) Sea surface height (m) at station M18. b) Wind vectors in m/s at station M18. c) Discharge of Rhine River in numerical model (m^3/s).

North West European Shelf Operational Oceanographic System (NOOS) for the coarser grids, and based on surveys carried out by the Dutch Hydrographic Service and Rijkswaterstaat for the finer grids. The bathymetry of the Sand Engine and the Port extension have been implemented in the model based on bathymetry data from year 2014 (Figure 4.2c). The southern North Sea has a maximum depth of about 20–30 meters in the waters more offshore and in the navigation channel.

The model uses the k-ϵ model to resolve vertical mixing of salt, temperature and momentum. A background vertical diffusivity of $1{\cdot}10^{-5}$ m^2/s and a horizontal diffusivity of 1 m^2/s are imposed on all grids. In addition, a background vertical viscosity of $5{\cdot}10^{-5}$ m^2/s is applied to all grids. A horizontal background viscosity of 5, 2.5 , 1.25 and 1.25 m^2/s is applied to the coarse, intermediate, fine and extra fine grid. A larger horizontal viscosity of 250 or 1000 m^2/s is applied to boundaries between different grids to prevent instabilities.

The model was initialized with a salinity of 34.5 PSU and a temperature of 11 degrees, which is based on the long term average for the North Sea (*Suijlen and Duin*, 2002). North and east velocities were rotated into along- and cross-shore direction using a rotation angle of 42.5 degrees from the North, where positive velocities are in northeast and offshore direction. The coordinate system throughout this study is defined as x is offshore directed and y is alongshore directed (Figure 4.1b). The spin-up period was 8 months, such that the impact of the initial conditions was limited. A numerical time step of 48 seconds has been used. The model has been set-up for the entire year 2014. However, this study is focussed on a typical neap and spring period, this is because the

Rhine ROFI responds differently during these periods as a result of the amount of tidal mixing (*Simpson et al.*, 1993; *de Boer et al.*, 2006). We selected a neap tide with relatively low wind speeds from the east (90 degrees, <= 5 m/s, days of the year 259–263), and a spring tide with relatively low wind speeds mainly from the southeast to southwest (135–225 degrees, < 6 m/s, days of the year 270– 274), which coincide with the STRAINS field-campaign in 2014 (*Flores et al.*, 2017) (Figure 4.3).

4.2.2. FIELD-DATA

Field-data is used to investigate the model performance. Moorings and frames were deployed from 17 September until 17 October 2014 (year days 260 to 290) 10 km northeast of the mouth of the Rotterdam Waterway at 2 and 6 km offshore, corresponding to water depths of 12 and 18 m (Figure 4.2b,c black dots). In total, 9 Seabird Microcat Conductivity Temperature Depth (CTD) instruments were attached to the two moorings, 4 at the 18 m site and 5 at the 12 m site. The CTD instruments were located at 12 and 18 m sites at 1, 3, 7, 8, and 10.5 m below the sea surface and at 1, 2.5, 10, and 15 m respectively, thus providing a detailed description of salinity and density throughout the water column at both sites. Vertical velocity profiles were measured using a four beam Acoustic Doppler Current Profiler (ADCP) attached to a bottom frame sampling at a frequency of 1 Hz. North and east velocities were rotated into along- and cross-shore direction using a rotation angle of 42.5 degrees from the North, where positive velocities are in northeast and offshore direction. Here, we used a 10 minute average of the CTD and ADCP data. For more details see *Flores et al.* (2017) and *Rijnsburger et al.* (2018).

4.2.3. PASSIVE TRACERS

Passive tracers, similar to dye injection, are added to the model simulations to follow the freshwater outflow from the Rhine-Meuse Delta (Figure 4.2). Passive tracers are released 2 hours before until 2 hours after low tide on 4 consecutive tidal cycles at the same location as the discharge (Figure 4.2c, Q). The timing of low water is determined by the M2 tidal constituent. It takes about 0.5 day for the tracer to leave the Rhine River mouth. Each tracer starts with a concentration of 1 kg/m^3, while a background concentration of 0 kg/m^3 is used. We define the contour of a tidal plume as the concentration where at least 85 % of the tracer concentration was within this contour. This choice is made based on the salinity gradient, where 85 % matches quite well with salinity gradients larger than 2 PSU/km (Figures 4.11 and 4.12 in Section 4.4.4).

4.2.4. FRONT IDENTIFICATION AND PROPERTIES

The fronts are identified using the horizontal salinity gradient, which is defined as

$$|\nabla_h s| = \sqrt{(\partial s/\partial x)^2 + (\partial s/\partial y)^2}, \tag{4.1}$$

where $(\partial s/\partial x)_n = (s_{n+1} - s_{n-1})/(x_{n+1} - x_{n-1})$, and similar for $\partial s/\partial y$ in the y-direction. The subscript n refers to a gridcell, and a central difference scheme has been used to calculate the gradients. In addition, more quantities are used throughout this study that highlight the location of the fronts, such as passive tracers (kg/m^3) and horizontal divergence, $\mathrm{Div}_h = \partial u/\partial x + \partial v/\partial y$. The passive tracers isolate the different tidal plume fronts,

because each tracer refers to a different release of freshwater from the river mouth. The fronts are expected to relate to a convergent flow ($\mathrm{Div}_h < 0$), which should lead to downwelling at the leading edge of the frontal head (*O'Donnell et al.*, 1998).

The tidal plume front is followed in time and space to analyze the evolution of its properties, such as tidal plume thickness, frontal speed and frontal Froude number. The tidal plume front is identified by $|\nabla_h s|$ close to the river mouth at the beginning of the flood. We select a point on this front that we then follow. Subsequent locations on the front are calculated using a lagrangian tracking method:

$$x_{t1} = x_{t0} + (\Delta t \cdot u_{t0}) \tag{4.2}$$

$$y_{t1} = y_{t0} + (\Delta t \cdot v_{t0}), \tag{4.3}$$

where x_{t0}, y_{t0}, u_{t0}, and v_{t0} are the frontal position and the surface velocities at the current time step. Δt is the time step, which is 8 minutes. x_{t1}, y_{t1} refer to the new position of the front on the next time step. Then, we use $|\nabla_h s|$ to verify that we are still on the front. This procedure results in a front trajectory in time and space on which we calculate the different properties. We use three different locations on the front trajectory to calculate front properties, which are 1) on the front, 2) ahead of the front, and 3) behind the front. A tidal plume front cannot be represented well by one point. Therefore, we select 9 to 12 locations on each tidal plume front, resulting in 9 to 12 front trajectories. These trajectories are averaged and a standard deviation is calculated for each frontal property.

There are multiple definitions of Froude numbers (see for example *Kilcher and Nash* (2010)). Here, we use the frontal Froude number in line with other front studies (*Britter and Simpson*, 1978; *Garvine and Monk*, 1974; *Luketina and Imberger*, 1987; *Kilcher and Nash*, 2010; *Horner-Devine et al.*, 2013), which is defined as the ratio of the frontal speed relative to the long wave phase speed behind the front:

$$F = \frac{u_f}{c_0}, \tag{4.4}$$

where u_f is the intrinsic frontal speed, c_0 is the linear long wave phase speed behind the front (excluding velocity shear). The linear long wave phase speed c_0 is calculated with the Taylor Goldstein equation only using density profiles. We calculate c_0 without shear to be in line with the other front studies (*Garvine and Monk*, 1974; *Luketina and Imberger*, 1987; *Kilcher and Nash*, 2010; *Horner-Devine et al.*, 2013). However, the presence of a strong velocity shear will change c_0, and therefore F. The frontal Froude number compares the frontal momentum with the buoyancy of the tidal plume. The front is supercritical (F > 1) when the momentum dominates over buoyancy, meaning that information (for example internal waves) can only travel downstream.

The frontal speed moving with the front, u_f, is estimated on the front trajectory as $u_f = (\partial x/\partial t) - \overline{u_0}$, where $\overline{u_0}$ is the front normal depth mean ambient current ahead of the front. Therefore, u_f is relative to the background current (intrinsic frontal speed). The tidal plume thickness, h, is obtained applying a hyperbolic tangent fit to the density profile behind the front. Vertical profiles of density indicate that a hyperbolic tangent fit can be used to estimate the tidal plume depth (Figure 4.5i-l, Section 4.3).

In this study, we define the strength of the fronts based on the horizontal salinity gradient. We choose the horizontal salinity gradient as a strength parameter, because of the definition of a front in the field. If there is no salinity gradient observed, there is no front. A sharp and large horizontal salinity gradient is defined as a strong front, while a diffuse low salinity gradient is defined as a weaker front (*Jay et al.*, 2009).

4.2.5. FRONTOGENESIS EQUATION

We use the frontogenesis equation to understand the processes controlling the evolution of the tidal plume fronts. The frontogenesis equation describes the evolution of a scalar gradient by derivating the scalar tendency equation in the front normal direction (*O'Donnell*, 1993; *Giddings et al.*, 2012; *Geyer and Ralston*, 2015; *Akan et al.*, 2018). Here, we chose the salinity (s) as scalar, because the density in this system is dominated by salinity. The frontogenesis equation in the alongshore direction (y) is:

$$\underbrace{\frac{\partial}{\partial t}\left(\frac{\partial s}{\partial y}\right)}_{\text{tendency}} = \underbrace{-v\frac{\partial}{\partial y}\left(\frac{\partial s}{\partial y}\right) - u\frac{\partial}{\partial x}\left(\frac{\partial s}{\partial y}\right) - w\frac{\partial}{\partial z}\left(\frac{\partial s}{\partial y}\right)}_{\text{advection}} \ldots \underbrace{-\frac{\partial v}{\partial y}\frac{\partial s}{\partial y} - \frac{\partial u}{\partial y}\frac{\partial s}{\partial x} - \frac{\partial w}{\partial y}\frac{\partial s}{\partial z}}_{\text{horizontal differential advection}} \underbrace{-\frac{\partial}{\partial y}\frac{\partial}{\partial z}\overline{s'w'}}_{\text{vertical mixing}} \tag{4.5}$$

, where x, y, and z denote the cross-shore, alongshore and vertical coordinates, u, v, and w are the velocities in these directions. We investigate the alongshore gradients, because the main part of the front moves alongshore during the flood period of the tide. The term on the left side of equation 4.5 is the local tendency of the horizontal salinity gradient. This term is balanced by the seven terms on the right hand side. The first, second and third terms on the right hand side represent the rate of change of the salinity gradient as a result of advecting an existing gradient. The fourth term represents the enhancement (reduction) of the alongshore salinity gradient in the presence of convergence (divergence) (*O'Donnell*, 1993). The fifth term represents horizontal differential advection of the salinity gradient in the presence of a cross-shore salinity gradient. The sixth term is the enhancement (reduction) of the alongshore salinity gradient in the presence of sinking (upwelling) (*O'Donnell*, 1993). The seventh term represents the alongshore gradient of vertical mixing (*Geyer and Ralston*, 2015). Several terms try to maintain the gradient, while other terms try to reduce the gradient dependent on the local conditions. These terms together generate, maintain or weaken a front. The advective terms (terms 1-3) often dominate in river plume fronts (*O'Donnell*, 1993). However, the other terms still play an important role in the rate of change of the gradient (*O'Donnell*, 1993).

4.3. COMPARISON OF THE MODEL WITH THE FIELD-DATA

This section validates the numerical model by direct comparison with the point measurements of the field-data for both a neap and spring period. The model is in good qualitative agreement with the field-data. This agreement is observed in the following key metrics: temporal salinity structure, vertical density structure, timing of the tidal plume front, structure and magnitude of the tidal currents. Both the model and field-

Table 4.1: Root-Mean-Squared Error (RMSE) and bias for the stations M18 and M12 for surface and near seabed (bed) salinity (PSU), alongshore (v) and cross-shore (u) velocity (m/s).

	RMSE sal		RMSE v		RMSE u		Bias sal		Bias v		Bias u	
station	surface	bed	surface	bed	surface	bed	surface	bed	surface	bed	surface	bed
M18	1.93	1.25	0.16	0.08	0.15	0.07	0.52	-1.12	0.008	0.014	-0.0055	0.0043
M12	1.93	1.99	0.15	0.10	0.12	0.08	-0.5	-1.75	-0.018	0.02	-0.028	0.0006

data are presented in the time zone UTC+1. Additionally, we calculate quantitative evaluation measures, such as the Root Mean Square Error (RMSE) and the bias, to assess the model performance for both mooring stations (See table 4.1). In the following, we will briefly highlight areas of agreement and minor discrepancies between model and field data (Figures 4.4 and 4.5).

Despite the coarse vertical resolution of the field-data, vertical salinity and density profiles indicate a similar structure between model and field-data near the surface and the bed (Figures 4.4 and 4.5i-l). This comparison shows that the model is systematically fresher near the bed (Table 4.1). Additionally, the surface salinity and density demonstrates the passage of a tidal plume front each tidal cycle after HW (Figures 4.4 and 4.7). Moreover, the surface density gradient in time indicates that the timing of the tidal plume fronts shows differences of 5 to 50 minutes (Figure 4.5c-d, black dots). This offset seems to align with the offset of the tidal elevation and current.

Overall, the model captures the vertical and temporal structure of the tidal velocity quite well (Figures 4.4 and 4.5e-h). A small delay in the modelled velocities is observed (Figure 4.5e-h). The alongshore velocity is slightly overestimated in the model (Figure 4.5e-f). Additionally, the magnitude of the offshore velocity coincides quite well with the field-data, while the onshore velocity is slightly overestimated (Figure 4.5g-h, Table 4.1). The modelled cross-shore velocity penetrates deeper into the water column during neap, while being thinner during spring. The same trend has been observed in the modelled vertical salinity resulting in an over- and underestimation of the pycnocline depth. In general, the model captures the strong cross-shore shear that alternates during one tidal cycle (Figures 4.4 and 4.5e-h). As a result, the model captures the interaction between the velocity shear and the horizontal salinity gradient resulting in the alternation of a stratified and well-mixed water column (cross-shore straining, Figure 4.4d,j).

After validating the model prediction with field data, we turn to examining model predictions across the entire Rhine ROFI area. Therefore, we plot surface fields of salinity and the velocity vector during one tidal cycle to qualitatively compare the spatial structure with previous studies (Figure 4.6). As indicated by Figures 4.4 and 4.5, the surface currents rotate anti-cyclonically near the surface and cyclonically near the bed (not shown) during one tidal cycle (Figure 4.6). The cross-shore surface velocities in the downstream plume are smaller during spring than during neap. These results are inline with the observations of *Visser et al.* (1994). In addition, the salinity shows a river plume formed along the coast with smaller horizontal gradients near the offshore boundary than close to the river mouth. We highlight the offshore boundary by selecting a salinity contour of 33 PSU. The general movement and change of the river plume structure during one tidal cycle is in good agreement with previous model studies (*de Boer et al.*, 2006,

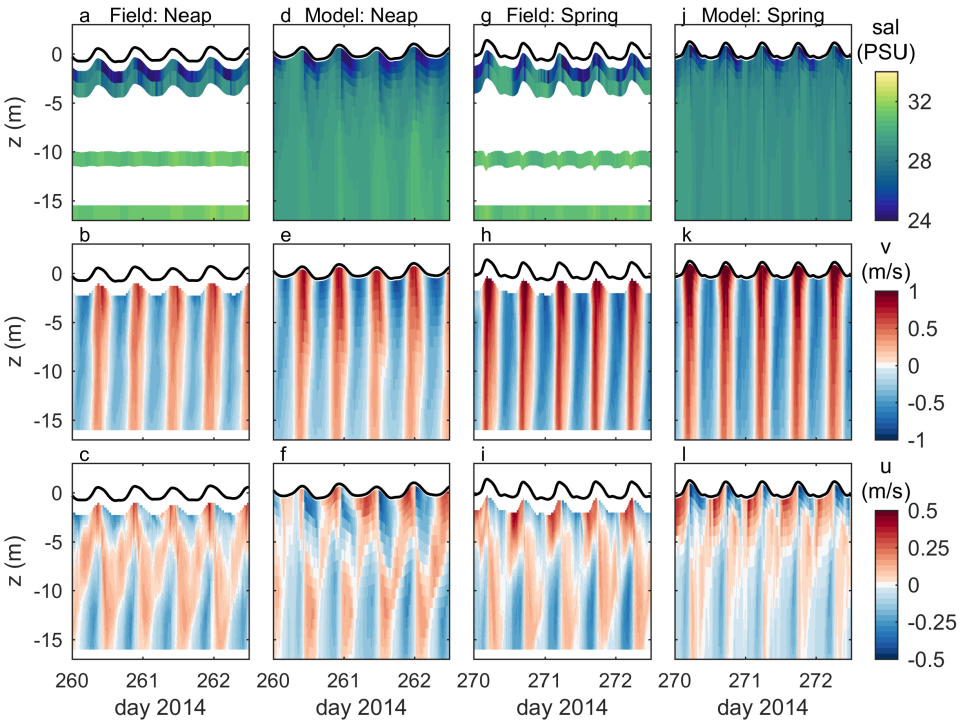

Figure 4.4: Comparison of field-data (a,b,c,g,h,i) and model (d,e,f,j,k,l) at station M18 for salinity, alongshore- (v) and cross-shore (u) velocity, where the x-axis is day of the year, y-axis is depth in meters. Two periods are plotted: neap (260-262.4) and spring (270-272.4). Positive velocities are in northeast and offshore direction, while negative velocities are in southwest and onshore direction.

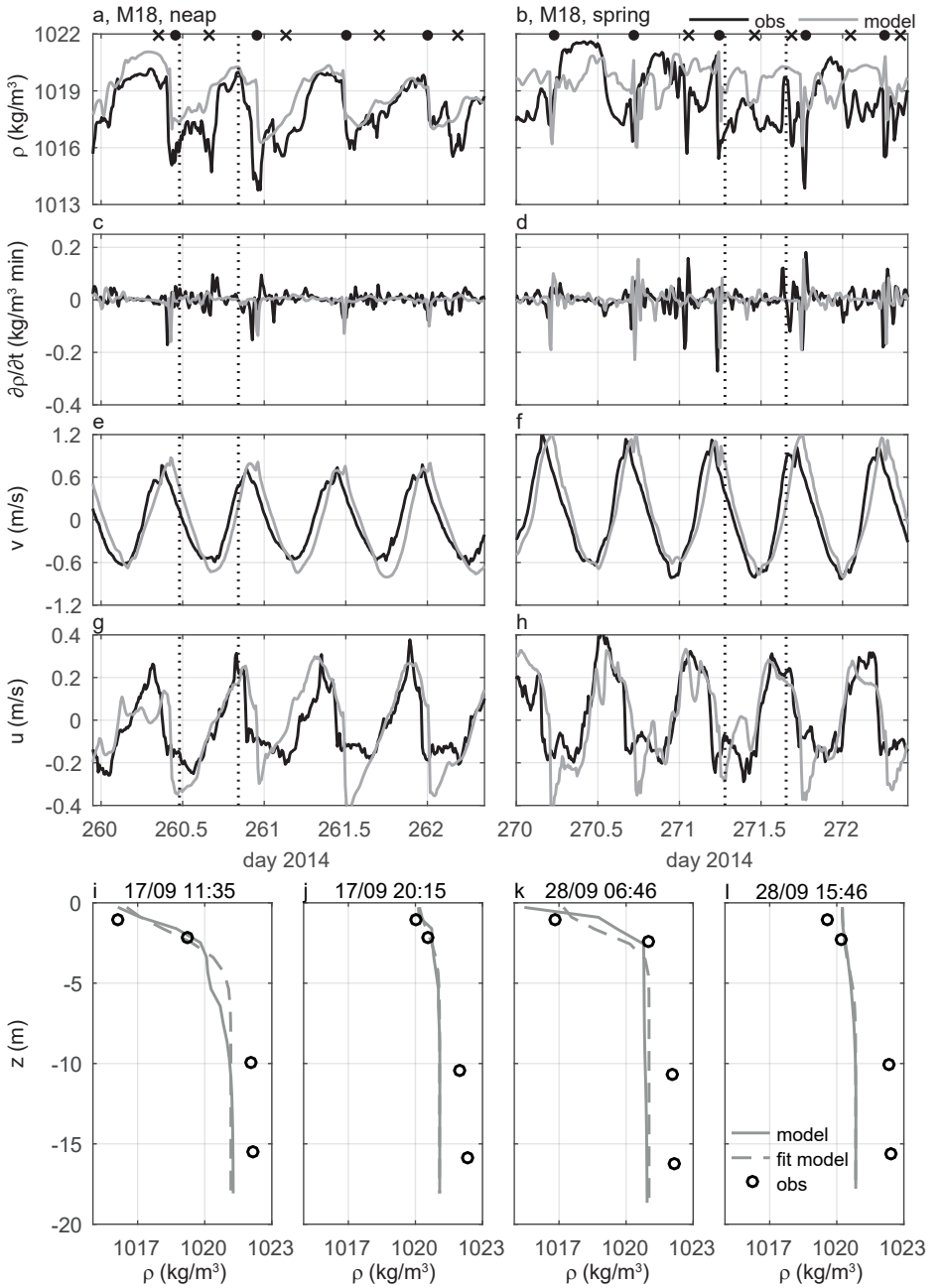

Figure 4.5: Comparison between model and field-data for a neap (left panels) and a spring tide (right panels) at station M18. a-b) surface density, c-d) surface density gradient in time, e-f) alongshore surface velocity (v), g-h) cross-shore surface velocity (u), i-l) vertical profiles of density. The grey lines refer to the model data, and the black lines refer to the field-data. The black dotted lines in panels a-h refer to the vertical density profiles in panels i-l. In panels i-l, the black circles refer to the mooring data (observations) and the dashed grey lines show a hyperbolic tangent fit to the model data. The black dots in panels a and b mark the newly released tidal plume front, while the black crosses mark other fronts.

2007, 2008; *Fischer et al.*, 2009).

4.4. RESULTS

4.4.1. DISTINCTION BETWEEN MULTIPLE FRONTS

In this section we use the model to investigate the multi-frontal structure, focusing initially on a calm neap tide (Figure 4.3). We use the horizontal salinity gradient at the surface to identify the spatial frontal structure, the normalized horizontal divergence (Div_h/f) at the surface to identify regions of divergence (convergence) (*O'Donnell et al.*, 1998), and the concentration of a tracer to identify water associated with the newly released tidal plume (Figure 4.7). Three times within a tidal cycle are plotted coinciding with Figure 4.6: LW (03:36), HW (09:44), HW+2.7 hours (around slack, 12:24). The horizontal salinity gradient shows many fronts in the near- and mid-field plume, with the largest gradients around the river mouth (Figure 4.7a-c). The different fronts are labelled inline with Figure 4.1a. The inner and outer fronts are identified as the frontal features of the entire river plume with salinity gradients of 0.8 PSU/km and a salinity contour of 33 PSU, respectively. These fronts are indicated in Figure 4.7g-i with grey and black dotted lines, and labeled as numbers 2 and 3. The tidal plume front has a horizontal salinity gradient with a minimum of 4 PSU/km and is indicated in Figure 4.7g-i as a dark red line and labeled as number 1. The other distinct fronts are indicated with label 4. The interest of this study is mainly on the fronts around the river mouth and northeastwards. The following subsections will discuss the observations of the inner front and the tidal plume front.

INNER FRONT

The inner front (2) is visible in the salinity gradients in Figure 4.7a as a distinct straight line parallel to the coast. Its surface signature starts to appear around LW-2, and accelerates offshore after LW. The inner front propagates offshore through the 18 m mooring site between LW and HW (Figure 4.7a-b). In addition, the inner front stretches and moves downstream (northeastwards) between LW and HW (not shown). *de Boer et al.* (2007) found that this front propagated back onshore between HW and LW due to the onshore tidal currents. On this neap day the model shows that the inner front dispersed between HW and HW+2.7. No clear onshore movement of the inner front through the mooring site is observed based on the horizontal salinity gradient. The timing of offshore propagation is similar to the timing of tidal straining observed by *Simpson and Souza* (1995) and *de Boer et al.* (2007), which is the mechanism behind the generation of this offshore propagating front (*de Boer et al.*, 2007). In the study of *de Boer et al.* (2007) the inner front reached its most offshore location on HW, which is in line with what we have found here. The inner front was located 6.4 km from the coastline at HW. Therefore, the cross-shore movement of the modelled inner front stayed within the 5-10 km range observed by *de Boer et al.* (2007) in sea surface temperature images.

TIDAL PLUME FRONTS

The high salinity gradients around the mouth at LW (03:36) correspond to the newly released tidal plume front (1) with minimum gradients of 4 PSU/km (figure 4.7a). Figure

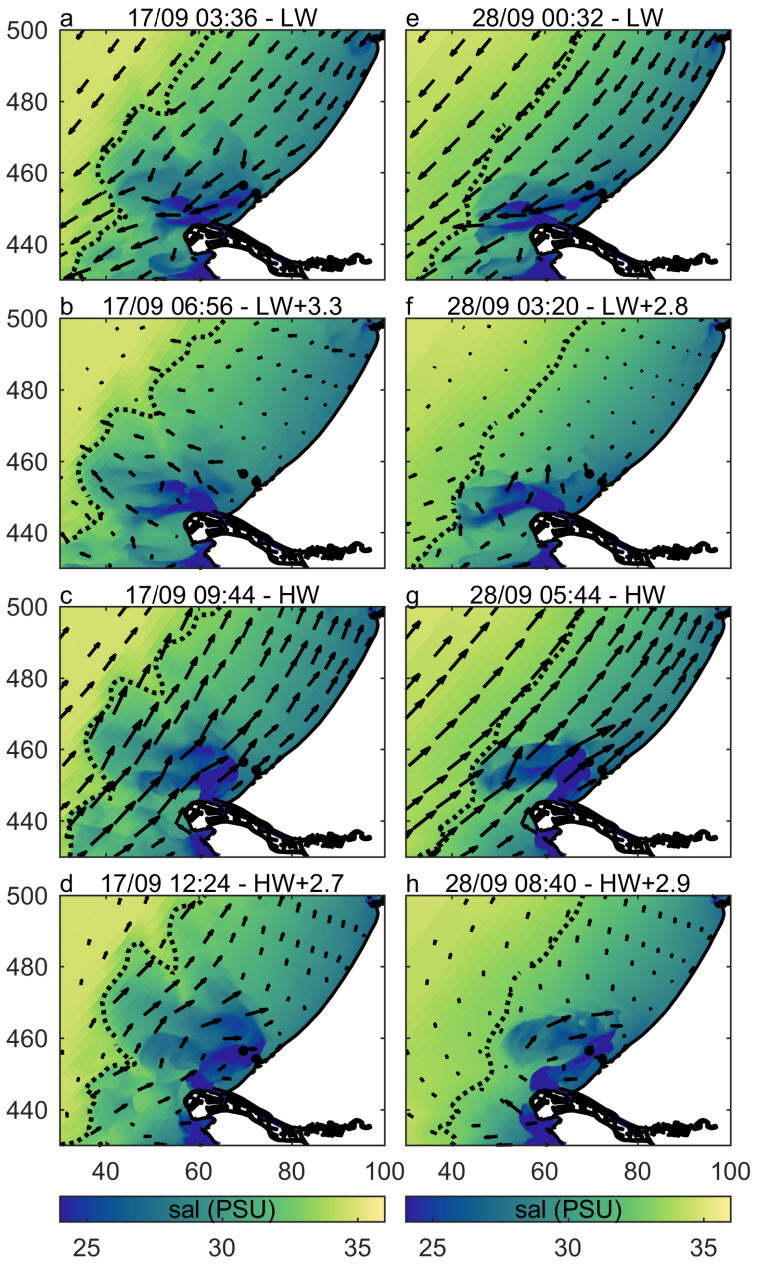

Figure 4.6: Surface salinity during one tidal cycle. The vectors represent the surface velocity. The first row represents low water (LW) (a,e), and the third row represents high water (HW) (c,g). The left column (a-d) is during the neap period on day 260 (17/09/2014) and the right column (e-h) is the spring period on day 271 (28/09/2014). The horizontal and vertical axes are displayed in RD coordinates in km. The dashed black line is the 33 PSU contour of salinity to mark the river plume. Black dots are measurement locations. The time zone is UTC+1.

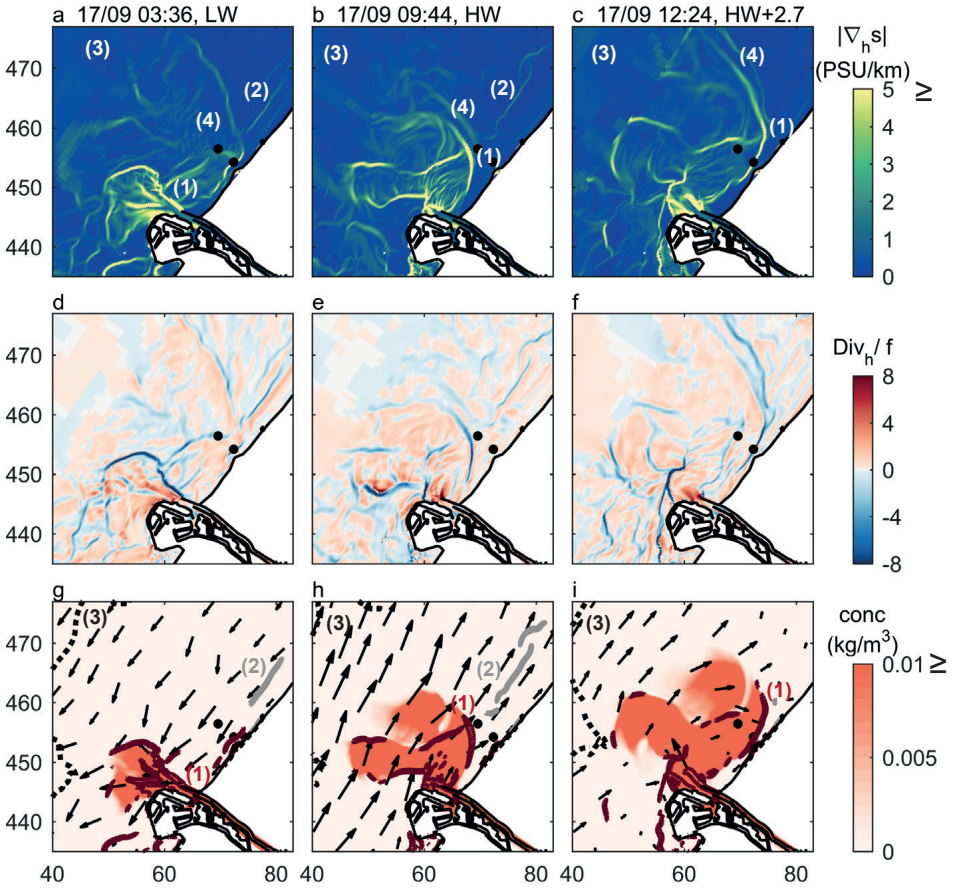

Figure 4.7: Plan view of the absolute value of the horizontal salinity gradient (a-c), normalized horizontal divergence (Div_h/f) (d-f), and a tracer concentration (g-i) in the surface layer during a tidal cycle at a neap tide (day 260 or 17/09). Each column represents a snapshot in time, where LW is around 03:36, HW is around 09:44, and slack water around HW+2.7 hours. The vectors represent surface velocity (m/s). The two black dots indicate the two mooring sites. The labels refer to the different fronts inline with Figure 4.1a. The black dotted line indicates the outer edge (3) of the river plume using the 33 PSU salinity contour. The grey line highlights the inner edge of the river plume (2), using the 0.8 PSU/km salinity gradient contour. The dark red solid line is the salinity gradient of 4 PSU/km or larger, highlighting the newly released tidal plume front (1). Older tidal plume fronts are labeled with (4). Note that a salinity gradient of 2.5 parallel to the coast is observed around 62, 477 km. This gradient is an artefact due to the grid boundary. The horizontal and vertical axes are displayed in RD coordinates in km. See Movie 1 for the horizontal salinity gradient in time (supplementary materials).

4.7 shows that the tracer concentration follows the largest gradients around the river mouth and can be used to identify this tidal plume front. The tidal plume front is clearly indicated by negative divergence values ($Div_h < 0$, convergence), suggesting downwelling at the leading edge of the front inline with *O'Donnell et al.* (1998). A strong front, defined by a large horizontal salinity gradient, has already formed around the mouth at LW. The northeastern front is arrested and initially remains attached to the mouth and strengthens due to convergence as it propagates against the ebb flow, while the southern front decreases in strength due to the additional southward spreading augmented by the ebb current (Figure 4.7a). These findings are in line with observations of *Hessner et al.* (2001), who found that during the ebb flow the northeastern front is arrested and strengthens. The tidal plume has spread during the ebb (Figure 4.7g,h). The flood current advects the tidal plume northeastwards and allows the northeastern front to start propagating and swinging onshore until the next LW. At HW+2.7 (12:24) the northeastern tidal plume front has passed through both the mooring sites, and propagated at least 12 km northeastwards and towards the coast. This distance is in line with the findings of *van Alphen et al.* (1988) and *Hessner et al.* (2001) who found that the northeastern front moved about 10–13 km downstream during one tidal cycle.

Figure 4.7a-c shows fronts with horizontal salinity gradients between 1 and 4 PSU/km, which are not related to the most recently released tidal plume front or inner front. These fronts (4) seem to become broader with lower salinity gradients during the ebb compared to the flood. Additionally, these fronts seem to align with a convergent flow as well. In subsection 4.4.4 we will investigate whether these other fronts are relic tidal plume fronts. First, we will explore the differences with a spring tide.

4.4.2. COMPARISON BETWEEN A NEAP AND A SPRING TIDE

The tide plays an important role in the stratification and structure of the Rhine River plume (*Simpson and Souza*, 1995; *de Boer et al.*, 2006). During spring tide vertical stratification is expected in the near- and mid-field with little tidal straining in the far-field (*Simpson et al.*, 1993; *de Boer et al.*, 2006), while strong vertical stratification is present along the entire coast during neap tide. The salinity gradient in Figure 4.8 indicates that an inner front is not present during the spring period, which is in agreement with the results of *de Boer et al.* (2007).

The horizontal salinity gradient shows that the near- and mid-field region is less spread out during the spring period (label 3); all the fronts around the river mouth are located within a radius of approximately 20 km (Figure 4.8). The gradients and the tracer concentration demonstrate the presence of a clear tidal plume front (1) that is propagating southwards and offshore, and is arrested on the northeastern side of the tidal plume due to the ebb flow (Figure 4.8a). Similar to neap, a distinct tidal plume front swings onshore during the flood period (Figure 4.8b). The tidal plume front during spring exhibits larger horizontal salinity gradients than the neap front, with maximum values around 25 PSU/km versus 15 PSU/km, respectively (not visible due to color scale). These gradients correspond to distinct regions of convergence (Figure 4.8d–f). Moreover, this tidal plume front does not extend as far offshore as during neap (Figures 4.6 and 4.8). Figure 4.6 shows that the tidal plume during neap propagates maximum 40 km offshore, while it reaches a maximum offshore distance of 30 km during spring.

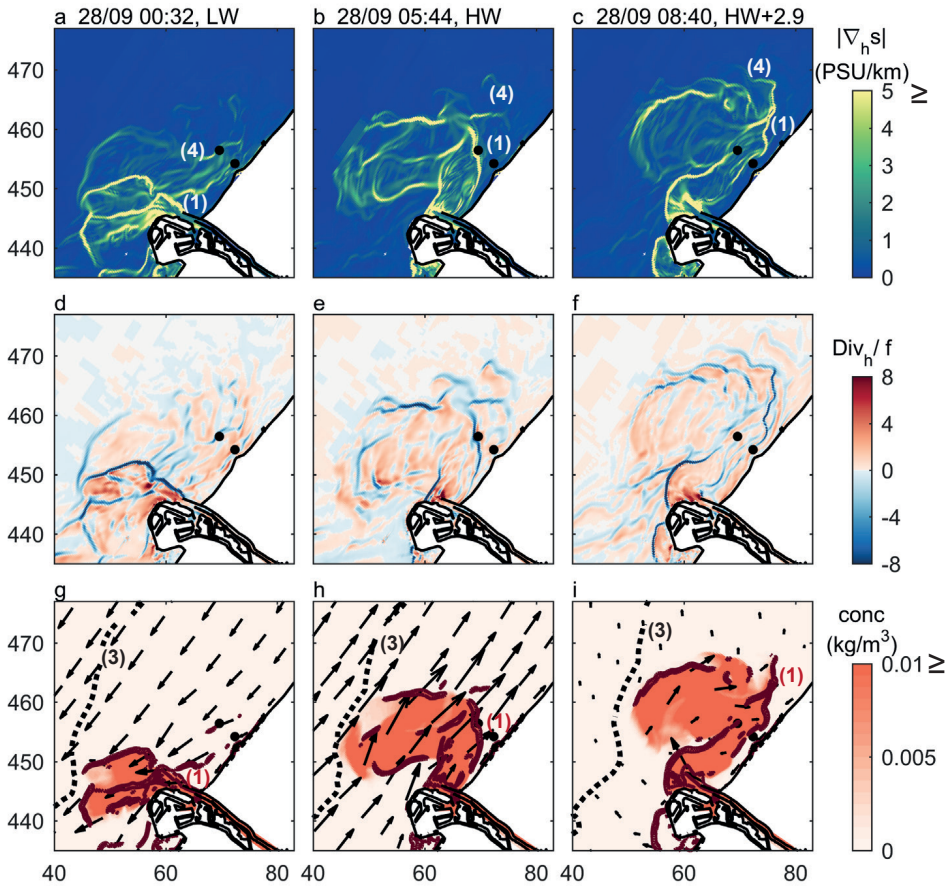

Figure 4.8: Plan view of the absolute value of the horizontal salinity gradient (a-c), normalized horizontal divergence (Div_h/f) (d-f), and a tracer concentration (g-i) in the surface layer during a tidal cycle at a spring tide (day 271 or 28/09). Same description as Figure 4.7. See Movie 2 for the horizontal salinity gradient in time (supplementary materials).

4.4.3. LIFE CYCLE OF THE TIDAL PLUME FRONT

The tidal plume front controls the dynamics in the near-field, and affects the evolution of the entire river plume (*Hetland*, 2005; *Cole et al.*, 2020). To understand the multi-frontal system, we first want to understand the life cycle and evolution of a tidal plume front. Here, we follow the northeastern edge of four tidal plume fronts per neap and spring period (released on 16/09–17/09, 27/09–29/09). Throughout this study, we label these fronts based on generation time for convenience; front 1 is generated first and front 4 last (coloured as orange, red, blue and green respectively). The spatial structure and propagation of one neap and spring front is shown in Figure 4.9, where the period has been split into flood and ebb. The front is represented by 9–12 points, which are indicated by the small dots in Figure 4.9. As mentioned in Section 4.2.4, the front is followed using the direction and magnitude of the surface velocity, and only shown when the horizontal salinity gradient is at least 1 PSU/km. The fronts shown in Figure 4.9 refer to the same tidal cycle as in Figures 4.7 and 4.8, and are labelled as front 3.

During the first flood period the downstream edge of the tidal plume front propagates in the northeast direction, turns onshore and gets close to the coast. The spacing between the lines showed that the front accelerated at the beginning of the flood and decelerated towards the end for both fronts. Additionally, Figures 4.9a,b show that the spring front moved faster than the neap front during the flood period, possibly because of higher tidal velocities or larger horizontal salinity gradients. When the tide reverses and the ebb current starts, both fronts are first stalled until the ebb flow accelerates and advectes the fronts southwestward. The onshore part of the front is almost parallel to the coastline, while propagating southwestwards.

As discussed in Section 4.2.4, the total horizontal salinity gradient ($|\nabla_h s|$) is used to indicate frontal strength. An increase in $|\nabla_h s|$ is defined as a strengthening of the fronts, while a decrease is defined as a weakening of the fronts. This value is plotted in Figure 4.10 for the four tidal plume fronts together with the alongshore distance relative to the river mouth, the frontal Froude number and the tidal plume thickness behind the fronts. The averaged values (thick lines) and standard deviation (shade) per tidal plume front are shown, giving information about the along front variation. Both the neap and spring fronts travelled between 12.5–22.5 km during the first flood, with the spring front travelling slightly farther and faster (Figures 4.10a,b). Almost all fronts reached a $|\nabla_h s| < 1$ (PSU/km) during the southwestwards propagation on the ebb, indicating a weakening of the fronts at 12-13 hours after LW. In addition, $|\nabla_h s|$ decreased for all fronts at the start of the flood, followed by an increase during peak flood and a decrease on the following ebb (Figure 4.10c,d).

The magnitude of the frontal Froude number (F) seems to increase and decrease in line with $|\nabla_h s|$ during flood, suggesting that the Froude number indicates frontal strength as well (Figure 4.10e,f). A slight offset between the maximum peak of F and $|\nabla_h s|$ is observed. All tidal plume fronts are critical or supercritical at the beginning of the trajectory. These Froude numbers are close to the value $\sqrt{2}$, suggesting that the fronts are propagating as inertial gravity currents (*Benjamin*, 1968; *Britter and Simpson*, 1978; *Shin et al.*, 2004). Remarkably, the Froude numbers increase around HW and then decrease again, but stay supercritical during the entire flood tide (Figure 4.10e,f). Note that this Froude number definition is based on gravity currents in laboratory studies without any

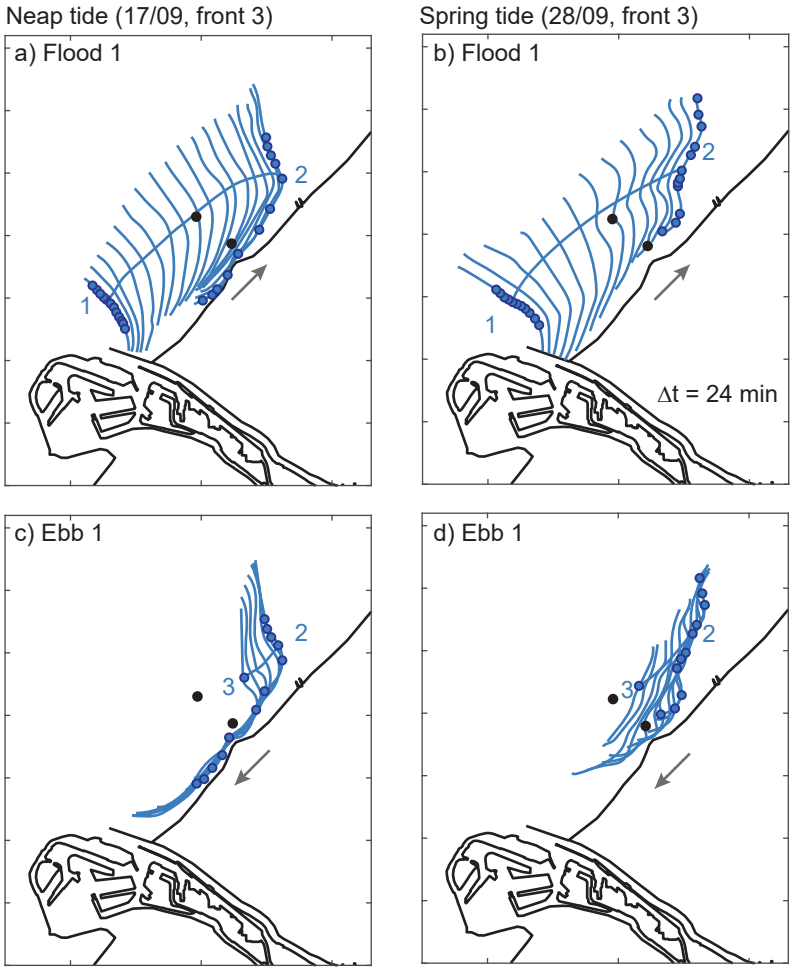

Figure 4.9: Front trajectory with front traces for a neap tide (a,c) and spring tide (b,d). The trajectory has been split into flood 1 and ebb 1. Grey arrows and numbers show propagation direction. The time between lines is 24 minutes. This is front 3 (third release) similar as in Figures 4.10, 4.11 and 4.12. The solid line indicates that $|\nabla_h s| > 1$ (PSU/km), otherwise the trajectory is ended. The dots at the beginning and sometimes at the end of the trajectory show the location of the 9–12 trajectories per front followed in time.

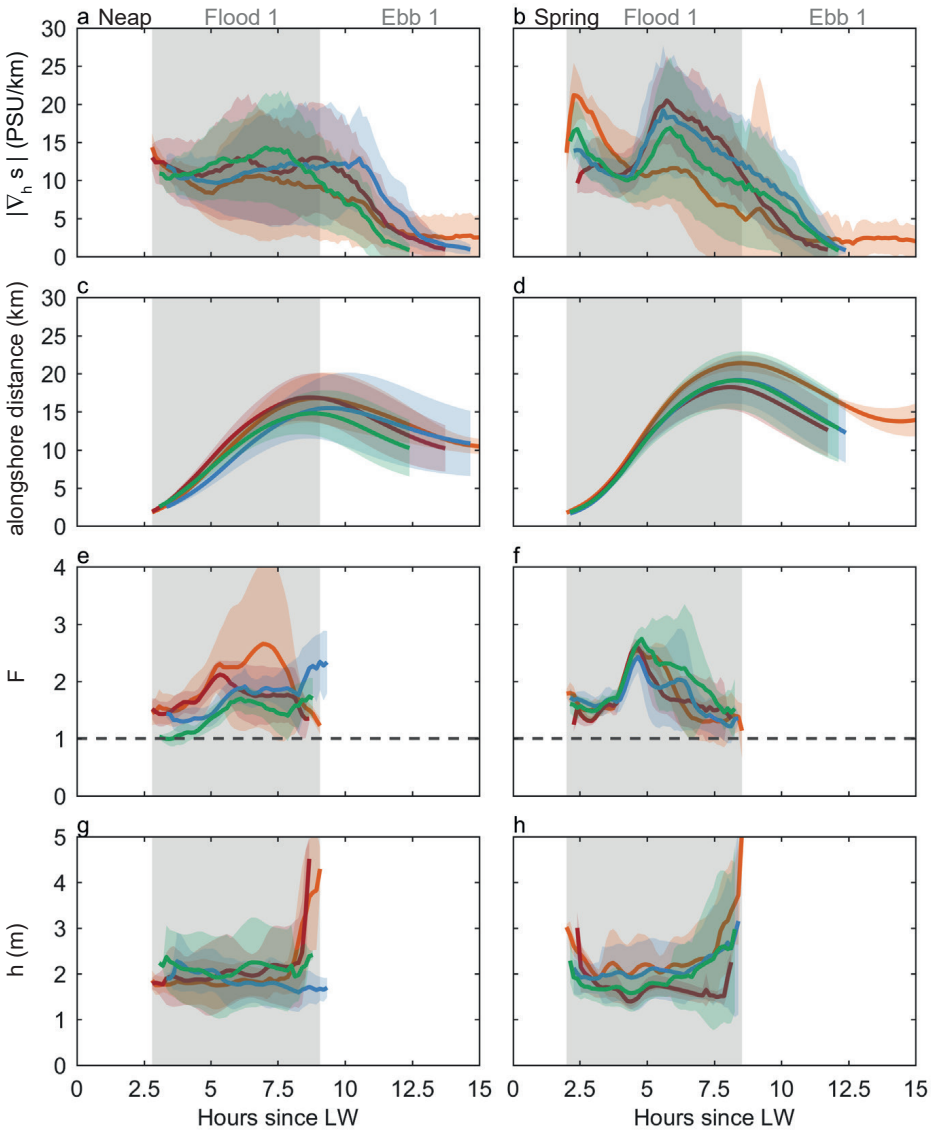

Figure 4.10: Front trajectories for a,c,e,g) neap (16/09–18/09 , days 260–262) and b,d,f,h) spring (27/09–29/09, days 270–272) tide. Horizontal axis is hours since low water (LW). Vertical axis is a,b) the absolute horizontal salinity gradient (PSU/km); c,d) the alongshore distance (km) from the river mouth, where northeastward is positive; e,f) frontal Froude number; g,h) tidal plume thickness behind the front (h). The four colours represent the four tidal plume fronts referring to a different tidal cycle: orange is front 1, red is front 2, blue is front 3 and green is front 4. The thick line refers to the average of 10-12 trajectories per tidal plume front, and the shade represents ± the standard deviation. The trajectory is ended when $|\nabla_h s| < 1$ (PSU/km) or at the end of the flood period (for F and h). The grey shaded areas refer to flood, and the white areas to ebb.

shear flow. In river plumes, a three-dimensional flow field is present and strong velocity shears can be present influencing the dynamics of tidal plume fronts. We obtain subcritical frontal Froude numbers for all the fronts in Figure 4.10 if we include the vertical velocity shear in the calculation of c_0.

Figure 4.10g,h shows the tidal plume thickness behind the front (in the tidal plume). The neap front seems to keep a relatively constant thickness during the first half of the flood tide, while the thickness of the spring fronts decreased at the start of the flood tide. This decrease could be explained by the spreading of the front, while the increase in thickness during the second half of the flood tide could be explained by vertical mixing. The thickness of the neap and spring fronts are found within the same range of 1.2 to 4.5 m.

4.4.4. EVOLUTION OF A TRACER CONCENTRATION

The four tidal plume front trajectories in Figure 4.10 ended 12-13 hours after LW due to the broadening and weakening of the fronts ($|\nabla_h s| < 1$). However, Figures 4.7 and 4.8 show the presence of weak fronts downstream of the newly released tidal plume front. Therefore, we follow tracers to investigate whether these weak fronts are relic tidal plume fronts. The tracers are related to the ebb release of the four consecutive tidal plume front trajectories shown in Figure 4.10. Figures 4.11 and 4.12 show the total horizontal surface salinity gradient with contour lines for the four tracers in panels a and b. Panels c and d show the vertical structure of the alongshore horizontal salinity gradient with tracer contour lines. These contour lines contain a minimum of 85% of the tracer concentration at the surface (panels a and b) or along the cross-section (panels c and d). We define that the contours represent fronts, and the entire “circle" represents the tidal plumes. Here, we label the tidal plumes and fronts as in Section 4.4.3, where tidal plume (front) 1 is generated first and tidal plume (front) 4 the last (orange, red, blue and green respectively). Two different times are plotted per period, HW-0.4 and HW+0.8 hours.

Both, the surface field and the cross-section demonstrate that the horizontal salinity gradients ahead of the tidal plume front overlap with tracer contours, suggesting that these weaker fronts are relic tidal plume fronts (Figures 4.11 and 4.12; the orange and red lines). During neap, the tracer contours indicate that the relic front in panels a and c originates from the release on the previous tidal cycle (red line, 2^{nd} release; Figure 4.11). Between HW-0.4 and HW+0.8, the fronts are spreading and moving northeastward. The distance between the blue and red line decreases during the 1.2 hours, suggesting that the blue front propagates faster than the red front (Figure 4.11a,b).

In general, the tracer contours demonstrate that a new tidal plume moves into a relic tidal plume. The tidal plumes spread and mix during each tidal cycle, resulting in the oldest tidal plume being wider, deeper and saltier with newer tidal plumes within it. The tracers show overlap between each other instead of separate pulses for both periods. Tidal mixing is larger during spring. As a result, the tracers stay horizontally quite confined but mix vertically. Therefore, after two tidal cycles, a tidal plume can already be mixed over the entire water column during spring tide. During neap the vertical mixing is less with more horizontal spreading, resulting in a distinct fresher upper layer consisting of three different ebb releases.

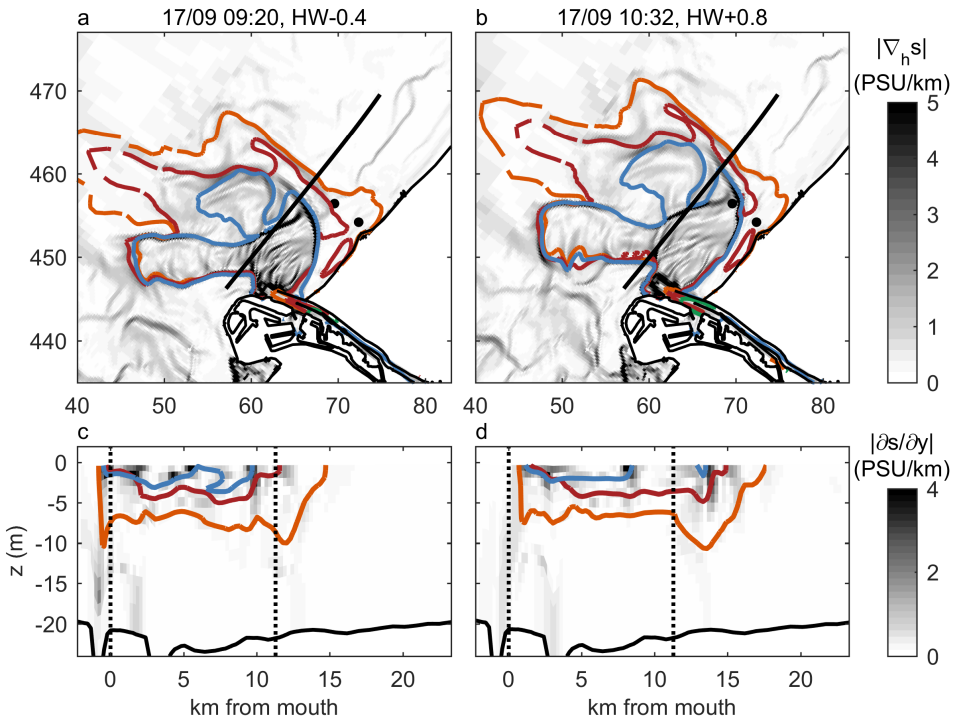

Figure 4.11: a,b) a,b) Plan view of horizontal salinity gradient (PSU/km), c,d) cross-section of salinity gradient in alongshore direction (PSU/km), both with contour lines of four tracers, for a neap tide at HW-0.4 and HW+0.8 hours (day 260 or 17/09). The solid coloured lines in panels a and b correspond to the 85% contour line of the plan view (surface). The solid lines in c and d, correspond to the 85% contour line of the cross-section. The four colours represent the different tracers: orange is tracer 1, red is tracer 2, blue is tracer 3 and green is tracer 4. Tracer 3 corresponds to Figure 4.7 g-i. The black line in panels a and b is the cross-section in panels c-h. The vertical dotted lines correspond to the location of the river mouth and the mooring stations. The horizontal and vertical axes in panels a and b are displayed in RD coordinates in km.

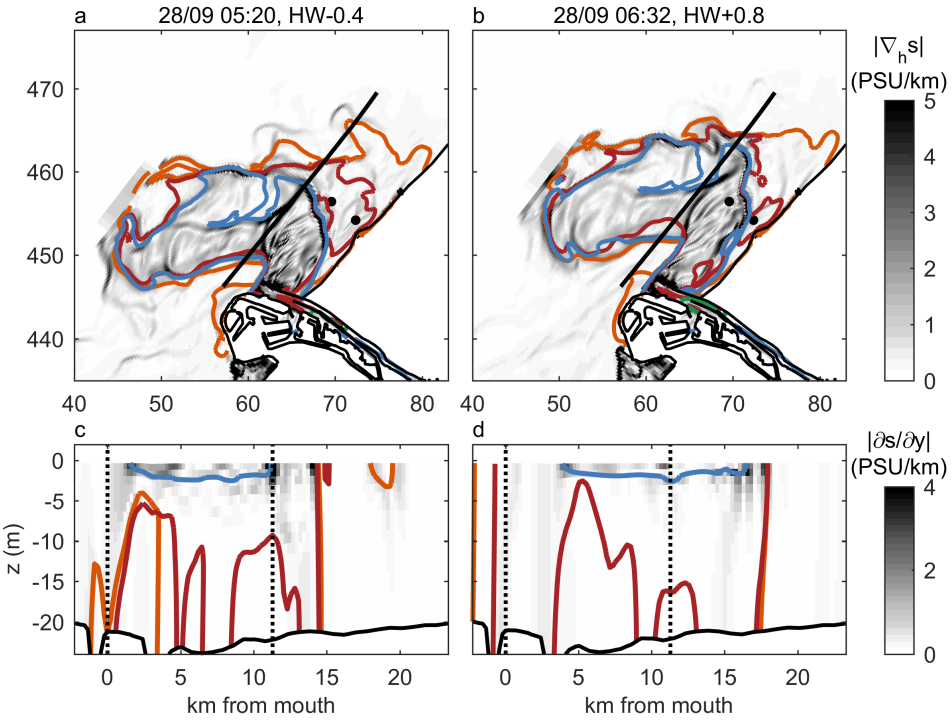

Figure 4.12: a,b) Plan view of horizontal salinity gradient (PSU/km), c,d) cross-section of salinity gradient in alongshore direction (PSU/km), both with contour lines of four tracers, for a spring tide at HW-0.4 and HW+0.8 hours (day 271 or 28/09). Tracer 3 (blue) corresponds to Figure 4.8 g-i. Same description as Figure 4.11.

4.4.5. FRONTOGENESIS

The tracer concentrations demonstrate that the fronts ahead of the tidal plume front are relic tidal plume fronts. We use the frontogenesis equation to investigate the processes driving these fronts (eq. 4.5). From now on, we focus on the neap period for simplicity. The equation is applied to the alongshore direction assessing the evolution of the alongshore salinity gradient (see Section 4.2.5). Around HW-0.4 hours, the relic front resharpened and appeared in the tendency term (Figure 4.13a), which corresponds to the time in Figure 4.11a,c. Figure 4.13a-h provides a spatial overview of the frontogenesis terms for this snapshot. The processes explaining the tendency term are mainly the presence of alongshore advection $\left(\nu \frac{\partial}{\partial y}\left(\frac{\partial s}{\partial y}\right)\right)$, convergence ($\frac{\partial v}{\partial y}\frac{\partial s}{\partial y}$), sinking $\left(\frac{\partial w}{\partial y}\frac{\partial s}{\partial z}\right)$, and vertical mixing $\left(\frac{\partial}{\partial y}\frac{\partial}{\partial z}\left(s'w'\right)\right)$ for the relic front. The tendency term of the tidal plume front can be explained by a competition of all plotted terms, which all have larger magnitudes compared to the relic front (Figure 4.13). However, the ratio of these terms change along the front and depend on the local position of the front.

The frontogenesis terms along a chosen transect in Figure 4.13e show that the tendency term is mainly balanced by the alongshore advection term. However, the convergence term drops at the location of the front, suggesting that the presence of convergence resharpens the horizontal salinity gradient. The magnitude of this term is roughly 3 times smaller for the relic front compared to the tidal plume front. Additionally, the drop in the convergence term seems to be aligned with a small positive sinking term at the trailing edge of the front (Figure 4.13j-l).

As already indicated by Figure 4.11, the distance between the tidal plume front and the relic front decreases in time (Figure 4.14a-b). This suggests that at a certain moment the tidal plume front will overtake the relic front. Figure 4.14c-d shows that the alongshore velocity is indeed larger at the tidal plume front than around the relic front. The frontogenesis terms representing the presence of convergence and sinking are visible at both the tidal plume front and the relic front. The width of these features, which coincide with the relic front, is reduced in time (Figure 4.14e-h). A distinct alternation of a negative-positive sinking term is observed at HW+0.8 hours (Figure 4.14h). Hence, the cross-sections support Figure 4.13 that the presence of convergence and sinking relate to the enhancement of the gradient of the relic front during the flood period of the tide. Moreover, the vertical eddy viscosity coefficient N_z is elevated at the location of both the tidal plume front and the relic front, indicating mixing at the fronts (Figure 4.14 i-j). Figure 4.14i-j shows that N_z penetrates deeper in the water column at the location where the sinking term changes sign. This effect seems to be larger around the relic front. The vertical eddy viscosity also demonstrates that tidal mixing dominates in this system, and is larger than the surface mixing located around the fronts.

4.5. DISCUSSION

4.5.1. MULTIPLE PLUME FRONTS

The model simulations and the mooring data created a conceptual picture of the frontal structure in the Rhine ROFI. This multiple front system is generated by different processes, where depth mean advection, straining (differential advection), convergence, and mixing play an important role. Every tidal cycle a tidal plume front is formed at

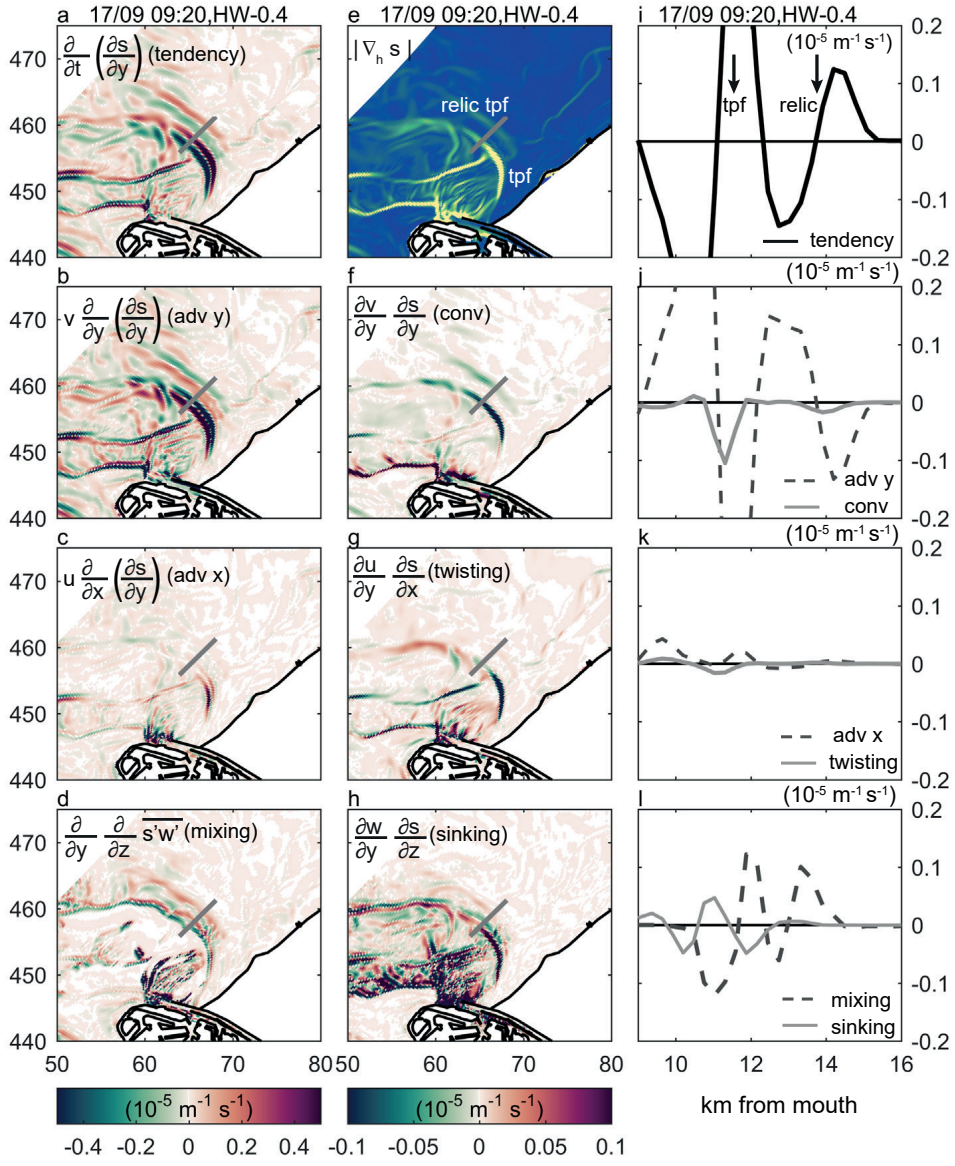

Figure 4.13: Frontogenesis analysis of alongshore gradient at the surface (Neap tide, 17/09/14 09:20, HW-0.4) a) tendency term (10^{-5} m^{-1} s^{-1}), b) alongshore advection term (10^{-5} m^{-1} s^{-1}), c) cross-shore advection term (10^{-5} m^{-1} s^{-1}), d) estimated mixing term (10^{-5} m^{-1} s^{-1}), e) total horizontal salinity gradient (PSU/km), f) convergence term (10^{-5} m^{-1} s^{-1}), g) cross-stream differential advection term ("twisting"; 10^{-5} m^{-1} s^{-1}), sinking term (10^{-5} m^{-1} s^{-1}). i–l) line plots of all the different terms along the cross-section (grey line in surface plots). Note the different color scales. The horizontal and vertical axes in panels a-h are displayed in RD coordinates in km. See Movie 3 for the frontogenesis terms in time (supplementary materials).

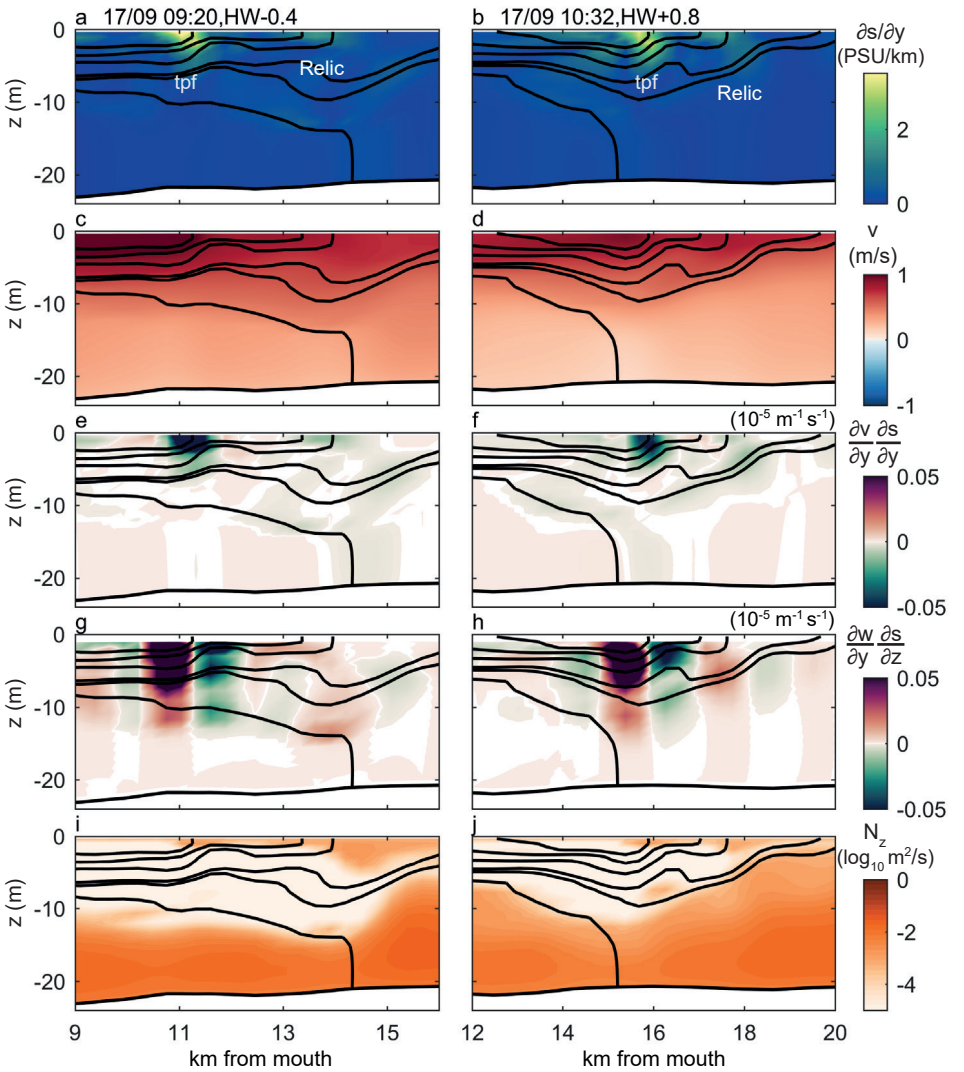

Figure 4.14: Transects across the tidal plume front (tpf) and a relic tidal plume front (relic) along the cross-section indicated in Figure 4.11 for HW-0.4 and HW+0.8 hours (inline with Figure 4.11). a-b) salinity gradient along the cross-section (alongshore; PSU/km), c-d) alongshore velocity (m/s), e-f) frontogenesis convergence term (10^{-5} m^{-1} s^{-1}), g-h) frontogenesis sinking term (10^{-5} m^{-1} s^{-1}), i-j) vertical eddy viscosity ($\log_{10}$ m^2/s). The black lines represent salinity contours of 27, 28, 28.9, 29.6, 29.8, and 30.3 PSU. The x-axis only shows the area around the fronts on the cross-section in Figure 4.11.

the river mouth, which propagates due to its intrinsic speed and tidal advection. The density gradients are relaxed and stratification is generated. As a result, the tidal currents are modified resulting in elliptical tidal currents. Therefore, the tidal plume front follows an elliptical pathway, where it weakens on the ebb flow and re-strengthens again on the following flood becoming a relic tidal plume front (Figures 4.7 and 4.8). These tidal plume fronts are present for at least 4 tidal cycles roughly within 20 km from the river mouth. This brackish water from the river mouth forms a background river plume. At the same moment, the modified tidal currents generate along- and cross-shore tidal straining, which leads to the on- and offshore movement of the inner front of the ROFI each tidal cycle.

Our findings suggest that the longevity of the tidal plume fronts in this system is larger than one tidal cycle resulting in a multi-frontal system, which is inline with the Sentinel image (Figure 4.1b) and the field-data (Figure 4.5a-d). The model simulations helped to differentiate between the different fronts. Therefore, mooring data within this dynamical area, will be easier to interpret in future work. The density signal in Figure 4.5a-d shows clearly the presence of the tidal plume front (black dot) and relic tidal plume fronts (black cross). Relic tidal plume water is observed in other river plume systems as well, where it influences the new tidal plume fronts, for example the Columbia River plume (*Horner-Devine et al.*, 2009; *Kilcher and Nash*, 2010). Additionally, the Columbia tidal plume fronts have sometimes been observed longer than one tidal cycle as well (*Horner-Devine et al.*, 2009; *Kilcher and Nash*, 2010).

4.5.2. DO THE TIDAL PLUME FRONTS INTERACT?

We found that tidal plumes and their fronts move within each other, while *de Ruijter et al.* (1997) suggested separate pulses along the coast. This difference could be ascribed to the different weather conditions, because here we only investigate a relatively calm neap and spring period. The numerical tracers demonstrate that the different tidal plumes and their fronts move and spread within each other, where the newest front seems to move faster than a relic one due to a larger horizontal salinity difference (Figures 4.11 and 4.14). Tidal mixing influences the structure of the different plumes and fronts by vertical mixing and inhibiting spreading, resulting in a different relic tidal plume structure between neap and spring. Based on our findings, we hypothesize that the observed tidal plume fronts and plumes interact by moving, spreading and mixing within each other. As a result, newer fronts can overtake and coalesce with slower ones. The detailed dynamics that coincide with this interaction needs more attention.

Another difference with the observations in *de Ruijter et al.* (1997) is the port extension next to the river mouth, which was completed in December 2013 (Figure 4.1). This reclamation of 8 by 5-6 km could potentially impact the flow field, and several studies have shown that reclamations into the sea can generate eddies (*Davies et al.*, 1990; *Signell and Geyer*, 1991; *Geyer*, 1993b; *Magaldi et al.*, 2008). A large recirculation, with a diameter of roughly 10 to 20 km, is indeed observed downstream of the river mouth between HW+2 and HW+4 (Figures 4.6, 4.7, 4.8, Movie 1 and 2 in supplementary materials). The nature of this recirculation, also called an eddy, can be similar to a bulge region as observed in many river plumes, generated by the port extension or a combination of coriolis and the port extension. Here, we only observe the eddy during a period of 60 to

90 minutes instead of continuously, coinciding with the period of onshore tidal currents, and only in the upper layer. This suggests that this eddy is an interaction between multiple processes from which one is the elliptical tidal current. The presence of this eddy has an impact on the pathway of the fronts.

4.5.3. WHICH PROCESSES ARE CONTROLLING THE LONGEVITY OF THE TIDAL PLUME FRONTS?

The frontogenesis equation suggests that the tidal plume fronts are sustained due to the competition of alongshore advection, convergence, sinking and vertical mixing. This competition can explain the existence of relic tidal plume fronts. The controlling terms are not surprising, because advection is known to play a dominant role in the mass balance of plume fronts (*O'Donnell*, 1993; *Giddings et al.*, 2012). Additionally, studies have shown that convergence and sinking can lead to frontogenesis (*Garvine and Monk*, 1974; *O'Donnell*, 1993; *O'Donnell et al.*, 1998; *Giddings et al.*, 2012; *Geyer and Ralston*, 2015). For example, the study of *Horner-Devine et al.* (2009) suggested that the Columbia tidal plume front was strengthened for a second time probably due to the opposite directed flood tide leading to convergence. Therefore, the combination of a convergent flow and advection creates conditions which allow for front generation and maintenance.

The frontogenesis analysis together with the tracers demonstrate that advection plays an important role in this multi-frontal system. The front trajectories show indeed that the Rhine tidal plume fronts are controlled by tidal advection, resulting in an elliptical pathway each tidal cycle (Figures 4.9). This is actually the total advection (Equation 4.5), which can be split into depth mean advection and straining (differential advection) (*Simpson and Souza*, 1995; *de Boer et al.*, 2008). Both processes have been shown important for the dynamics in the Rhine ROFI (*Simpson and Souza*, 1995; *de Boer et al.*, 2008). The dominant role of the tidal advection leads to the trapping of the fronts within a radius of roughly 20 km from the river mouth (Figures 4.11 and 4.12). The travelled distance of the fronts per tidal cycle seems to align with the tidal intrusion length. We obtain a tidal intrusion length of 15 km based on a maximum tidal velocity of 1 m/s and on the M2 tidal frequency.

Another indication that tidal advection plays an important role is the ratio of the intrinsic frontal speed and the ambient tidal current. In the Rhine ROFI, the intrinsic frontal speed is 2 times smaller than the ambient tidal currents based on field measurements (*Rijnsburger et al.*, 2018). This characteristic of the Rhine ROFI seems to be slightly different in other systems, where smaller ambient tidal currents have been observed. One example is the Columbia River plume where the intrinsic frontal speed is 3 times larger than the ambient coastal currents, based on mean values of 0.6 ms^{-1} (*Kilcher and Nash*, 2010) and 0.2 ms^{-1} (*García Berdeal et al.*, 2002; *Hickey et al.*, 2005, 1998). This gives a ratio of $u_f/u_0 \approx 0.6/0.2 \approx 3$, while the Rhine River plume has a ratio of $u_f/u_0 \approx 0.5/1 \approx 0.5$. These ratios suggest that the front is dominant in the Columbia River plume and the impact of advection on frontal strength might be lower as in the Rhine River plume. However, the Columbia River plume has a bulge circulation that traps relic plume waters for a few tidal cycles within a minimum radius of 10 km from the river mouth (*Horner-Devine*, 2009). This seems similar to the tidal advection that happens here. A river plume that seems to be strongly influenced by the tidal current is the Connecticut River plume.

The location of the plume is dependent on the direction of the alongshore tidal currents (*Garvine*, 1974b; *O'Donnell*, 1993; *O'Donnell et al.*, 1998), similar to what we observed in the Rhine ROFI.

The trapping poses the question how the freshwater from the tidal plumes is transported into the far-field when these fronts are kept within 20 km from the river mouth. Therefore, we calculated the total mass of tracer concentration transported into the far-field compared to the total mass present in the entire river plume, where we set the boundary to the far-field roughly at 18 km downstream and offshore over the entire model domain. After 5 tidal cycles, approximately 30 % and 10 % of one tracer concentration is located in the far-field for neap and spring respectively. These numbers suggest that roughly three times as much water is transported into the far-field for the neap as for the spring. Tidal mixing is expected to be larger during spring. Therefore, the tracer concentration is vertically mixed after 5 tidal cycles in contrast to the neap tide (see Movie 4 and 5 in supplementary materials). Hence, a balance between the horizontal salinity gradients, tidal mixing and tidal advection is expected to determine the alongshore transport.

Figures 4.13 and 4.14 indicate that convergence and sinking are present during flood, resulting in the enhancement of a relic tidal plume front. Sinking (upwelling) is often caused by the presence of convergence (divergence). This poses the question which mechanism is leading to the presence of convergence during flood at that location. Figure 4.14c,d shows that the alongshore velocity behind the relic front is larger. Therefore, we hypothesize that the increase in convergence and sinking at the relic front is caused due to a compression generated by the faster propagating tidal plume front, which will eventually overtake the relic front. Additionally, a small intrinsic relic front velocity, due to the salinity difference with the ambient water, is directed in the same direction as the tidal velocity. Therefore, this results in a slightly larger velocity at the relic front compared to the ambient water ahead of the relic front leading to convergence.

4.6. CONCLUSIONS

A 3D numerical model has allowed us to interpret in-situ measurements creating a conceptual picture of the frontal structure in the Rhine ROFI. The horizontal salinity gradient and numerical tracers have shown to be a useful tool to identify the different fronts as the inner front, the tidal plume front and relic tidal plume fronts. The combination of salinity gradients and numerical tracers showed that a tidal plume front can sustain longer than 1 tidal cycle becoming a relic tidal plume front. The frontogenesis equation suggests that relic tidal plume fronts are sustained due to the presence of depth mean alongshore advection, alongshore differential advection, convergence, and sinking. These processes seem to enhance the alongshore salinity gradient on the flood tide. As a result, the tidal plume fronts are kept for at least four tidal cycles within 20 km from the river mouth due to these processes. We stress that the presence of multiple fronts will change the transport, cross-shore exchange and stratification in the river plume, which are key processes important for the ecosystem health, water quality and coastal erosion.

5

OBSERVATIONS OF MULTIPLE INTERNAL WAVE PACKETS IN A TIDAL RIVER PLUME

Internal solitary waves (ISWs) generated by tidal plume fronts impact frontal processes and enhance vertical and horizontal mixing in coastal areas. Here, we reveal that the Rhine River plume is a multi-frontal system that sustains multiple coincident ISW packets. Observations show that at certain times there are two different ISW packets ahead of the newly released tidal plume front. We analyze one example in detail. These ISW packets differ mainly in wave period. The amplitudes of the ISWs are 1 - 1.5 meter in a water depth of 18 meter. The first ISW packet has an average period of 3.5 minutes, while the second ISW packet has an average period of 2 minutes. Field-data and numerical modelling show that the tidal plume front is trapped in the mid-field plume for more than one tidal cycle. A frontal Froude number analysis shows that fronts generated during the previous ebb tide can release ISWs in addition to the newly released tidal plume front, resulting in multiple ISW packets. ISWs have been observed to form in several plume systems when the energetic plume front slows late in the ebb. This results in the release of a single packet of ISWs. In the Rhine plume we observe that coastal tidal processes can re-strengthen the plume front long after the initial release, causing multiple releases of ISWs.

This chapter is based on S. Rijnsburger, R.P. Flores, J.D. Pietrzak, K.G. Lamb, N.L. Jones, A.R. Horner-Devine, and A.J. Souza. Observations of multiple internal wave packets in a tidal river plume. *submitted to Journal of Geophysical research: Oceans*

5.1. INTRODUCTION

Internal solitary waves (ISWs) are nonlinear-dispersive waves that propagate in stratified waters (*Ostrovsky and Stepanyants*, 1989). They can induce strong currents which generate turbulence, leading to vertical and horizontal transport of nutrients, phytoplankton and fine sediment (*Sandstrom and Elliott*, 1984; *Bogucki et al.*, 1997; *Da Silva et al.*, 2002; *Klymak and Moum*, 2003). Several different ISW generation mechanisms have been observed; the most common being the nonlinear-dispersive evolution of internal waves generated by the tidal flow of stratified fluid over topography (*Maxworthy*, 1979; *Farmer and Armi*, 1999; *Pietrzak et al.*, 1990). More recently, some novel ISW generation mechanisms have been observed, including generation by river plumes (*Nash and Moum*, 2005; *Li and Pawlowicz*, 2018; *Osadchiev*, 2018), intrusion fronts (*Bourgault et al.*, 2016), and bottom gravity currents (*Xie et al.*, 2017).

At a river mouth, the release of freshwater on every ebb results in a pulsed discharge forming tidal plumes bounded by distinct tidal plume fronts, which are sharp transitions in density formed by convergence with the ambient water (*Garvine and Monk*, 1974). These tidal plume fronts, which are important in the near-field plume, interact strongly with the ambient water, influencing vertical mixing and changing local water properties (*Garvine and Monk*, 1974; *Luketina and Imberger*, 1987; *Kilcher and Nash*, 2010; *Jay et al.*, 2009). *Nash and Moum* (2005) observed the generation and fission of ISWs from the Columbia River plume after the front speed (u_f) transitioned from super to subcritical relative to the ambient long wave speed (c_a; $u_f < c_a$). This process was corroborated by numerical modelling (*Stashchuk and Vlasenko*, 2009). Similar results for gravity currents with linear background stratification were observed in laboratory experiments (*Maxworthy et al.*, 2002). The generation of ISWs at tidal plume fronts has a profound impact on coastal ecosystems (*Orton and Jay*, 2005; *Pan and Jay*, 2009a; *Hickey et al.*, 2010). Despite their importance, knowledge of tidal plume front generated ISWs is limited, particularly in shallow systems. In shallow systems, ISWs can generate large near bed velocities and bed shear stresses, which may result in sediment mobilization and resuspension (*Aghsaee and Boegman*, 2015).

The Rhine River plume or Region Of Freshwater Influence (ROFI) is a river plume that exists in a shallow system dominated by tides. The Rhine River flows into the southern North Sea with a yearly mean discharge of about 2300 m^3/s forming a 20-40 km wide river plume extending 100 km along the Dutch coast (*de Kok*, 1996; *de Ruijter et al.*, 1992; *Simpson et al.*, 1993). This coastal area is shallow with maximum water depths of about 25-30 m. The combination of a progressive tide, a shallow shelf and stratification results in a highly frictional system which is dominated by counter-rotating tidal currents between the surface and the bed. This leads to cross-shore tidal straining (*Simpson and Souza*, 1995; *de Boer et al.*, 2008). Tidal straining modifies the river plume, generates mixing and shear, and impacts the ecosystem (*Huthnance*, 1997; *Joordens et al.*, 2001).

Moreover, distinct tidal plume fronts are known to form at the Rhine River mouth (*van Alphen et al.*, 1988; *Hessner et al.*, 2001). These fronts share similarities with gravity currents and other tidal plume fronts (*Benjamin*, 1968; *Garvine and Monk*, 1974; *Britter and Simpson*, 1978; *Luketina and Imberger*, 1987; *Kilcher and Nash*, 2010), such as a plunging head and intrinsic frontal speed (*Rijnsburger et al.*, 2018). These fronts are an important mechanism regarding coastal transport, for example *Fischer et al.* (2009)

observed elevated turbulence when the tidal plume front passed in a numerical study. These fronts were shown to propagate towards the coast, increase bed stresses and generate a cross-shore exchange flow causing offshore sediment transport (*Flores et al.*, 2017; *Horner-Devine et al.*, 2017; *Rijnsburger et al.*, 2018). Moreover, *Rijnsburger et al.* (2020) showed that the tidal plume fronts are trapped by strong re-circulation in the mid-field plume for a number of tidal cycles.

Transects indicated the presence of long internal waves, order 2.5 - 5 km wave length, at the mouth of the Rotterdam Waterway (*van Alphen et al.*, 1988). However, no field observations have been previously reported of front generated ISWs in the Rhine ROFI, despite the extensive field campaigns. The Stokes number (Stk), which estimates the relative importance of friction and inertia in a tidal flow (*Prandle*, 1982b; *Baumert and Radach*, 1992; *Winant*, 2007; *Burchard and Hetland*, 2010; *Souza*, 2013) is large (Stk > 1.0) in the Rhine ROFI (*Flores et al.*, 2020). Hence strong mixing from wind and tidal driven bed stresses and internal shear from tidal straining were thought to preclude their generation. In addition, most field studies were carried out 30–70 km downstream in the far-field plume (*Simpson and Souza*, 1995; *Huthnance*, 1997; *Rijnsburger et al.*, 2016) where tidal straining is known to dominate. *Hetland* (2005) showed the importance of the processes in the near-field plume for the downstream evolution of river plumes. While *Pan and Jay* (2009a) found that front-generated ISWs impact plume dynamics by changing their energy transport and have been reported to dissipate as much as 70% of the total frontal energy. Therefore, in this study, we explore whether tidal plume fronts in a high Stokes number river plume can generate ISWs.

Figure 5.1 presents a Copernicus Sentinel-2 optical image showing the presence of the tidal plume front within the near- and mid-field regions of the Rhine River plume. Remarkably this image shows multiple internal solitary wave (ISW) packets within the mid-field plume; for example, four ISW packets are evident in the satellite image shown in Figure 5.1. Moreover, this contrasts with other systems such as the Columbia River plume (*Nash and Moum*, 2005; *Pan et al.*, 2007; *Jay et al.*, 2009) in which only one band of ISWs is typically observed. In the Columbia River plume and other similar systems, the ISWs are generated by the tidal plume front; they propagate away from the river mouth and escape the near-field plume region on each tide.

In this work we use field and numerical model data to investigate the processes responsible for the generation of ISWs and the occurrence of these multiple ISW packets in the Rhine River plume. We further explore the role of the tidal trapping of the fronts on the generation of these multiple ISW packets. Therefore, a combination of different data sources is required (Section 5.2). We first analyse the satellite image in Figure 5.1 (Section 5.3.1), then we use the STRAINS II data (*Flores et al.*, 2017, 2018; *Horner-Devine et al.*, 2017; *Rijnsburger et al.*, 2018) collected 10 km downstream from the mouth of the Rotterdam Waterway to investigate whether tidal plume fronts in this shallow frictional system generate ISWs (Section 5.3.2). Although the field data clearly shows the ISWs; it does not have enough spatial and temporal resolution to fully understand the dynamics and formation of the ISWs. Therefore, we use two kinds of numerical models. On the one hand we use a simplified 2-dimensional non-hydrostatic model to study the development and evolution of the ISWs (Section 5.3.3). On the other hand we use a three-dimensional hydrostatic model to study the tidal plume fronts, investigate the water column structure

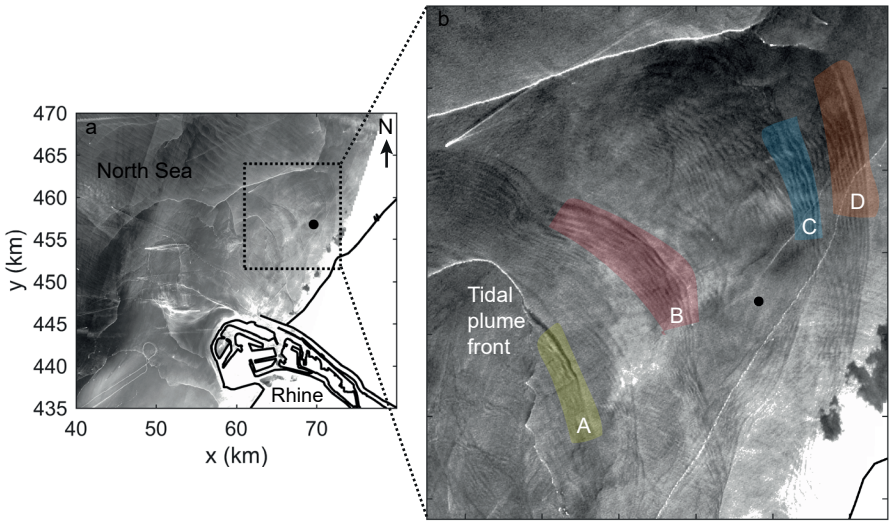

Figure 5.1: Copernicus Sentinel-2 optical image with a spatial resolution of 10–60 m. a) Satellite image of the south-eastern North Sea in the vicinity of the Rhine River mouth taken at 04-05-2016 during neap tide with wind speeds < 5 m/s coming from the south. The black dot indicates the mooring site at 18 m depth. b) inset of the ISW bands shown by the dotted box in panel a. Four ISW trains are highlighted by color and letter. The satellite image is Copernicus Sentinel-2 data.

of the plume within the shelf, and calculate Froude numbers in time and space (Section 5.3.4 and 5.3.5). Finally, we discuss the generation mechanism of the different ISW packets, and how this differs from other tidal plume systems, such as the Columbia River plume.

5.2. METHODS

5.2.1. OBSERVATIONS

Field measurements were conducted during fall 2014 within the Rhine River plume as part of the STRAINS II campaign (Stratification Impacts Near-shore Sediment) (*Flores et al.*, 2017, 2018; *Rijnsburger et al.*, 2018). Here we focus on data from a mooring site 10 km northeast of the river mouth and 6 km offshore, at a depth of 18 m (Figure 5.1, black dot). The mooring consisted of an upward-looking four beam RDI Workhorse acoustic Doppler current profiler (ADCP) with a sampling frequency of 1 Hz and vertical bins of 0.25 m. We applied a running average of 30 seconds with steps of 10 seconds to the ADCP data to filter out surface waves. In addition, four Seabird Microcat Conductivity Temperature Depth (CTD) instruments were at depths of 1, 2.5, 10, and 15 m below the surface with sampling periods between 20 and 50 seconds.

Since the CTD data did not have the spatial or temporal resolution to fully resolve the ISWs we reconstructed the isopycnals using the vertical velocity measured by the ADCP, resulting in an estimation of wave amplitude and period. The ADCP acoustic backscatter signal is used to verify these reconstructed isopycnals. In addition, we used the velocity

data to estimate wave direction. First, we applied a highpass Butterworth filter with a filter time of 45 minutes to remove the background flow. Then, wave direction was estimated using the filtering method of *Mirshak and Kelley* (2009) around the core of the internal wave signal. The high frequency data was rotated in the estimated wave direction to obtain wave velocities.

The speed and direction of the freshwater front was obtained by using the acoustic backscatter signal of the ADCP data (*Scotti et al.*, 2005; *Mirshak and Kelley*, 2009; *Li and Pawlowicz*, 2018). First, a cross-correlation was applied to the intensity signal of the ADCP data to obtain the time lag ($\delta T_{i,j}$) between the different beams. Second, the speed (C_p) and direction (θ) of the front was related to this time lag by

$$\delta T_{i,j} = \frac{X_{i,j}\cos(\theta - \beta_{i,j})}{C_p}, \tag{5.1}$$

where i, j refer to the different beams, and $X_{i,j}$ and $\beta_{i,j}$ are the horizontal distances and angles between beams i and j. We shifted the obtained time lag by ±2 seconds to estimate the sensitivity of the calculation to the time lag, and therefore the possible increase and decrease in frontal speed.

5.2.2. NON-HYDROSTATIC NUMERICAL MODEL

Two-dimensional non-hydrostatic simulations were carried out with the Internal Gravity Wave (IGW) model (*Lamb*, 1994, 2007). This model solves the fully nonlinear, non-hydrostatic Boussinesq equations. The numerical scheme uses a second-order Godunov upwind scheme with a monotonized slope computation which provides selective numerical dissipation and diffusion near sharp gradients. This damps energy accumulation at small scales. We used a constant water depth of 18 meter with vertical and horizontal resolutions of 0.09 and 1 m, respectively. Rotational effects were included using the f-plane approximation with $f = 1.15 \cdot 10^{-4}\ s^{-1}$. The model was initialized with a density field based on the field-data and the front is driven by a prescribed vertically sheared inflow with lighter near-surface water (Figure 5.2). The inflow consisted of a vertically uniform current u_0 and a surface current u_s. The uniform current was included to eliminate the formation of overturns at the inflow (left) boundary, and did not have a physical meaning. The inflow was increased linearly over 1200 s. Results were plotted in a reference frame moving with speed u_0. The in-flowing surface current behind the front was $u_s \approx 0.23$ m/s, and the uniform current was $u_0 \approx 1.12$ m/s. This model set-up did not include tidal currents and bottom friction.

5.2.3. HYDROSTATIC NUMERICAL MODEL

We used the three-dimensional hydrostatic numerical flow-model Delft3D to obtain spatial fields of density and currents for the period of the field-campaign (e.g. *Deltares* (2014), *Stelling and Van Kester* (1994)). The model covered the entire southern North Sea by using four grids with increasing horizontal resolution towards the coast, with coastal area grid cells of about 100-330 m in cross-shore and 300-500 m in alongshore direction. The model had 20 non-equidistant sigma-layers in the vertical with smaller cells near the surface and the bottom. The model was forced by water levels constructed from 50 tidal constituents at the boundaries, space- and time-varying meteorological fields, and

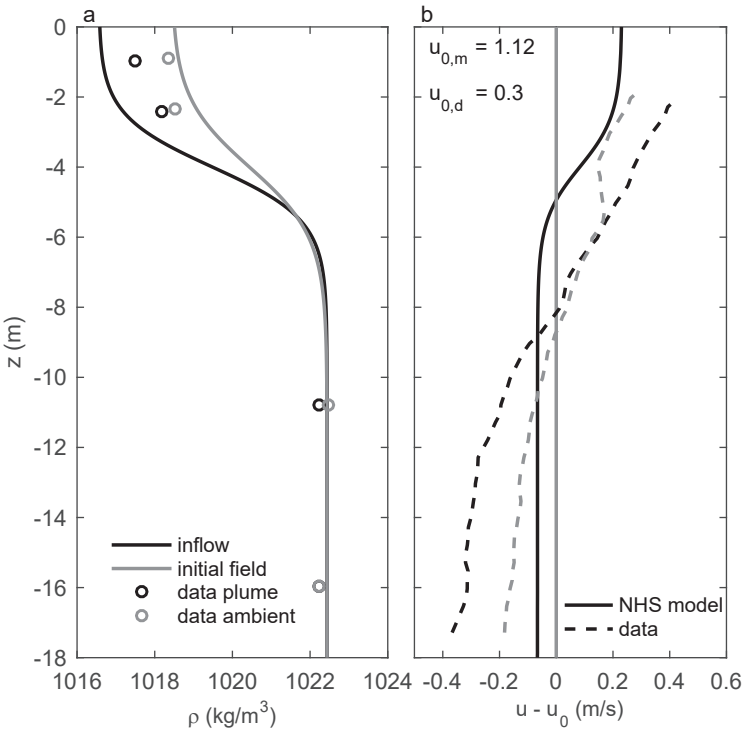

Figure 5.2: Non-hydrostatic model (NHS) set-up based on mooring data at day 277 (04/10/2014 around 10:43). a) Profiles of initial density (grey line) and inflow density (black line). b) Profiles of initial current (grey) and inflow current (black). The current is plotted in a reference frame moving with a vertically uniform current u_0 ($u - u_0$). Corresponding field-data has been plotted for both the density (circles) and velocity (dashed line), where black is behind the front and grey is ahead of the front (in ambient). $u_{0,m}$ and $u_{0,d}$ refer to the depth averaged ambient current in the model and data, respectively.

time-varying discharges for 85 rivers among which the Meuse and Rhine Rivers are the most important. Additionally, realistic bathymetry was used, and the model was initialized with uniform salinity and temperature values of 34.5 psu and 11 °C, respectively (*Suijlen and Duin*, 2002). See Chapter 4 for more information about the model.

Passive tracers, similar to dye injection, were added to the model to follow the freshwater outflow and tidal plume front. Each tracer was released from 2 hours before until 2 hours after low water and starts with a concentration of 1 kg/m^3, while a background concentration of 0 kg/m^3 was used. The timing of low water was determined using the dominant M2 tidal constituent.

As Delft3D is a hydrostatic numerical model it cannot simulate ISWs, but does capture the fronts. This is in agreement with *Ralston et al.* (2017) who showed that a hydrostatic numerical model can be used to resolve sharp gradients, when horizontal and temporal resolution is sufficient. Validation of the model demonstrated that it captures the tidal, wind and buoyancy driven flow, including the tidal plume fronts (Chapter 4).

5.3. RESULTS

5.3.1. SATELLITE OBSERVATIONS OF INTERNAL SOLITARY WAVES

We investigated whether the ISW packets observed in Figure 5.1 could have been generated by the same tidal plume front. The Copernicus Sentinel-2 data in Figure 5.1 has a spatial resolution between 10 and 60 m. The image shows the presence of multiple fronts (white thin lines), but not all fronts are associated with the ISW packets. We highlighted four ISW packets and the tidal plume front in the satellite image (Figure 5.1), where packet A seemed to be released by the front with a distance of 0.65 km to the leading wave. Figure 5.1 shows that the front is approximately 5.8 km from the river mouth. Figure 5.1 also shows that packets B, C, and D are observed to be approximately 4.2, 8.6, and 10.3 km from the front.

In previous work, we found that fronts in the Rhine ROFI have an average propagation speed of approximately 0.8 m/s relative to the ground (*Rijnsburger et al.*, 2018). Using that value as an estimate of the propagation speed of the tidal plume front in Figure 5.1, we estimated that the tidal plume front, highlighted in Figure 5.1b, travelled 2 hours since it was released from the mouth. Therefore, for the ISWs packets in Figure 5.1 to have been released from the tidal plume front, this must have happened within 2 hours. Additionally, these waves should have a larger speed than the tidal plume front.

Here, we investigate further whether these ISWs can be released from the tidal plume front. Based on *Nash and Moum* (2005) we assumed that the ISWs propagate 0.1–0.15 m/s faster than the front. Using these speeds, a first order approximation suggested that packet D is 29–19 hours ahead of the front, which is much larger than 2 hours. Packets A, B and C are 1.8–1.2, 12–8, and 24–16 hours ahead of the front, respectively. Note that these calculations did not take into account the change of speed during one tidal cycle.

The estimated travel times indicated that it is unlikely that the ISW packets B, C, and D were generated by the tidal plume front highlighted in Figure 5.1. These packets could only be released from the tidal plume front if they propagated much faster than 0.15 m/s relative to the front. The estimated travel times of packets C and D were larger than 12 hours, and therefore were likely generated on the previous tidal cycle. Based on this

analysis, we concluded that packets A, B, C and D must have been generated by different fronts. Although, the satellite image did not show obvious fronts related to all the ISW packets. In the following sections, we used observations and numerical modelling to investigate this process in more detail.

5.3.2. IN-SITU OBSERVATIONS OF INTERNAL SOLITARY WAVES

We found seventeen frontal events with ISWs, from which only ten showed pronounced ISW signals. Figure 5.3 shows these ten events. From these ten events, five were observed during low energy conditions, i.e., neap tide and a relatively low wind speed directed offshore or southwards (Figure 5.3). The other five events occurred during variable wind and tide conditions, resulting in different stratification and frontal behaviour (*Rijnsburger et al.*, 2018). Note that it is possible that ISWs generated at the tidal plume front did not reach the mooring site under all conditions.

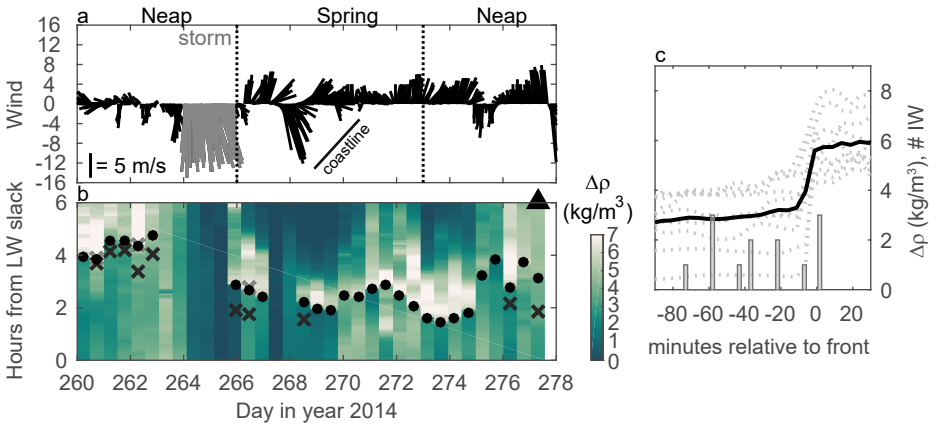

Figure 5.3: ISW events at the 18 m mooring site. a) Wind vectors (m/s). Spring, neap and storm periods are highlighted above the panel. The direction of the coastline is also indicated. b) Density difference (color, bottom−top) over six hours commencing at low water slack for the entire period in days of year (t = 0 is slack water). The black dots indicate the arrival of the fronts, the black X is the first observed ISW ahead of the front and the grey X is the first ISW behind the front. Note that the X only indicates the first wave observed ahead or behind the front. The black triangle indicates the example plotted in Figure 5.4. c) Density difference and number of ISW events (grey bars) versus minutes relative to the front in bins of 5 minutes. The black line is the density difference averaged over the 10 tidal cycles (grey dotted lines) where ISWs were observed (see panel b). The histogram shows the start time of the internal wave event relative to the front and the occurrence during the campaign.

ISW events commenced between 5 and 70 minutes before and within 5 minutes after frontal passage. The first observed wave was marked by an X, and a differentiation was made between before and after the front (Figures 5.3b). This definition resulted in a maximum of two X's per frontal event (Figure 5.3b). More waves appeared before the front than after (Figures 5.3b,c). The event-averaged top to bottom density difference $\Delta\rho$ in the ambient waters was about 3 ± 1 kg/m^3, while within the plume it was 6 ± 1 kg/m^3. The $\Delta\rho$ across the front was quite variable (Figure 5.3b,c), indicating a wide range of background conditions.

We focussed on one frontal event, day 277.44 (black triangle in Figure 5.3b), when a 70 minute record of ISWs before frontal passage was observed (Figure 5.4). The presence of the waves and the freshwater front was captured in the acoustic backscatter (Figure 5.4a). The event had clear downwelling and upwelling at the frontal head as expected for gravity currents (*Britter and Simpson*, 1978), and an estimated frontal speed of 0.76 m/s. Only a small density difference was observed at front arrival (Figure 5.4b, dot 2). In addition, the front normal velocity highlighted the presence of the plume, which had increased surface velocities compared to the ambient waters ahead and below. We observed ISWs of depression (Figure 5.4).

Figure 5.4e-g zooms in on three ISWs for which we estimated amplitudes between 1 and 1.5 m, and periods of 3.5, 2.5 and 2 minutes, respectively. As discussed in section 5.2.1, we removed the background flow from the velocity signal using a highpass Butterworth filter, and rotated this high frequency velocity in the estimated wave direction. This resulted in the ISW velocity vectors in Figure 5.4d-g. These ISW velocity vectors showed periods of convergence at the leading edge and divergence at the trailing edge of the ISW, resulting in downwelling and upwelling, respectively (Figure 5.4d-g). In addition, the velocity vectors showed distinct opposite surface and bottom directed velocities. Notably, the ISWs 45 to 70 minutes before the front (09:25 - 10:00) were longer period compared with the waves between 0-45 minutes before the front (10:00 - 10:45) (Figure 5.4, dot 1 and dot 2). In addition, the front normal velocity suggested a small difference in pycnocline depth before 10:00 compared to after (Figure 5.4c, light red band starting at 15 and 16 meter, respectively). No large change in surface density was observed at 10:00 (Figure 5.4b).

Internal wave packets are generally formed by the nonlinear dispersive evolution of a disturbance (*Helfrich and Melville*, 2006). The propagation speed of ISWs increases with wave amplitude. Therefore, these waves typically evolve into a rank-ordered packet of ISWs with gradually decreasing amplitude from the front to the back of the packet. However, an abrupt change in the properties of the waves was observed around 10:00 (Figure 5.4), which is not expected across such a wave packet. The waves before 10:00 appeared to be rank-ordered larger period ISWs, while after 10:00 the waves appeared to be smaller amplitude, more sinusoidal, smaller period waves that are not clearly rank-ordered. Therefore, the data suggested that two different wave packets, with different properties, were observed. This appeared to have some similarities with the satellite image (Figure 5.1). Two other events displayed similar behaviour with abrupt changes in IW properties before the front arrival. Each of these events had a corresponding change in the pycnocline depth, and no large change in surface density (days 262.48 and 266.57, not shown here).

5.3.3. NON-HYDROSTATIC NUMERICAL MODEL SIMULATIONS

We carried out non-hydrostatic numerical model simulations to obtain further evidence that the tidal plume front is able to release ISWs as suggested by the field-data. Given the complexity of the region, the analysis used an idealized two-dimensional simulation based on the in-situ density observations (Figure 5.2). We plotted the density, horizontal and vertical velocity at two moments in time, 45 and 90 minutes after initialization (Figure 5.5). We observed similarities with the field-data (Figures 5.2 and 5.4). A clear sur-

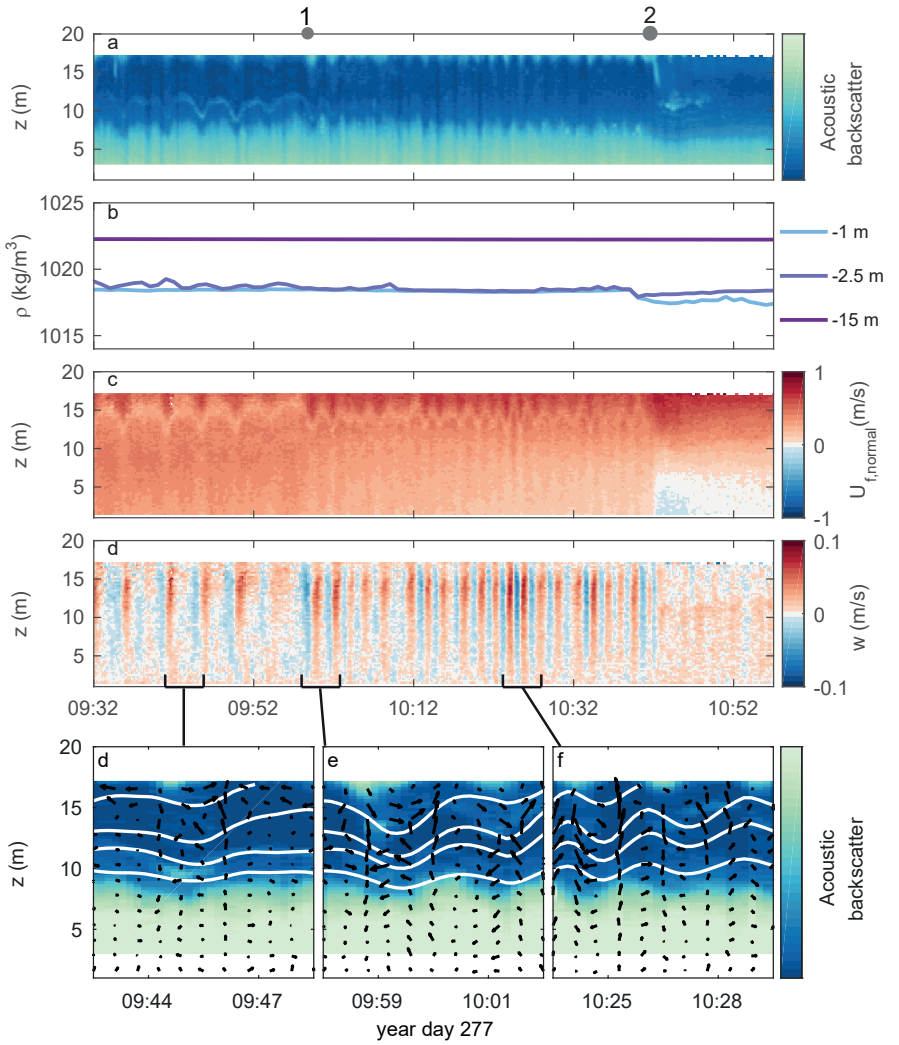

Figure 5.4: ISW example on day 277 (04/10/2014). a) acoustic backscatter signal from the ADCP at the mooring site b) density at three different heights in the water column, -1 m, -2.5 m and -15 m. c) front normal velocity (m/s), where positive values indicate flow in the direction of frontal propagation. d) vertical velocity w (m/s), where upward is positive. e-g) represent three internal wave events of 5 minutes, where color represents acoustic backscatter. White lines are reconstructed isopycnals, velocity vectors represent the wave velocity. The grey dots represent 1) 10:00 and 2) 10:43 arrival of tidal plume front.

face front was formed that thins during propagation (Figure 5.5). At the same moment a strong vertical velocity shear formed, where the bottom current was in the opposite direction to the surface current. The vertical velocity showed downwelling followed by upwelling at the tip of the front as observed in the field-data. One difference with the field-data was that the idealized model seemed to form a thinner front.

In the simulation ISWs were continually emitted from the front and propagated ahead of it. The first ISW was about 0.75 m larger than the following ISWs which have amplitudes of approximately 6 m. This leading ISW was generated as the inflow commences and was likely an artifact of the startup procedure. Relative to the fluid ahead of it, the front propagated with a speed of about 0.23 m/s and the first and second ISWs had propagation speeds of about 0.35 and 0.34 m/s, respectively. Excluding the leading ISW, the trailing ISWs were separated by about 60 m with a period of approximately 3 min. Behind the front there were much shorter period and smaller amplitude oscillations. This idealistic simulation showed that the tidal plume front is able to generate ISWs, supporting the field-data.

The Rhine ROFI contains background shear due to the counter rotating tidal currents. These tidal currents have not been taken into account in the idealistic non-hydrostatic model, which was only forced by the density data. Adding such a sheared background current will change the result of the idealistic numerical model. Although, we expect that it will mainly change the properties of the ISWs and the propagation speed of the front as shown by *Pan and Jay* (2009b). We still expect to observe the generation of ISW packets as suggested by the field-data. Additionally, the idealized simulation was based on the tidal plume front observed in the field-data (Figure 5.4, dot 2). The horizontal density gradient at the surface was roughly 2 kg/m^3 (Figure 5.2). That suggests that fronts do not need a large horizontal density gradient to release ISWs.

5.3.4. ISW FISSION MECHANISM

Previous studies have demonstrated that tidal plume fronts can release ISWs if a frontal Froude number criterion is met (*Nash and Moum*, 2005; *Stashchuk and Vlasenko*, 2009). Therefore, we estimated the linear longwave phase speed ahead of the front (c_a), which is the ISW propagation speed in the limit of zero wave amplitude. To do this we used the Taylor Goldstein (TG) equation with observed five minute averaged density and velocity profiles (*Platell*, 2019). A hyperbolic tangent fit was applied to the scarce density data to obtain a continuous density profile. We chose a hyperbolic tangent fit because of the good agreement in the Rotterdam Waterway (*Pietrzak et al.*, 1990). The linear longwave phase speed ahead of the front was estimated as 0.81 (m/s) relative to the ground, and therefore exceeded the frontal speed. This resulted in a frontal Froude number, $F = u_f / c_a < 1$, that was subcritical flow similar to *Nash and Moum* (2005). This result suggested that the front was able to release ISWs.

A 3D hydrostatic numerical model (Delft3D) was used to simulate the tidal plume fronts, estimate the frontal Froude number in space, and to identify the location of release. Comparison of the field-data and the numerical model at the mooring station showed a good correspondence between the front normal velocity and the surface and near bottom density (Figure 5.4b,c and Figure 5.6). The vertical profiles of density supported the hyperbolic tangent fit on the field-data (Figure 5.6c-f). We used the model to

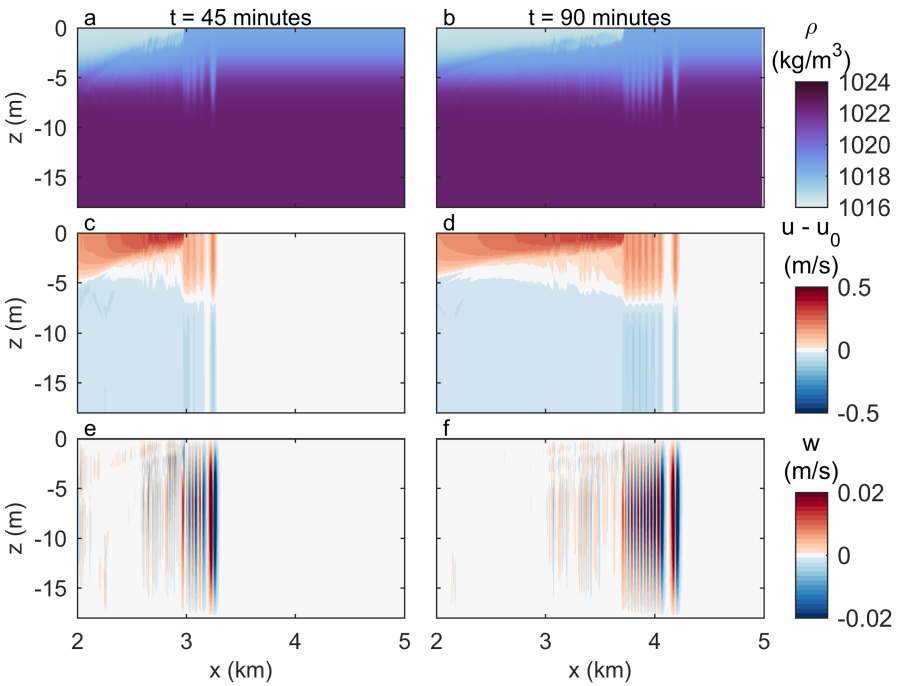

Figure 5.5: Non-hydrostatic model results of frontally forced ISWs at two different times. a-b) density, c-d) horizontal velocity, e-f) vertical velocity. The results are plotted in a reference frame moving with background current u_0. The first column represents 45 minutes (a,c,e), and the second column 90 minutes (b,d,f) after initialization.

follow the tidal plume front in time and space, from the river mouth to the mooring station and defined a front trajectory as shown in Figure 5.7. We identified the front using the horizontal density gradient and selected a point on the front that we then followed (Figure 5.7a, grey dots). Then, the magnitude and direction of the surface velocity were used to calculate subsequent locations of the front. We used the horizontal density gradient to verify that we are still on the front. We calculated Froude numbers on the front trajectory as $F = (u_f - \overline{u_a})/(c_a - \overline{u_a})$, where u_f is the surface velocity, c_a the linear phase speed ahead of the front, and $\overline{u_a}$ the depth mean current ahead of the front.

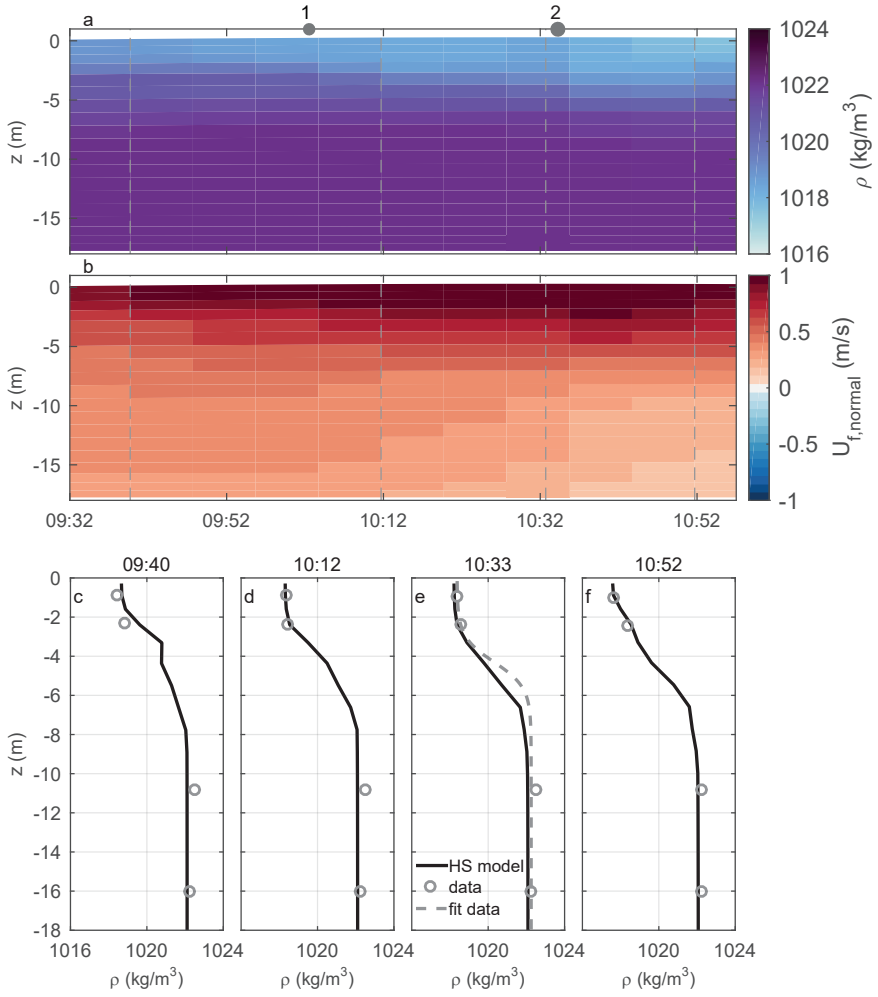

Figure 5.6: Time series of a) density and b) front normal velocity of the hydrostatic numerical model (HS) around the location of the mooring station. The grey dashed lines correspond to the four density profiles over depth in panels c-f, where the black line is the HS model data, the grey circles the field-data and the grey dashed line the fit to the field-data. The number 1 corresponds to the change in water properties around 10:00, and number 2 to the arrival of the tidal plume front around 10:36 - 10:43.

We followed three locations of the tidal plume front (Figures 5.7a,d), identified by the grey dots, for four to six hours. All three tidal plume front trajectories showed a transition from supercritical to subcritical flow (dark to light green, Figure 5.7a and 5.7d). Trajectory II transitioned first around 09:24 followed by I around 10:00 and III around 11:16, suggesting that the release of ISWs from the tidal plume front has occurred. In addition, this result suggested that the properties of the tidal plume front change along the front, and are able to release ISWs at different moments in time.

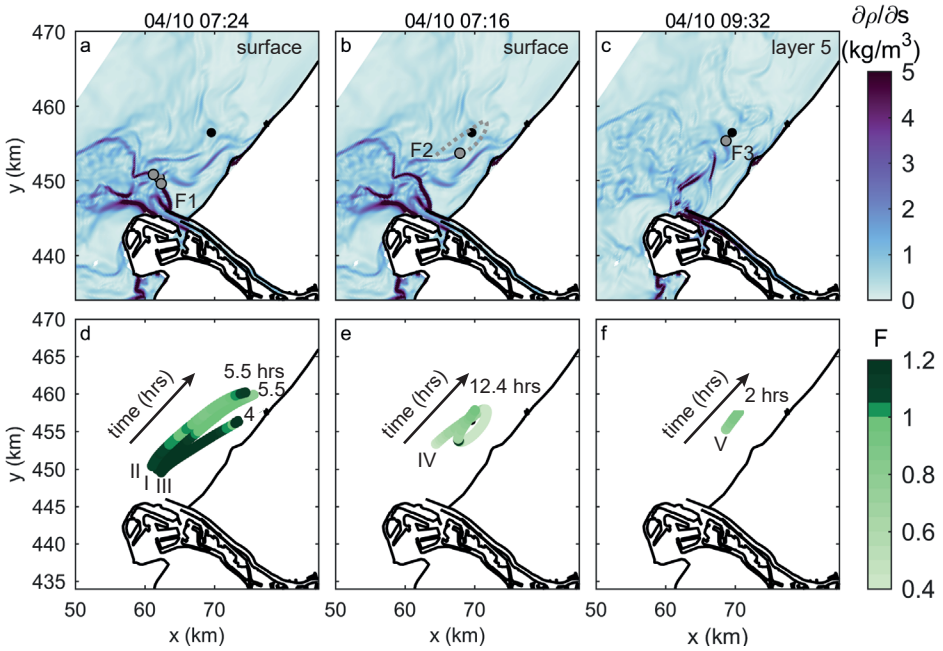

Figure 5.7: Spatial fields of the horizontal density gradient and Froude numbers predicted by the hydrostatic numerical model for day 277.4 (04/10/2014). a-c) horizontal density gradient at the surface layer or the 5th layer. The grey dots are the location of the fronts at a given moment in time and correspond to the different front trajectories in the panels beneath. The fronts are labelled with F1-F3. Panel b represents a front that already propagated for some time, its trajectory beforehand is indicated with the dotted grey line. d-f) Front trajectories in time and space where colour indicates the Froude number. The trajectories correspond to the dots in a-c, and are indicated with numbers from I to V. The numbers indicate the duration of the trajectory in hours (hrs). The x and y axes are displayed in the Dutch national coordinate system (Rijksdriehoek coordinates).

5.3.5. MECHANISM EXPLAINING MULTIPLE ISW PACKETS

The field-data suggested the presence of two different ISW packets due to an abrupt change in wave period and pycnocline depth around 10:00. Therefore, we used the hydrostatic model to understand what process is responsible for this change in properties. One possibility is the generation by a front other than the current tidal plume front; however, the hydrostatic model did not show a clear surface density gradient propagating through the mooring site around the expected time. The horizontal density gradi-

ents did, however, show the presence of multiple fronts at other locations (Figure 5.7a). Previous studies have shown that alongshore advection is important in the Rhine ROFI (*de Boer et al.*, 2008; *Rijnsburger et al.*, 2018). A scaling of typical values of intrinsic frontal speeds and ambient tidal currents, $u_f/u_a \approx 0.5/1 \approx 0.5$ (*Rijnsburger et al.*, 2018; *de Kok*, 1997), indicated that the newly released tidal plume front is controlled by tidal advection. Tidal advection resulted in an elliptical pathway each tidal cycle, which is characteristic of the Rhine ROFI currents (*Visser et al.*, 1994; *Simpson and Souza*, 1995). This is different to the Columbia River plume, where frontal propagation dominates, based on a ratio of $\approx 0.6/0.2 \approx 3$ (*García Berdeal et al.*, 2002; *Hickey et al.*, 2005, 1998; *Kilcher and Nash*, 2010).

Rijnsburger et al. (2020) found that a tidal plume front could last longer than one tidal cycle in the mid-field plume as a result of tidal advection. This front was kept within a distance of 15–20 km from the river mouth generating a multi frontal system. This distance compares well with the tidal excursion, which is roughly 15 km based on a maximum tidal velocity of 1 m/s and the M2 tidal frequency. Here we explored the consequences of their findings on the trapping of tidal plume fronts and the generation of this multi-frontal system (Figure 5.8). The horizontal density gradient showed the presence of multiple fronts at different moments within a tidal cycle (Figure 5.8b-d). We followed the "previous" (relic) tidal plume front (F0 and F2) on two locations (grey dots) to observe their trajectory in time and space (Figure 5.8). Tracer concentrations of the corresponding ebb releases separated the relic from the new tidal plume front (Figure 5.8e-j). The front trajectories (grey lines) showed that these fronts were still visible at the end of the ebb tide when a new front (F1) had already formed (Figure 5.8c,d). Therefore, the tracer concentrations and front trajectories indicated that these fronts are trapped by the tidal current (Figure 5.8d,g,j).

Tracer 1 followed the relic freshwater release with the corresponding tidal plume front (F0 and F2; Figures 5.8d-f), while tracer 2 followed the new freshwater release and tidal plume front (F1; Figures 5.8d-f). Tracer 1 clearly spread during the flood, and was advected back towards the river mouth during ebb. During ebb, tracer 2 was released into the area covered by tracer 1 and spread throughout the rest of the tidal cycle. Moreover, the tracers highlighted the important role of tidal advection and dispersion of the tracer concentrations, while at the same time they gave information about the evolution and trapping of the tidal plume fronts (Figure 5.8).

The two tracer concentrations clearly explained some of the fronts visible in the density gradient, such as the current tidal plume front (F1) and the relic tidal plume front (labelled as F0 and F2). We used the model to trace front F2 and calculated the Froude number. This trajectory was labelled as trajectory IV and followed the front for 12.4 hours (Figures 5.7b and 5.7e). Trajectory IV showed a transition from super- to subcritical around 07:56, roughly after 9.5 hours, which suggests that this front can release an ISW based on the theory of *Nash and Moum* (2005).

As discussed before, an abrupt change in ISW properties is observed around 10:00 (Figure 5.4). We expected to observe a front propagating through the measurement site at that moment in time, but the horizontal density gradient did not show this in neither the field- and hydrostatic model data. However, the hydrostatic model did show a clear horizontal density gradient at 3 to 4 m below the sea surface (Figures 5.6 and 5.7),

suggesting the presence of a front at depth (F3). Therefore, we investigated this front in more detail, followed its trajectory and calculated Froude numbers. The density profiles showed that after 10:00 the fresh upper layer thickened from roughly 3 to 4 m below the sea surface, coinciding with an increased pycnocline depth observed in the field-data (Figure 5.6). This thicker layer formed a horizontal density gradient at 3 to 4 m below the sea surface (layer 5 in the model) that moved towards the mooring station (Figure 5.7c). This front was difficult to follow, and we only managed to follow it close to the mooring station for 2 hours where the Froude number remained subcritical (Figure 5.7f). A transition from super- to subcritical was not observed, but the front was subcritical suggesting there is a possiblity it is able to release ISWs.

5.4. DISCUSSION

In this study, we observed multiple internal wave packets propagating ahead of the Rhine River tidal plume front in field data, satellite imagery and in both the hydrostatic and non-hydrostatic models. More specifically, on day 277.44, we observed two distinct packets of waves, with longer period waves between 09.25 to 10:00 preceding shorter period waves between 10:00 and 10:42 (Figure 5.4e-h). Different front trajectories indicated that the ISW packets were generated by different fronts, as the horizontal density gradient showed a multi-frontal system (Figure 5.7). Using the hydrostatic model, we estimated the expected arrival time of an ISW released by each of these trajectories and compared these with the ISW packets in the observations. This resulted in a figure that summarizes the information obtained from these two data sources and displays the possible generation mechanism (Figure 5.9).

Trajectories I to III are related to the same tidal plume front, which is labelled as F1. Trajectory I transitioned about 2 km from the mooring station, with an average u_f of 0.9 m/s and c_a of 0.93 m/s. This would lead to a predicted arrival time of an ISW around 10:30 and the front around 10:35 (Figure 5.9a). An ISW released by trajectory II will arrive around 10:40 at the mooring site (about 4 km, $c_a \approx 0.95$ m/s), while an ISW released by trajectory III would not reach the mooring site. These estimations suggest that the shorter period waves (packet 2) could have been released by the new tidal plume front F1 (Figure 5.9a).

An ISW released by trajectory IV, which is related to the relic tidal plume front F2, will arrive around 09:20 at the mooring station (about 2.6 km, $c_a \approx 0.88$ m/s). The corresponding front will arrive 10 - 15 minutes later. If we assume that an ISW is released at the start of trajectory V, it would arrive at the mooring roughly between 09:56 and 10:04. The longer period waves in the observations (packet 1) were observed between 09:32 and 10:00 suggesting that the trapped front F2 (trajectory IV) theoretically could have released these ISWs (Figure 5.9a). It should be noted that we used the linear long wave phase speeds (c_a), calculated with the Taylor Goldstein equation, to estimate ISW propagation and arrival.

These simple calculations supported the hypothesis that multiple tidal plume fronts were kept within the plume by the tidal currents, generating a multi-frontal system. As a result, both the new and a relic tidal plume front released internal waves, explaining the multiple internal wave packets (Figure 5.9b). The combined result of the in-situ observations and the two models helped to explain the observed packets of ISWs in the

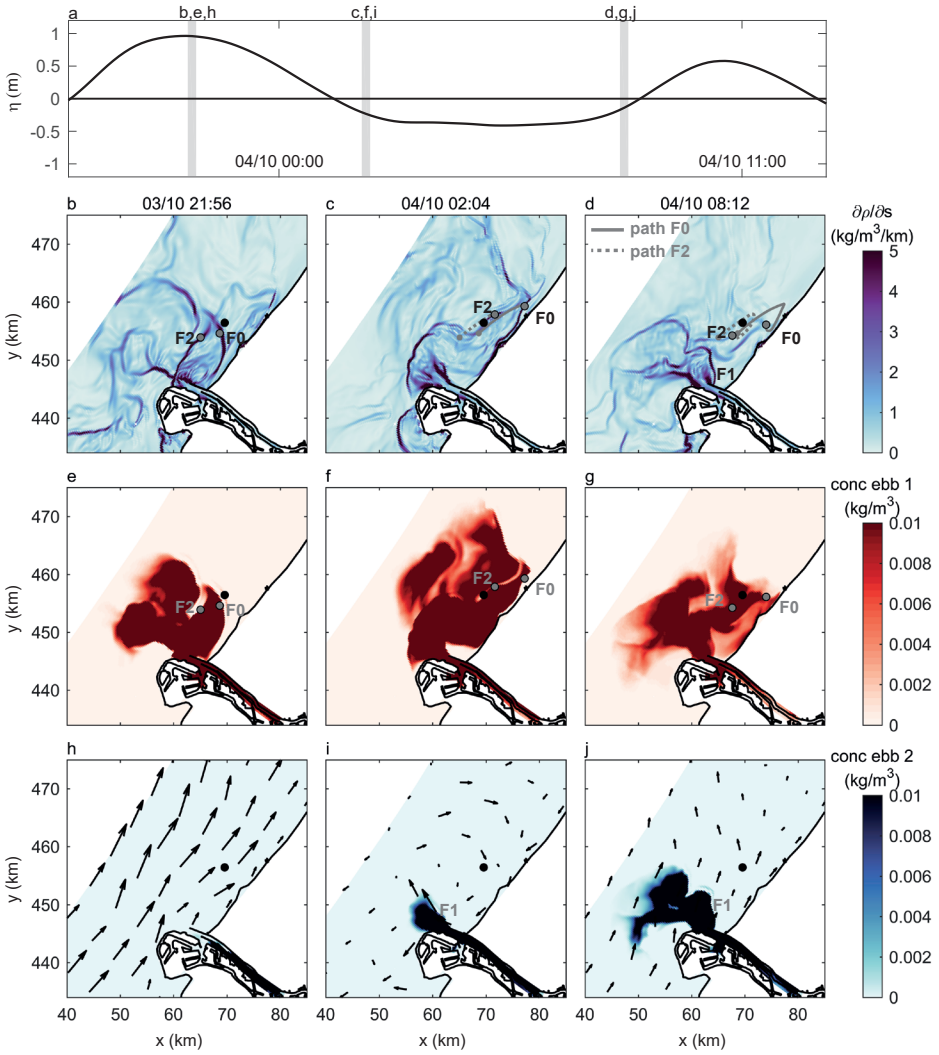

Figure 5.8: Trapping of tidal plume fronts using the hydrostatic model. a) Tidal cycle showing the location of each panel in time. Plan view of absolute value of the horizontal density gradient (b-d), and tracer concentrations (kg/m^3) in the surface layer of two freshwater releases (03/10/2014 and 04/10/2014), referred to as concentration ebb 1 (e-g) and ebb 2 (h-j). Each column represents a snapshot in time during a tidal cycle. The vectors represent surface velocity (m/s). The black dot indicates the mooring site. F0 refers to the tidal plume front formed on 03/10/2014, F1 refers to the front formed on 04/10/2014, and F2 refers to a front related to the release on 03/10/2014. The grey dots (b-g) mark a location on fronts F0 and F2. The trajectories of these fronts are shown by the lines, where solid is front F0 and dotted is front F2. The small grey dot (e-g) refers to the starting point of the trajectory back in time. The x and y axes are displayed in the Dutch national coordinate system (Rijksdriehoek coordinates).

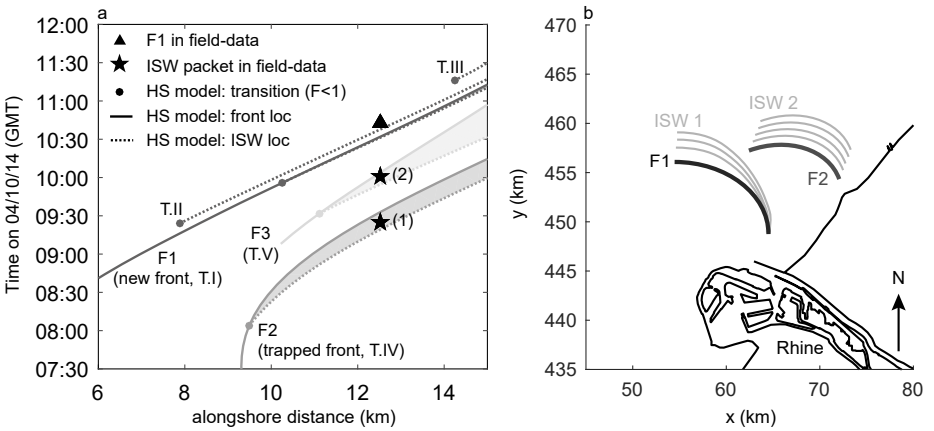

Figure 5.9: Summary of the evolution of the fronts and ISWs in time. a) Location of front and ISWs in time and space, where the black triangle and stars represent the information from the field-data, and the lines represent the information obtained from the hydrostatic model. The black triangle is the location of the tidal plume front, and the stars the location of the ISW packets (1 and 2). The solid lines represent the location of front F1 (dark grey), front F2 (middle grey), and front F3 (light grey) in time, while the dashed line is the estimated location of released ISWs. The area inbetween is shaded. The grey dots refer to the location, where the Froude number transitioned to F < 1, indicating the release of ISWs. The location of the front and ISW in the model (lines) are based on the trajectories I-V (T.I-T.V; Figure 5.7) b) Schematic of the release of multiple ISW packets due to the trapping of tidal plume fronts.

satellite image (Figure 5.1), although the satellite image is on a different day than the observations and model simulations. The field-data only captured two ISW packets, while on the satellite image four packets were visible. Packet A was generated by the new tidal plume front, while packet B was likely generated by a previous tidal plume front. Packets C and D were likely released by a relic tidal plume front during the current tidal cycle in the same manner as packet B. However, the simplified calculation in subsection 5.3.1 suggested that these two packets could have been released on the previous tidal cycle as well. For this further research is recommended.

As the Stokes number is large in the Rhine River plume (> 1), the anti-cyclonic boundary layer extends throughout the entire water column resulting in elliptical tidal currents, and associated tidal straining (*Flores et al.*, 2020). The Columbia River plume is a low Stokes number region, without much influence of bed friction. A key difference between the Rhine and the Columbia River plume is in the number of observed ISW packets. In the Rhine River plume multiple ISW packets are observed, while in the Columbia River plume only one ISW packet per tidal cycle has been observed so far (*Nash and Moum*, 2005; *Pan et al.*, 2007; *Jay et al.*, 2009). This difference could be due to the influence of friction and tidal straining in the Rhine River plume, which enhances a re-circulation. As the tidal currents are larger than the intrinsic frontal speed, the tidal plume fronts are advected and trapped. Although, this trapping has not been observed in other systems, a similar circulation, such as found in the bulge region in many river plumes, could potentially lead to trapping too. However, the recirculating currents should dominate over the intrinsic frontal speed, otherwise it is expected that the fronts escape from the near-

to mid-field plume.

Some studies have shown that tidal plume fronts play an important role in the dispersion and transport of freshwater in coastal oceans (*Hickey et al.*, 2010; *Horner-Devine et al.*, 2015). The spreading of the tracers in Figure 5.8 suggested dispersion by the tidal plume fronts. These tracers showed that the spreading is dependent on the tidal current. The spreading in the northeast direction (alongshore) was accelerated during the flood, but inhibited during the ebb. Other studies have shown that these tidal plume fronts can release ISWs, and that these waves are an important source for transporting and mixing river plume water further into the ocean (*Nash and Moum*, 2005; *Pan and Jay*, 2009a). Moreover, front generated ISWs are reported to change the plume dynamics and dissipate frontal energy (*Pan and Jay*, 2009a).

Therefore, we would expect that the ISWs generated in this system are important for turbulence, dissipation and transport as well. However, the ISWs in the Rhine River plume had a ratio of wave amplitude over water depth (η/H) of 0.04 - 0.08, while this ratio was estimated to be roughly $20/60 \approx 0.33$ to $8.5/136 \approx 0.06$ in the Columbia River plume (*Nash and Moum*, 2005; *Pan et al.*, 2007; *Pan and Jay*, 2009a). *Pan and Jay* (2009a) estimated that the fronts play an important role in dissipating energy from the tidal plume front even for waves with an amplitude ratio as small as 0.06. The above estimation showed that the ISWs generated by the Rhine front are small, but sometimes come close to the ratio of the Columbia ISWs found by *Pan and Jay* (2009a). Moreover, *Pietrzak et al.* (1991) showed that small short internal waves can still be significant for the production of turbulent kinetic energy in a sheared environment and should not be neglected.

5.5. CONCLUSIONS

We documented the presence of multiple ISW packets in the Rhine ROFI, generated by different tidal plume fronts. A combination of multiple data sources was required. Field-data showed the presence of ISWs ahead of the tidal plume front. Non-hydrostatic numerical model simulations confirmed that tidal plume fronts in shallow river plume systems, such as the Rhine River plume, can generate ISWs. Analysis of a satellite image showed that the different ISW packets cannot all have been generated by the same tidal plume front; instead hydrostatic numerical modelling showed that tidal plume fronts are sustained for longer than one tidal cycle in the mid-field river plume due to the advection of the elliptical tidal currents. This led to a multi-frontal system. A Froude number analysis demonstrated that both the new and relic tidal plume front are able to release ISWs. All the results together explained the formation of different ISW packets observed in the field-data and satellite image. The presence of multiple tidal plume fronts with associated ISW packets has not been observed before. These observations are different to the Columbia River plume and similar systems where only one ISW packet has been observed to be released by the new tidal plume front. It is likely that multiple ISW packets occur in other frictional river plume systems with a large Stokes number, where tidal advection dominates the intrinsic frontal speed. However, it is possible that systems like the Columbia River plume also experience some recirculation and associated trapping in the bulge region.

6

DISCUSSION AND OUTLOOK

This thesis has provided new insights into the Rhine River Plume dynamics ranging from the near- to the far-field plume. As such, it has advanced our understanding of the processes controlling the far-field plume, demonstrating the important role of advection and strain induced periodic stratification (ASIPS) in controlling the downstream circulation. Moreover, this thesis has shown the important role of tidal trapping and tidal plume fronts in the near- and mid-field Rhine River Plume. To this end, we leveraged two in-situ field-campaigns, remote sensing: land based x band radar, optical and SAR satellite images, a three-dimensional hydrostatic numerical model, and a two-dimensional non-hydrostatic numerical model. In this thesis it has been shown that this combination of techniques is a powerful means of understanding plume dynamics. Overall, we obtained an advanced and comprehensive picture of the dominant river plume processes important for cross-shelf exchange and alongshore transport. This chapter synthesizes the main findings of each chapter, it then provides a new, synoptic picture of the Rhine River Plume. The penultimate section highlights the global significance for other river plume systems. Finally, in the last section opportunities for future research are presented.

6.1. THE DYNAMICS IN THE FAR-FIELD PLUME

Several studies highlighted the crucial role of straining (S) and depth mean advection (A) regarding water column stability and therefore the alternation between a stratified and mixed water column in the Rhine River Plume (*van Alphen et al.*, 1988; *Simpson and Souza*, 1995; *Souza and James*, 1996; *de Boer et al.*, 2008). However, these studies were limited to 50 - 60 km downstream from the river mouth. Therefore in chapter 2, two simultaneously sailed transects were used to evaluate the role of these processes over one tidal cycle at a location 70 – 80 km downstream. The three-dimensional Potential Energy Anomaly analysis highlighted the important role of advection and strain induced periodic stratification (ASIPS). At this location, dispersion (C) and another non-linear term (N) were less pronounced than observed in the mid-field plume by *de Boer et al.* (2008). The mid-field plume feeds freshwater with certain properties into the far-field plume.

In turn, it is the far-field plume that is responsible for the transport of this freshwater and associated substances farther downstream. ASIPS controls the far-field plume, and therefore determines the pathway of the freshwater and associated substances that it receives.

Consequently, both straining and depth mean advection contribute to stratification in the more well-mixed waters far downstream. Therefore, in the entire Rhine River Plume a complex interplay between all depth mean advection and straining processes occurs, both in the cross- and along-shore direction. Nevertheless, cross-shore straining was found to have the largest contribution of the four ASIPS processes which is in line with the findings of *de Boer et al.* (2008) 30 km downstream. Moreover, in *Flores et al.* (2020) it was found that cross-shore straining plays an important role in the generation of a turbidity maximum zone along the entire Dutch coast. They found that it was responsible for the accumulation of fine sediment as observed by *Visser et al.* (1991) and *van der Hout et al.* (2015). In addition, a large concentration of suspended sediment is transported along the coast by a combination of the tidal current, wind stress and baroclinic effects (*Otto et al.*, 1990; *Visser et al.*, 1991; *van der Hout et al.*, 2015; *Flores et al.*, 2017). Thus, ASIPS has an important role regarding the fate of freshwater, fine sediment and other substances in the far field.

6.2. TIDAL PLUME FRONTS

The properties of the freshwater fed into the far-field are set in the near- and mid-field plume, where the tidal plume fronts play an important role regarding dispersion and transport. However, little is known about the role of these fronts in shallow frictional systems such as the Rhine River Plume. Tidal plume fronts can be modelled as gravity currents, which are dependent on the ratio of thickness of the gravity current and the total water depth (h/H). In this system, tidal straining is adding extra dissipation to the watercolumn and changing the vertical and horizontal stratification. Therefore, differences between the Rhine tidal plume fronts and deeper systems is expected. Although tidal straining is present in the near-field, we also expected some similarities of the Rhine tidal plume fronts with tidal plume fronts in other systems. In chapter 3, we have found that frontal properties, such as thickness, downwelling and speed, are indeed consistent with tidal plume front properties observed in other river plumes, such as the Connecticut, Koombana Bay, and Columbia River Plume (*Garvine and Monk*, 1974; *Luketina and Imberger*, 1987; *Kilcher and Nash*, 2010). This is significant as it shows that tidal plume fronts have similar properties across a wide range of river plume processes and geographic locations. However, different environmental conditions and ambient stratification can alter the shape, direction, thickness, and speed of tidal plume fronts (*Kilcher and Nash*, 2010). This is in line with our observations that highlight that the frontal properties and structure are influenced by the tidal current, wind speed and direction.

However, these fronts have differences with other tidal plume fronts as well, such as the dominance of ambient tidal currents. In the Rhine River Plume, dominant currents, generated by wind and tide, are faster than the intrinsic frontal speeds. Therefore, the wind and tide influence the frontal dynamics by depth mean advection. The fronts are thinner, move faster relative to the ground and are more mixed during a calm spring compared to a calm neap tide. So, larger tidal currents generate more vertical

mixing and a larger advection velocity. Downwelling winds are relatively common along the Dutch coast (from the southwest), and accelerate the fronts towards the coast and northwards as a result the fronts thicken. Significantly, these thick and fast fronts cause peak bed stresses around the timing of frontal passage, coinciding with high near bed velocities. The strong tidal stresses, modified by the rapidly changing stratification associated with frontal passage, impact the seabed. However, sometimes the fronts directly impact the bed beneath them. In these cases, large near bed currents and associated high bed stresses show that thick fronts can initiate sediment resuspension contributing to sediment transport processes and cross-shelf exchange.

6.3. EVOLUTION AND TRAPPING OF TIDAL PLUME FRONTS

The tidal plume front is formed on the ebb tide, where its northern edge is arrested by the southward flowing ebb tide. This inhibits the tidal plume from spreading on the ebb flow, resulting in asymmetric spreading similar to the Connecticut (*O'Donnell*, 1988) and Columbia tidal plume front (*Jay et al.*, 2009). The northern front is supercritical when released if the vertical velocity shear is excluded. So, the momentum of freshwater exceeds its buoyancy as observed in other front studies (*Luketina and Imberger*, 1987; *Kilcher and Nash*, 2010; *Horner-Devine et al.*, 2013). In the meantime the front spreads and thins. The three-dimensional numerical model shows that the tidal plume fronts move onshore and persist longer than one tidal cycle.

The model simulations are in agreement with the field-data, highlighting the role of advection resulting in tidal trapping of the tidal plume fronts. The tidal plume fronts are advected by the tidal current and they are still visible at the beginning of the next ebb tide. These fronts are advected back by the ebb flow, and are still visible 12 hours later. An important result we have found is that the total advection leads to the trapping of the tidal plume fronts in the mid-field where they stay for roughly four tidal cycles. Horizontal convergence and downwelling, together with advection, seem to control the strength and the longevity of the fronts. The trapping creates a multi-frontal structure where the trapped plume fronts interact with each other and sometimes coalesce.

6.4. THE ROLE OF INTERNAL SOLITARY WAVES

Tidal plume fronts in the Rhine River Plume have been shown to release internal solitary waves ahead of the front (ISWs). This is in agreement with studies in the Columbia River Plume, where tidal plume fronts are able to release large internal solitary waves (*Nash and Moum*, 2005). The release of these ISWs changes the dynamics of the fronts and therefore the pathway of the freshwater and other substances. The field-data in the mid-field plume showed the presence of these waves ahead of the tidal plume front for at least 10 events. However, the field-data had limited density data over the vertical making it more difficult to calculate accurate phase speeds for the internal waves. Therefore, we used a two-dimensional non-hydrostatic model to investigate whether the observed density field is able to generate ISWs. Moreover, we used the hydrostatic numerical model to estimate vertical profiles of density. With these vertical profiles we could estimate internal wave speeds using the Taylor Goldstein Equation. These calculations indicated that tidal plume fronts can fission ISWs. Furthermore, satellite images

supported this. This is an important result because these waves impact the frontal energetics and are likely to influence the mixing (*Pan and Jay*, 2009a) in this frictional plume.

However, both the optical satellite image and the field-data observed multiple ISW packets instead of one as found in the Columbia River Plume (e.g. *Nash and Moum*, 2005; *Pan et al.*, 2007; *Jay et al.*, 2009). These multiple packets can be explained by the trapped tidal plume fronts in the mid-field plume for multiple tidal cycles creating a multi-frontal system. The hydrostatic numerical model indicates that these trapped tidal plume fronts are able to release ISWs as well, resulting in the fission of multiple ISWs packets per tidal cycle. This mechanism causes multiple ISW packets along the Dutch coast. These multiple wave packets increase vertical shear and dissipation influencing the mixing in the near- and mid-field plume. As a result, they influence the stratification in this area and hence impact the far-field plume. In conclusion, tidal plume fronts in a shallow shelf sea are able to fission ISWs. In systems dominated by tidal advection, they possibly can even fission ISWs on a successive tidal cycle.

6.5. SYNOPTIC PICTURE OF THE RHINE ROFI

The Rhine River Plume or ROFI begins at the river mouth where freshwater is released into the coastal ocean, forming a tidal plume front. This front spreads, disperses and causes mixing with surrounding waters. This freshwater is transported through different dynamical regions eventually forming the far-field plume that extends over 100 km downstream. The idealized numerical model simulations of *de Boer et al.* (2008) are complemented by the observations in chapter 2 and show that the stratification in the entire river plume from the near-field to at least 80 km downstream is controlled by ASIPS in both cross- and alongshore direction (Figure 6.1). As a result, the entire plume is subject to on- and offshore movement during one tidal cycle. In the far-field, cross-shore tidal straining dominates, while in the near- and mid-field plume complexity is added due to the presence of the tidal plume fronts. The dynamics of these fronts seem mainly related to processes such as convergence (divergence) and downwelling (upwelling). It is expected that ASIPS and the tidal plume fronts interact in the mid-field plume based on the timing of onshore propagation.

de Boer et al. (2008) already showed that alongshore advection and straining play an important role at the boundary of the mid-field plume, where the ROFI interacts with the barotropic tidal current. Furthermore, the work in this thesis highlights the important role of advection on the propagation of the tidal plume fronts by trapping the tidal plume fronts in the mid-field plume (Figure 6.1 #3). These fronts are trapped within the mid-field for at least 3-4 tidal cycles, where they release ISW packets (Figure 6.1 #4). Therefore, the mid-field plume is expected to be a complex region where multiple tidal plume fronts, ISWs and ASIPS interact. This interaction will lead to the transport and dispersion of freshwater and substances, which eventually will be transported into the far-field where ASIPS dominates the pathway of this water.

In addition to the trapping, a large recirculation is observed downstream of the river mouth. From the model simulation it is not clear whether this flow recirculation is barotropic or baroclinic. Neither is it clear whether this is generated by the port extension or by a bulge circulation. The trapping and the observed circulation have consequences for other materials by keeping it in the mid-field plume. For example, sediment

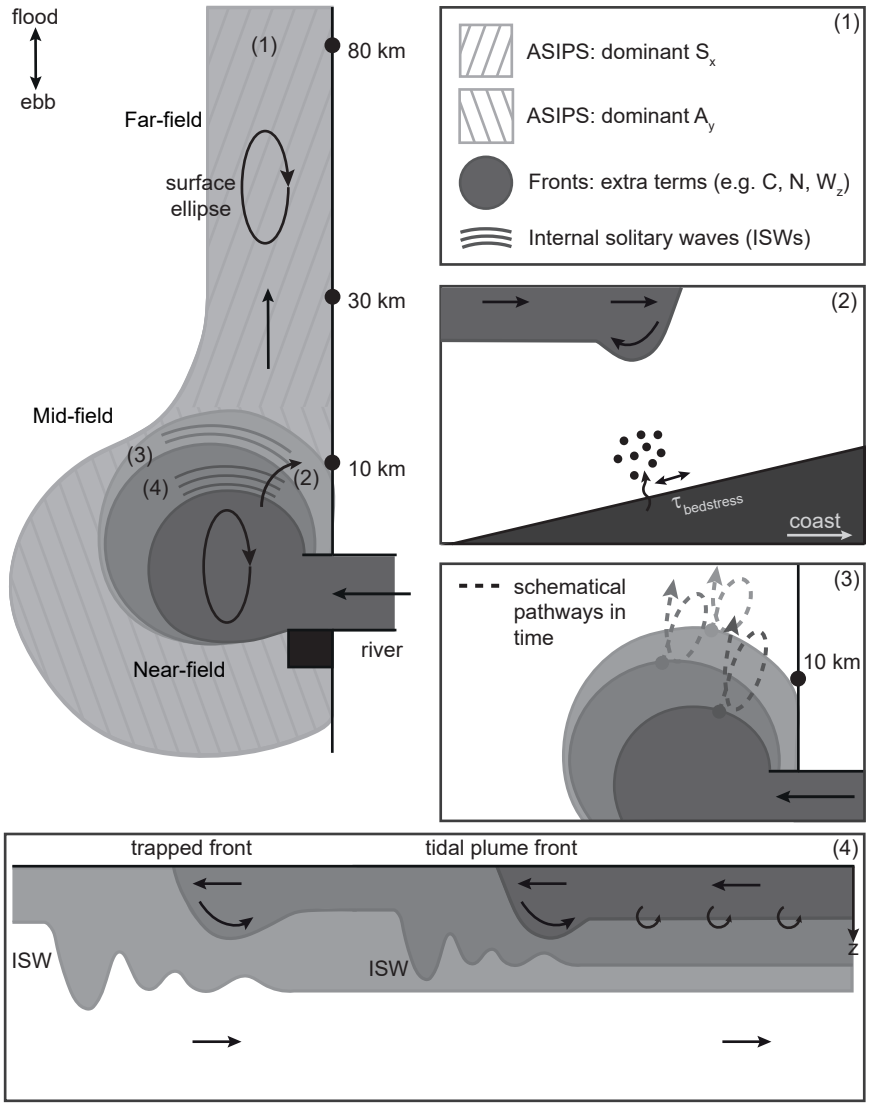

Figure 6.1: Signoptic picture of the Rhine River Plume with different dynamical processes based on the results in this thesis and *de Boer et al.* (2008). Top left: schematic of the river plume where different highlights are numbered. (1) entire river plume can be described by ASIPS, where straining or advection dominates in different areas. On top of ASIPS, tidal plume fronts are moving. (2) Onshore propagation of tidal plume front. (3) Trapping of tidal plume fronts by e.g. the elliptical tidal current (4) Release of internal solitary waves (ISWs) by the current and trapped tidal plume front.

could settle during low energetic periods and get resuspended again during storms. *Chant et al.* (2008) and *Kudela et al.* (2010) showed that a recirculation with a few days retention time can have positive or negative consequences for the coastal ecosystem. Therefore, the trapping in the mid-field together with the continuous input of riverine-borne materials by the river can influence the biological production positively or negatively. When the materials get transported into the far-field, ASIPS will determine its pathway. There, cross-shore straining leads to the cross-shore convergence of these materials and the formation of a nearshore turbidity maximum zone (*van der Hout et al.*, 2015; *Flores et al.*, 2020).

Identifying processes generating fine sediment transport is of interest for the Dutch coast. This thesis focused on ASIPS and the tidal plume fronts, where both seem to have an impact on sediment transport. Both the radar images and the model simulations show a clear onshore propagation of the tidal plume fronts (Figure 6.1 #2). These fronts influence cross-shore transport in different ways. First, *Horner-Devine et al.* (2017) showed that the onshore propagation of the fronts generate a strong offshore directed current beneath it. This offshore directed near-bed current transports fine sediment with it, which appears to be generated by wave resuspension in the nearshore. This process is called frontal pumping, and is most significant during spring tides (*Flores et al.*, 2017). In addition, the onshore propagating fronts can exert large stresses on the seabed in 12 meter water depth (see chapter 3). These large bed stresses are often timed with peaks in near bottom sediment concentrations (*Flores et al.*, 2017), suggesting resuspension due to the front itself or due to the rapid return flow generated by the front and the fast changing tidal current. Moreover, the front generated ISWs can be a potential source for transport or resuspending sediment as well during their along- or cross-shore propagation.

Tidal straining is active in the entire river plume and has been shown to play a crucial role in cross-shore sediment transport in the far-field plume (*Joordens et al.*, 2001; *Flores et al.*, 2020). *Flores et al.* (2017) confirmed that tidal straining can also generate cross-shore sediment transport in the mid-field plume, which is onshore directed in contrast to the offshore transport by fronts near the seabed. However, on its own tidal straining does not seem to generate a significantly large onshore transport compared to storms or offshore transport by fronts (*Flores et al.*, 2017). The magnitude of this transport at depth depends on the coastal ambient stratification (*Flores et al.*, 2017). Thus, straining and tidal plume fronts contribute to the transport of fine sediment and other substances in the Rhine ROFI and determine whether this sediment is transported onshore or into the deeper ocean.

6.6. GLOBAL IMPORTANCE

As the river plume is the interface between the river and the ocean, the processes controlling cross-shelf exchange, alongshore transport, dispersion and dilution are important to identify and understand. The main contributions of this thesis are threefold. First, this thesis shows that tidal plume fronts are important for cross-shelf exchange due to their onshore propagation, the generation of a strong return current at depth and their impact on the seabed. Second, front-generated ISWs packets are common and impact the front dynamics and dissipation. Third, this work highlights that depth mean

advection is important in the near- to mid-field plume for the structure of the plume, the fronts and the pathway of the freshwater and other materials.

The work in this thesis only studies one specific river plume. However, the lessons learned from this river plume can be significant for other systems as well. One example is the consequences for the coastline as a result of the onshore propagation of the tidal plume fronts. Many tidal plume front studies focused mainly on the offshore propagation of these fronts, while a tidal plume spreads in all directions and will turn towards the coast under the influence of Earth's rotation. Even in a deep system, such as the Columbia River Plume, tidal plume fronts are able to generate strong return currents near the seabed inducing large bed stresses at a location offshore (*Orton and Jay*, 2005). Therefore, we would expect an impact on the cross-shelf exchange and maybe even on sediment resuspension and transport in other systems due to the onshore propagation of fronts and their strong return currents (*Horner-Devine et al.*, 2017). This mechanism is especially important in systems subject to coastal erosion and flooding.

Another example that is relevant is the influence of the wind. Previous studies have shown that the wind magnitude and direction can alter the shape and transport of the entire river plume or the far-field plume (*Fong and Geyer*, 2001; *Lentz and Largier*, 2006; *Moffat and Lentz*, 2012; *Hickey et al.*, 2005). Moreover, wind straining can enhance or decrease estuarine circulation, velocity shear and stratification (*Scully et al.*, 2005). The cross-shelf movement of river plumes are sensitive to wind stress. In addition, these changes can have an impact on the local ecosystem, e.g. phytoplankton growth (*Hickey et al.*, 2005, 2010). In this thesis, it has been found that a certain wind magnitude and direction can accelerate and thicken the tidal plume fronts. Faster and thicker fronts lead to a stronger return current beneath the front resulting in an impact on the seabed. This shows that the wind direction and magnitude play an important role in the structure, speed and direction of these fronts. Therefore, the wind indirectly impacts the transport, dilution and dispersion of the freshwater and other materials in the mid-field plume. Understanding the impact of the wind will be relevant in the light of climate change, because of the expected changes in the wind fields.

6.7. FUTURE RESEARCH

Another unanswered question is the quantification of mixing, which can help in understanding the fate of freshwater and other substances. Many studies have focused on quantifying mixing in river plumes with the use of different techniques and they focus on an isolated region. The integration of all these different analyses would be valuable for the evaluation of the overall functioning and impact of a river plume. Such an analysis would be interesting for the Rhine River Plume as well, where multiple processes generate mixing, such as the tidal stresses, tidal straining (*Fisher et al.*, 2002; *Souza et al.*, 2008), tidal plume fronts, and front-generated internal solitary waves. The presence of these multiple processes together makes it a complex region and therefore should be the topic of future investigations. In chapter 4, a first indication for mixing indicated that the Rhine tidal plume fronts are related to some mixing, which is in line with other tidal plume front studies (e.g. *Orton and Jay*, 2005; *O'Donnell et al.*, 2008). However, tidal mixing seems to be dominant. Therefore, the next step would be to quantify the mixing of the different processes and evaluate the isolated and combined impact.

Satellite images show multiple ISW packets propagating along the coast within the plume. Chapter 5 hypothesizes that these packets are generated by multiple tidal plume fronts during one tidal cycle. The field-data was too limited to confirm this hypothesis, and the hydrostatic numerical model is not able to capture these waves. Therefore, a more thorough analysis on the generation of these ISWs is recommended and will be valuable for understanding the dynamics in the mid-field plume, and will help quantifying the total mixing and pathway. In addition, we did not observe multiple ISW packets on every tidal cycle, and the field-data did not indicate a clear correlation. Therefore, it would also be interesting to investigate the conditions under which multiple ISW packets are expected to be released and under which conditions only one or none. The wind and tide could be an important factor for trapping the fronts and generating ISWs, because it influences the density field and the fronts as shown in chapter 3. Consequently, the density field and tidal current structure influence the generation and properties of ISWs (e.g. *Stashchuk and Vlasenko*, 2009; *Pan and Jay*, 2009b).

This thesis measured and investigated a system that has been changed compared to previous research, such as the construction of the Sand Engine and the extension of the Port of Rotterdam next to the river mouth. Therefore, the work in this thesis raised the question of how these anthropogenic changes influence the river plume dynamics and the flow field. A construction of a 6 by 8 km land reclamation next to the river outflow would induce changes in the flow field and the spreading of the freshwater, that could lead to changes in sediment transport. Model simulations showed indeed different flow fields, river plume shapes, and a large recirculation downstream of the extension compared to older studies (see chapter 4). However, the model simulations used in this thesis were not designed to identify the impact of these changes. Therefore, research focused on this topic would be a valuable addition for many parties, because nowadays, more structures are built within coastal regions influenced by river plumes. Understanding the impact of these large-scale structures will help setting regulations for the construction of these structures, which is important for managing water quality and the fate of freshwater, fine sediment and other substances.

BIBLIOGRAPHY

Aghsaee, P., and L. Boegman (2015), Experimental investigation of sediment resuspension beneath internal solitary waves of depression, *Journal of Geophysical Research: Oceans*, *120*, 3301–3314.

Akan, Ç., J. C. McWilliams, S. Moghimi, and H. T. Özkan-Haller (2018), Frontal dynamics at the edge of the Columbia River plume, *Ocean Modelling*, *122*, 1–12.

Baumert, H., and G. Radach (1992), Hysteresis of turbulent kinetic energy in nonrotational tidal flows: A model study, *Journal of Geophysical Research*, *97*, 3669–3677.

Becherer, J., M. T. Stacey, L. Umlauf, and H. Burchard (2015), Lateral circulation generates flood-tide stratification and estuarine exchange flow in a curved tidal inlet, *Journal of Physical Oceanography*, *45*, 638–656.

Benjamin, T. B. (1968), Gravity currents and related phenomena, *Journal of Fluid Mechanics*, *31*, 209–248.

Bogucki, D., T. Dickey, and L. Redekopp (1997), Sediment resuspension and mixing by resonantly generated internal solitary waves, *Journal of Physical Oceanography*, *27*, 1181–1196.

Bourgault, D., P. S. Galbraith, and C. Chavanne (2016), Generation of internal solitary waves by frontally forced intrusions in geophysical flows, *Nature Communications*, *7*, 1–9.

Britter, R., and J. Simpson (1978), Experiments on the dynamics of a gravity current head, *Journal of Fluid Mechanics*, *88*, 223–240.

Burchard, H., and H. Baumert (1998), The formation of estuarine turbidity maxima due to density effects in the salt wedge. A hydrodynamic process study, *Journal of Physical Oceanography*, *28*, 309–321.

Burchard, H., and R. D. Hetland (2010), Quantifying the contributions of tidal straining and gravitational circulation to residual circulation in periodically stratified tidal estuaries, *Journal of Physical Oceanography*, *40*, 1243–1262.

Burchard, H., and R. Hofmeister (2008), A dynamic equation for the potential energy anomaly for analysing mixing and stratification in estuaries and coastal seas, *Estuarine, Coastal and Shelf Science*, *77*, 679–687.

Chant, R. J., J. Wilkin, W. Zhang, B.-J. Choi, E. Hunter, R. Castelao, S. Glenn, J. Jurisa, O. Schofield, R. Houghton, J. Kohut, T. K. Frazer, and M. A. Moline (2008), Dispersal of the Hudson river plume in the New York Bight, *Oceanography*, *21*, 148–161.

Chao, S. (1988), Wind-Driven Motion of Estuarine Plumes, *Journal of Physical Oceanography*, *18*, 1144–1166.

Chao, S., and W. Boicourt (1986), Onset of estuarine plumes*, *Journal of Physical Oceanography*, *16*, 2137–2149.

Chao, Y., J. D. Farrara, G. Schumann, K. M. Andreadis, and D. Moller (2015), Sea surface salinity variability in response to the Congo river discharge, *Continental Shelf Research*, *99*, 35–45.

Cochrane, J. D., and F. J. Kelly (1986), Low-frequency circulation on the Texas-Louisiana continental shelf, *Journal of Geophysical Research*, *91*, 10,645 – 10,659.

Cole, K. L., D. G. MacDonald, G. Kakoulaki, and R. D. Hetland (2020), River plume source-front connectivity, *Ocean Modelling*, *150*, 1–11.

Cromwell, T., and J. L. Reid Jr. (1956), A Study of Oceanic Fronts, *Tellus*, *8*, 94–101.

Da Silva, J. C., A. L. New, M. A. Srokosz, and T. J. Smyth (2002), On the observability of internal tidal waves in remotely-sensed ocean colour data, *Geophysical Research Letters*, *29*, 10–14.

Dagg, M., R. Benner, S. Lohrenz, and D. Lawrence (2004), Transformation of dissolved and particulate materials on continental shelves influenced by large rivers: plume processes, *Continental Shelf Research*, *24*, 833–858.

Davies, P. A., R. G. Davis, and M. R. Foster (1990), Flow past a circular cylinder in a rotating stratified fluid, *Philosophical transactions of the Royal Society of London A*, *331*, 245–286.

de Boer, G. J. (2008), On the interaction between tides and stratification in the Rhine Region of Freshwater Influence, Ph.D. thesis, Delft University of Technology, the Netherlands.

de Boer, G. J., J. D. Pietrzak, and J. C. Winterwerp (2006), On the vertical structure of the Rhine region of freshwater influence, *Ocean Dynamics*, *56*, 198–216.

de Boer, G. J., J. D. Pietrzak, and J. C. Winterwerp (2007), SST observations of upwelling induced by tidal straining in the Rhine ROFI, *Continental Shelf Research*, *29*, 263–277.

de Boer, G. J., J. D. Pietrzak, and J. C. Winterwerp (2008), Using the potential energy anomaly equation to investigate tidal straining and advection of stratification in a region of freshwater influence, *Ocean Modelling*, *22*, 1–11.

de Kok, J. (1996), A two-layer model of the Rhine plume, *Journal of Marine Systems*, *8*, 269–284.

de Kok, J. (1997), Baroclinic eddy formation in a Rhine plume model, *Journal of Marine Systems*, *12*, 35–52.

de Kok, J., C. de Valk, J. van Kester, E. de Goede, and R. Uittenbogaard (2001), Salinity and Temperature Stratification in the Rhine Plume, *Estuarine, Coastal and Shelf Science*, *53*, 467–475.

de Nijs, M. A., and J. D. Pietrzak (2012), Saltwater intrusion and ETM dynamics in a tidally-energetic stratified estuary, *Ocean Modelling*, *49-50*, 60–85.

de Nijs, M. A. J., J. C. Winterwerp, and J. D. Pietrzak (2010), The effects of the internal flow structure on SPM entrapment in the Rotterdam Waterway, *Journal of Physical Oceanography*, *40*, 2357–2380.

de Nijs, M. A. J., J. D. Pietrzak, and J. C. Winterwerp (2011), Advection of the salt wedge and evolution of the internal flow structure in the Rotterdam Waterway, *Journal of Physical Oceanography*, *41*, 3–27.

de Ruijter, W. P., A. W. Visser, and W. Bos (1997), The Rhine outflow: A prototypical pulsed discharge plume in a high energy shallow sea, *Journal of Marine Systems*, *12*, 263–276.

de Ruijter, W. P. M., A. van der Giessen, and F. C. Groenendijk (1992), Current and density structure in the Netherlands coastal zone, *Dynamics and exchanges in estuaries and the coastal zone*, *40*, 529–550.

de Schipper, M. A., S. de Vries, G. Ruessink, R. C. de Zeeuw, J. Rutten, C. van Gelder-Maas, and M. J. F. Stive (2016), Initial spreading of a mega feeder nourishment: Observations of the Sand Engine pilot project, *Coastal Engineering*, *111*, 23–38.

Deltares (2014), Delft3D-Flow User Manual, *Tech. rep.*, Delft, The Netherlands.

Farmer, D., and L. Armi (1999), The generation and trapping of solitary waves over topography, *Science*, *283*, 188–190.

Fischer, E., H. Burchard, and R. D. Hetland (2009), Numerical investigations of the turbulent kinetic energy dissipation rate in the Rhine region of freshwater influence, *Ocean Dynamics*, *59*, 629–641.

Fisher, N. R., J. H. Simpson, and M. J. Howarth (2002), Turbulent dissipation in the Rhine ROFI forced by tidal flow and wind stress, *Journal of Sea Research*, *48*, 249–258.

Flores, R. P., S. Rijnsburger, A. R. Horner-Devine, A. J. Souza, and J. D. Pietrzak (2017), The impact of storms and stratification on sediment transport in the Rhine region of freshwater influence, *Journal of Geophysical Research: Oceans*, *122*, 4456–4477.

Flores, R. P., S. Rijnsburger, S. Meirelles, A. R. Horner-Devine, A. J. Souza, J. D. Pietrzak, M. Henriquez, and A. Reniers (2018), Wave generation of gravity-driven sediment flows on a predominantly sandy seabed, *Geophysical Research Letters*, *45*, 7634–7645.

Flores, R. P., S. Rijnsburger, A. R. Horner-Devine, N. Kumar, A. J. Souza, and J. D. Pietrzak (2020), The formation of turbidity maximum zones by minor axis tidal straining in regions of freshwater influence, *Journal of Physical Oceanography*, *50*, 1265–1287.

Fong, D. A. (1998), Dynamics of freshwater plumes: observations and numerical modeling of the wind-forced response and alongsore transport, Ph.D. thesis, Massaschusetts Institute of Technology / Woods Hole Oceanography Institution joint program in oceanography, Massaschusetts, USA.

Fong, D. A., and W. R. Geyer (2001), Response of a river plume during an upwelling favorable wind event, *Journal of Geophysical Research*, *106*, 1067–1084.

Fong, D. A., W. R. Geyer, and R. P. Signell (1997), The wind-forced response on a buoyant coastal current: Observations of the western {Gulf of Maine} plume, *Journal of marine Systems*, *12*, 69–81.

García Berdeal, I., B. M. Hickey, and M. Kawase (2002), Influence of wind stress and ambient flow on a high discharge river plume, *Journal of Geophysical Research: Oceans*, *107*.

Garvine, R. (1999), Penetration of buoyant coastal discharge onto the continental shelf: A numerical model experiment, *Journal of Physical Oceanography*, pp. 1892–1909.

Garvine, R. W. (1974a), Dynamics of small-scale oceanic fronts, *Journal of Physical Oceanography*, *4*, 557–569.

Garvine, R. W. (1974b), Physical features of the Connecticut River outflow during high discharge, *Journal of Geophysical Research*, *79*, 831.

Garvine, R. W. (1984), Radial spreading of buoyant, surface plumes in coastal waters, *Journal of Geophysical Research*, *89*, 1989–1996.

Garvine, R. W. (1995), A dynamical system for classifying buoyant coastal discharges, *Continental Shelf Research*, *15*, 1585–1596.

Garvine, R. W., and J. D. Monk (1974), Frontal structure of a river plume, *Journal of Geophysical Research*, *79*, 2251–2259.

Geyer, W., R. Signell, D. Fong, J. Wang, D. Anderson, and B. Keafer (2004), The freshwater transport and dynamics of the western Maine coastal current, *Continental Shelf Research*, *24*, 1339–1357.

Geyer, W. R. (1993a), The importance of suppression of turbulence by stratification on the estuarine turbidity maximum, *Estuaries*, *16*, 113–125.

Geyer, W. R. (1993b), Three-dimensional tidal flow around headlands, *Journal of Geophysical Research*, *98*, 955–966.

Geyer, W. R., and D. K. Ralston (2015), Estuarine frontogenesis, *Journal of Physical Oceanography*, *45*, 546–561.

Giddings, S. N., D. A. Fong, S. G. Monismith, C. C. Chickadel, K. A. Edwards, W. J. Plant, B. Wang, O. B. Fringer, A. R. Horner-Devine, and A. T. Jessup (2012), Frontogenesis and frontal progression of a trapping-generated estuarine convergence front and its influence on mixing and stratification, *Estuaries and Coasts*, *35*, 665–681.

Goring, D. G., and V. I. Nikora (2002), Despiking Acoustic Doppler Velocimeter data, *Journal of Hydraulic Engineering, 128*, 117–126.

Halpern, B. S., S. Walbridge, K. A. Selkoe, C. V. Kappel, F. Micheli, C. D'Agrosa, J. F. Bruno, K. S. Casey, C. Ebert, H. E. Fox, R. Fujita, D. Heinemann, H. S. Lenihan, E. M. P. Madin, M. T. Perry, E. R. Selig, M. Spalding, R. Steneck, and R. Watson (2008), A global map of human impact on marine ecosystems, *Science*, *319*, 948–953.

Helfrich, K. R., and W. K. Melville (2006), Long nonlinear internal waves, *Annual Review of Fluid Mechanics*, *38*, 395–425.

Hessner, K., A. Rubino, P. Brandt, and W. Alpers (2001), The Rhine outflow plume studied by the analysis of synthetic aperture radar data and numerical simulations, *Journal of Physical Oceanography*, *31*, 3030–3044.

Hetland, R. D. (2005), Relating river plume structure to vertical mixing, *Journal of Physical Oceanography*, *35*, 1667–1688.

Hickey, B., L. Pietrafesa, D. Jay, and W. Boicourt (1998), The Columbia River plume study: Subtidal variability in the velocity and salinity fields, *Journal of Geophysical Research: Oceans*, *103*, 10,339–10,368.

Hickey, B., S. Geier, N. Kachel, and A. MacFayden (2005), A bi-directional river plume: The Columbia in summer, *Continental Shelf Research*, *25*, 1631–1656.

Hickey, B., R. M. Kudela, J. D. Nash, K. W. Bruland, W. T. Peterson, P. MacCready, E. J. Lessard, D. A. Jay, N. S. Banas, A. M. Baptista, E. P. Dever, P. M. Kosro, L. K. Kilcher, A. R. Horner-Devine, E. D. Zaron, R. M. McCabe, J. O. Peterson, P. M. Orton, J. Pan, and M. C. Lohan (2010), River influences on shelf ecosystems: Introduction and synthesis, *Journal of Geophysical Research: Oceans*, *115*, 1–26.

Horner-Devine, A. R. (2009), The bulge circulation in the Columbia River plume, *Continental Shelf Research*, *29*, 234–251.

Horner-Devine, A. R., D. a. Jay, P. M. Orton, and E. Y. Spahn (2009), A conceptual model of the strongly tidal Columbia River plume, *Journal of Marine Systems*, *78*, 460–475.

Horner-Devine, A. R., C. C. Chickadel, and D. G. MacDonald (2013), Coherent Structures and Mixing at a River Plume Front, in *Coherent Flow Structures at Earth's Surface*, edited by J. G. Venditti, J. L. Best, M. Church, and R. J. Hardy, John Wiley & Sons, Chichester, UK.

Horner-Devine, A. R., R. D. Hetland, and D. G. MacDonald (2015), Mixing and Transport in Coastal River Plumes, *Annual Review of Fluid Mechanics*, *47*, 569–594.

Horner-Devine, A. R., J. D. Pietrzak, A. J. Souza, M. A. Mckeon, S. Meirelles, M. Henriquez, R. P. Flores, and S. Rijnsburger (2017), Cross-shore transport of nearshore sediment by river plume frontal pumping, *Geophysical Reseach Letters*, *44*, 6343–6351.

Huthnance, J. M. (1997), The PROFILE project: An overview, *Journal of Marine Systems*, *12*, 249–261.

Jay, D. A., J. Pan, P. M. Orton, and A. R. Horner-Devine (2009), Asymmetry of Columbia River tidal plume fronts, *Journal of Marine Systems*, *78*, 442–459.

Joordens, J. C. A., A. J. Souza, and A. Visser (2001), The influence of tidal straining and wind on suspended matter and phytoplankton distribution in the Rhine outflow region, *Continental Shelf Research*, *21*, 301–325.

Kabat, P., L. O. Fresco, M. J. F. Stive, C. P. Veerman, J. S. L. J. van Alphen, B. W. a. H. Parmet, W. Hazeleger, and C. a. Katsman (2009), Dutch coasts in transition, *Nature Geoscience*, *2*, 450–452.

Kilcher, L. F., and J. D. Nash (2010), Structure and dynamics of the Columbia River tidal plume front, *Journal of Geophysical Research: Oceans*, *115*, 1–20.

Klymak, J. M., and J. N. Moum (2003), Internal solitary waves of elevation advancing on a shoaling shelf, *Geophysical Research Letters*, *30*, 8–11.

Korotenko, K. A., A. V. Sentchev, and F. G. Schmitt (2012), Effect of variable winds on current structure and Reynolds stresses in a tidal flow: Analysis of experimental data in the eastern English Channel, *Ocean Science*, *8*, 1025–1040.

Korotenko, K. A., A. A. Osadchiev, P. O. Zavialov, R.-C. Kao, and C.-F. Ding (2014), Effects of bottom topography on dynamics of river discharges in tidal regions: case study of twin plumes in Taiwan Strait, *Ocean Science*, *10*, 863–879.

Kourafalou, V. H., L.-Y. Oey, J. Wang, and T. N. Lee (1996), The fate of river discharge on the continental shelf: 1. Modeling the river plume and the inner shelf coastal current, *Journal of Geophysical Research*, *101*, 3415–3434.

Kudela, R. M., A. R. Horner-Devine, N. S. Banas, B. M. Hickey, T. D. Peterson, R. M. McCabe, E. J. Lessard, E. Frame, K. W. Bruland, D. A. Jay, J. O. Peterson, W. T. Peterson, P. M. Kosro, S. L. Palacios, M. C. Lohan, and E. P. Dever (2010), Multiple trophic levels fueled by recirculation in the Columbia River plume, *Geophysical Research Letters*, *37*, 1–7.

Lamb, K. G. (1994), Numerical experiments of internal wave generation by strong tidal flow across a finite amplitude bank edge, *Journal of Geophysical Research*, *99*, 843–864.

Lamb, K. G. (2007), Energy and pseudoenergy flux in the internal wave field generated by tidal flow over topography, *Continental Shelf Research*, *27*, 1208–1232.

Lentz, S., and J. Largier (2006), The Influence of Wind Forcing on the Chesapeake Bay Buoyant Coastal Current, *Journal of Physical Oceanography*, (2005), 1305–1316.

Lentz, S. J., and R. Limeburner (1995), The Amazon River plume during AMASSEDS: subtidal current variability and the importance of wind forcing, *Journal of Geophysical Research*, *100*, 2377–2390.

Lesser, G. R., J. A. Roelvink, J. A. van Kester, and G. S. Stelling (2004), Development and validation of a three-dimensional morphological model, *Coastal Engineering*, *51*, 883–915.

Li, L., and R. Pawlowicz (2018), Seasonal variability and generation mechanisms of nonlinear internal waves in the Strait of Georgia, *Journal of Geophysical Research : Oceans*, *123*, 1–21.

Los, F. J., M. T. Villars, and M. W. M. Van der Tol (2008), A 3-dimensional primary production model (BLOOM/GEM) and its applications to the (southern) North Sea (coupled physical-chemical-ecological model), *Journal of Marine Systems*, *74*, 259–294.

Luketina, D. A., and J. Imberger (1987), Characteristics of a surface buoyant jet, *Journal of Geophysical Research: Oceans*, *92*, 5435–5447.

Macdonald, R. W., D. W. Paten, and E. C. Carmack (1995), The freshwater budget and under-ice spreading of Mackenzie River water in the Canadian Beaufort Sea based on salinity and 18O/16O measurement in water and ice, *Journal of Geophysical research*, *100*, 895–919.

Macdonald, R. W., E. C. Carmack, F. A. McLaughlin, K. K. Falkner, and J. H. Swift (1999), Connections among ice, runoff and atmospheric forcing in the Beaufort Gyre, *Geophysical Research Letters*, *26*, 2223–2226.

Magaldi, M. G., T. M. Özgökmen, A. Griffa, E. P. Chassignet, M. Iskandarani, and H. Peters (2008), Turbulent flow regimes behind a coastal cape in a stratified and rotating environment, *Ocean Modelling*, *25*, 65–82.

Marmorino, G. O., and C. L. Trump (2000), Gravity current structure of the Chesapeake Bay outflow plume, *Journal of Geophysical Research*, *105*, 28,847–28,861.

Maxworthy, T. (1979), A note on the internal solitary waves produced by tidal flow over a three-dimensional ridge, *Journal of Geophysical Research*, *84*.

Maxworthy, T., J. Leilich, J. E. Simpson, and E. H. Meiburg (2002), The propagation of a gravity current into a linearly stratified fluid, *Journal of Fluid Mechanics*, *453*, 371–394.

McCandliss, R., S. Jones, M. Hearn, R. Latter, and C. Jago (2002), Dynamics of suspended particles in coastal waters (southern North Sea) during a spring bloom, *Journal of Sea Research*, *47*, 285–302.

Mirshak, R., and D. E. Kelley (2009), Inferring propagation direction of nonlinear internal waves in a vertically sheared background flow, *Journal of Atmospheric and Oceanic Technology*, *26*, 615–625.

Moffat, C., and S. Lentz (2012), On the response of a buoyant plume to downwelling-favorable wind stress, *Journal of Physical Oceanography*, *42*, 1083–1098.

Mulligan, R. P., and W. Perrie (2019), Circulation and structure of the Mackenzie River plume in the coastal Arctic Ocean, *Continental Shelf Research*, *177*, 59–68.

Munchow, A., and R. W. Garvine (1993), Dynamical properties of a a buoyancy-driven coastal current, *Journal of Geophysical Research*, *98*, 20,063 – 20,077.

Nash, J. D., and J. N. Moum (2005), River plumes as a source of large-amplitude internal waves in the coastal ocean., *Nature*, *437*, 400–403.

Nash, J. D., L. F. Kilcher, and J. N. Moum (2009), Structure and composition of a strongly stratified, tidally pulsed river plume, *Journal of Geophysical Research: Oceans*, *114*, 1–16.

Nicholls, R. J., and A. Cazenave (2010), Sea level rise and its impact on coastal zones, *Science*, *328*, 1517–1520.

Nicholls, R. J., P. Wong, V. Burket, J. Codignotto, J. Hay, R. McLean, S. Ragoonaden, and C. Woodroffe (2007), Coastal systems and low-lying areas, in *Climate Change 2007: Impacts, Adaptation and Vulnerability. Contribution ofWorking Group II to the Fourth Assessment Report of the Intergovernmental Panel on Climate Change*, pp. 315–356, Cambridge University Press.

O'Donnell, J. (1988), A numerical technique to incorporate frontal boundaries in two-dimensional layer models of ocean dynamics, *Journal of Physical Oceanography*, *18*, 1584–1600.

O'Donnell, J. (1990), The formation and fate of a river plume: A numerical model, *Journal of Physical Oceanography*, *20*, 551–569.

O'Donnell, J. (1993), Surface fronts in estuaries: A review, *Estuaries*, *16*, 12–39.

O'Donnell, J., G. O. Marmorino, and C. L. Trump (1998), Convergence and downwelling at a river plume front, *Journal of Physical Oceanography*, *28*, 1481–1495.

O'Donnell, J., S. G. Ackleson, and E. R. Levine (2008), On the spatial scales of a river plume, *Journal of Geophysical Research*, *113*, 1–12.

Orton, P. M., and D. A. Jay (2005), Observations at the tidal plume front of a high-volume river outflow, *Geophysical Research Letters*, *32*, 1–4.

Osadchiev, A. A. (2018), Small mountainous rivers generate high-frequency internal waves in coastal ocean, *Scientific Reports*, *8*, 1–8.

Osadchiev, A. A., A. Izhitskiy, P. Zavialov, V. Kremenetskiy, A. Polukhin, V. Pelevin, and Z. Toktamysova (2017), Structure of the buoyant plume formed by Ob and Yenisei river discharge in the southern part of the Kara Sea during summer and autumn, *Journal of Geophysical Research: Oceans*, *122*, 5916–5935.

Ostrovsky, L. A., and Y. A. Stepanyants (1989), Do internal solitions exist in the ocean?, *Reviews of Geophysics*, *27*, 293–310.

Otto, L., J. T. Zimmerman, G. K. Furnes, M. Mork, R. Saetre, and G. Becker (1990), Review of the physical oceanography of the North Sea, *Netherlands Journal of Sea Research*, *26*, 161 – 238.

Palmer, M. R. (2009), The modification of current ellipses by stratification in the Liverpool Bay ROFI, *Ocean Dynamics*, *60*(2), 219–226, doi:10.1007/s10236-009-0246-x.

Pan, J., and D. A. Jay (2009a), Dynamic characteristics and horizontal transports of internal solitons generated at the Columbia River plume front, *Continental Shelf Research*, *29*, 252–262.

Pan, J., and D. A. Jay (2009b), Effects of ambient velocity shear on nonlinear internal wave associated mixing at the Columbia River plume front, *Journal of Geophysical Research*, *114*, 1–13.

Pan, J., D. A. Jay, and P. M. Orton (2007), Analyses of internal solitary waves generated at the Columbia River plume front using SAR imagery, *Journal of Geophysical Research: Oceans*, *112*, 1–11.

Pawlowicz, R., B. Beardsley, and S. Lentz (2002), Classical tidal harmonic analysis including werror estimates in MATLAB using T_TIDE, *Computers and Geosciences*, *28*, 929–937.

Pietrzak, J., C. Kranenburg, and G. Abraham (1990), Resonant internal waves in fluid flow, *Nature*, *344*, 844–847.

Pietrzak, J., C. Kranenburg, G. Abraham, B. Kranenborg, and A. V. D. Wekken (1991), Internal wave activity in rotterdam waterway, *Journal of Hydraulic Engineering*, *117*, 738–757.

Pietrzak, J. D., G. J. de Boer, and M. a. Eleveld (2011), Mechanisms controlling the intra-annual mesoscale variability of SST and SPM in the southern North Sea, *Continental Shelf Research*, *31*, 594–610.

Platell, H. (2019), Internal gravity waves in the Rhine ROFI; applicability of the KdV model, Msc. thesis, Delft University of Technology.

Prandle, D. (1982a), The vertical structure of tidal currents, *Geophysical & Astrophysical Fluid Dynamics*, *22*, 37–41.

Prandle, D. (1982b), The vertical structure of tidal currents and other oscillatory flows, *Continental Shelf Research*, *1*, 191–207.

Pritchard, M., and D. A. Huntley (2006), A simplified energy and mixing budget for a small river plume discharge, *Journal of Geophysical Research: Oceans*, *111*, 1–11.

Radermacher, M., and A. J. H. M. Reniers (2016), Tidal flow separation at protruding beach nourishments, *Journal of Geophysical Research: Oceans*, *122*, 1–17.

Ralston, D. K., G. W. Cowles, W. R. Geyer, and R. C. Holleman (2017), Turbulent and numerical mixing in a salt wedge estuary: Dependence on grid resolution, bottom roughness, and turbulence closure, *Journal of Geophysical Research : Oceans*, *122*, 692–712.

Rijkswaterstaat (2015), Watergegegevens.

Rijnsburger, S. (2014), Stratification and mixing in the Rhine Region of Freshwater Influence Analysing two parallel transects, Msc. thesis, Delft University of Technology.

Rijnsburger, S., C. M. van der Hout, O. van Tongeren, G. J. de Boer, B. C. van Prooijen, W. G. Borst, and J. D. Pietrzak (2016), Simultaneous measurements of tidal straining and advection at two parallel transects far downstream in the Rhine ROFI, *Ocean Dynamics*, *66*, 719–736.

Rijnsburger, S., R. P. Flores, J. D. Pietrzak, A. R. Horner-devine, and A. J. Souza (2018), The influence of tide and wind on the propagation of fronts in a shallow river plume, *Journal of Geophysical Research C: Oceans*, *123*, 1–17.

Rijnsburger, S., R. P. Flores, J. D. Pietrzak, A. R. Horner-Devine, A. J. Souza, and F. Zijl (2020), The evolution and interaction of multiple plume fronts in the tidal Rhine region of freshwater influence, *submitted to Journal of Geophysical Research: Oceans, under revision*, (Special Issue PECS 2018).

Rippeth, T. P., N. R. Fisher, and J. H. Simpson (2001), The cycle of turbulent dissipation in the presence of tidal straining, *Journal of Physical Oceanography*, *31*, 2458–2471.

Sandstrom, H., and J. Elliott (1984), Internal tide and solitons on the Scotian Shelf, *Journal of Geophysical Research*, *89*, 6419–6426.

Scotti, A., B. Butman, R. Beardsley, P. S. Alexander, and S. Anderson (2005), A modified beam-to-earth transformation to measure short-wavelength internal waves with an acoustic Doppler current profiler, *Journal of Atmospheric and Oceanic Technology*, *22*, 583–591.

Scully, M. E., C. Friedrichs, and J. Brubaker (2005), Control of estuarine stratification and mixing by wind-induced straining of the estuarine density field, *Estuaries*, *28*, 321–326.

Sharples, J., J. J. Middelburg, K. Fennel, and T. D. Jickells (2017), What proportion of riverine nutrients reaches the open ocean?, *Global Biogeochemical Cycles*, *31*, 39–58.

Shaw, W. J., and J. H. Trowbridge (2001), The direct estimation of near-bottom turbulent fluxes in the presence of energetic wave motions, *Journal of Atmospheric and Oceanic Technology*, *18*, 1540–1557.

Shin, J. O., S. B. Dalziel, and P. F. Linden (2004), Gravity currents produced by lock exchange, *Journal of Fluid Mechanics*, *521*, 1–34.

Signell, R. P., and W. R. Geyer (1991), Transient eddy formation around headlands, *Journal of Geophysical Research: Oceans*, *96*, 2561–2575.

Simpson, J. H. (1997), Physical processes in the ROFI regime, *Journal of Marine Systems*, *7963*, 3–15.

Simpson, J. H., and A. J. Souza (1995), Semidiurnal switching of stratification in the region of the Rhine, *Journal of Geophysical research*, *100*, 7037–7044.

Simpson, J. H., J. Brown, J. Matthews, and G. Allen (1990), Tidal straining, density currents, and stirring in the control of estuarine stratification, *Estuaries*, *13*, 125–132.

Simpson, J. H., J. Sharples, and T. P. Rippeth (1991), A prescriptive model induced by freshwater of stratification runoff, *Estuarine Coastal and Shelf Science*, *33*, 23–35.

Simpson, J. H., W. G. Bos, F. Schirmer, A. J. Souza, T. P. Rippeth, S. E. Jones, and D. Hydes (1993), Periodic stratification in the Rhine ROFI in the North Sea, *Oceanologica Acta*, *16*, 23–32.

Souza, A., and J. Simpson (1996), The modification of tidal ellipses by stratification in the Rhine ROFI, *Continental Shelf Research*, *16*, 997–1007.

Souza, A. J. (2013), On the use of the Stokes number to explain frictional tidal dynamics and water column structure in shelf seas, *Ocean Science*, *9*, 391–398.

Souza, A. J., and I. D. James (1996), A two-dimensional (x-z) model of tidal straining in the Rhine ROFI, *Continental Shelf Research*, *16*, 949–966.

Souza, A. J., and A. Lane (2013), Effects of freshwater inflow on sediment transport, *Journal of Operational Oceanography*, *6*, 27–31.

Souza, A. J., and J. H. Simpson (1997), Controls on stratification in the Rhine ROFI system, *Journal of Marine Systems*, *7963*, 311–323.

Souza, A. J., J. T. Holt, and R. Proctor (2007), Modelling SPM on the NW European shelf seas, *Geological Society, London, Special Publications*, *274*, 147–158.

Souza, A. J., N. R. Fisher, J. H. Simpson, and M. J. Howarth (2008), Effects of tidal straining on the semidiurnal cycle of dissipation in the Rhine region of freshwater influence: Comparison of model and measurements, *Journal of Geophysical Research*, *113*.

Spahn, E. Y., A. R. Horner-Devine, J. D. Nash, D. A. Jay, and L. Kilcher (2009), Particle resuspension in the Columbia River plume near field, *Journal of Geophysical Research: Oceans*, *114*, 1–16.

Stashchuk, N., and V. Vlasenko (2009), Generation of internal waves by a supercritical stratified plume, *Journal of Geophysical Research: Oceans*, *114*, 1–17.

Stelling, G. S., and J. A. M. Van Kester (1994), On the approximation of horizontal gradients in sigma coordinates for bathymetry with steep bottom slopes, *International Journal for Numerical Methods in Fluids*, *18*, 915–935.

Stive, M. J., M. A. de Schipper, A. P. Luijendijk, S. G. Aarninkhof, C. van Gelder-Maas, J. S. v. T. de Vries, S. de Vries, M. Henriquez, S. Marx, and R. Ranasinghe (2013), A new alternative to saving our beaches from sea-level rise: The Sand Engine, *Journal of Coastal Research*, *29*, 1001–1008.

Suijlen, J., and R. D. Duin (2002), Atlas of near-surface Total Suspended Matter concentrations in the Dutch coastal zone of the North Sea, *Tech. Rep. December*, National Institute for Coastal and Marine Management.

van Alphen, J., W. P. M. De Ruijter, and J. C. Borst (1988), Outflow and three-dimensional spreading of Rhine river water in the Netherlands coastal zone, in *Physical processes in estuaries*, edited by J. Dronkers and W. van Leussen, pp. 70–92, Springer-Verlag, Berlin.

van der Giesen, A., W. de Ruijter, and J. Borst (1990), Three-dimensional current structure in the Dutch coastal zone, *Netherlands Journal of Sea Research*, *25*, 45–55.

van der Hout, C. M., T. Gerkema, J. J. Nauw, and H. Ridderinkhof (2015), Observations of a narrow zone of high suspended particulate matter (SPM) concentrations along the Dutch coast, *Continental Shelf Research*, *95*, 27–38.

van der Hout, C. M., R. Witbaard, M. J. Bergman, G. C. Duineveld, M. J. Rozemeijer, and T. Gerkema (2017), The dynamics of suspended particulate matter (SPM) and chlorophyll-a from intratidal to annual time scales in a coastal turbidity maximum, *Journal of Sea Research*, *127*, 105–118.

van der Voet, E., R. Kleijn, and H. A. Udo de Haes (1996), Nitrogen pollution in the European Union – an economy-environment confrontation, *Environmental Conservation*, *23*, 198–206.

Verboom, G., J. de Ronde, and R. van Dijk (1992), A fine grid tidal flow and storm surge model of the North Sea, *Continental Shelf Research*, *12*, 213–233.

Verlaan, M., A. Zuderveld, H. De Vries, and J. Kroos (2005), Operational storm surge forecasting in the Netherlands: Developments in the last decade, *Philosophical Transactions of the Royal Society A: Mathematical, Physical and Engineering Sciences*, *363*, 1441–1453.

Verspecht, F., T. P. Rippeth, M. J. Howarth, a. J. Souza, J. H. Simpson, and H. Burchard (2009), Processes impacting on stratification in a region of freshwater influence: Application to Liverpool Bay, *Journal of Geophysical Research*, *114*.

Visser, A. W., A. J. Souza, K. Hessner, and J. H. Simpson (1994), The effect of stratification on tidal current profiles in a region of freshwater influence, *Oceanologica Acta*, *17*, 369–381.

Visser, M., W. de Ruijter, and L. Postma (1991), The distribution of suspended matter in the Dutch coastal zone, *Netherlands Journal of Sea Research*, *27*, 127–143.

Voulgaris, G., and J. H. Trowbridge (1998), Evaluation of the Acoustic Doppler Velocimeter (ADV) for Turbulence Measurements *, *Journal of Atmospheric and Oceanic Technology*, *15*, 272–289.

Whitney, M. M., and R. W. Garvine (2006), Simulating the Delaware Bay buoyant outflow: Comparison with observations, *Journal of Physical Oceanography*, *36*, 3–21.

Wiechen, J. V. (2011), Modelling the wind-driven motions in the Rhine ROFI, Msc. thesis, Delft University of Technology.

Wiles, P. J., T. P. Rippeth, J. H. Simpson, and P. J. Hendricks (2006), A novel technique for measuring the rate of turbulent dissipation in the marine environment, *Geophysical Research Letters*, *33*.

Winant, C. D. (2007), Three-dimensional tidal flow in an elongated, rotating basin, *Journal of Physical Oceanography*, *37*, 2345–2362.

Xie, X., M. Li, and W. C. Boicourt (2017), Breaking of internal solitary waves generated by an estuarine gravity current, *Geophysical Research Letters*, *44*, 7366–7373.

Yankovsky, A. E., and D. C. Chapman (1997), A Simple Theory for the Fate of Buoyant Coastal Discharges*, *Journal of Physical Oceanography*, *27*, 1386–1401.

Yuan, Y., and A. R. Horner-Devine (2017), Experimental investigation of large-scale vortices in a freely spreading gravity current, *Physics of Fluids*, *29*.

Zavala-Hidalgo, J., S. L. Morey, and J. J. O'Brien (2003), Seasonal circulation on the western shelf of the Gulf of Mexico using a high-resolution numerical model, *Journal of Geophysical Research: Oceans*, *108*.

ACKNOWLEDGEMENTS

During the past years, I had the privilege to meet, work with and learn from many amazing individuals. Not to mention the friends I made along the way. These collaborations made my scientific journey enjoyable and helped me to finish this thesis.

Julie, I am really grateful that you gave me the opportunity to dive deeper into the world of river plumes. Your enthusiasm for river plumes is contagious, and has fed my motivation time and time again. You always reminded me of my accomplishments instead of the length of my to do list. Thank you for enabling me to go to several conferences, and on several visits to NOC Liverpool and the University of Washington. I cherish all the times that you included me and introduced me to other scientists whether it was at conferences, meetings or just at the University. I will not forget the time we went swimming in the Atlantic Ocean.

Alejandro Souza and Alexander Horner-Devine, it was a pleasure to work with both of you during my PhD. Thank you for making time and taking care of me when I was visiting NOC Liverpool and the University of Washington. Alex Souza, you taught me a lot about ROFI's and sediment dynamics. I really appreciate all your effort regarding the measurement frames, which resulted in a great dataset. Alex Horner-Devine, I admire your passion for science and your endless ideas. Thank you for being critical about my work and all the help with the field-campaign.

I would like to thank the doctoral committee members for taking the time to read this thesis and for previous discussions on conferences and meetings.

My PhD was part of a research project funded by the NWO Domain Applied and Engineering Sciences. Steven, I am glad we were together on this project and could support each other when preparing project meetings together. You showed me new insights into non-hydrostatic LES modelling, which was often way too complicated for me. I would like to thank all members of the user committee for their relevant questions and valuable feedback.

Raul, I am really happy to have worked with you during the previous years. I admire your positivity and perseverance. I could always count on you for in-depth discussions with great outcomes. You are a great scientist and will have lot of success in academia in the future.

My research wouldn't have been possible without a successful field-campaign, which can be attributed to many people. Martijn Henriquez, thank you for showing me how to organise a field-campaign. Maggie McKeon, without you the mooring data wouldn't have been so successful. Thank you for coming to the Netherlands and sharing your expertise on the different measurement devices. Richard Cooke and Christopher Balfour, thank you for setting up the measurement frames and answering all my technical questions even a year or two after the actual field campaign. Saulo Meirelles, thank you for sharing your data analysis skills. I really enjoyed our visit to NOC Liverpool, where we tried every evening a different restaurant or bar.

The field campaign resulted not only in data, but also in many bottles full of sediment taken from the sea bed. Claire and Maria, it was great to spend a few days together in the Deltares lab, sieving and analysing these sediment samples. Thank you for your help and showing me how to do this. Additionally, Claire, I always enjoyed our scientific and non-scientific discussions, thank you for your quick wits and insightful viewpoints. Zeinab, I really enjoyed being involved in your project. It was fun working with you, and learning more about flocculation and algae. I am looking forward to reading your thesis!

During my PhD I have had the privilege to visit the University of Washington multiple times for a couple of months. Every time, I felt very welcome. Raul and Daniela, I was very lucky to have you as hosts. Thank you for taking care of me, giving me a glimpse of the Chilean culture, taking me on hiking trips, dinners and much more. I hope I can provide a similar experience to you if you ever come to visit Switzerland. Additionally, I would like to thank the EFM group of the University of Washington for always including me in all activities and making me feel welcome. I really enjoyed the weekly barbecues, all the drinks and dinners! It was great to meet you all!

As mentioned in the beginning, many researchers have helped me to write this thesis and to gain knowledge in different fields. Gerben de Boer, thank you for making me curious about research. I always enjoyed our discussions about ROFI's, and was always impressed by all the ideas you had. Your dissertation has been the starting point of mine. Firmijn Zijl and Wouter Kranenburg, thank you for helping me with the Delft3D model, providing valuable feedback and showing me the ins and outs of modelling. Kevin Lamb, it was a pleasure to work with you. I am impressed by your quick replies, because I know you were very busy. You gave me a crash course about internal solitary waves, and took the time to explain the physics whenever I had questions. Thank you for all your help and always being critical. Nicole Jones, I felt honoured to work with you during your sabbatical in Delft. I have learned a lot from your stay, especially in the field of internal waves and data analysis. Thank you that your door was always open and for all the evening Skype meetings. Hugo, it was great fun to explore the internal waves together. I have learned a lot from your coding skills.

The PhD would not have been the same without the support and joy from my colleagues at the Environmental Fluid Mechanics Section (both 2nd floor and Waterlab). Ad and Caroline, thank you for your support and flexibility. I really cherish the fact that you were there when I needed your help. Otti, thank you for your organizational skills, and for chats about a plethora of topics. I will not forget your advice, to stay positive and calm, and will definitely use it in the future. Xuexue, Marion, Olga, Adam, Nils, Juanma, Floris, Carine, Gal, Said, Lennart, and everyone from the Waterlab, thank you for all the nice lunches, coffee breaks, walks across campus and dinners. And not to forget, my fellow office mates over the years, who provided a great atmosphere to work in. James and Dirk, thank you for always making time to help me in the first years of my PhD. Alejandra, Silke and Irene, I was always looking forward to our Oatly cappuccino's and chats about everything. I miss our little in-person coffee breaks!

Sotiria and Steffie, we have visited summer schools and conferences together. Not to forget our writing sessions, that made writing more fun (for me at least). Maybe, we really should have rented a little house in the woods. Thank you for always being there when I needed anything. Sotiria, I am still surprised by your punctuality as a Greek. Thank you

for all your care, delicious food and not forgetting important moments in peoples life. Steffie, thank you for the endless walks on campus, the diversity of chats and a listening ear. I am really happy that I got to experience this journey together with both of you! Hopefully, more adventures will come!

During my PhD, I also had the privilege to meet great people outside my research group and department. Jasmine, Nikos and Fardin, I am glad that we shared our journeys together since the "PhD start-up course". I look back with a smile to all our nice meetups. James, Alex, Michiel, Peter and Toivo, I enjoyed all the house parties, watching football, dinners, boulder sessions and in-depth discussions.
Anouk & Linda, thank you for all the sweet cards and boundless support!

To all my friends that have supported me over these years, maybe even unknowingly, by providing a nice environment outside work. I have great memories of dinners, trips, walks, yoga sessions, overseas phone calls and not to forget a lot of tea. Thank you Ludiek, de Casa, my former housemates of RS80, my friends from Delft and from school.

I would like to thank my parents for all their patience, their everlasting faith in me, and that I can always count on them. I wouldn't be where I am now without you. Menno, thank you for being an amazing brother with whom I can always share a good laugh.

Norbert, there are not enough words to describe your contribution. Thank you for bursting my little bubble, putting a smile on my face and reminding me of my stubbornness. You introduced me to an entire new world and I hope to see much more of it.

Sabine Rijnsburger
Zürich, November 2020

List of Publications

Journal articles as first author

S. Rijnsburger, R.P. Flores, J.D. Pietrzak, K.G. Lamb, N.L. Jones, A.R. Horner-Devine, and A.J. Souza (Manuscript submitted to Journal of Geophysical Research: Oceans). Observations of multiple internal wave packets in a tidal river plume.

S. Rijnsburger, R.P. Flores, J.D. Pietrzak, A.R. Horner-Devine, A.J. Souza, and F. Zijl (Manuscript submitted to Journal of Geophysical research: Oceans). The evolution of multiple plume fronts in the tidal Rhine region of freshwater influence.

S. Rijnsburger, R.P. Flores, J.D. Pietrzak, A.R. Horner-Devine, and A.J. Souza (2018). The Influence of tide and wind on the propagation of fronts in a shallow river plume. *Journal of Geophysical Research: Oceans*, 123, 5426–5442.

S. Rijnsburger, C.M. van der Hout, O. van Tongeren, G.J. de Boer, B.C. van Prooijen, W.G. Borst, and J.D. Pietrzak (2016). Simultaneous measurements of tidal straining and advection at two parallel transects far downstream in the Rhine ROFI. *Ocean Dynamics*, 66, 719-–736.

Journal articles as co-author

S. Meirelles, A.J. Souza, A.R. Horner-Devine, J.D. Pietrzak, R.P. Flores, M. Henriquez, **S. Rijnsburger**, M. Stive, and A. Reniers (Manuscript submitted to Journal of Geophysical Research: Earth surface). The imprint of stratified tidal flow processes on ripple dynamics beneath the Rhine River plume.

R.P. Flores, **S. Rijnsburger**, A.R. Horner-Devine, N. Kumar, A.J. Souza, and J.D. Pietrzak. The formation of turbidity maximum zones by minor axis tidal straining in regions of freshwater influence. *Journal of Physical Oceanography*, 50, 1265–1287.

R.P. Flores, **S. Rijnsburger**, S. Meirelles, A.R. Horner-Devine, A.J. Souza, J.D. Pietrzak, M. Henriquez, and A. Reniers (2018). Wave Generation of gravity-driven sediment flows on a predominantly sandy seabed. *Geophysical Research Letters*, 45, 7634–7645.

A.R. Horner-Devine, J.D. Pietrzak, A.J. Souza, M.A. McKeon, S. Meirelles, M. Henriquez, R.P. Flores, and **S. Rijnsburger** (2017). Cross-shore transport of nearshore sediment by river plume frontal pumping. *Geophysical Research Letters*, 44, 6343–6351.

R.P. Flores, **S. Rijnsburger**, A.R. Horner-Devine, A.J. Souza, and J.D. Pietrzak (2017). The impact of storms and stratification on sediment transport in the Rhine region of freshwater influence. *Journal of Geophysical Research: Oceans*, 122, 4456–447.7

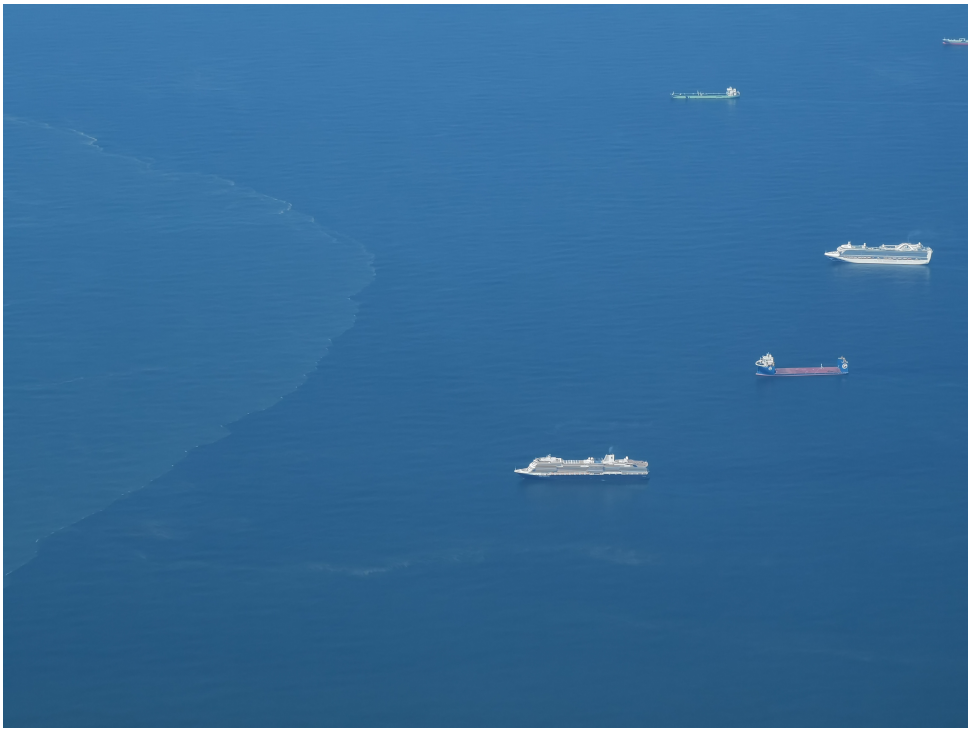

Outflow of the Rhine river just outside of the Port of Rotterdam. © Photo by Olfert Cleveringa

The Rhine tidal plume front propagating towards the coast. The photo has been taken during the STRAINS II field campaign. © Photo by Julie Pietrzak